DESIGN AND SYNTHESIS OF SELF-ASSEMBLING PEPTIDES FOR FABRICATION OF FUNCTIONAL NANOMATERIALS

A DISSERTATION SUBMITTED TO

THE GRADUATE SCHOOL OF ENGINEERING AND SCIENCE

OF BILKENT UNIVERSITY

IN PARTIAL FULFILLMENT OF THE REQUIREMENTS FOR

THE DEGREE OF

DOCTOR OF PHILOSOPHY

IN

MATERIALS SCIENCE AND NANOTECHNOLOGY

By

Mohammad Aref Khalily

December 2016

DESIGN AND SYNTHESIS OF SELF-ASSEMBLING PEPTIDES FOR FABRICATION OF FUNCTIONAL NANOMATERIALS

By Mohammad Aref Khalily

December 2016

We certify that we have read this dissertation and that in our opinion it is fully adequate, in scope and in quality, as a thesis for the degree of Doctor of Philosophy.

———————————————————
Engin Umut Akkaya (Advisor)

———————————————————
Mustafa Özgür Güler (Co-Advisor)

———————————————————
Emrah Özensoy

———————————————————
Hasan Tarık Baytekin

———————————————————
Özdemir Doğan

———————————————————
Canan Ünaleroğlu

Approved for the Graduate School of Engineering and Science:

———————————————————
Ezhan Karaşan
Director of the Graduate School

ABSTRACT

DESIGN AND SYNTHESIS OF SELF-ASSEMBLING PEPTIDES

FOR FABRICATION OF FUNCTIONAL

NANOMATERIALS

Mohammad Aref Khalily

PhD in Materials Science and Nanotechnology

Supervisor: Engin Umut Akkaya

December 2016

Self-assembling peptides are a class of supramolecular polymers, which exploit noncovalent interactions such as hydrogen bonding, hydrophobic, electrostatic, charge-transfer complex, π-π, and van der Waals interactions to generate well-defined supramolecular nanostructures including nanospheres, nanosheets, nanotubes, and nanofibers. These versatile peptide-based supramolecular nanomaterials have been utilized in variety of applications including catalysis, sensing, light harvesting, optoelectronic, bioelectronic and tissue engineering.

In this thesis, use of supramolecular peptide nanofibers formed by specially designed short peptide sequences that can form sheet-like hydrogen bonded structures for controlled synthesis of nanometer scale functional materials were explored. Specifically, n-type and p-type β-sheet forming short peptide sequences were synthesized, which assemble separately into well-ordered nanofibers in aqueous media. These p-type and n-type nanofibers coassemble via hydrogen bonding and electrostatic interactions to generate highly uniform supramolecular n/p-coassembled 1D nanowires. This smart molecular design ensures alternating arrangement of D and A chromophores within n/p-coassembled supramolecular nanowires. Supramolecular n/p-

coassembled nanowires were found to be formed by alternating A-D-A unit cells having an association constant of (K_A) of $5 \times 10^5 \, M^{-1}$.

Moreover, I designed and synthesized β-sheet forming peptide nanofibers to fabricate different metal and metal oxide nanostructures in highly controlled manner using wet chemistry and atomic layer deposition techniques. These hybrid organic-inorganic nanostructures were employed in model Suzuki coupling, alkyne-azide cycloaddition and hydrolysis of ammonia borane reactions.

Keywords: Supramolecular chemistry, self-assembling peptides, nanostructured materials, optoelectronics, atomic layer deposition, catalysis

ÖZET

FONKSİYONEL NANOMALZEMELERİN ÜRETİMİ İÇİN
KENDİLİĞİNDEN DÜZENLENEN PEPTİTLERİN
TASARIM VE SENTEZİ

Mohammad Aref Khalily

Malzeme Bilimi ve Nanoteknoloji, Doktora

Tez Danışmanı: Engin Umut Akkaya

Aralık 2016

Kendiliğinden düzenlenen peptitler, nanoküreler, nanotabakalar, nanotüpler ve nanofiberleri içeren iyi tanımlanmış supramoleküler nanoyapıları oluşturmak için, hidrojen bağı, hidrofobik, elektrostatik, yük-transfer kompleksi, π-π, ve Van der Waals etkileşimleri gibi non-kovalent etkileşimleri kullanan supramoleküler polimerlerin bir sınıfıdır. Bu çok yönlü peptit temelli supramoleküler nanomalzemeler, kataliz, algılama, ışık-hasatı, optoelektronik, biyoelektronik ve doku mühendisliğini içeren çeşitli uygulamalarda kullanılmaktadır.

Bu tezde, nanometre boyutunda fonksiyonel malzemelerin kontrollü sentezi için, özel olarak tasarlanmış, tabakaya benzer hidrojen bağlı yapılar oluşturabilen kısa peptit dizilimlerinin meydana getirdiği supramoleküler peptit nanofiberlerin kullanımını araştırılmıştır. Özellikle, sulu ortamda düzenli nanofiberleri ayrı ayrı biraya getiren, n tipi ve p tipi β-yaprağı oluşturan kısa peptit sekansleri sentezlendi. Bu n tipi ve p tipi nanofiberler, hidrojen bağı ve elektrostatik etkileşimler aracılığıyla, oldukça düzenli supramoleküler n/p-düzenli, 1D nanoteller oluşturmak

için bir araya gelmektedirler. Bu akıllı moleküler tasarım, n/p-düzenli supramoleküler nanoteller içinde D ve A kromoforlarının alternatif şekilde düzenlenmesini sağlar. Supramoleküler n/p-düzenli nanotellerin, birleşme sabiti (K_A) of 5 x 10^5 M^{-1} olan, değişimli A-D-A birim hücrelerinden oluştuğu bulunmuştur.

Ayrıca, farklı metal ve metal oksit nanoyapıları, sıvı kimyası ve atomik katman kaplama teknikleri kullanarak, oldukça kontrollü biçimde üretmek için, β-sheet yapan peptit nanofiberleri tasarlandı ve sentezlendi. Bu hibrit organik-inorganik nanoyapılar, Suzuki kenetlenme, azid-alkin siklo katılma ve amonyum boran'ın hidroliz reaksiyonlarında kullanılmıştır.

.

Anahtar kelimeler: Supramolekular kimya, kendiliğinden düzenlenen peptitler nanomalzemeler optoelektronik, atomik katman kaplama, kataliz

Acknowledgements

Contents

List of Figures

List of Tables

Abbreviations

CD : Circular dichroism

DCM : Dichloromethane

DMF : N, N-Dimethylformamide

FBS : Fetal bovine serum

dd : Double distilled

ACN : Acetonitrile

EtOH : Ethanol

D : π-electron donor

A : π-electron acceptor

HPLC : High performance liquid chromatography

LC-MS : Liquid chromatography-mass spectrometry

GC-MS : Gas chromatography-mass spectrometry

PA : Peptide amphiphile

PBS : Phosphate-buffered saline

Q-TOF : Quadrupole time of flight

AFM : Atomic force microscopy

SEM   : Scanning electron microscopy

XRD   : X-ray diffraction

STEM   : Scanning transmission electron microscopy

TIS   : Triisopropylsilane

TCP   : Tissue culture plate

TEM   : Transmission electron microscopy

TFA   : Trifluoroacetic acid

XPS   : X-ray photoelectron spectroscopy

NMR   : Nuclear magnetic resonance spectroscopy

FT-IR   : Fourier transform-infrared spectroscopy

ITC   : Isothermal titration calorimetry

TOF   : Turnover frequency

HBTU   : N,N,N′,N′-Tetramethyl-O-(1H-benzotriazol-1-yl)uranium

                 hexafluorophosphate

FMOC   : Fluorenylmethyloxycarbonyl

DIEA   : N,N-Diisopropylethylamine

Chapter 1

Introduction: Designing Peptide Based Nanomaterials

Bottom-up and top-down processing are the two strategies to fabricate nanomaterials with well-defined size, shape, composition and property [1, 2]. In latter approach, sophisticated techniques such as e-beam and atomic force microscopy based lithography are required to construct nanomaterials from bulk. While former approach, exploits noncovalent interactions such as hydrogen bonding, hydrophobic, electrostatic, charge-transfer complex, π-π, and van der Waals interactions to organize molecular elements into desired supramolecular nanostructures. Particularly, biomolecules such as peptides, nucleic acids, and lipids interact and self-organize through noncovalent interactions to produce complex structures like collagen, keratin, pearl, shell, coral, calcite microlenses, DNA and RNA which perform important functions in biological systems[3]. Although these noncovalent interactions are weak in nature, when combined together as a whole, they shape biomolecules with stable structures and crucial functions. Self-organization of biomolecules through molecular self-assembly has been of a source of inspiration for many research groups to utilize peptides, proteins, lipids, DNA and RNA as building blocks to synthesize novel nanomaterials with a broad range of applications including tissue engineering, catalysis, sensing, light harvesting, optoelectronic, and bioelectronic [4-7]. Owing to complex structure and complicated synthetic protocols of these giant biomolecules, researchers have developed bioinspired minimalistic designs based on short sequence peptides which self-assemble through noncovalent interactions into hierarchical structures. Self-assembling short peptides are a class of supramolecular polymers, which exploit supramolecular interactions to generate well-defined nanostructures including nanospheres, nanosheets,

nanotubes, and nanofibers (Figure 1) [8]. These versatile peptide-based supramolecular nanomaterials have been utilized in variety of applications which will be discussed in next section .
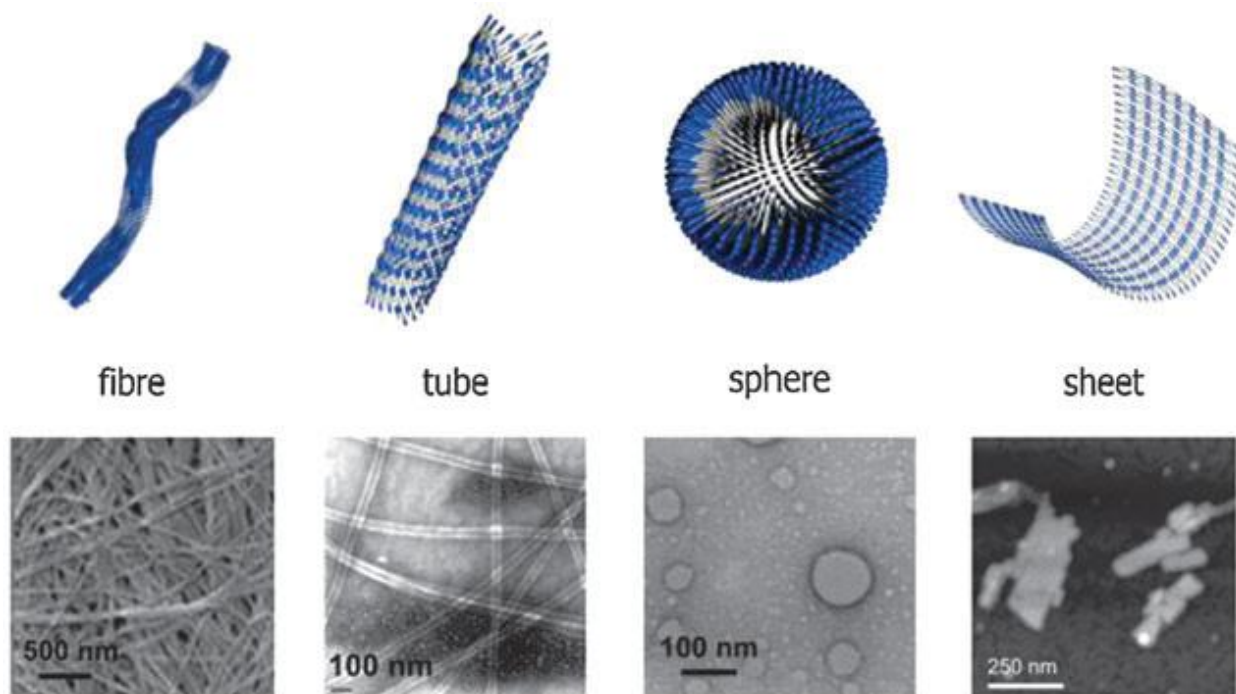
Figure 1.1 Supramolecular structures formed via short peptide self-assembly. (Figure adapted from ref. 8)

There are 20 natural amino acids (Figure 1.2) which are the building blocks for synthesis of peptides and proteins in biological systems. All amino acids have a stereogenic center with L configuration accept glycine. The basic chemical structure of amino acids is similar with different side chains in central carbon (C_α). Based on diverse side chains, amino acids can be classified as hydrophobic (A, V, L, l, and M), aromatic (F, W and Y), negatively charged (D and E), positively charged (H, K and R) and hydrophilic (S, N, Q and T) (Figure 1.2) [9].
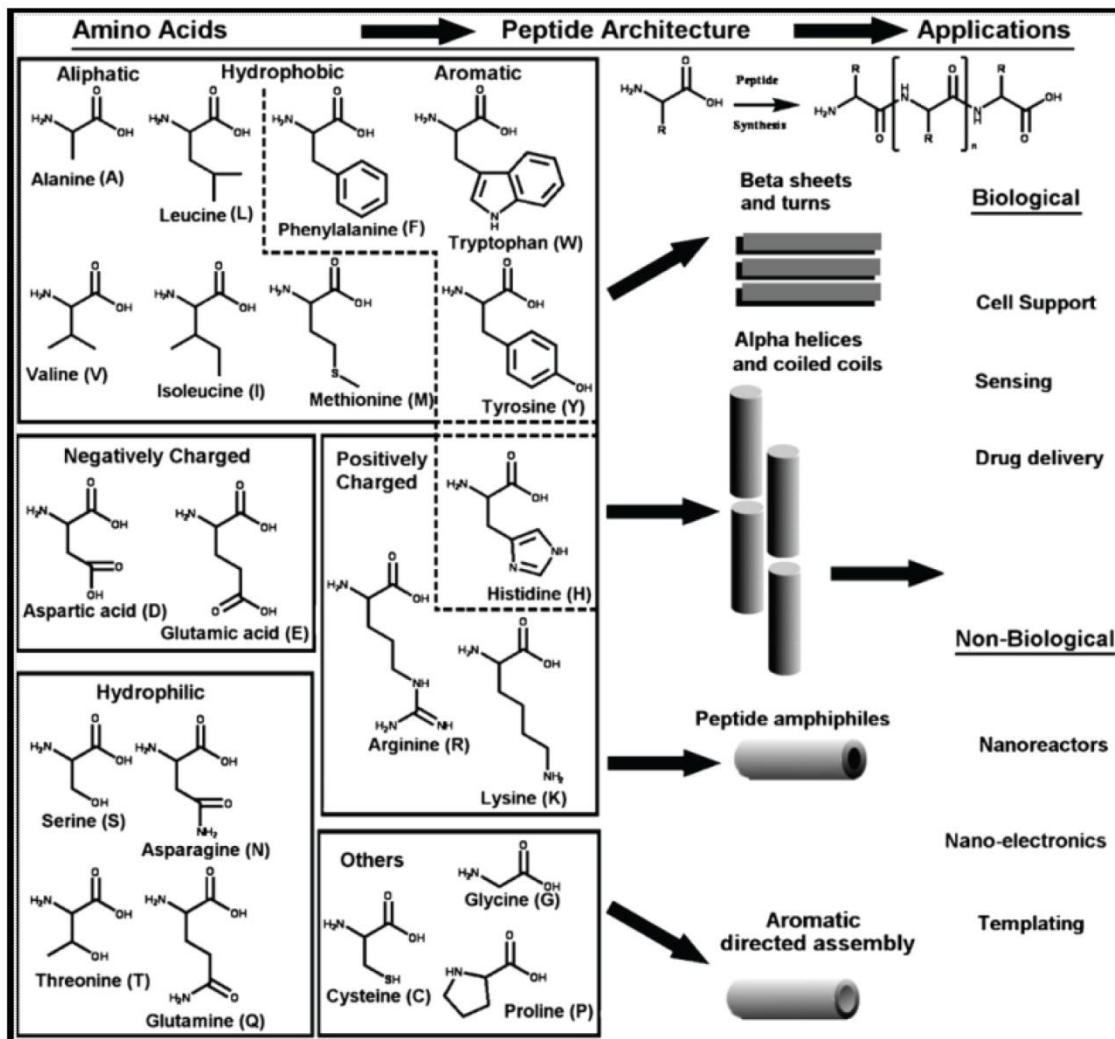
Figure 1.2 Chemical structures of natural amino acids. Different peptide-based nanostructures with some potential applications. (Figure adapted from ref. 9).

The chemical nature of side chains of amino acids is highly important in governing the structure and function of peptides and proteins in biological environment. Due to large number of amino acids with rich functional groups, the number of peptide sequences and structures is endless. Therefore, rational arrangement of amino acid sequence is extremely vital to get the desired nanostructures. Several research groups have put effort to design self-assembling short sequences

based on dipeptides, tripeptides, and longer peptide sequences to acquire different supramolecular nanostructures. Self-assembling peptide designs to produce nanostructures will be explained in coming section.

1.1 Amyloid-inspired peptide nanostructures

Formation of amyloid nanostructures which is associated with neurodegenerative diseases including Alzheimer's disease and Parkinson's disease has long been under study. Amyloids are produced from different peptide and protein aggregates. Structural studies and mechanistic understanding of amyloid structures have come out with various peptide sequences which can self-assemble into β-fibrils. Heptapeptide Aβ (16–22), Ac-KLVFFAE-Am, cationic core section of the Alzheimer's disease can assemble into β-sheets and forming nanotubes [10]. These well-defined nanotubes have a 52 nm cross-sectional diameter and lengths in microns (Figure 1.3). Many groups have been inspired by these short self-assembling peptide sequences and made trivial modifications to get different nanostructures. For example, Ac-E-FFAA-E-Am and Ac-K-FFAA-K-Am sequences can form nanofibers having negative and positive charges respectively[11]. FF in AAKLVFF-OH can be replaced by aromatic moieties like thiophene (2-Thi)(2-Thi)VLKAA) to generate well-ordered nanofibers in methanol [12].
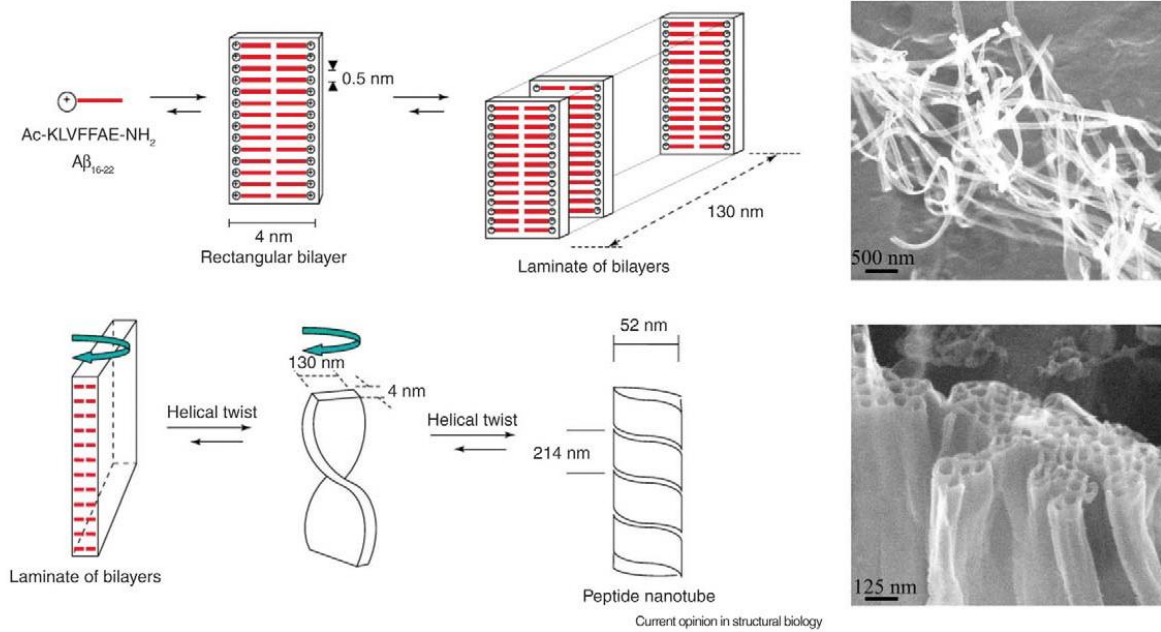
Figure 1.3 Proposed mechanism for the self-assembly of Ac-KLVFFAE-Am into nanotubes (left). High resolution cryo-TEM images of nanotubes (right). (Figure adapted from ref. 10)

Another interesting bioinspired self-assembling peptide molecule is diphenylalanine (FF) dipeptide, the core recognition motif of the β-amyloid polypeptide, self-organizes via π-π interactions between phenyl groups to form highly-ordered nanostructures [13]. Diphenylalanine dipeptide is one of the simplest self-assembling sequences which can aggregate into different structures from nanoscale to microscale (Figure 1.4). Owing to its structural simplicity, facile synthesis, and widespread applications, it is a widely studied self-assembling peptide. FF supramolecular nanotubes can easily be formed by diluting the concentrated solution of FF in fluorinated alcohol by water. The morphology of the FF nanostructures can be readily manipulated and controlled by experimental conditions such as pH, temperature, peptide concentration and solvent to get vesicles, tubes, rods and strips at nano to microscale [14].
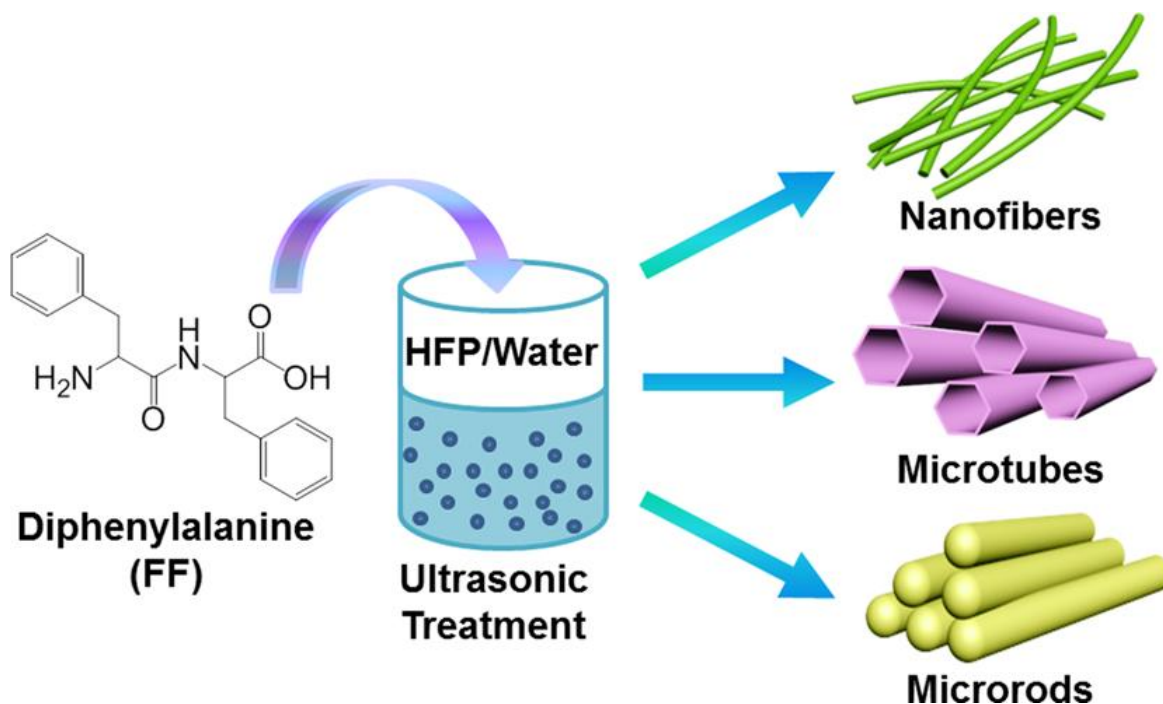
Figure 1.4 Self-assembly of FF into different morphologies. (Figure adapted from ref. 13 Copyright 2015 American Chemical Society)

1.2 Peptide bolaamphiphile based nanostructures

Bolaamphiphilic peptides are another well studied design composed of peptidic and non-peptidic parts. In this design, a hydrophobic molecule (aliphatic or aromatic molecules) is integrated polar or charged amino acids from two arms (Figure 1.5). When dissolved in aqueous media, the bolaamphiphilic monomers arrange themselves in such way that charged motifs expose to water while hydrophobic segments escapes from water and forming nanotubes. The driving force for the formation of nanotubes in this peptide design is either hydrogen bonding and/or π-π interactions [10, 15]. Depending on the design of monomer molecules, the nanotubes can adopt diameters ranging from nanometers to micrometers. Bolaamphiphilic peptide design is especially important in construction of supramolecular organic nanowires in aqueous media by providing

efficient cofacial π-π interactions among hydrophobic semiconducting chromophores. Efficiency of charge transport, energy migration and mobility of charge carriers in these supramolecular one-dimensional (1D) nanowires is directly dependent on supramolecular order of π-conjugated chromophores. Interestingly, this molecular design ensures *H*-type π-π interactions among hydrophobic semiconducting chromophores in aqueous medium. More examples and explanations will be provided in section 1.6.
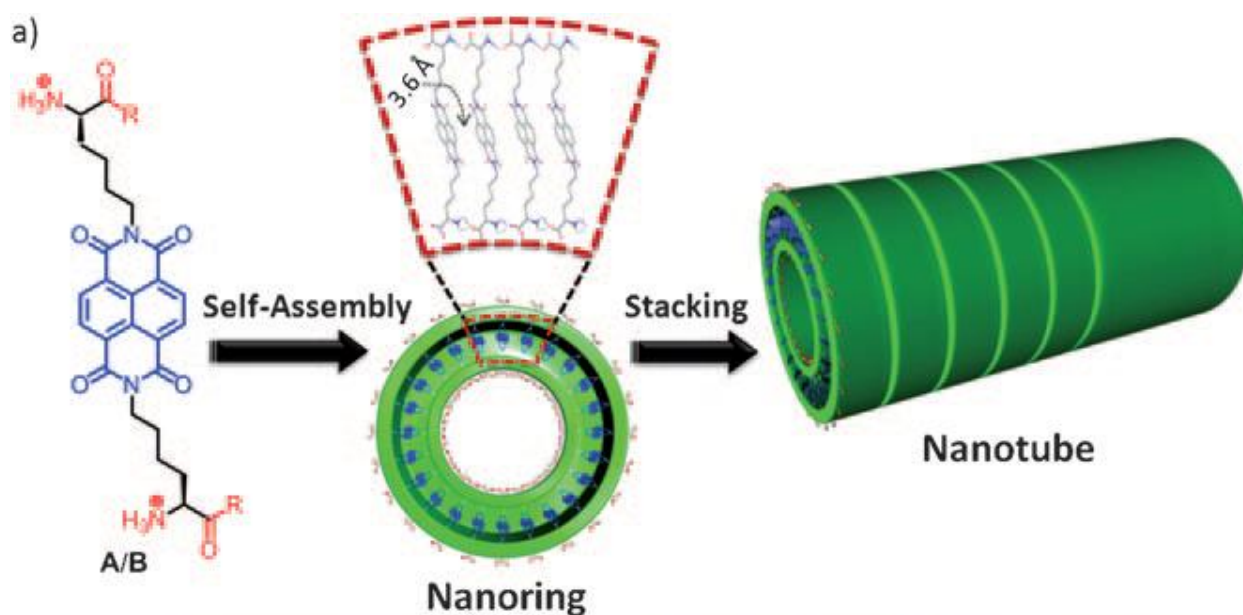
Figure 1.5 Self-assembly of bolaamphiphile monomers into nanotube morphology. (Figure adapted from ref. 15. Copyright © 2010 WILEY-VCH Verlag GmbH & Co.)

1.3 Cyclic peptide based nanostructures

In 1993 Ghadari [16] demonstrated that stacking of cyclic D, L-peptide rings can produce high respect ratio hollow nanostructures (Figure 1.6). The sequence of octapeptide cyclo [-(l-Gln-d-Ala-l-Glu-d-Ala)$_2$-] dissolved in basic solution could not aggregate due to columbic charge repulsion among carboxylate groups (COO$^-$). Well-ordered nanotubes were formed upon charge neutralization by controlled addition of acid into solution of cyclo [-(l-Gln-d-Ala-l-Glu-d-Ala)$_2$-]. The divining force behind self-assembly of cyclic D, L-peptide rings is anti-parallel β-sheet hydrogen bonding to form nanotubes with a van der Waals internal diameter of approximately 7 Å. Several derivatives of cyclic D, L-peptide were synthesized to be utilized in wide range of applications like sensing, targeted drug delivery and optoelectronics [16, 17].
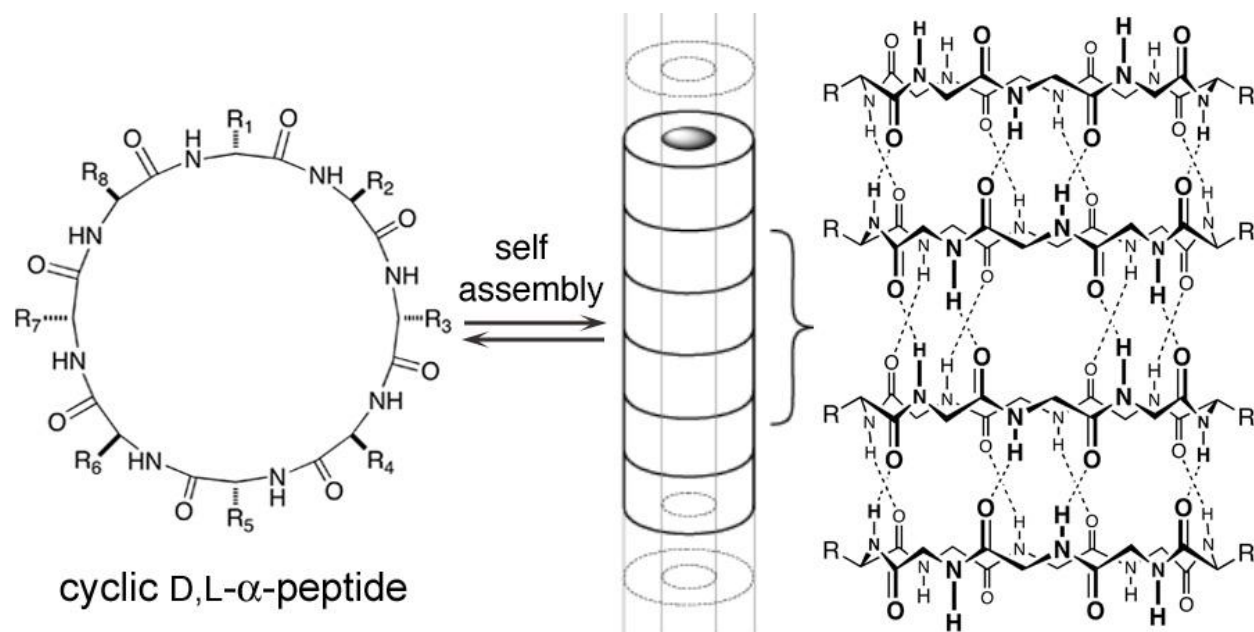
Figure 1.6 Self-assembly of cyclic D, L- peptide into nanotubes morphology. (Figure adapted from ref. 16. Copyright © 2001 WILEY-VCH Verlag GmbH & Co.)

1.4 Peptide amphiphile based nanostructures

Another interesting class of short self-assembling peptides is amphilphilic peptides [18]. Typical peptide amphiphile molecule is consisted of hydrophobic and hydrophilic segments. Hydrophobic fragment is composed of an aliphatic tail or an aromatic moiety plus β-sheet hydrogen bonding amino acids such a valine and alanine. While charged amino acids like glutamic acid or lysine constitutes the rest of peptide amphiphile fraction (Figure 1.7).
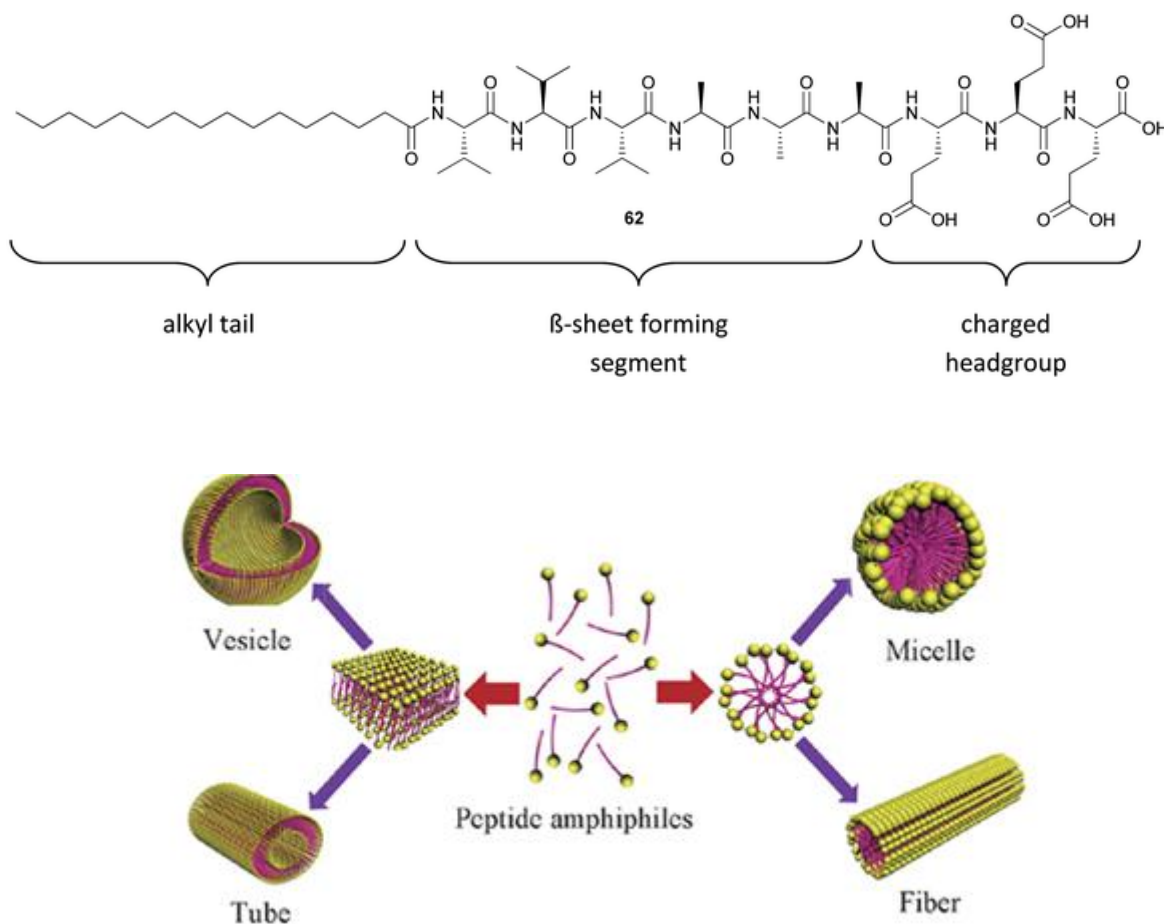
Figure 1.7 Typical chemical structure of peptide amphiphile and it's self-assembly into various supramolecular nanostructures.

The peptide sequence in figure 1.7 with an alkyl tail and β-sheet sequence prefers to form cylindrical nanofibers. Replacing β-sheet forming residues (valine and alanine) with hydrogen breaking moieties such as proline give rise to spherical nanostructures. Slight changes in chemical structure of peptide amphiphile or experimental conditions such as pH, temperature, sonication, ionic gradient, peptide concentration and solvent can produce well-defined nanostructures with diverse morphologies (Figure 1.7) [19].

Besides above mentioned self-assembling peptide designs, many research groups have designed and synthesized novel self-assembling peptide sequences based on pure amino acids, peptide-small molecule and peptide-polymer conjugates to obtain supramolecular nanostructures having various morphologies for variety of applications [18, 20] .

One of the main reasons for the widespread studying and utilization of short self-assembling peptides is the development of well established synthetic procedures to get peptides with high purity and efficiency without rigorous purification and work-up processes. Solid-phase peptide synthesis (SPPS), pioneered by Robert Bruce Merrifield, is now the classic synthetic method to manufacture peptides and proteins [21]. There are mainly two forms of SPPS- **Fmoc** and **Boc**. Chemically stable and insoluble polystyrene microbeads (resin) are used as solid support to grow peptide chains step by step. These polymer based solid supports are functionalized by linkers having amine or hydroxyl groups. Peptides can be obtained with amide or carboxylic acid C-terminal depending on choice of functionalized polystyrene solid supports. Unlike natural synthesis of proteins in ribosome, peptides are synthesized from C to N-terminal. Fmoc protected amino acids are now commercially available in large scales for suitable prices. To start peptide synthesis (Figure 1.8), polystyrene bead is swelled in DCM for 30 minutes then carboxylic acid group of N-terminal Fmoc protected amino acid is activated by HBTU and then reacted with free

amine groups on solid resin to form amide bonds. A Kaiser test is performed after thoroughly

washing of resin with DMF and DCM to test if the amino acid is successfully conjugated on

resin. For the conjugation of second amino acid, Fmoc of first amino acid is removed by solution

of piperidine to get free amine groups to react with carboxylic acid groups of second amino acid.

Using this simple procedure a peptide sequence up to 70 amino acids can readily be grown on

solid resins (Figure 1.8). The peptide sequence can be cleaved from solid resin in the presence of

concentrated TFA solution. After cold ether precipitation, pure peptide powder can be obtained

in high yield.
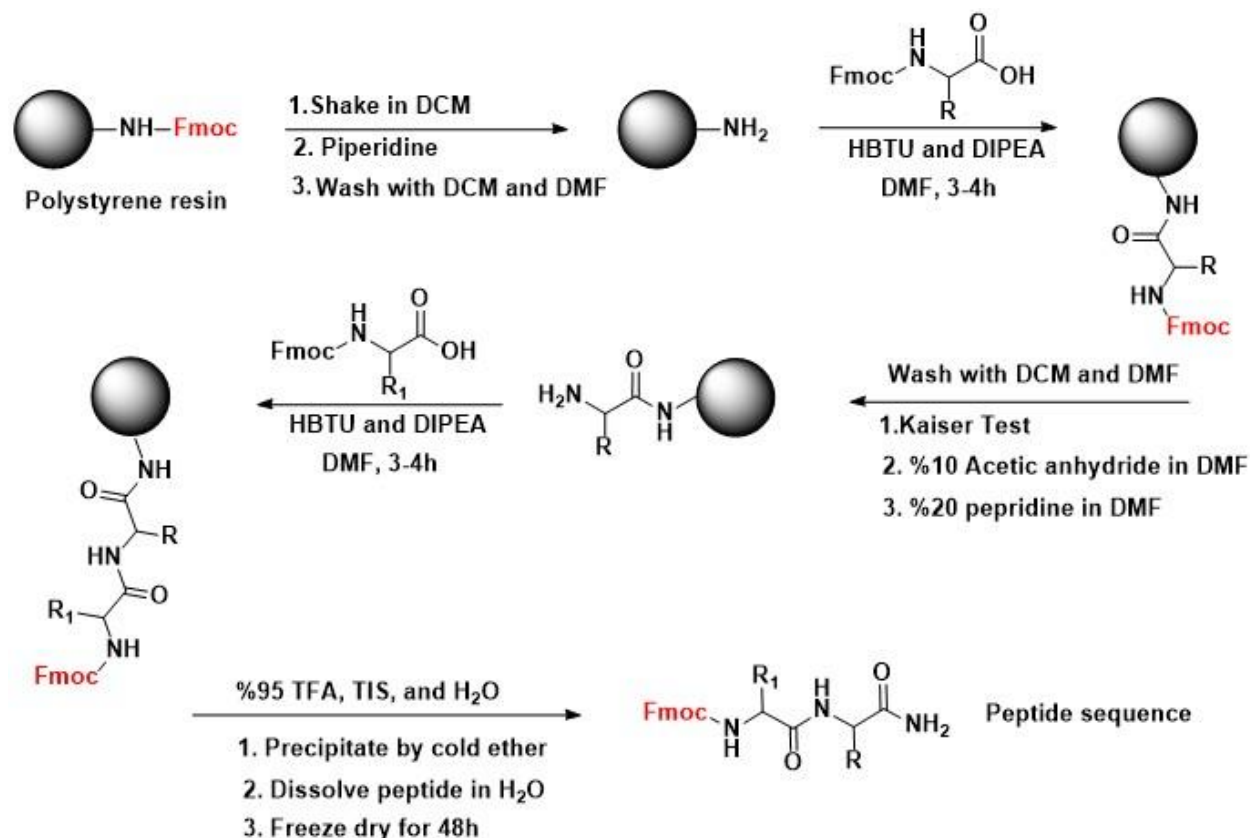
Figure 1.8 Standard solid-phase peptide synthesis procedure based on Fmoc chemistry.

11

Applications of self-assembled peptide nanostructures

This part is partially described in the following publication:

Melis Sardan Ekiz, Goksu Cinar, Mohammad Aref Khalily and Mustafa O Guler "Self-assembled peptide nanostructures for functional materials" *Nanotechnology 27 (2016) 402002*

In this section, I will review technological applications of short self-assembled peptide nanostructures.

1.5 Supramolecular Self-Assembled Peptide Catalysts

Extraordinary catalytic performance and superior selectivity of enzymes in organic transformations under physiological conditions have always been a source of inspiration to scientists. Complex structure and function of biocatalysts has enforced scientists to develop minimalistic approaches and mimic a fragment of multifaceted biocatalysts such as active site, hydrophobic pocket, or structure [22]. Of those minimalistic approaches, supramolecular self-assembled peptide nanostructures have been utilized to assemble essential functional groups within a nanoenviroment to catalyze desired organic transformations in an efficient manner.

Stupp showed self-assembling peptide amphiphiles which aggregated into well-defined catalytic nanostructures in aqueous media [23]. In this study, four different peptide sequences containing histidine residue as reactive site were designed and synthesized (Figure 1.9A and B). The peptide **1** having alanine and valine residues promoted formation of β-sheet and palmitoyl tail assisted hydrophobic collapse of the peptide molecules into high respect ratio 1D nanofibers as shown in Figure 1.9C.
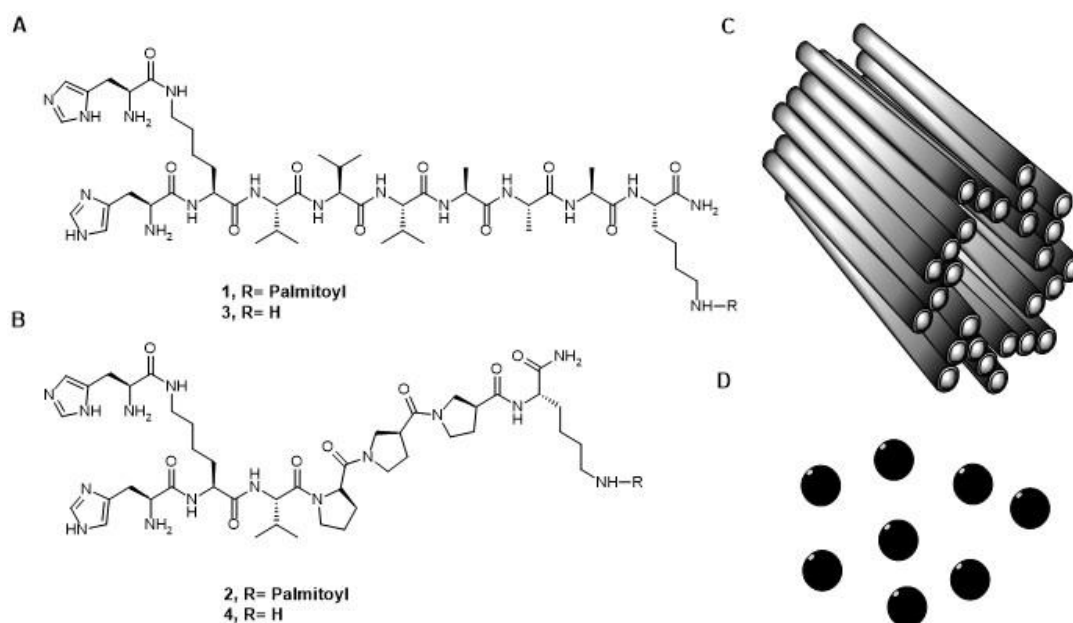
Figure 1.9 Chemical structures of peptide molecules (A and B), schematic representation of self-assembled nanofibers (C) and spherical aggregates (D).

The same peptide sequence without palmitoyl tail (**3**) formed nanospheres (Figure 1.9D), meanwhile, the peptide sequences having proline residues (**2 and 4**) also formed polydisperse nanospheres. Hydrolysis of 2, 4-dinitrophenyl acetate (DNPA) by these nanostructures have shown that 1D nanofibers promoted highest hydrolysis rate when compared to nanospheres or soluble histidine residue. Interestingly, 1D nanofibers showed a Michaelis-Menten enzyme-like behavior whereas the other peptide sequences (**2-4**) demonstrated a linear rate increase with substrate concentration increase. This study showed that assembling reactive sites within a nanoenviroment could afford a synergistic effect which enhanced the rate of hydrolysis of DNPA.

This study was one of the first examples of supramolecular assembled peptide catalyst which inspired many research groups to develop new catalytic supramolecular peptide nanostructures. Escuder and Miravet research groups have extensively studied the structure and catalytic activity of proline based supramolecular gelators [24]. L-proline is a well-known stereoselective organocatalyst to catalyze C-C bond formation reactions, such as aldol and Michael addition reactions [25]. A series of bolaamphiphilic molecules consisting of two L-prolines were designed and used in aldol reactions [26]. Due to presence of hydrogen-bond promoting valine residues in the structure of bolaamphiphilic peptide molecules, they could encapsulate large amount of organic solvents (acetonitrile and ethyl acetate) to form organogels. These peptide molecules catalyzed the aldol reaction in solution state while racemisation of the products was observed in gel state when the reactions were left for several days. The reason for racemisation was explained by increase of basicity of the solution due to the close assembly of prolines in the gel state. The authors exploited the emergence of new property (increased basicity) caused by cooperativity of neighboring prolines in gel state [27]. They chose Henry (nitro-aldol) reaction which requires a basic catalyst for deprotonation of nitroalkane and then addition to carbonyl functional group to form new C-C bond. A bolaamphiphile peptide molecule was used to form gel in nitromethne and nitroethane. This basic catalytic gel promoted the addition of nitroalkane to 4-nitrobenzylaldehyde as shown in Figure 1.10. The assembled bolaamphiphile peptide molecules into fibrous networks showed excellent catalytic activity while dispersed peptide molecules showed poor catalytic activity.
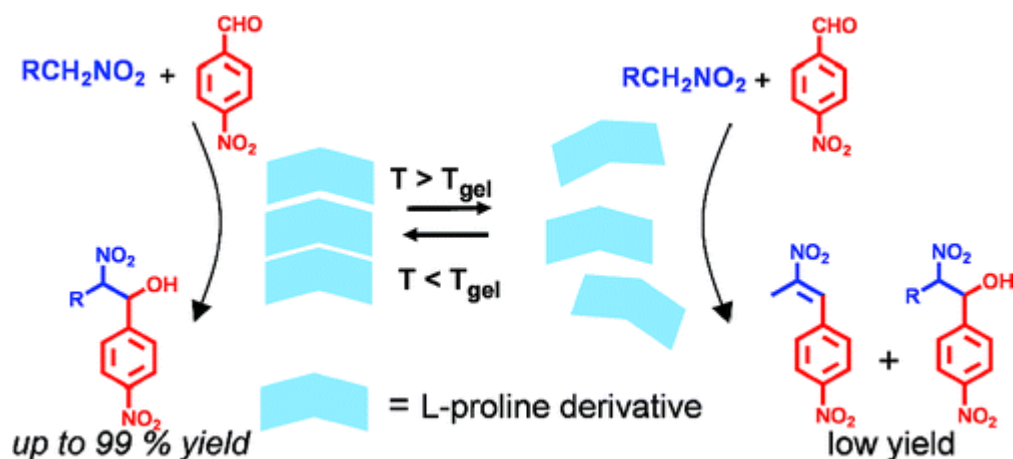
Figure 1.10 Schematic representation of L-proline catalyzed Henry nitroaldol reaction.

Performing organic reactions in aqueous media motivated the researchers to synthesize a new proline conjugated amphilphilic peptide molecules which formed hydrogels [28]. This catalytic hydrogel assisted the direct aldol reaction between cyclohexanone and 4-nitrobenzaldehyde. The reactants dissolved in toluene were gently dropped on pre-formed peptide hydrogel showed high stereoselectivity (anti: syn 92:8, 88% ee). The catalytic hydrogel was recycled three times without loss of efficiency and stereoselectivity.

Beside L-proline based supramolecular catalysts, the researchers have also developed different novel approaches to mimic active sites of enzymes. Junqiu Liu and his co-workers demonstrated that co-assembly of two different amino acid residues could enhance the rate of hydrolysis [29]. They synthesized two short amphilphilic peptide sequences one bearing histidine (Fmoc-FFH-$CONH_2$) and other bearing arginine residues (Fmoc-FFR-$CONH_2$). The Fmoc-FFH-$CONH_2$ molecules aggregated into nanotube in aqueous medium could catalyze p-nitrophenyl acetate in efficient manner. Upon co-assembly of Fmoc-FFH-$CONH_2$ and Fmoc-FFR-$CONH_2$ peptides into nanotubes, the catalytic activity was further enhanced. A similar study was conducted by Liang

research group [30]. Co-assembly of histidine and arginine bearing self-assembled peptide nanofibers could enhance the hydrolysis of catalyze p-nitrophenyl acetate. These two studies underlined the importance of arginine residues which stabilized the transition state of the hydrolytic reaction.

Metal ions play an important role as cofactors in metalloenzymes. The metal ion based cofactors are present in the active site of enzymes which aid the chemical reactions to proceed [31]. Mimicking a part of metalloenzyme by short sequenced self-assembled supramolecular peptide nanostructures decorated metal ions is another interesting research field. Liu and coworkers have designed and synthesized glutamic acid bearing bolaamphiphile nanotubes which copper (II) ions could bind via electrostatic interactions. The produced nanotubes induced chirality to copper (II) ions could catalyze the Diels-Alder reaction between cyclopentadiene and an aza-chalcone [32]. Korendovych research group conducted a more detailed and systematic study on short sequenced metallopeptides to mimic metalloenzyme. A series of short amyloid-forming peptides which have binding affinity towards Zn (II) ions were designed and synthesized [33]. A β-sheet forming heptapeptide sequence (LKLKLKL) was modified at position 2, 4 and 6 by different amino acids. Hydrophobic leucine (L) required for self-assembly kept unchanged while Lysine (K) residues at positions 2 and 4 were replaced by Zn^{+2}-binding histidines. K at position 6 was replaced by either acidic (Asp, Glu), neutral (Gln, Tyr) or basic residues with various pKa values (His, Lys, Arg). The peptide sequence Ac-LHLHLRL-CONH$_2$ in the presence of ZnCl showed Michaelis–Menten behavior with catalytic efficiency of $K_{cat}/K_M = 18\pm4$ M^{-1} s^{-1}. When the R was replaced by Q residue (Ac-LHLHLQL-CONH$_2$) the catalytic efficiency was further increased to $k_{cat}/K_M = 30\pm3$ M^{-1} s^{-1}. Peptides having Asp, Glu or His residues at position 6 had little catalytic activity. When the hydrophobic L was replaced by isoleucine (I) in the heptapeptide sequence

keeping Gln at 6th position (Ac-IHIHIQI-CONH$_2$) further enhancement of catalytic efficiency ($k_{cat}/K_M = 62\pm2$ M^{-1} s^{-1}) was observed.

We recently also developed a β-sheet forming peptide amphiphile which had high binding affinity towards copper ions. This short peptide sequence assembled into nanofibers having histidine residues over the surface. The copper ions bound on pre-assembled peptide nanofibers could catalyze click alkyne- azide cycloaddition in aqueous media [34]. The conversion of the reactants into product was almost quantitive (95%) by our supramolecular nanocatalyst while soluble histidine-Cu complexes showed a moderate efficiency of 65%. Active sites demonstrated positive cooperativity when assembled within a nanoenviroment on peptide nanofibers. Supramolecular nanocatalyst did not only show superior catalytic activity but also lowered the cytotoxicity of the copper ions. Therefore, we utilized the metallopeptide to label alkyne decorated live cells by click alkyne- azide cycloaddition.

1.6 Supramolecular Semiconductor Peptide Nanostructures

Organic electronics can be divided into three major field's namingly supramolecular, plastic, and molecular electronics [35]. The latter two fields are studied in detail and Nobel Prize in chemistry was awarded to discovery of electrically conductive polymers (plastic electronics) in year 2000. While supramolecular electronics is much lesser studied research field but promising research progress has been achieved in last decade. Supramolecular chemistry is a powerful tool to design and construct well-defined nanowires for nanosized optoelectronic devices using noncovalent interactions. The rich chemistry of 20 natural amino acids makes them an eye-catching tool to build novel supramolecular soft semiconducting materials which could be

employed for bioelectronics [36], light harvesting systems [37], OFETS, nanosized devices and nanosensors [38].

The main strategy to fabricate a nanosized semiconducting wire is to conjugate hydrophobic, pi conjugated p-n type semiconductor molecules to hydrophilic or charged self assembling peptide sequences. Upon hydrophobic collapse in aqueous media, the semiconducting conjugated peptide molecules can form variety of nanostructures. This strategy also allows working with highly hydrophobic molecules in aqueous media. Parquette and co-workers conjugated a n-type semiconducting molecule (1,4,5,8-naphthalenetetracarboxylic acid diimide, NDI) to s series of dipeptides (Ac-KK-NH$_2$) and studied their self-assembly in aqueous medium and trifluoroethanol (TFE) [39]. The NDI semiconductor peptide conjugate assembly was studied by UV and circular dichroism spectroscopies. The NDI-peptide molecule dissolved in TFE showed absorption peaks at 240 nm (band II) and in the range of 300-400 nm (band I) which are characteristic absorption peaks of molecular NDI molecules. When TFE changed with water there was a decrease in absorption intensities followed by large red shift in the absorption bands of NDI. This change showed the formation of j-aggregates in water. The IR bands at 1612 and 1608 cm^{-1}, and XRD analysis proved the presence of β-sheet in Ac-KK (NDI)-NH$_2$ and in Ac-K(NDI)-KNH$_2$ peptides. TEM and AFM images of Ac-KK(NDI)-NH$_2$ peptide molecules showed helical nanofibers while Ac-K(NDI)-KNH$_2$ peptides showed flattened, twisted nanoribbons morphology. The same research group conducted a similar study by conjugating two lysine moieties to the two arms of NDI forming n-type bolaamphiphile [15]. Bolaamphiphile molecules formed hydrogel when in dissolved 1% (w/w). The designed molecule formed nanotubes as imaged by TEM and AFM. Uv-vis absorption spectroscopy demonstrated a red shift in the absorption bands showing the formation of NDI *j*-aggregates in assembled state. CD

18

spectra revealed peaks at the absorption bands of NDI molecule demonstrating induced chirality rooted from supramolecular organization of NDI molecules within the assembled nanotubes. Fluorescence decay of 350 nm excited nanotubes was followed by time-correlated single photon counting at 410 and 505 nm. The life time (64 ps) of excited NDI nanotubes were slightly longer than the molecular NDI. The excimer emission at 505 nm showed much longer decay life time (197 ps (86%) and 950 ps (14%)) which is due to closely stacked and packed NDI molecules in nanotube.

Tovar [40-45] and others [46-48] have developed semiconducting oligomers conjugated to peptides (Figure 1.11) assembled into well defined nanostructures in aqueous media. In this design, oligomers are located at middle and peptide sequences are conjugated at two sides. This strategy facilitates face to face aggregation of the semiconducting molecules which can enhance the hole or electron transporting properties as a consequence amplified conductivities could be achieved. Tovar research group also developed a straightforward method to conjugate oligomers molecules on solid phase resin. On resin synthesis avoids multiple synthetic routs and complex purification techniques. Charge transport properties of assembled soft fibrous nanonetwork were measured by constructing a field-effect transistor. The peptide conjugated quaterthiophene was used as semiconductor layer and mobility of 10^{-3} -10^{-5} cm^2 /(V s) was measured. When the nanowires were aligned via shear-assembly the mobility were increased to 0.03 cm^2 /(V s).
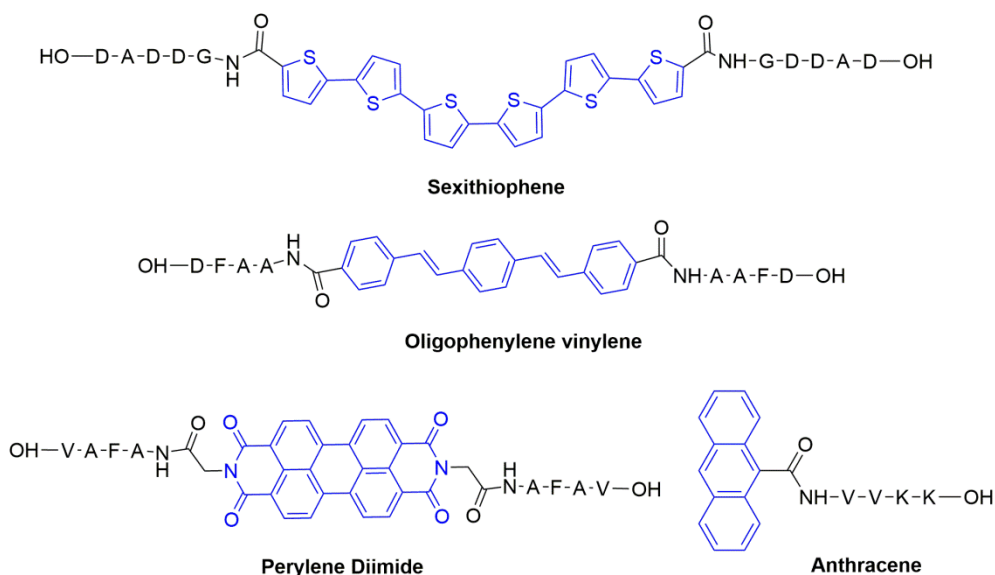
Figure 1.11 Semiconducting oligomers conjugated to peptide molecules.

Ashkenasy and her workers conducted a detailed study of conductivities of self-assembled semiconducting peptide nanostructures [12, 49]. A well-known amyloid β-peptide AAKLVFF was studied by incorporating 2-thienylalanine and 3-thienylalanine moieties instead of FF. They investigated the self-assembly of these molecules in different solvents and different morphologies were formed. They observed that peptide molecule forming long range and straight nanofibers show highest conductivity. In another research work, Ashkenasy demonstrated that the both protons and electrons are responsible for charge transport process in self-assembled nanostructures. In highly humid environment proton conductivity dominated electron conductivity. Hodgkiss *et.al.* has recently constructed a water-processed bio-organic field-effect transistor (biOFET) based on bioinspired assembled peptide-pyrelene conjugates [50]. The peptide sequence IKHLSVN which is responsible for homo dimmerization of peroxiredoxin protein was modified as IRHLSVN. Three glumatic acid residues were conjugated to IRHLSVN to enhance the solubility of IRHLSVN-perylene molecules in water. The self-

assembly of these bioinspired molecules were studied by CD and Uv-vis spectroscopy to see whether the β-sheet forming characteristic of native IKHLSVN sequence was affected by the modifications and perylene conjugation. Long nanofibers of assembled IRHLSVN-perylene were imaged by TEM and AFM. Interestingly, the semiconducting nanofibers showed p-type behavior upon increasing positive gate bias a decreasing current trend was measured.

One component semiconductor-peptide self-assembly was further extended to two components including co-assembly of p-n type semiconductors to achieve charge-transfer or photo (conductive) supramolecular nanomaterials. Ulijn group [51-53] have conducted a series of research on biocatalytic self of n-type semiconductor conjugated peptides that could form charge-transfer supramolecular nanostructures with variety of p-type semiconductors (Figure 1.12). NDI-functionalized tyrosine (NDI-Y) was conjugated to phenylalanine-amide (F-NH$_2$) by addition of thermolysin to trigger the self-assembly and forming thermodynamic nanostructures. At the presence of p-type dihydroxy/alkoxy naphthalene donors, NDI-Y forms polydisperse spherical nanostructures when thermolysin was absent as imaged by TEM and AFM. Upon addition of biocatalyst to solution of NDI-Y and naphthalene donors, a yellowish gel was formed and spherical nanostructures were converted to highly-ordered long nanofibers. The change in color of solution followed by donor emission quenching and appearance of new absorption at 550 nm was the evidence for formation of charge-transfer complex. The same group conjugated a well-known p-type tetrathiafulvalene (TTF) to a self-assembling peptide sequence (-FF-NH$_2$). TTF-FF-NH$_2$ molecules formed self standing gel in chloroform and dried gels showed conductivity of 1.9×10^{-10} S cm^{-1}. When the organogel was doped by an acceptor molecule (TCNQ) the conductively was increased to 3.6×10^{-4} S cm−1. However, iodine vapor doping did not enhance the conductivity to a great extent as in case of acceptor doping [54]. There are also

some studies showing the energy transfer within self-assembled peptide nanostructures through donor-acceptor interactions [55, 56].
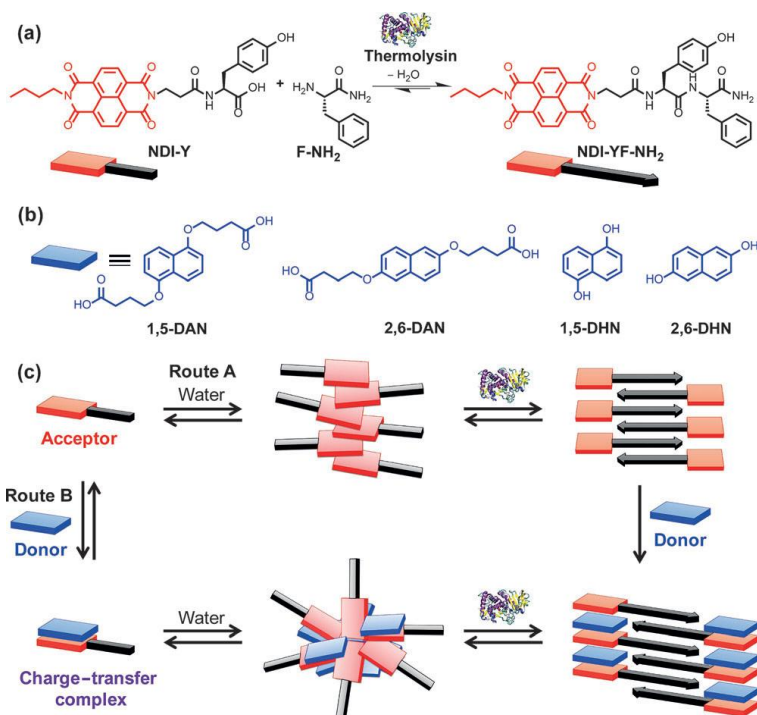
Figure 1.12 Biocatalytic self-assembly of acceptor-appended peptides to form charge-transfer nanostructures.

Recently, Martín research group has exploited electrostatic interactions to assemble donor-acceptor molecules in highly organized manner within a peptide nanofiber [57]. Electron donor tetrathiafulvalene was conjugated to anionic peptide sequence bearing glutamic acid while electron-acceptor perylene-bisimide was conjugated to cationic peptide sequence bearing residue. These two complimentary p-n nanofibers could co-assemble into highly alternating p-n stacks in the single nanofiber. The co-assembled p-n nanofibers showed photoconductivity of 0.8 cm^2 V^{-1} s^{-1}. These kinds of novel and straightforward methodologies are promising for design and fabrication of next generation nanodevices.

1.7 Self-Assembled Peptide Templated Synthesis of Inorganic Nanomaterials

Synthesis of inorganic nanomaterials with precise shape, size and composition has potential industrial applications. Biomolecules having well-defined shapes and sizes are remarkable platforms for synthesis of inorganic functional nanomaterials [58]. Cutting-edge developments have been achieved by utilizing biotemplates such as viruses [59-61], bacteria [62, 63], nucleic acids [64] (DNA or RNA) and proteins [65, 66] to mineralize clear-cut functional nanomaterials for catalysis, sensing, imaging, therapy, energy storage/ conversion, electronic and piezoelectric devices. Self-assembling peptide templated synthesis of functional nanostructures is another emerging area which has been extensively studied.

Matsui *et. al* designed a bolaamphiphile peptide molecule (bis (*N*-R-amido-glycylglycine)-1,7-heptane dicarboxylate) which assembled into nanotubes at pH 6 citric acid/NaOH solution. The amide groups on preassembled nanotubes could coordinate with metal ions (Cu and Ni) which served as nucleation sites. Nanotube coated ions were further reduced by reducing agents to get metalized nanotubes [67]. In another study conducted by Matsui, same bolaamphiphile peptide nanotube was further modified by a histidine rich peptide sequence (A-H-H-A-H-H-A-A-D). Histidine modified nanotubes were treated with gold ions followed by $NaBH_4$ reduction to form gold nanoparticles (Figure 1.13). Metal binding histidine residues directed formation of gold nanoparticles over nanotubes homogenously. The crystal lattice of gold nanoparticles were calculated as (111) and (220) from electron diffraction patterns[68].
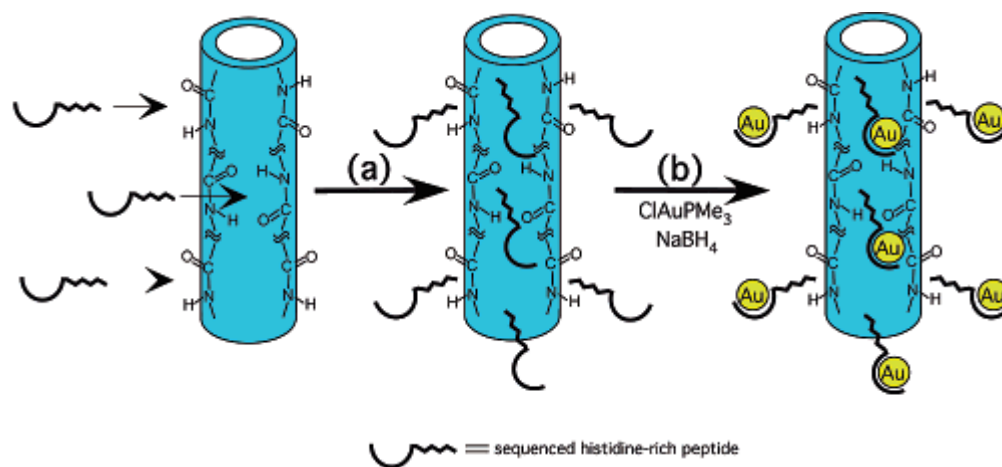
Figure 1.13 Scheme of Au nanowire fabrications. (a) Modification of preassembled nanofibers by histidine-rich peptide (b) Formation of gold nanoparticles on nanofibers.

Stupp research group also developed unasymmetric bolaamphiphile peptide molecules such as (L-Glutamyl)$_3$ glycine-terminated bolaamphiphile (**1**) and (L-lysine)$_3$- terminated bolaamphiphile (**2**). Molecule **2** formed self standing hydrogel in the presence of ammonia vapor. The secondary structures of these two molecules were studied by circular dichroism (CD). The peptide molecules showed random coil structure in their soluble form while β-sheets were observed upon gelation. These 1D nanofibrous networks made of **1** and **2** were utilized to mineralize CdS nanostructures. Peptide hydrogels of **1** and **2** were treated with dilute solution of Cd(NO$_3$)$_2$ followed by exposure to H$_2$S vapor. Molecule **1** templated CdS nanostructures having wurtzite polymorph crystal structure while molecule **2** templated CdS nanostructures having zinc blende crystal polymorph structure [69].

In another study, Stupp *et. al* developed a self-assembling peptide amphiphile bearing 3 histidine residues as metal ion binding [70]. The peptide amphiphile molecule dissolved in water formed hydrogel upon increasing pH above 6. The hydrogel was consisted of peptide nanofibers having

8-10 nm diameters and micron in length as imaged by TEM. This nanofibrous network was used to template magnetite mineralization. A black precipitate was formed upon mixing of 1:2 ratio of $FeCl_2$:$FeCl_3$ solutions with peptide nanofibers followed by exposure to NH_3 vapor. Black precipitate was responsive to magnetic field showing the formation of magnetite (γ-Fe2O3) nanostructures. Raman spectroscopy showed peak at 674 cm^{-1} which further confirmed the presence of magnetite (γ-Fe2O3) mineralized on peptide nanofibers.

Our group also developed various self-assembled peptide templates to synthesize Pd, Au, SiO_2, TiO_2, and ZnO nanostructures. An amyloid inspired short peptide sequence (Ac-KFFAAK-Am) was designed and synthesized which formed 1D nanofibers. This fibrous nanonetwork was used as template to mineralize SiO_2 and TiO_2. After calcination of organic part micron long nanotubes of SiO_2 and TiO_2 were formed [71]. Amyloid inspired templated porous silica nanotubes were used as high surface area explosive detector. Surface of silica nanotubes were modified by fluorescent probe by physical adsorption. These fluorescent silica nanotubes demonstrated fast, sensitive, and highly selective fluorescence quenching towards nitro-explosive vapors [71]. We further utilized amyloid inspired templated porous titania nanotubes as dye sensitized solar cell anodic materials. In this study we showed that porous, high surface area (150 m^2/g) titania nanotubes could adsorb more dye than the nontemplated titania. As a result dye sensitized solar cell constructed from porous titania nanotubes showed efficiency of 0.83% which is 3 fold better than nontemplated titania [72].

Amyloid inspired peptide nanofibers were further exploited to template gold nanostructures synthesis. Amine decorated peptide nanofibers interacted with gold ions and upon reduction by ascorbic acid gold nanostructures were grown. Atomic force microscopy was used to investigate nanoscale electrical properties of gold decorated peptide nanofibers. Bias dependent current (IV)

measurements on gold nanofibers demonstrated tunneling dominated transport and resistive switching [73].

Besides amyloid inspired peptide templates, our group also designed self-assembling peptide amphiphiles which could template palladium nanoparticles synthesis. A histidine rich peptide amphiphile nanofiber was designed to synthesize Pd nanoparticles which could be utilized as nanocatalyst for Suzuki coupling reactions. Our designed Pd nanocatalyst showed high catalytic activities under environmental friendly conditions. Reaction products were obtained almost quantitatively in the presence of our catalyst besides ease of recycling [74]. In another research study, we combined advantages of critically dried porous and high surface area peptide 3D nanonetwork with atomic layer deposition (ALD) to produce highly conformal and uniform titania and silica nanotubes. These highly precise nanostructures showed high photocatalytic activities towards methylene blue degradation. The photocatalytic exclusively was dependant on wall thickness and surface area per unit mass of titania and silica nanotubes [75].

Other research groups have also exploited different self-assembled peptide templates such as I_3K, phage-displayed P7A peptides [76] and aniline–GGAAKLVFF [77] to synthesize Pt nanoparticles for different applications. I_3K assembled nanofibers were used to template Pt nanoparticles while phage-displayed P7A peptides were utilized to tune morphologies of Pt nanoparticles. I_3K assembled nanofibers decorated Pt nanostructures were used for electrochemical oxidation of hydrogen and methanol while aniline–GGAAKLVFF supported Pt nanoparticles were used as electrocatalyst to improve oxygen reduction reaction [77].

Tuning metallic nanostructures spatial arrangement via peptide morphology to induce new properties is another exciting field. A peptide amphiphile (C_{12}-FPPMPPAGAYSS) which formed double helices directed the formation of left-handed gold nanoparticles [78]. Liu research group produced chiral silica nanotubes via helical bolaamphiphilic peptide templates. Chiral silica nanotubes modified by photoactive azobenzene moieties could recognize a chiroptical switch [79].

.

Chapter 2

Fabrication of Supramolecular n/p- Nanowires via Coassembly of Oppositely Charged Peptide-Chromophore Systems in Aqueous Media

2.1 Introduction

Supramolecular electronics is an emerging research field, which exploits noncovalent interactions to assemble π-conjugated molecular elements into well-defined nanomaterials with semiconductor properties such as light emission, light harvesting, and charge carrier transport for optoelectronic, photovoltaic, bioelectronics and tissue engineering applications [80-82]. Efficiency of charge transport, energy migration and mobility of charge carriers in these supramolecular one-dimensional (1D) nanowires is directly dependent on supramolecular order of π-conjugated chromophores [83].Therefore achieving efficient cofacial π-π interactions among hydrophobic semiconducting chromophores in aqueous medium is highly desired goal in area of supramolecular electronics. A promising strategy to fabricate 1D electroactive nanomaterials with maximum cofacial π-π interactions in aqueous media is to conjugate n-type or p-type semiconducting molecules to self-assembling short peptide sequences [81, 84]. Particularly, conjugation to β-sheet forming peptides not only ensures solubility of hydrophobic semiconducting building blocks in aqueous medium but also allow directing long-range spatial organization of semiconducting chromophores [50, 85]. The n-type and p-type semiconducting supramolecular nanowires usually suffer from low conductivities [12, 86, 87]. To address this problem, p-type and n-type semiconducting 1D nanowires are doped by either an oxidizing [87] (iodine) or reducing agent [86] (hydrazine) respectively to generate charges. Another strategy is

to assemble suitable π-electron donor with an π-electron acceptor in alternating manner to form charge-transfer complexes (CTC) with enhanced charge transport, energy migration and higher mobility of charge carriers, thus enhanced (photo) conductivities [87-90]. The pioneering work by Naziro group demonstrated that fabricated CTC made up of alternately segregated A-D nanodomains exhibited tremendous photoconductivities of 0.8 $cm^2 V^{-1} s^{-1}$ [89]. Moreover, Ulijin group constructed a charge-transfer complex xerogels composed of A-D domains enhancing the conductivity up to 10^6 fold [87]. Despite promising efforts, there are only few reports, which illustrate fabrication of well-defined supramolecular CTC 1D nanowires in aqueous medium [52, 89, 91].
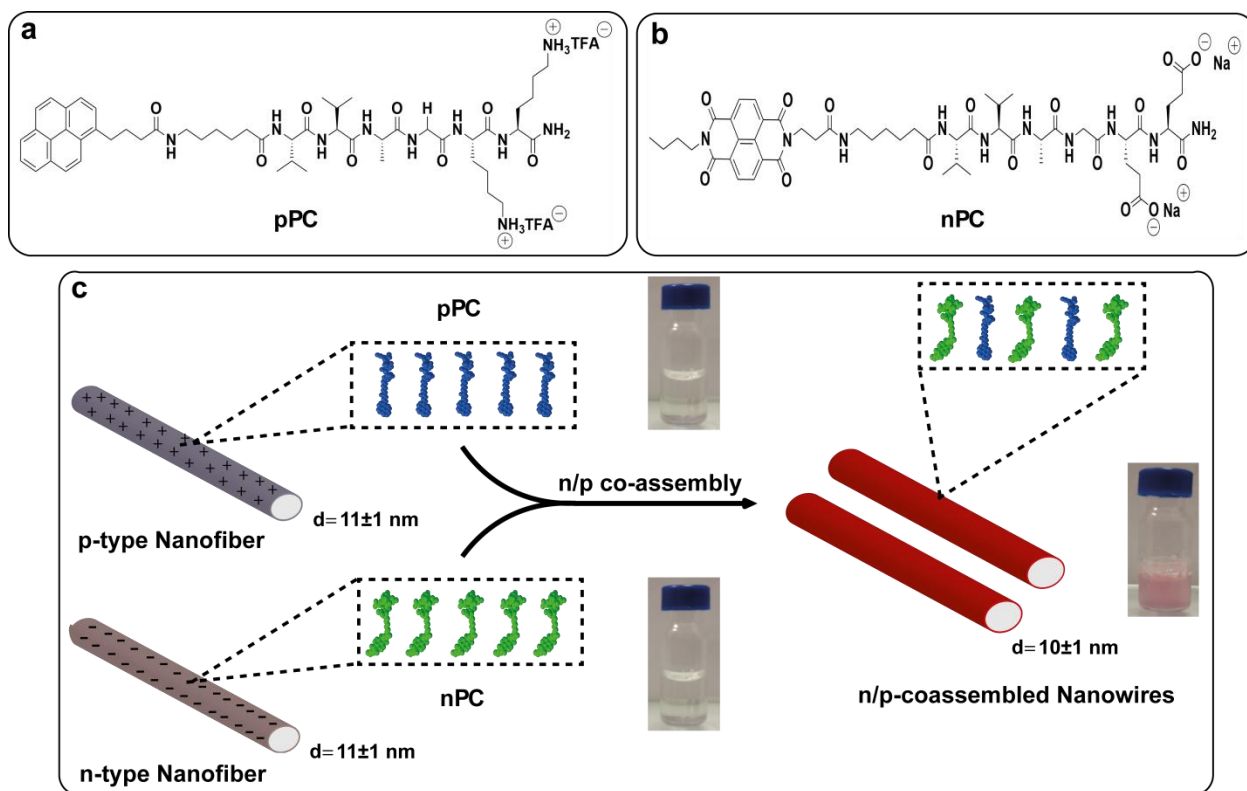
Scheme 1. a) Chemical structure of p-type PC (pPC), b) n-type PC (nPC) molecules. c) Coassembly of p and n-type nanofibers into supramolecular n/p-coassembled nanowires.

In this chapter, we report construction of 1D supramolecular CTC nanowires in aqueous media. We designed and synthesized β-sheet forming p-type peptide-chromophore (pPC) (Scheme 1a) and n-type peptide-chromophore (nPC) (Scheme 1b) conjugates. Positively charged pPC and negatively charged nPC molecules individually assemble into highly uniform p-type and n-type nanofibers, respectively, having diameters of 11±1 nm and microns in length as imaged by transmission electron microscopy (TEM) (Figure 2.1). These complementary p-type and n-type nanofibers can coassemble via hydrogen-bonding and electrostatic interactions to generate well-ordered supramolecular n/p-coassembled 1D nanowires (Scheme 1c). This smart and novel molecular design ensures alternating arrangement of D and A chromophores within n/p-coassembled supramolecular nanowires. Moreover, our experimental findings demonstrate that supramolecular n/p-coassembled nanowire is formed from highly alternating A-D-A unit cells having a strong K_A of 5 x 10^5 M^{-1}. This facile strategy allows fabrication of well-defined supramolecular electroactive nanomaterials, which can find a variety of applications in optoelectronics, photovoltaics, bioelectronics and tissue engineering.
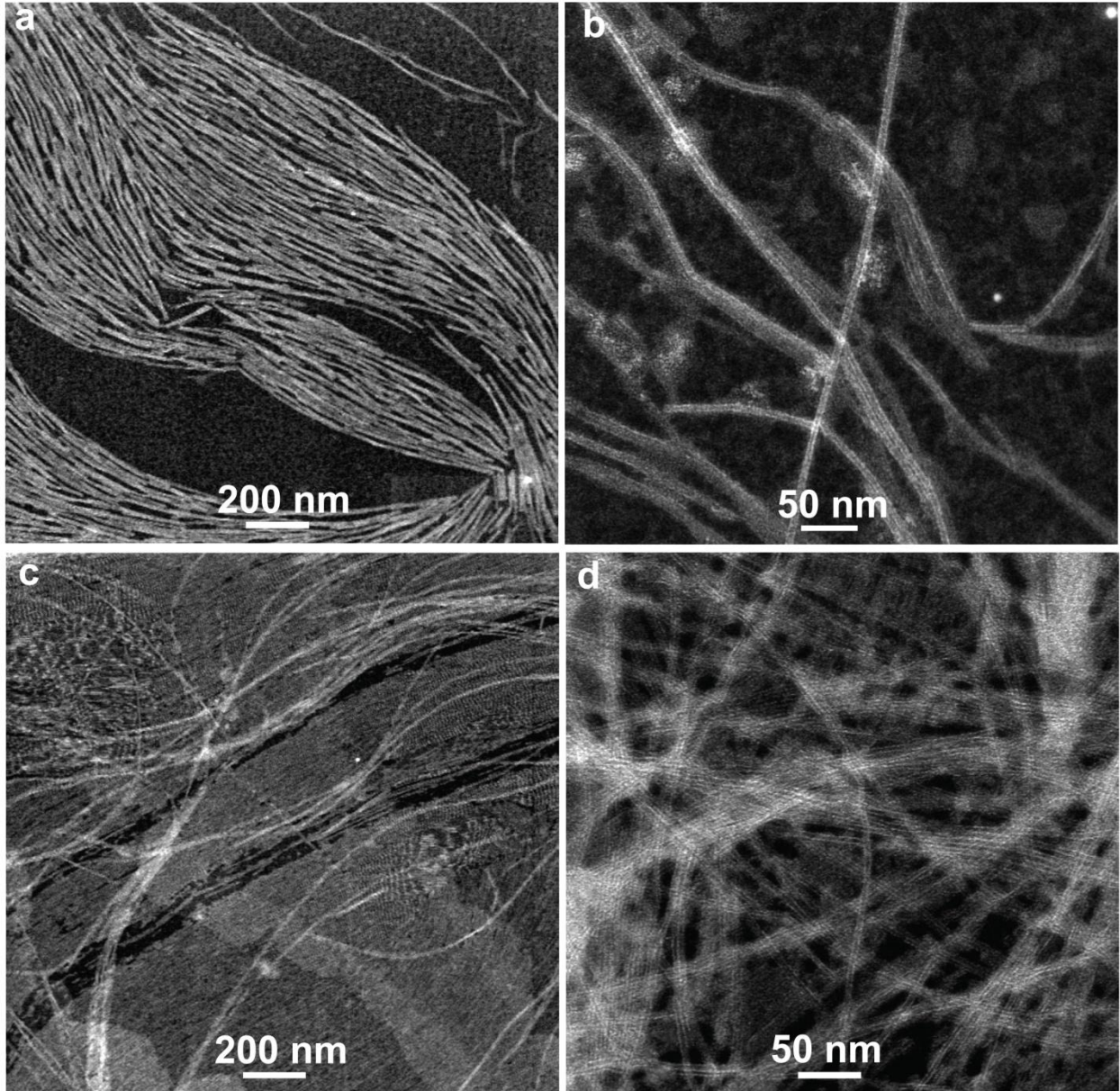
Figure 2.1 STEM images of pPC (a and b) and nPC (c and d) nanofibers with diameters of 11±1 nm.

2.2 Experimental Section

2.2.1 Synthesis of 7-butyl-1H-isochromeno[6,5,4-def]isoquinoline-1,3,6,8(7H)-tetraone (n-Bu-NTA)

In a 500 mL round bottom flask containing 200 mL of water was added 1072 mg (2 mmol) of 1,4,5,8- naphthalenetetracarboxylic acid dianhydride (NTA) and 20 mL of KOH (1M). The mixture was stirred until a clear yellow solution was obtained. The pH of solution was adjusted to 6.4 by addition of 1M H_3PO_4 solution. 434 µl (2.2 mmol) of n-butyl amine was added to the solution then the pH was readjusted to 6.4 by addition of 1M H_3PO_4 solution. The solution was refluxed overnight then cooled to room temperature. The solution was filtered and then 10 mL of acetic acid was added to filtrate to get a precipitate. The precipitate was collected through filtration and then vacuum dried to get the desired pale yellow product (660 mg, **n-Bu-NTA**). **^{1}H NMR (400 MHz, DMSO-d6, ppm): δ=** 8.53 (d, *J* = 7.43 Hz, 2H), 8.13 (d, *J* = 7.43 2H), 4.12-3.99 (m, 2H), 1.71-1.57 (m, 2H), 1.44-1.30 (m, 2H), 0.95 (t, *J* = 7.13 Hz, 3H) **^{13}C NMR (100 MHz, DMSO-d6, ppm): δ=** 168.93, 163.27, 137.23, 130.54, 129.65, 129.01, 125.93, 40.15 (NCH2, overlapped with solvent peaks), 30.01, 20.25, 14.18.

2.2.2 Synthesis of n-Bu-NTA- ß alanine

300 mg of n-Bu-NTA dissolved in DMF (10 mL). To this solution, beta alanine (166 mg, 2 eqv) and DIPEA (334µL, 2 eqv.) were added then stirred at 90 ^{o}C overnight. DMF was evaporated by rotary (60 ^{o}C, 10 mbar) then the residue was dissolved in 40 mL of water: methanol (2:1). The solution was basified by 1M of KOH then filtered. The pH of the filtrate was readjusted to 3 by addition of HCl (2M). The precipitate was washed by methanol and centrifuged successfully to get the product (**n-Bu-NTA- ß alanine). ^{1}H NMR (400 MHz, DMSO-d6, ppm): δ=** 12.39 (s,

1H), 8.64 (s, 4H), 4.28 (t, J = 7.45 Hz, 2H), 4.06 (t, J = 7.45 Hz, 2H), 2.64 (t, J = 7.65 Hz, 2H), 1.65 (m, 2H) , 1.39 (m, 2H), 0.95 (t, J = 7.3 Hz, 3H). **^{13}C NMR (100 MHz, DMSO-d6, ppm):** **δ=** 172.83, 163.02, 162.95, 130.87, 130.85, 126.80, 126.67, 126.57, 40.15 (NCH2, overlapped with solvent peaks), 36.55, 32.47, 30.01, 20.27, 14.17. **ESI-HRMS (m/z):** Calculated for $[C_{21}H_{18}N_2O_6 - H]^-$: 393.1165; Found: 393.1184
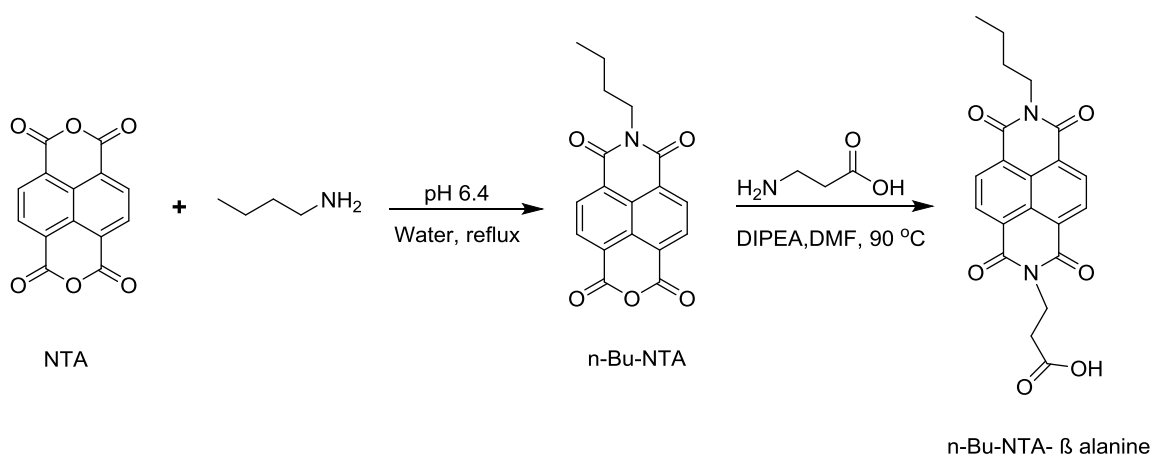
Figure 2.2 Schematic presentation of synthesis of n-Bu-NTA- ß alanine
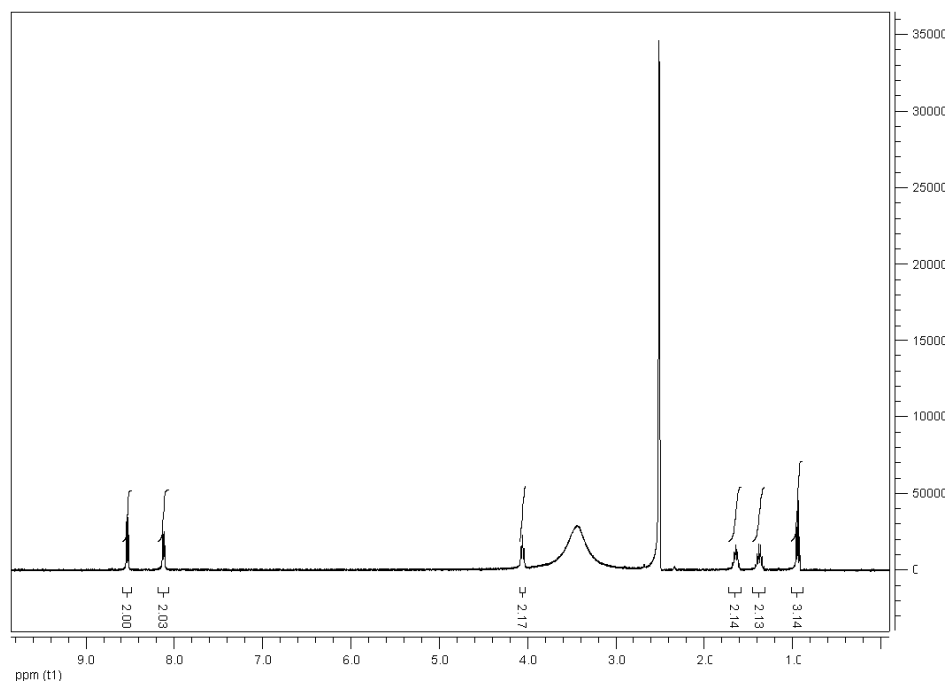
Figure 2.3 ^{1}H NMR of n-Bu-NTA

33
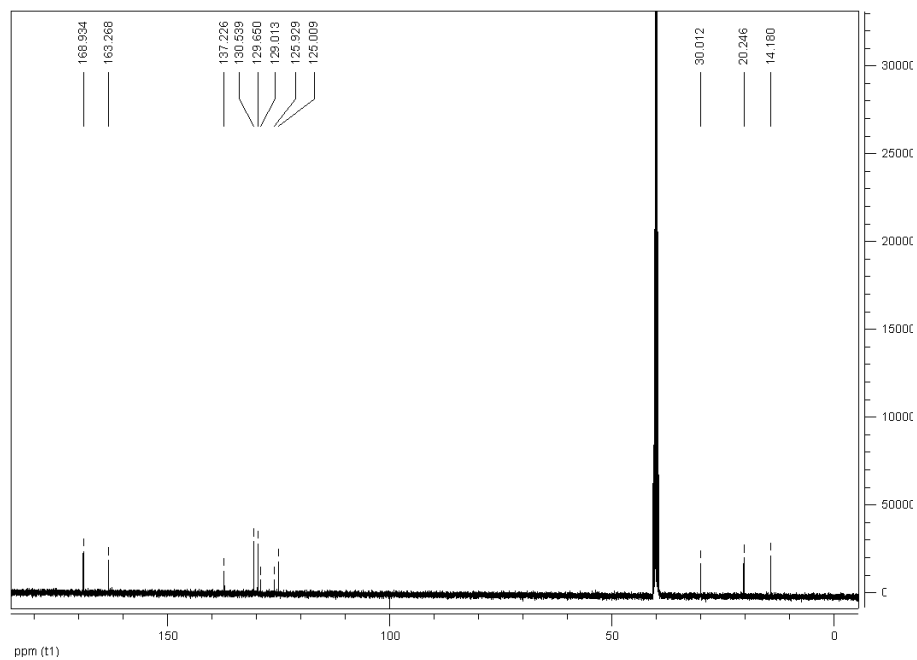
Figure 2.4 ^{13}C NMR of n-Bu-NTA
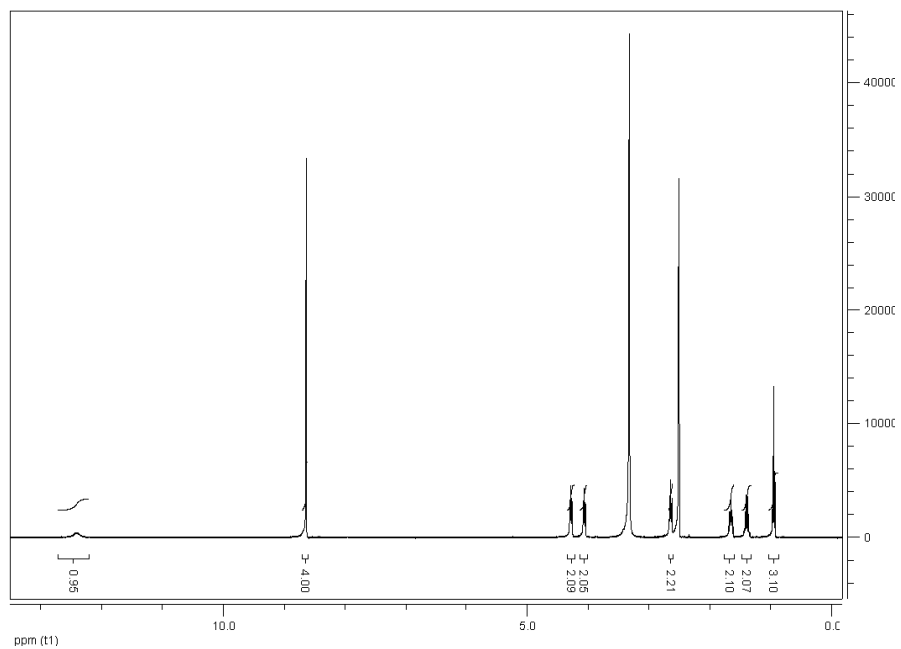
Figure 2.5 ^{1}H NMR of n-Bu-NTA- ß alanine
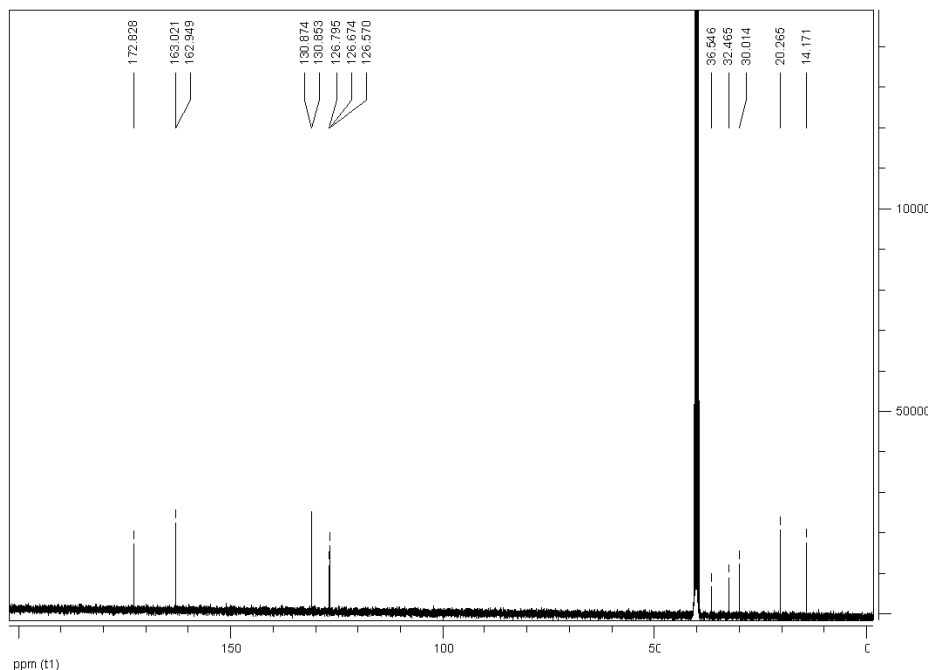
Figure 2.6 ^{13}C NMR of n-Bu-NTA- ß alanine
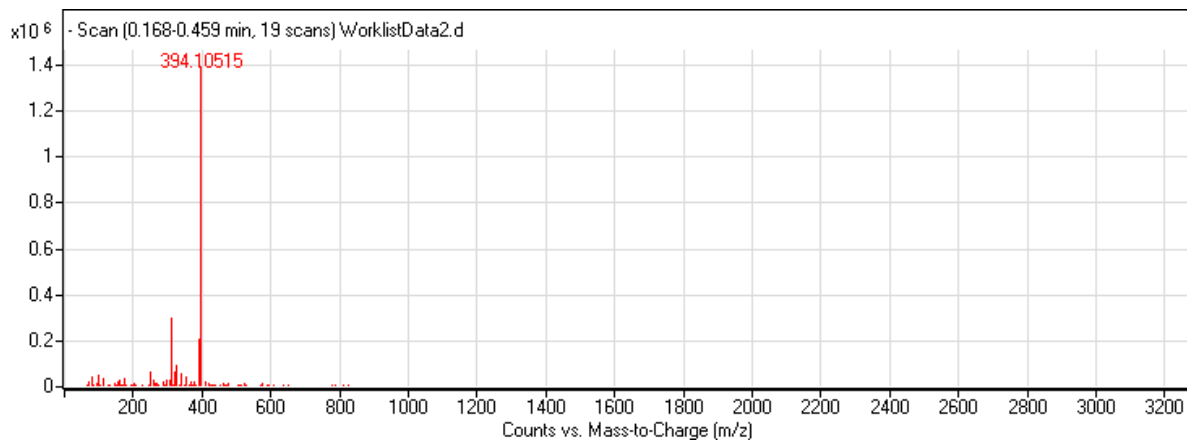
Figure 2.7 Mass spectrum of n-Bu-NTA- ß alanine

2.2.3 Synthesis of Peptide Molecules

All peptide molecules were synthesized by using solid phase peptide synthesis (SSPPS) method. The synthesis were performed on MBHA Rink Amide resin and 2 equivalents of fluorenylmethyloxycarbonyl (Fmoc) protected amino acids, 1.95 equivalents of O-Benzotriazole-N,N,N',N'-tetramethyl-uroniµM-hexafluoro-phosphate (HBTU) and 3 equivalents of N,N-diisopropylethylamine (DIEA) for 6 h. Fmoc protecting groups were removed by 20% of piperidine in dimethylformamide for 20 minutes. The peptides were cleaved from the solid Resin by a mixture of trifluoroacetic acid: triisopropylsilane: H_2O in the ratio of 95:2.5:2.5 for 2 h. The product was collected into a round bottom flask by washing the resin with DCM. The DCM was evaporated by rotary evaporation and cold ether was poured to precipitate the peptide. The final product was collected by centrifuging and then lyophilizing for 72 h to get a white powder.

2.2.4 Synthesis of pPC molecule

In the last step of the synthesis, 2 equivalents of commercial available 1-pyrenebutyric acid were used and the coupling was left for 24 h.

2.2.5 Synthesis of nPC molecule

In the last step of the synthesis, 1.5 equivalents of n-Bu-NTA- ß alanine were used and the coupling was left for 24 h.

2.2.6 Preparative High Performance Liquid Chromatography

In purification of positively charged peptide molecules, reverse phase silica column (C18) and 0.1% TFA in water and 0.1% in CAN were used as eluents. While negatively charged peptide molecules were eluted by 0.1% NH_4OH in water and 0.1% NH_4OH in CAN. Preparative Liquid Chromatography System (Prep-HPLC Agilent 1200 series) integrated with a sample collector was used.

2.2.7 Liquid Chromatography-Mass Spectrometry (LC-MS)

After purification of the peptide molecules by Prep HPLC, the purity of the molecules were determined by Agilent Technologies 6530 Accurate-Mass Q-TOF LC-MS. Zorbax SB-C18 column and 0.1% formic acid in water and 0.1% formic acid in acetonitrile were used as mobile phase for positively charged molecules and 0.1% NH_4OH in water and 0.1% NH_4OH in ACN were used for negatively charged peptide molecules. All peptides were obtained with high purity.

2.2.8 UV-Vis Spectroscopy

The peptide solutions were prepared in a 3 mL quartz cell having 1 cm path length. Stock solution of Py was prepared by dissolving 2 mg of pPC in 200 μL of water. 3 mL of pPC having a concentration of 55 μM was prepared from stock solution. For nPC peptide, 1.6 mg of molecule was dissolved in 140 μL of 1mM NaOH plus 25 μl of 0.5 M NaOH. 3 mL of nPC having a concentration of 55 μM was prepared from stock solution. The dilutions were performed by 1 mM NaOH to keep the pH around 8. The absorbance values were recorded on CaryBio100 instrument.

2.2.9 Fluorescence Spectroscopy

The peptide solutions were prepared in a 3 mL quartz cell having 1 cm path length. Stock solution of pPC was prepared by dissolving 2 mg of pPC in 200 μl of dd water. 3 mL of pPC having a concentration of 55 μM was prepared from stock solution. For nPC peptide, 1.6 mg of molecule was dissolved in 140 μL of 1mM NaOH plus 25 μL of 0.5 M NaOH. 3 mL of nPC having a concentration of 55 μM was prepared from stock solution. The dilutions were performed by 1mM NaOH solution to keep the pH around 8. The samples were excited at 340 nm and excitation slit and emission slit widths were adjusted at 1.5 and 5 respectively. The emission intensities were recorded on Fluorescence Spectrometer (Cary Eclipse) instrument.

2.2.10 Circular Dichroism (CD) Spectroscopy

The peptide solutions were prepared in a 3 mL quartz cell having 1 cm path length. Stock solution of pPC was prepared by dissolving 2 mg of pPC in 200 μL of dd water. 3 mL of pPC having a concentration of 55 μM was prepared from stock solution. For nPC peptide, 1.6 mg of molecule was dissolved in 140 μL of 1mM NaOH plus 25 μL of 0.5 M NaOH. 3 mL of nPC having a concentration of 55 μM was prepared from stock solution. The dilutions were performed by 1mM NaOH to keep the pH around 7-8. The samples were measured from 500 nm to 190 nm with 0.1 data pitch, 100 nm/min scanning speed, 1 nm band width and 4 s D.I.T. Average of two measurements were adjusted and sensitivity was selected as standard. All measurements were recorded on Jasco **J**-815 circular dichroism spectrometer.

2.2.11 X-ray Photoelectron Spectroscopy (XPS)

Solutions of pPC and nPC were prepared in dd water then they were mixed into 1:1 mole ratio to form a reddish suspension. The suspension was centrifuged at 8500 rpm for 10 minutes and the upper part was decanted. Then fresh dd water was added followed by centrifugation. This process was performed for seven times to get rid of any unbound pPC and nPC molecules. The peptide suspension was freeze dried to get reddish powder. This powder was analyzed by Thermo K-alpha monochromatic high performance X-ray photoelectron spectrometer. The survey analyses were performed at 10 scans.

2.2.12 Ultrafast Pump Probe Spectroscopy

The ultrafast wavelength dependent pump probe spectroscopy measurements were performed using a Ti: Sapphire laser amplifier-optical parametric amplifier system (Spectra Physics, Spitfire Pro XP, TOPAS) with commercial pump probe setup (Spectra Physics, Helios). Pulse duration was measured as 100 fs with a cross correlation. Wavelengths of the pump beam were 340 nm for pPC molecules and 350 nm for pPC-nPC CT complex. White light continuum was used as a probe beam.

2.2.13 Fourier Transform Infrared (FT-IR) Spectroscopy

Samples prepared for XPS analyses were pressed into KBr pellets. Only KBr pellet was used as background. The measurements were recorded on Fourier Transform Infrared Spectrometer (FT-IR) (Bruker VERTEX 70). 64 scans were recorded between 4000- 400 cm^{-1} at a resolution of 4 cm^{-1}.

2.2.14 Transmission Electron Microscopy (TEM)

FEI Tecnai G2 F30 transmission electron microscope was used to image the stained (%2 uranyl acetate solutions) peptide nanofibers. 10 µl of peptide solutions prepared for Uv-vis and fluorescence spectroscopies were dropped on carbon covered copper grid followed by air-drying at temperature. The stainings were performed for 90 seconds

2.2.15 Nuclear Overhauser effect spectroscopy (NOESY)

6 mg of pPC was dissolved in D_2O and 6 mg of nPC was dissolved in 500 µl of D_2O + 150 µl of NaOD (30% solution). The pPC and nPC solutions were mixed and NOESY spectrum was recorded at 64 scans using 400 MHz NMR.

2.2.16 Isothermal Titration Calorimetry (ITC)

0.1 mM of nPC (200 µL) solution was titrated by 1 mM of pPC solution using iTC200 system (MicroCal, GE Healthcare). The titration was performed at 25 °C with 500 rpm stirring speed. Twenty injections were done, where the injection period was 4 s and the space between injections was 180 s. ITC binding isotherms were best fitted by a one-sets of site mode.

2.2.16 Atomic Force Microscopy (AFM)

Solutions of pPC and nPC were prepared in dd water then they were mixed into 1:1 mole ratio to form a reddish suspension. The suspension was centrifuged at 8500 rpm for 10 minutes and the upper part was decanted. The suspension was dispersed and diluted in fresh water and 10 µL of it dropped on clean silicon wafer. The dried sample was imaged by MFP3D Asylum microscope.

2.3 Results and Discussion

In present study, pyrene (π-basic with molecular quadrupole moment Qzz = -13.8 B) as π-electron donor (D) was conjugated to a β-sheet forming hexapeptide sequence (H$_2$N-Ahx-VVAGKK-Am)[92] by using solid phase peptide synthesis (SPPS) procedure to obtain pPC molecule (Figure 2.8-2.10). In the molecular design, VVA residues promote β-sheet formation and KK residues not only ensure solubility of hydrophobic pyrene molecules in aqueous media but also provide positive charge (Figure 2.8). A six carbon linker (Ahx) was introduced between pyrene chromophore and hexapeptide to provide flexibility among chromophores and allow them to arrange favorable orientation during self-assembly.

Chemical Formula: C$_{53}$H$_{78}$N$_{10}$O$_8$
Exact Mass: 982.60
Molecular Weight: 983.27
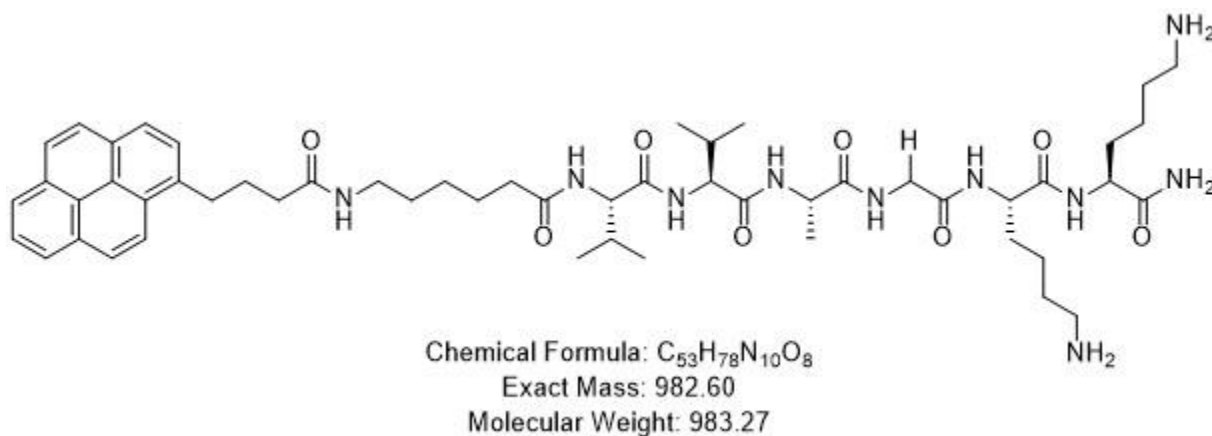
Figure 2.8 Chemical structure of pPC molecule.
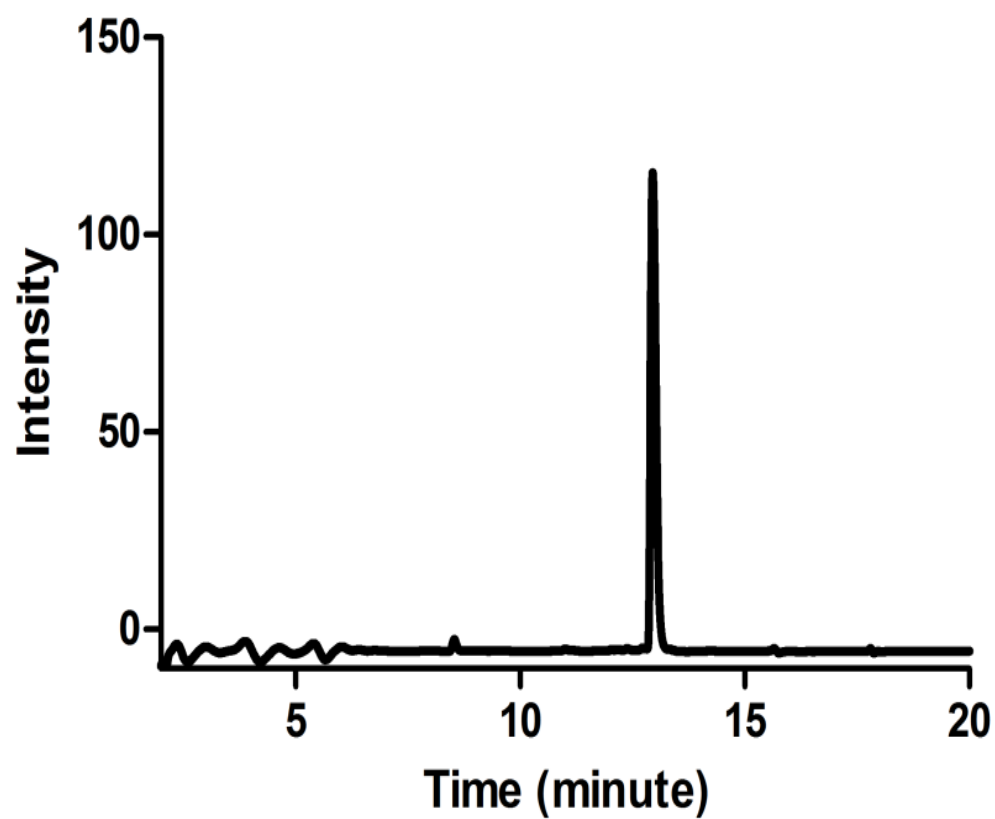
Figure 2.9 Liquid chromatogram of pPC molecule.
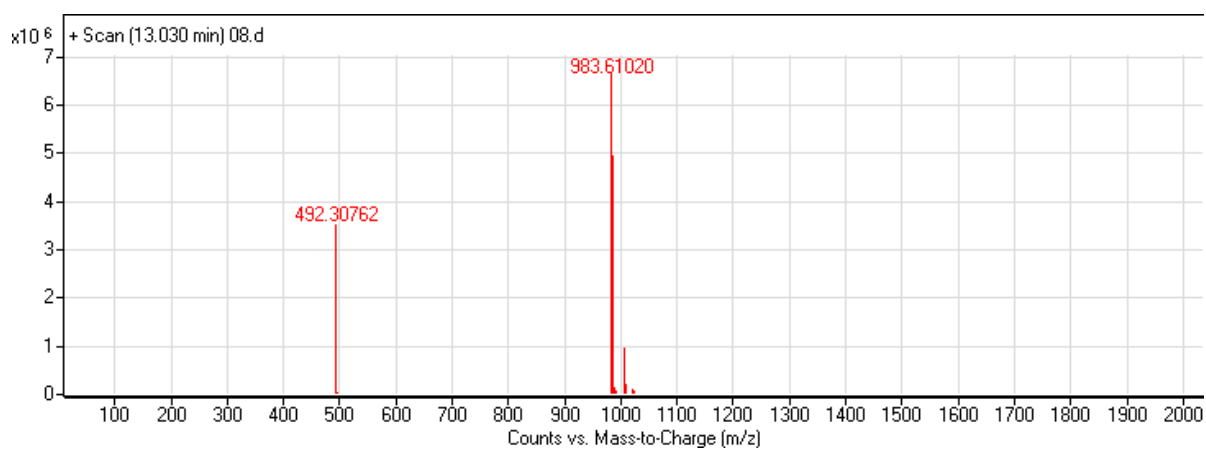
Figure 2.10 Mass spectrum of pPC molecule.

Aggregation of pPC molecule was studied by UV-vis, fluorescence, circular dichroism (CD) and X-ray photoelectron spectroscopies (XPS). The absorption of pPC molecules in trifluoroethanol (pPC-TFE) and in water (pPC-H_2O) showed well-resolved vibronic structure ranging from 250 to 350 nm, which is characteristic for monomer pyrene chromophores (Figure 2.11a) [93]. Due to partial aggregation of pPC in water, a slight red shift was observed in the absorption bands of pyrene. Upon complete charge neutralization by increasing pH to 10 (pPC-pH 10), the pPC molecules demonstrated a 17 nm red-shift followed by a decrease in intensity and broadening of absorption bands.
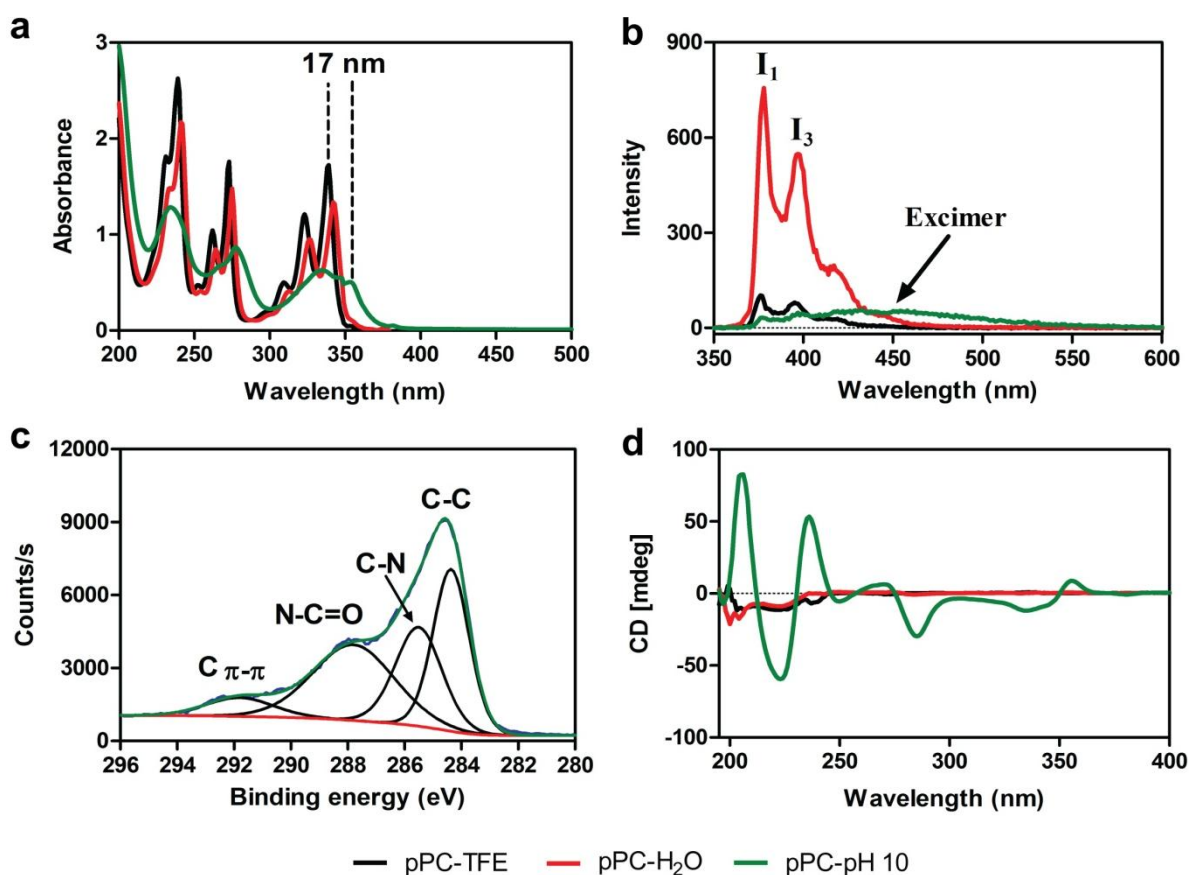
Figure 2.11 Spectroscopic characterization of pPC assembly in aqueous media. (a) UV-vis absorption and (b) fluorescence emission spectra (excitation wavelength = 340 nm) of pPC. (c) XPS analysis of assembled pPC powder and (d) CD spectrum of pPC molecules in different conditions.

These drastic changes in absorption bands revealed *J*-type π-π interactions among pyrene molecules within p-type nanofibers [93]. The emission profile of pPC in water (pPC-H$_2$O) showed vibronic structures which is caused by pyrene monomers (Figure 2.11b). The ratio of emission vibronic peaks I$_3$ (375 nm) and I$_1$ (395 nm) is extremely sensitive to polarity of the solvent and is widely used to probe the vicinity of highly hydrophobic pyrene chromophores [94]. Electrostatic repulsion caused by protonated amine (-NH$_3^{+)}$ groups of lysine residues prevent complete aggregation, thus pyrene molecules are exposed to relatively hydrophilic environment as the value of vibronic peaks (I$_3$/I$_1$) is less than unity (pPC-H$_2$O). Upon charge neutralization by increasing pH to 10 (pPC-pH 10), a drastic quenching in emission intensity of pPC followed by appearance of a new broad emission (440-550 nm) peak, which corresponds to pyrene excimers (Figure 2.11b) [94]. Self-assembly of pPC molecules triggered by charge neutralization does not only allow π-π stacking of pyrene molecules but also allow them to closely position in a relatively hydrophobic environment (core of p-type nanofibers) as the ratio of vibronic peaks (I$_3$/I$_1$) exceeds unity (Figure 2.11b). Lyophilized pPC-pH 10 sample analyzed by XPS exhibited a peak at 292 eV (Figure 2.11c), which further confirmed the presence of π-π stacking among closely spaced and spatially constrained pyrene molecules within p-PC nanofibers [95].

To investigate the long-range spatial organization of pyrene molecules within the p-type nanofibers, we further conducted CD analysis (Figure 2.11d). At basic condition (pPC-pH 10), the pPC showed a strong bisignate signal with a positive Cotton effect at 200 nm and a negative Cotton effect at 220 nm, which is attributed to formation of β-sheet secondary structures [34]. In addition, weak CD signals were observed between 250-360 nm, which confirms induction of chirality to pyrene chromophores via pPC self-assembly. On the other hand, partial aggregation

of pPC molecules in water (pPC-H_2O) and in TFE (pPC-TFE) did not show significant CD signals (Figure 2.11d).

Naphthalenediimides (NDI) are one of the widely studied n-type organic semiconductor with potential applications in organic-field-transistor, light harvesting systems and photovoltaics [96, 97]. NDI (π-acidic with Qzz = +18.6 B) as π-electron acceptor (A) forms preferentially CT complex with π-electron donor (D) pyrene. Owing to maximum overlap of $LUMO_{NDI}$ with $HOMO_{pyrene}$, NDI-pyrene CT complex has strong K_A of 9.6 X 10^4 M^{-1} [98]. Therefore, NDI was functionalized (Figure 2.2) to be compatible with SPPS method and then was conjugated to a β-sheet forming hexapeptide sequence (H_2N-Ahx-VVAGEE-Am) to obtain nPC molecule bearing negative charge (Figure 2.12-2.14).

Chemical Formula: $C_{52}H_{70}N_{10}O_{16}$
Exact Mass: 1090.50
Molecular Weight: 1091.17
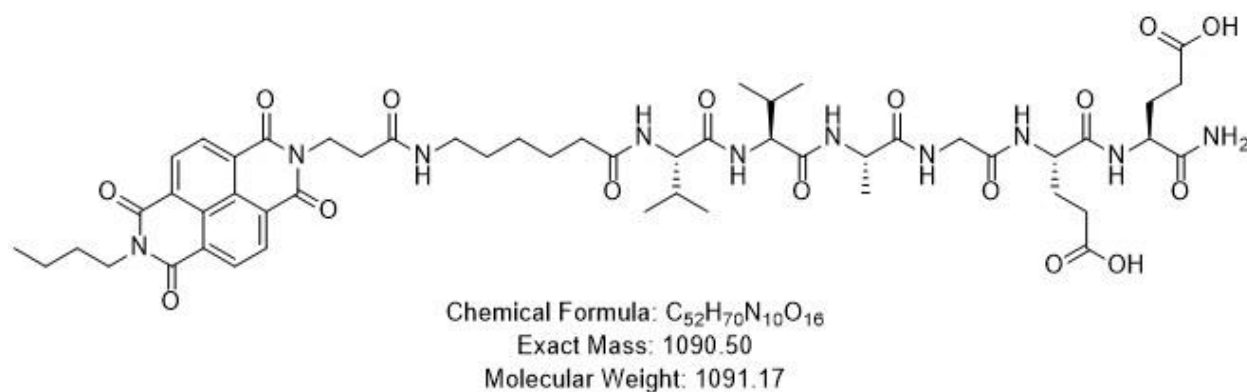
Figure 2.12 Chemical structure of nPC molecule.
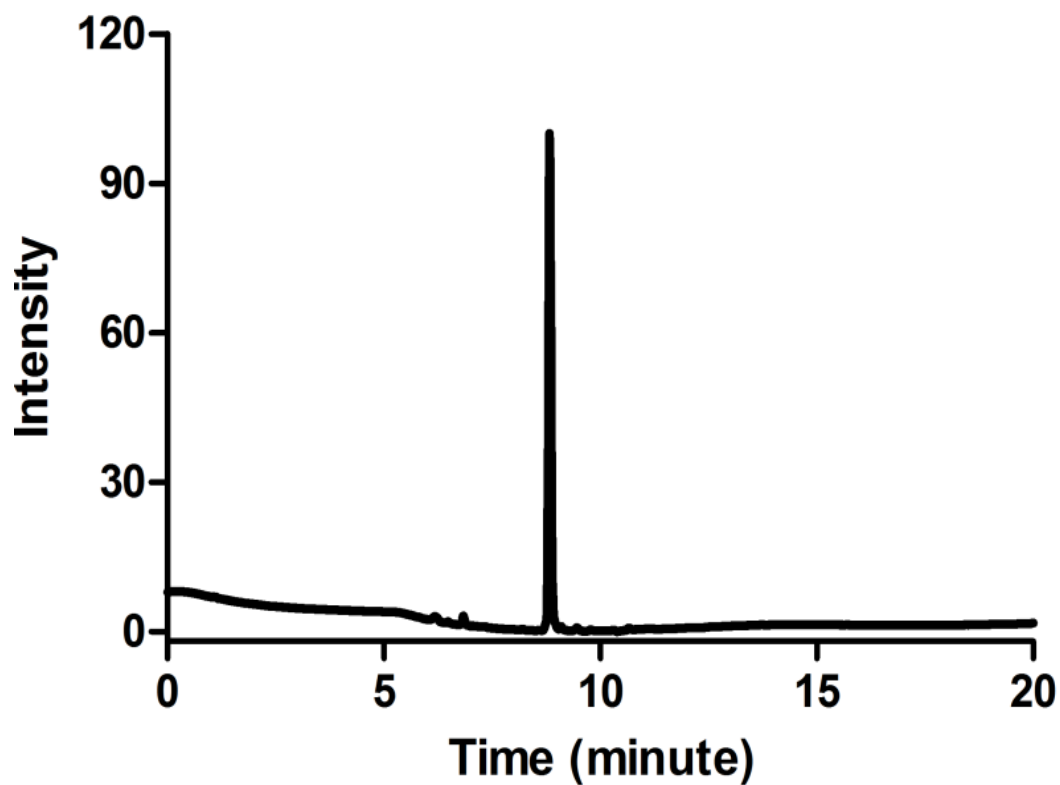
Figure 2.13 Liquid chromatogram of nPC molecule.
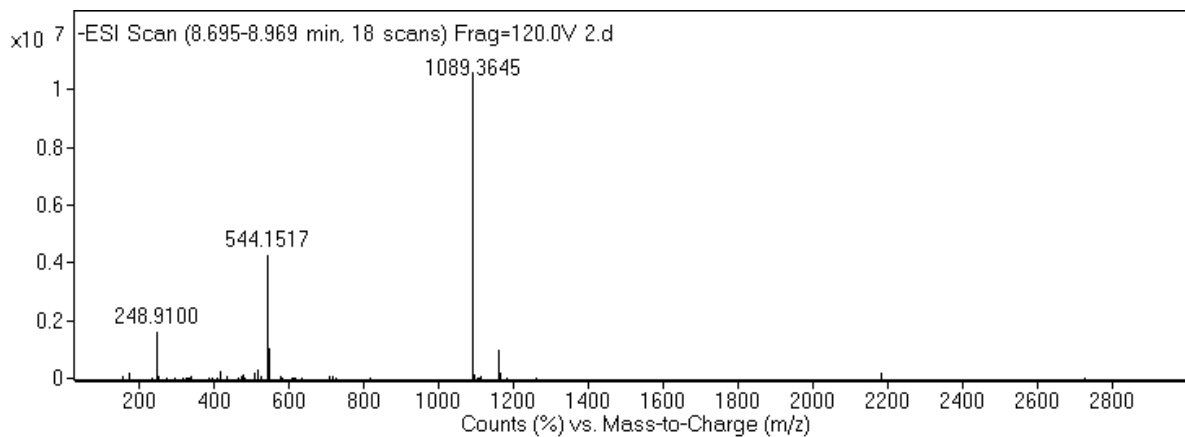
Figure 2.14 Mass spectrum of nPC molecule.

The molecule nPC was designed to have a similar molecular size, sequence and complementary charge with pPC. The nPC in mild basic condition (nPC-H$_2$O) and in TFE (nPC-TFE) demonstrated two absorption bands at 240 nm and in the range of 300-400 nm, which are attributed to π-π* transitions polarized along the short and long axis of the NDI monomer, respectively (Figure 15a) [15]. Despite charge repulsion caused by carboxylate groups (COO⁻), amphilphilic character of nPC caused partial aggregation in mild basic condition (nPC-H$_2$O) as slight bathochromic shift was observed (Figure 2.15a).
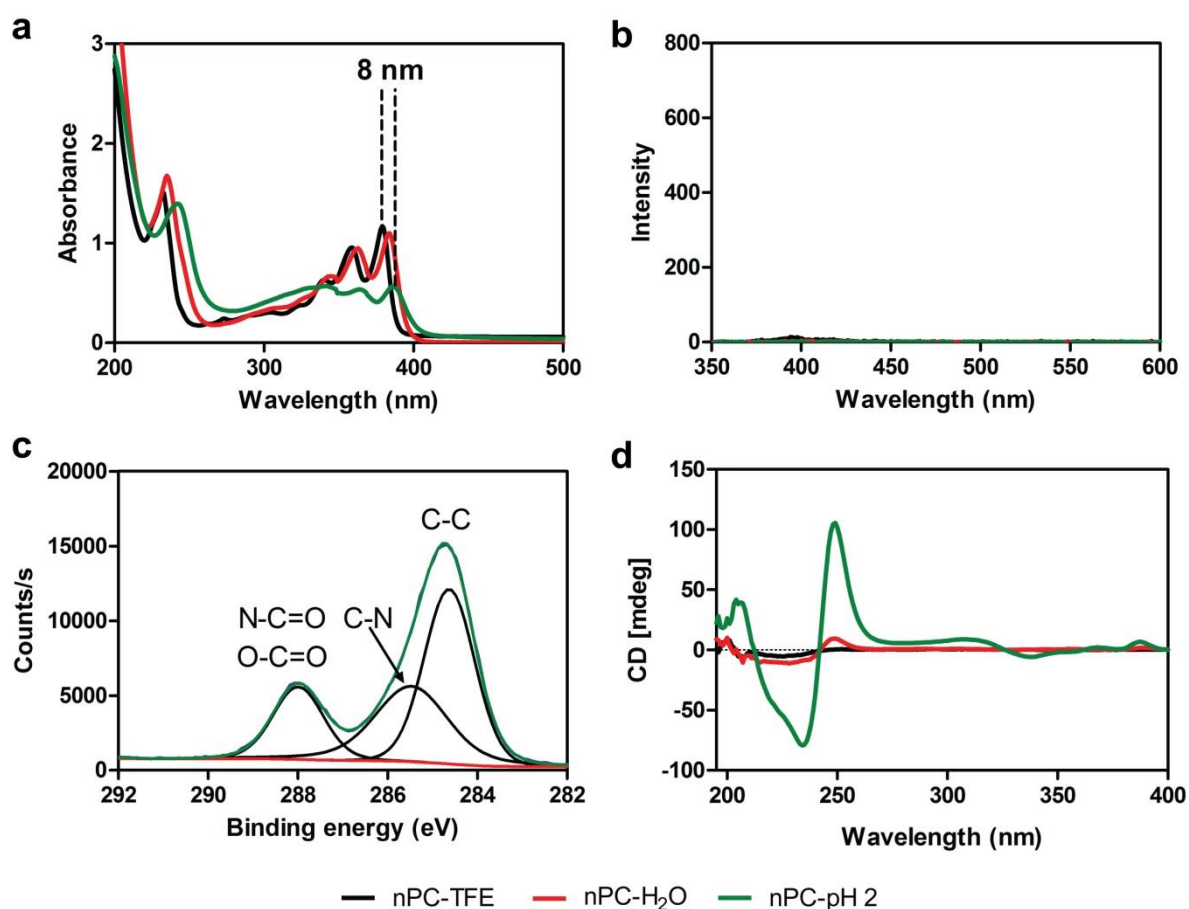
Figure 2.15 Spectroscopic characterization of nPC assembly in aqueous media. (a) UV-vis absorption spectrum and (b) fluorescence emission spectra (excitation wavelength = 340 nm) of nPC. (c) XPS analysis of assembled nPC powder and (d) CD spectrum of nPC molecule in different conditions.

Decreasing the pH to 2 (nPC-pH 2) caused an 8 nm red-shift followed by shrinkage in absorption intensity in the range of 300-400 nm. Decrease in the absorption intensity and bathochromic shift in the absorption bands showed the presence of *J*-type π-π interactions among NDI chromophores within n-type nanofibers [15]. The nPA excited at 340 nm (Figure 2.15b) did not show any emission and due to electron deficient character of NDI, we did not also observe π-π stacking of NDI molecules by XPS (Figure 2.15c).

We further investigated long-range organization of NDI chromophores within the supramolecular n-type nanofibers by carrying out CD of nPC in different conditions (Figure S13d). Partially self-assembled nPC in mild basic condition (nPC-H$_2$O) and in TFE (nPC-TFE) does not assemble all revealing weak signals in CD (Figure 2.15d). In contrast, acid triggered assembly of nPC (nPC-pH 2) demonstrated strong excitonic negative cotton effect at 220 nm corresponding to highly ordered β-sheet secondary structures. Moreover, chiral signals between 240-400 nm were also observed due to π-π* transitions polarized along the short and long axis of the NDI monomer verifying assembly of highly ordered chiral NDI chromophores within nPC nanofibers [15].

After detailed investigation of individual self-assembly of pPC and nPC peptides in aqueous environment, we studied their coassembly, which formed a new hybrid material by utilizing hydrogen bonding and electrostatic interactions among positively charged amine groups (NH$_3^+$) of pPC and negatively charged carboxylate groups of (COO$^-$) of nPC nanofibers. When transparent solutions of pPC and nPC mixed in 1 to 1 ratio, pink color was observed, which is an indication of formation of pPC-nPC (n/p-coassembled) CT complex (Figure 2.16a) [98].
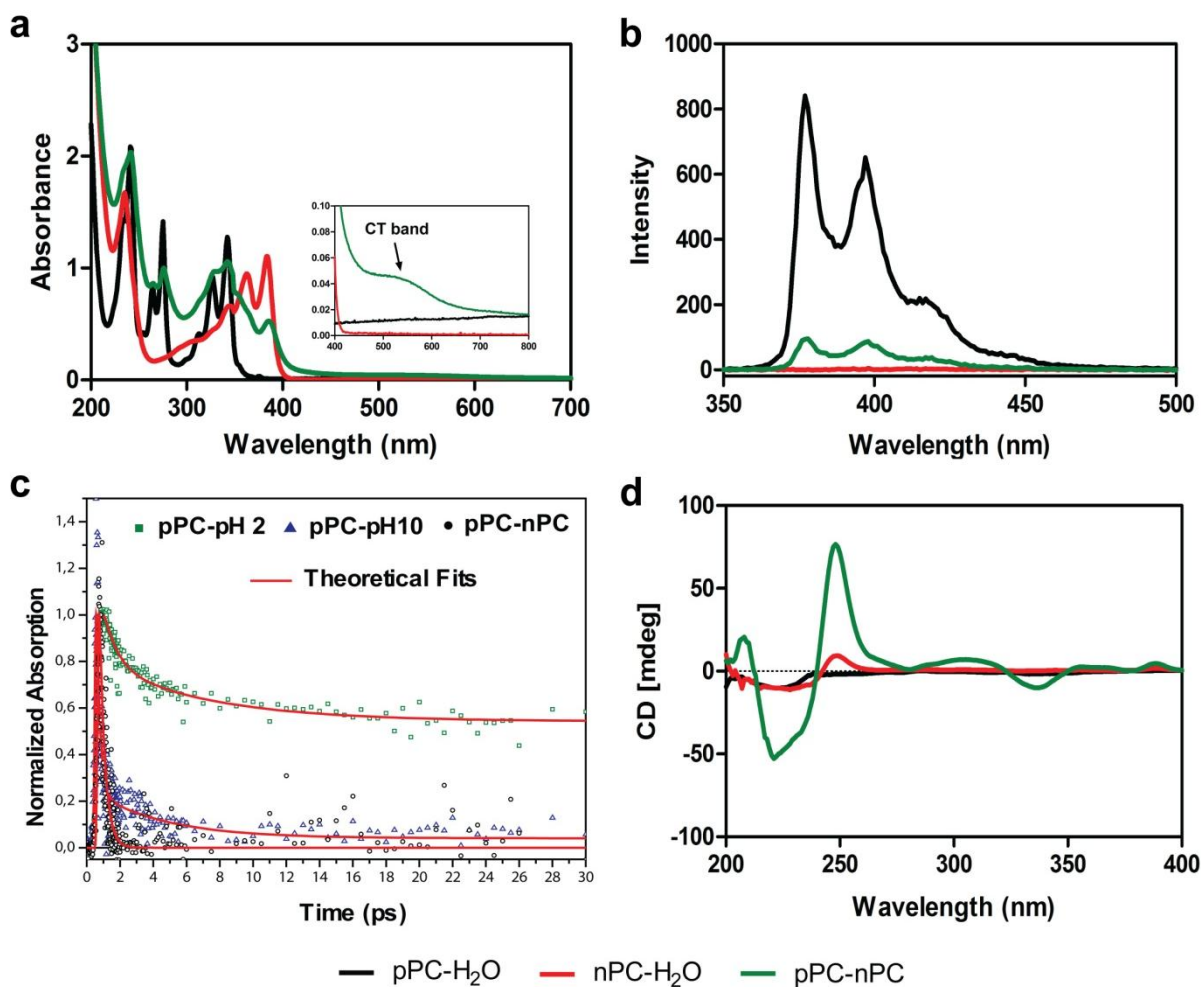
Figure 2.16 Spectroscopic characterization of pPC and nPC coassembly in aqueous media. (a) UV-vis absorption spectra and inset shows appearance of CT band. (b) Fluorescence emission spectra (excitation wavelength = 340 nm) of pPC-nPC CT complex. (c) Decay curves of pPC-pH 2, pPC-pH 10 samples and pPC-nPC CT complex pair at 477 nm probe wavelength. (d) CD spectra of pPC and nPC coassembly in aqueous media.

The UV-vis spectroscopy analysis of pPC-nPC CT complex in aqueous medium demonstrated a new broad absorption band at 520 nm which is attributed to charge-transfer (CT) band of NDI-pyrene (Figure 2.16a) [98]. Emission of highly fluorescing pPC nanofibers was quenched as soon as nPC nanofibers was mixed, which further confirms effective π-π interactions between

pPC and nPC and formation of n/p-coassembled CT complex (Figure 2.16b). Quenching of fluorescence was not followed by appearance of pyrene excimer emission, which is prevented by successful incorporation of NDI molecules between pyrene chromophores in mixed-stack pPC-nPC complex.
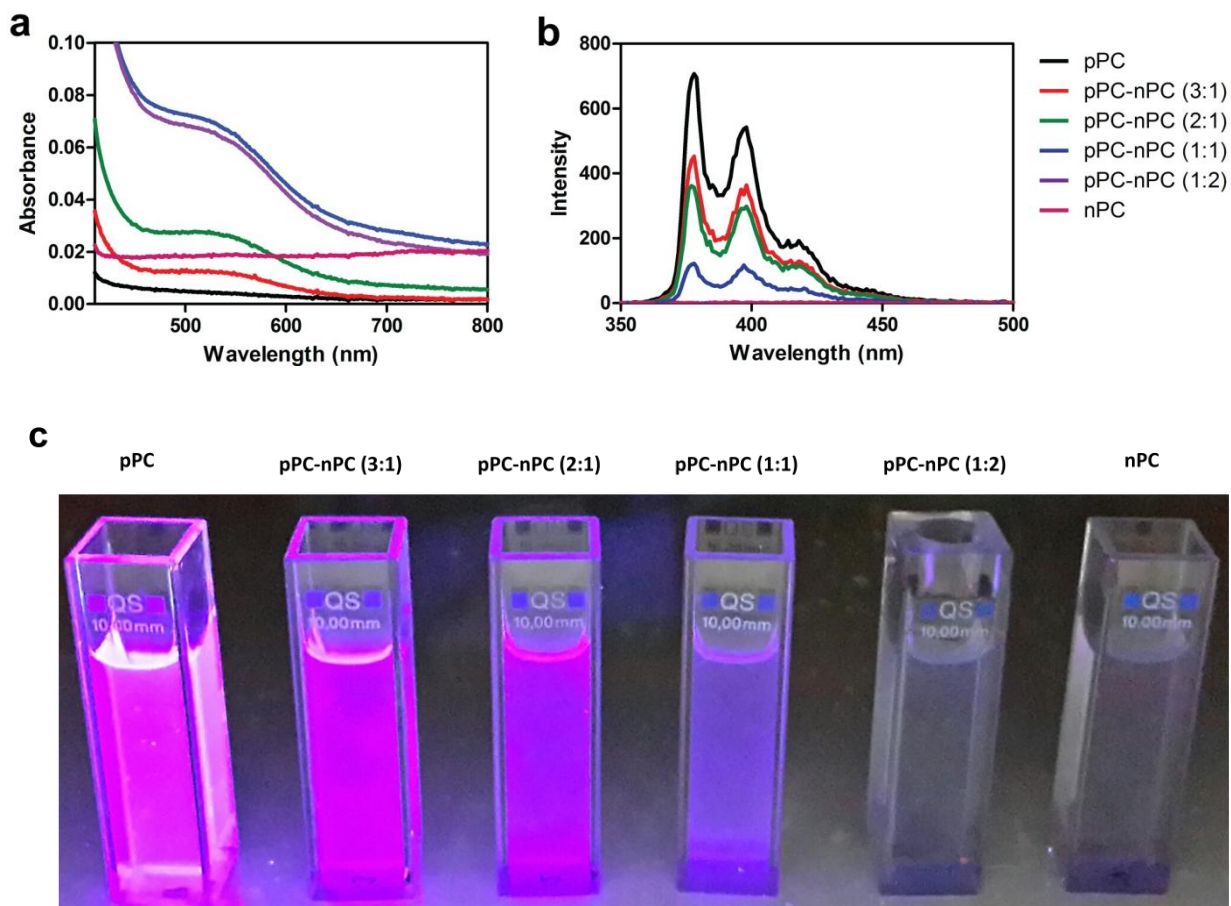
Figure 2.17 Uv-vis absorption of Charge-Transfer Complex formation (a), fluorescence quenching measurements of pPC by nPC (b) and quenching of pPC by nPC under 254 nm illumination (c).

The pPC solution was titrated with nPC molecules and formation of CT complex was monitored by UV-vis and fluorescence spectroscopies (Figure 2.17a-b). As the molar ratio of the nPC

increases in the solution, CT band at 520 nm increases (Figure 2.17a) meanwhile emission of pyrene quenches (Figure 2.17b) until all pyrene molecules complexed with NDI. Quenching of pPC by nPC can also be clearly observed with 254 nm illumination (Figure 2.17c).

Upon self-assembly, intermolecular charge transfer is expected to increase, causing the lifetime of the excited state absorption signals measured with ultrafast pump probe experiments to reduce [99]. We conducted ultrafast pump probe spectroscopy experiments to understand long-range order of pPC and nPC molecules within CT complex (Figure 2.16c). Experiments on neutralized pPC molecules by increasing pH values (pH10) and by adding negatively charged nPC molecules (pPC-nPC) were performed. Pump wavelengths were chosen based on the linear absorption spectra (340-350 nm), while white light continuum was used as probe beam for all the samples. Very broad excited state absorption signals were observed within the white light continuum spectra for all the investigated samples, which is the indication of the aggregation characteristics of the samples. Figure 2.16c shows the decay curves of the normalized excited state absorption signals at 477 nm probe wavelength. Decay time components were measured as 7 ps, 4 ps and 300 fs for samples pPC-pH 2, pPC-pH 10, and pPC-nPC CT complex, respectively. Faster decay of the excited state absorption signal of pPC-pH 10, than that of pPC-pH 2 is the indication of aggregation characteristics increasing with pH value. Furthermore, fastest decay time component (300 fs) of pPC-nPC CT complex within the investigated samples is the indication of stronger charge transfer and therefore aggregation caused by stronger self-assembly nature of this sample. These results also support fluorescence experiments showing that self-assembly process causing fluorescence quenching of the investigated CT complexes.

Coassembly of pPC and nPC nanofibers triggered by electrostatic interactions, hydrogen bonding and charge-transfer complex formation was further studied by CD spectroscopy (Figure 2.17d).

51

Individual solutions of pPC and nPC nanofibers revealed flat signals in CD while their coassembly via charge neutralization induced chiral signals. The negative Cotton effect at 220 nm confirms the presence of highly ordered β-sheet secondary structures [34]. Moreover, we observed chiral peaks between 220-400 nm, which are attributed to pyrene and NDI molecules. CD results revealed that coassembly pPC and nPC into pPC-nPC CT complex induce chirality and long-range spatial organization to achiral pyrene and NDI molecules.
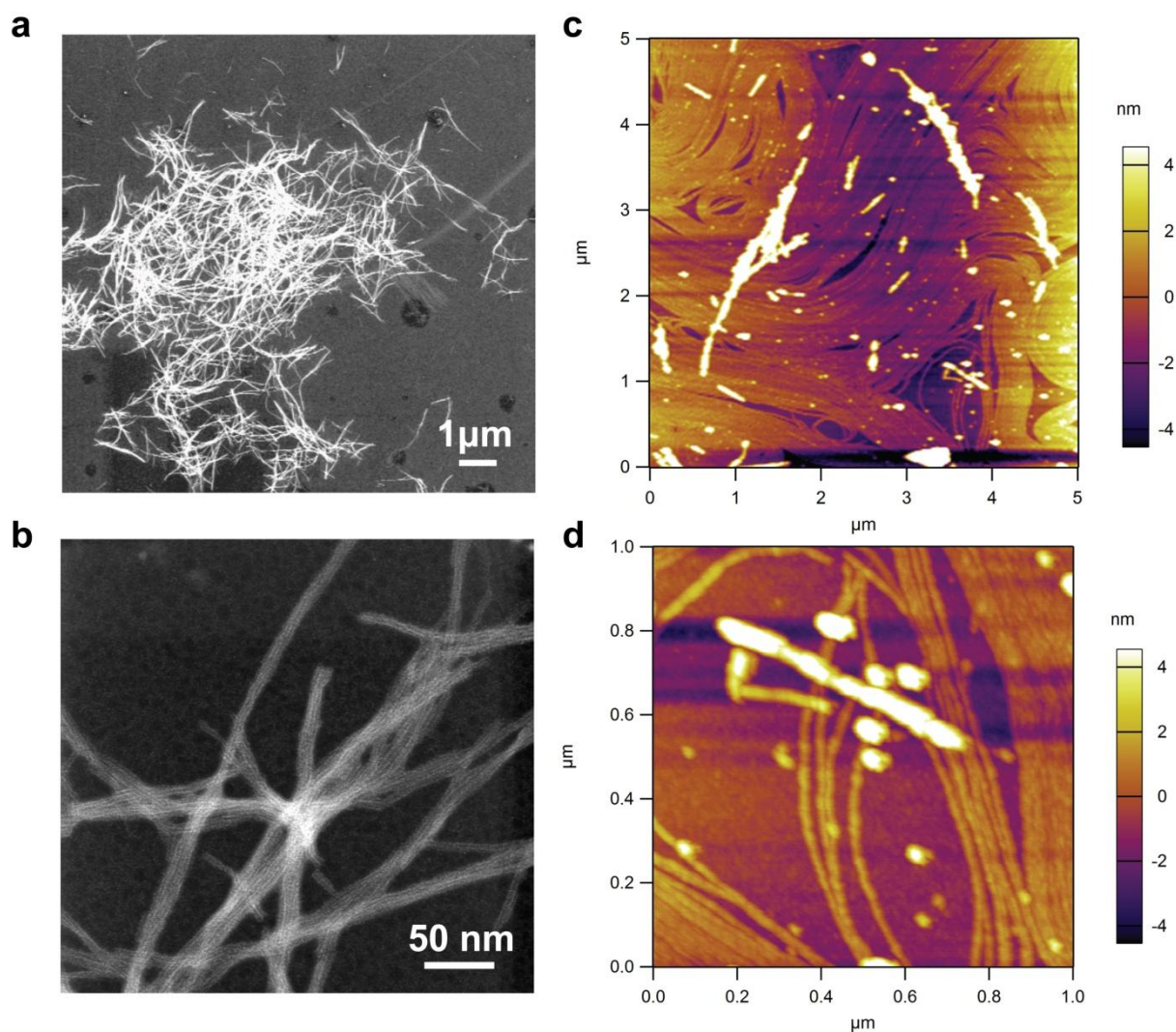
Figure 2.18 Imaging of pPC-nPC CT complex nanowires. STEM images (a and b) and AFM images (c and d) of n/p-coassembled supramolecular nanowires.

STEM images of positively stained supramolecular n/p-coassembled CT complex revealed a network of highly uniform nanofibrous morphology with diameters of 10±1 nm and microns long in length (Figure 2.18a-b). These results confirmed that the average diameter of n/p-coassembled supramolecular nanowires is similar to those of individual pPC and nPC nanofibers. Moreover, atomic force microscope (AFM) images of dried pPC-nPC sample further verified formation of highly uniform nanofibers (Figure 2.18c-d).
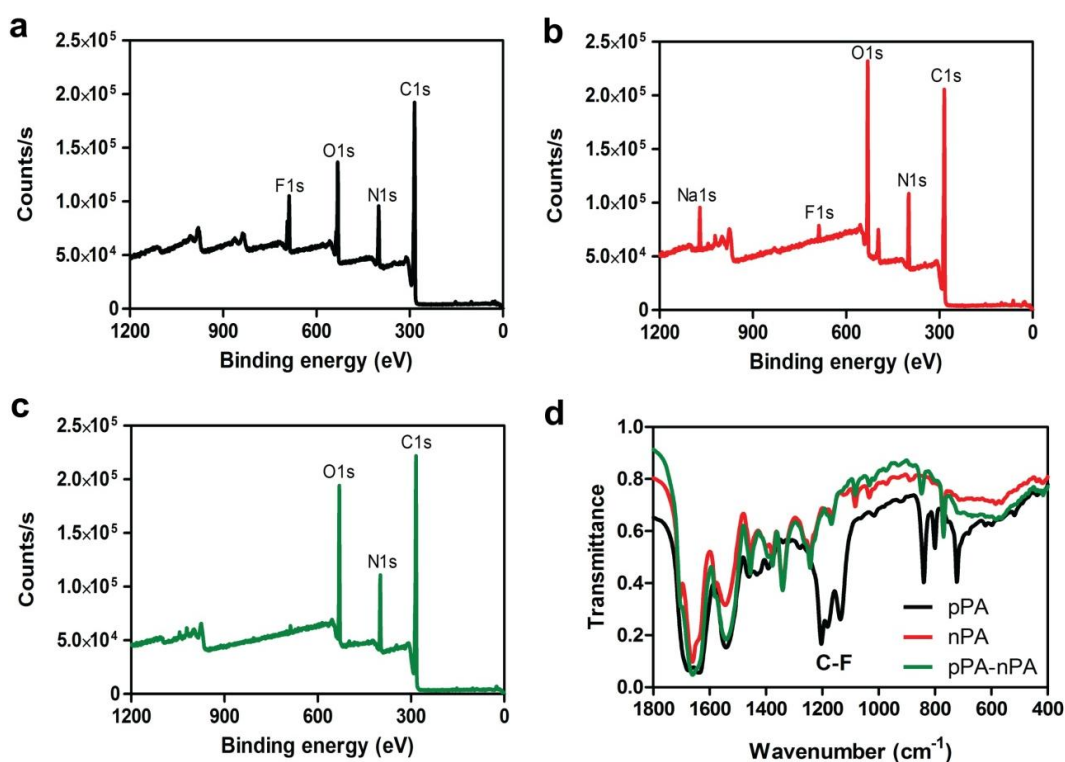
Figure 2.19 XPS analysis of pPC (a), nPC (b), and pPC-nPC (c) powders. FT-IR analysis (d).

XPS, FT-IR and Nuclear Overhauser Effect Spectroscopy (NOESY) were conducted to study the efficient electrostatic interactions between positively charged quaternary amine groups (NH_3^+) of the pPC and negatively charged carboxylate groups (COO^-) of the nPC within n/p-coassembled supramolecular nanowires. The pink suspension of n/p-coassembled CT complex was

centrifuged at 8500 rpm and the upper solution part was decanted followed by addition of fresh water and centrifuged again. This procedure was repeated several times to get rid of any uncomplexed pPC and nPC molecules and then lyophilized to get a pink powder. XPS analysis of the pPC powder shows existence of F1s at 689 eV (Figure 2.18a). This corresponds to presence of counterion trifluoroacetate anion (TFA$^-$) [100]. Meanwhile, nPC powder shows Na 1s at 1072 eV (Figure 2.18b) which is attributed to presence of counterion sodium cation (Na$^+$). On the other hand, no detectable signal at 689 eV (F1s) and 1072 eV (Na1s) in n/p-coassembled CT complex (Figure 2.18c) was observed, which is due to efficient electrostatic interaction between NH$_3^+$ and COO$^-$ groups where Na$^+$ and TFA$^-$ forms soluble sodium trifluoroacetate salt, which is washed away during centrifugation steps. FTIR measurements further confirmed removal of sodium trifluoroacetate during washing as the C–F stretching mode (1110–1220 cm^{-1}) completely disappeared in n/p-coassembled CT complex powder (Figure 2.18d) [101].
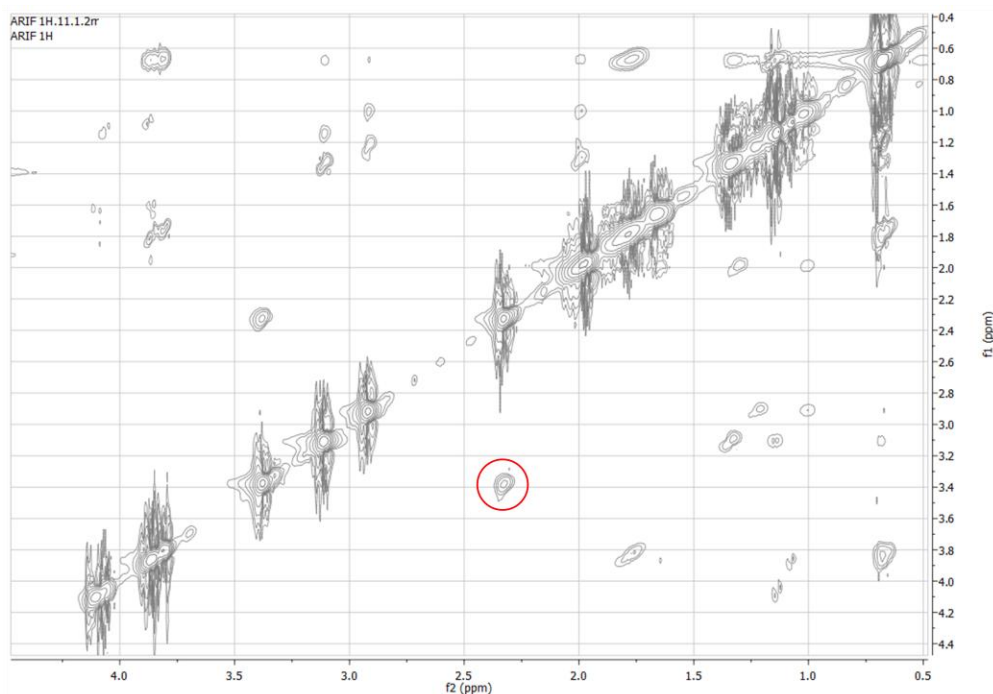
Figure 2.20 NOESY spectrum of pPC-nPC CT complex. Close contact is shown by red circle.

To further elucidate the electrostatic interactions within n/p-coassembled CT nanowires we carried out 2D NOESY, which is a powerful nuclear magnetic resonance (NMR) technique for structural studies. When a proton is close in space (> 5Å) to another proton (or any other nuclei with spin > 0), their magnetic dipoles interact, therefore it can be easily detected by NOESY technique. Typical distance between D-A charge-transfer complex and β-sheet structure is approximately in the range of 3-5 Å. Hence, interacting protons of the pPC with the nPC is within the range of NOE signal and can easily be detected. We observed close contacts (<3 Å) between Glu-H_β protons of nPC and Lys-H_ε protons of pPC (Figure 2.20) which further proved that the pPC and the nPC are positioned in close proximity by electrostatic interactions within the n/p-coassembled CT complex nanowires [102].

Pyrene and NDI moieties can form a variety of CT complexes in different molecular structures such as A-D, D-A-D, and A-D-A where each CT complex has heat of formation and specific K_A value [103, 104]. UV-vis, XPS, mass spectrometry (MS) and isothermal titration calorimetry (ITC) were carried out to determine the accurate molecular structure of CT complex and its K_A value. We followed the Job's Method to estimate the stoichiometry of D-A [105]. Solutions of the pPC and the nPC were mixed in known ratios to form the CT complex where the total concentrations of the pPC and the nPC in solution were kept constant (Figure 2.21). Absorbance at 520 nm (CT band) was plotted against the molar ratio of the nPC and the maximum absorbance value intersecting x-axis corresponds to the stoichiometry of D-A (1:2).
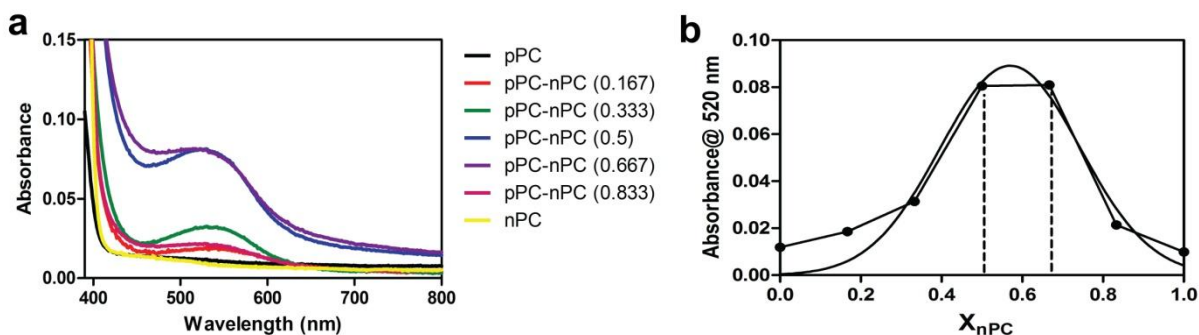
Figure 2.21 (a) UV-vis absorbance spectra of pPC and nPC molecules mixed at different mole ratios. (b) Plot of absorbance at 520 nm (CT band) versus mole ratio of nPC (X_{nPC}).
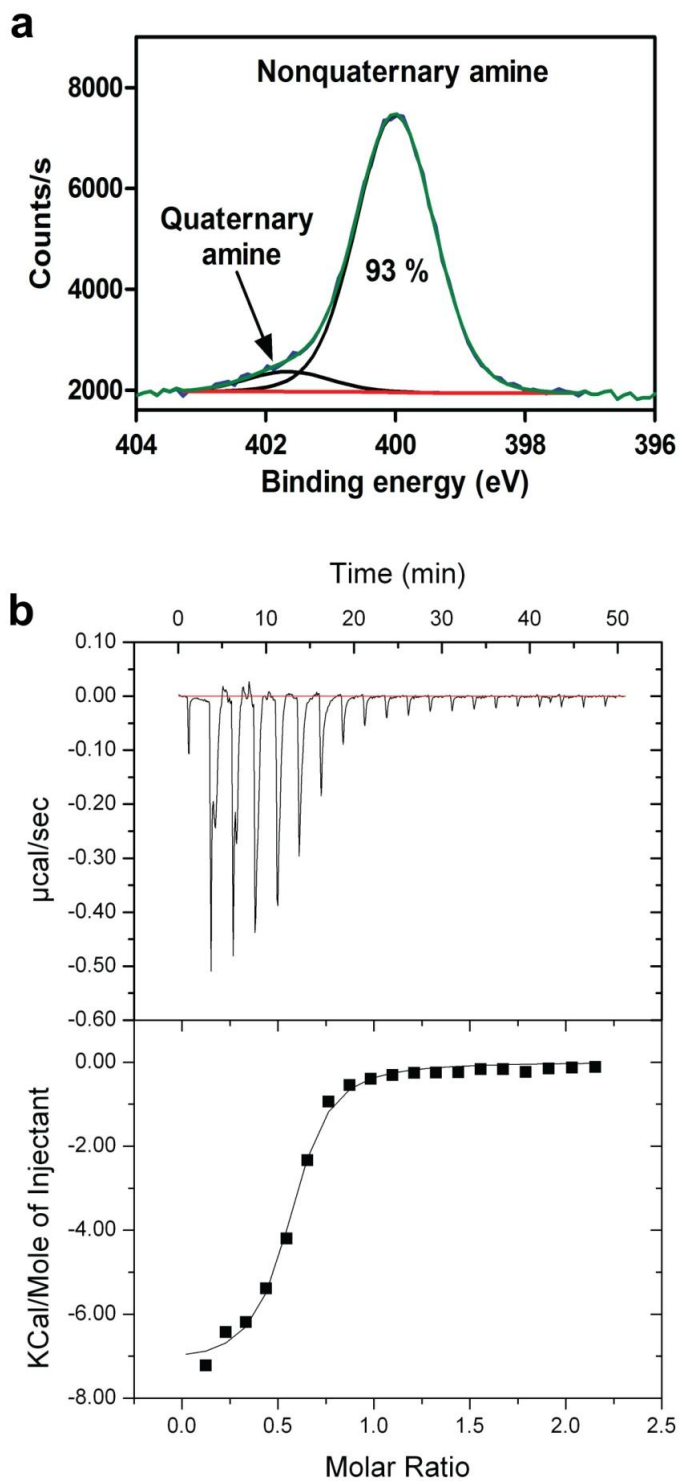
Figure 2.22 (a) Gaussian deconvolution of the N1s signal acquired by XPS. (b) Isothermal calorimetry titration of nPC (0.1 mM) by pPC (1 mM).

Gaussian deconvolution of the N1s signal acquired by XPS (Figure 2.22a) can be utilized to determine the exact proportion of quaternary ($-NH_3^+$) and nonquaternary amine groups in n/p-coassembled CT complex [89]. Signal at 402 eV ($-NH_3^+$) and at 400 eV (R) corresponds to 7% and 93 % of total amine groups respectively. Only CT complex with nPC-pPC-nPC (A-D-A) structure satisfy this ratio . Mass spectrometry of CT complex shows a signal at 1582 m/z, which further supports that D molecules are sandwiched between two A molecules (A-D-A) (Figure 2.23). Results obtained from spectroscopic techniques verify the presence of A-D-A unit cells within n/p-coassembled CT complex nanowires.
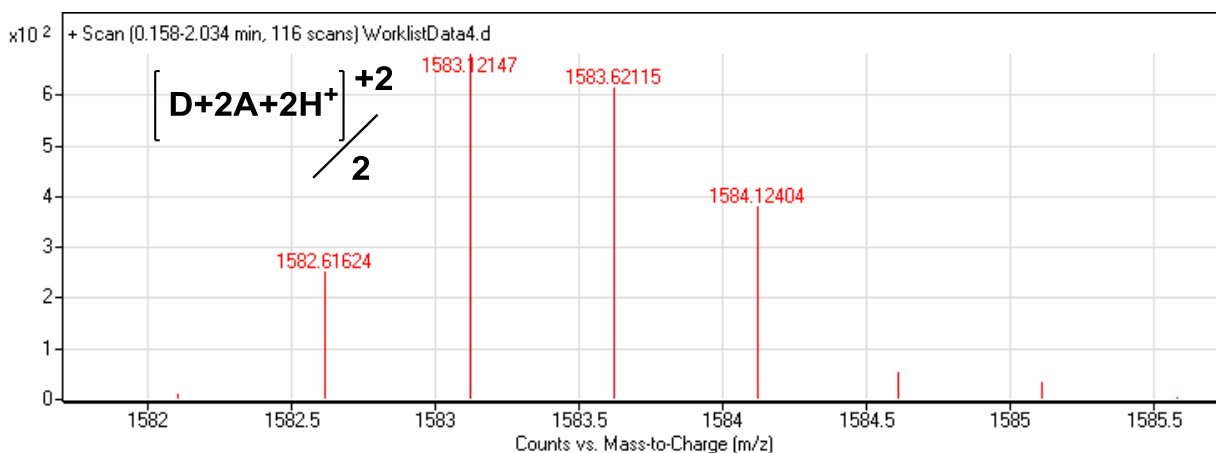
Figure 2.23 Mass spectrum at positive mode showing formation of nPC-pPC-nPC (A-D-A) CT complex.

ITC was performed to further support the spectroscopic results. A very strong binding constant of (K_A) of 5.18×10^5 M^{-1} and enthalpy (ΔH) of -7215 cal/mol were calculated from isothermal titrations (Figure 2.22b). Owing to synergic interactions arising from charge-transfer formation, hydrogen-bonding and electrostatic interactions between the pPC and the nPC molecules, a very strong K_A value was obtained for n/p-coassembled CT nanowires. Moreover, a ratio of 1:2 was calculated for the pPC-nPC (Figure 2.22a). It is worth mentioning that this is the first study to

determine the K_A and thermodynamic parameters for such supramolecular complex system consist of multiple noncovalent interactions.

2.4 Conclusion

In conclusion, we presented self-assembling p-type and n-type β-sheet forming peptide-chromophore conjugates. Positively charged pPC and negatively charged nPC molecules individually assembled into highly uniform p-type and n-type nanofibers, respectively, with diameter of 11±1 nm and microns in length. These complementary p-type and n-type nanofibers coassembled via hydrogen bonding and electrostatic interactions to generate highly uniform supramolecular n/p-coassembled 1D nanowires. This smart and novel molecular design ensured alternating arrangement of D and A chromophores within n/p-coassembled supramolecular nanowires. Moreover, we demonstrated that supramolecular n/p-coassembled nanowire is formed by highly alternating A-D-A unit cells having a strong K_A of 5 x 10^5 M^{-1}. This smart, novel and facile strategy allows fabrication of well-defined supramolecular electroactive nanomaterials in aqueous media, which can find a variety of applications in optoelectronics, photovoltaics, bioelectronics and tissue engineering.

Chapter 3

Supramolecular Peptide Nanofiber Templated Pd Nanocatalyst for Efficient Suzuki Coupling Reactions in Aqueous Conditions

This work is partially described in the following publication:

3.1 Introduction

Metal nanostructures are attractive catalysts for a wide variety of organic reactions due to increased accessibility to surface atoms and lower coordination numbers compared to bulk equivalents, which results in enhanced catalytic activity [106]. Palladium nanoparticles have been used as catalysts for C-C coupling such as Suzuki and Heck reactions as a suspension or adsorbed onto a support i.e. carbon structures [107], dendrimers [108], polymers[109], metal-organic frameworks [110] and mesoporous silica [111]. In most cases, solid support materials provide easy separation and enable reuse of the catalyst. Catalytic activity of palladium nanoparticles is further enhanced by employing nanoscale template directed synthesis providing high surface area nanoparticles [112, 113]. However, not only the catalyst performance is important, but also environmental concerns should be taken into account during development of novel catalysts [114]. The research for environmentally friendly chemical synthesis led to a search in catalytic reactions in cheap, readily available, non-toxic, non-flammable and

environmentally friendly solvents such as water at room temperature [115]. Suzuki–Miyaura reactions in water with improved yield and simple reaction protocol still remains a major challenge. In general, various additives such as phosphine ligands and quaternary ammonium salts such as tetrabutylammonium bromide (TBAB) or cetyltrimethylammonium bromide (CTAB) are required for effective reaction progress in aqueous media [116, 117]. These additives lower the atom economy of the reaction and produce extra waste products.
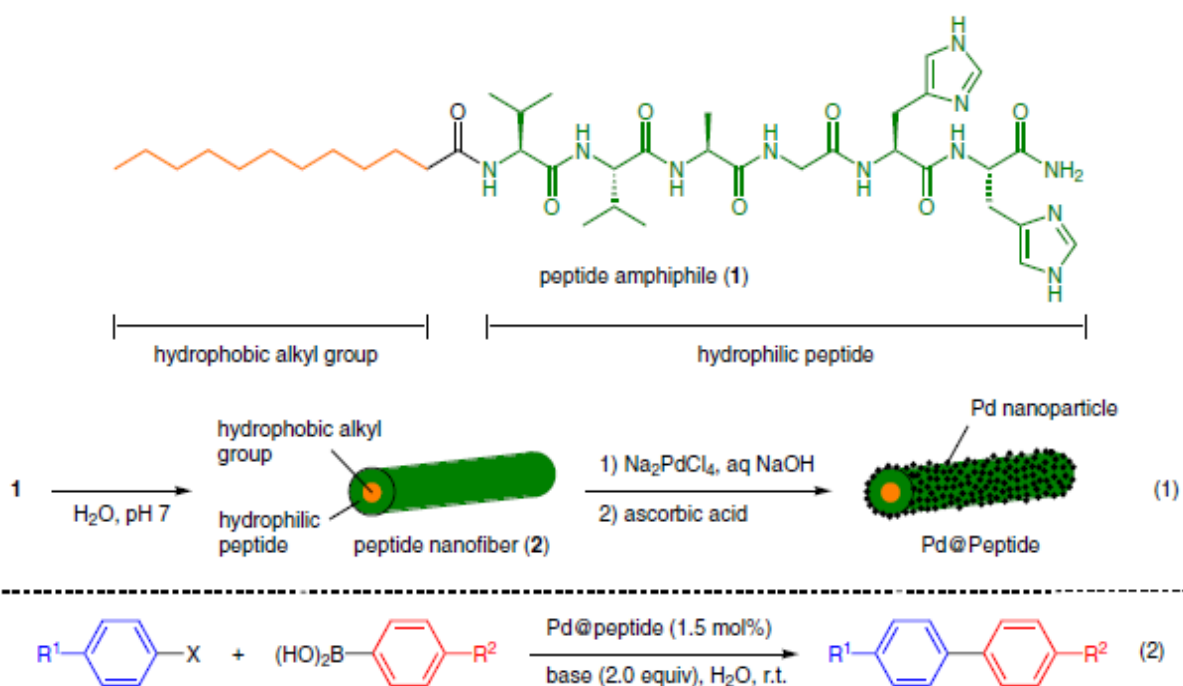
Scheme 2. Self-assembly of peptide amphiphile molecules generates nanofibers with 10 nm in diameter (1). Seeding and reduction of Pd^{II} ions on the surface of peptide nanofibers form hybrid peptide and Pd^0 nanostructures (Pd@Peptide). Pd@Peptide nanostructures can be used as catalyst in C-C coupling reactions (2).

Biological template materials (e.g. peptide, protein, virus, and bacteria) in the synthesis of metal nanostructures as catalysts are of great interest because of their versatile chemical and physical

properties [118]. A few studies previously reported heterogeneous palladium catalysts, which were synthesized by a nanoscale and environmentally friendly template for C-C coupling reactions [119]. Self-assembled peptide amphiphile (PA) nanofibers are promising candidates as a template and support due to their tailorable surface properties. By employing metal-binding amino acids into PA structure (e.g. lysine, glutamic acid and DOPA), peptide nanofibers can specifically bind metal ions for functional materials applications [120, 121]. These bioinspired peptide nanostructures can be further exploited for seeding and nucleation of metal ions for producing nanoscale inorganic nanostructures [120].

Herein, we report bioinspired supramolecular peptide nanofiber templated Pd^0 hybrid nanocatalyst (Pd@Peptide) for mild and efficient Suzuki–Miyaura coupling reactions in aqueous media at room temperature without additives. The efficiency of the Pd@Peptide nanocatalyst system was demonstrated by successful application in a variety of reagents.

3.2 Experimental Section

3.2.1 Materials

9-Fluorenylmethoxycarbonyl protected amino acids, MBHA Rink Amide Resin, HBTU (O-Benzotriazole-N,N,N',N'-tetramethyl-uronium-hexafluoro-phosphate) are purchased from Novabiochem, lauric acid is purchased from Merck. All boronic acid derivatives, aryl halides, K_3PO_4, K_2CO_3 and sodium tetrachloropalladate, L-(+)-ascorbic acid were purchased from Sigma Aldrich. All chemicals were used directly without any further purification.

3.2.2 Peptide Synthesis

Peptide amphiphile molecule is synthesized using standard solid phase peptide synthesis. MBHA Rink Amide resin was used as solid phase. Amino acid couplings were performed by 2 equivalents of fluorenylmethyloxycarbonyl (Fmoc) protected amino acids, 1.95 equivalents O-Benzotriazole-N,N,N',N'-tetramethyl-uronium-hexafluoro-phosphate (HBTU) and 3 equivalents of N,N-diisopropylethylamine (DIEA) for 3 h. Fmoc protecting groups were removed by 20% piperidine /dimethylformamide solution for 20 minutes. Cleavage of the product from the Rink Amide was carried out by a mixture of trifluoroacetic acid: triisopropylsilane: H_2O in the ratio of 95:2.5:2.5 for 2 h. The resin was washed thoroughly with DCM. Collected peptide solution was concentrated by rotary evaporation. The residual viscous peptide mixture was treated with cold ether and the resulting precipitate was lyophilized to get a white powder.

3.2.3 Liquid Chromatography

For the structural analysis of the peptide Agilent Technologies 6530 Accurate-Mass Q-TOF LC-MS and Zorbax SB-C8 column were used. Concentration of the sample for LC-MS measurement was 0.5 mg/ml. Solvents were water (0.1% formic acid) and acetonitrile (ACN) (0.1% formic acid). LC-MS was run for 25 min for each sample and it started with 2% ACN and 98% H_2O for 5 minutes. Then, gradiently ACN concentration reached to 100% until 20 minutes. Finally, its concentration was dropped to 2% and it kept running for 5 minutes. Solvent flow was 0.65 mL/min and 5 μL sample was injected.

3.2.4 Circular Dichroism (CD) Spectroscopy

Secondary structure of peptide amphiphile was analyzed with Jasco **J**-815 circular dichroism spectrometer. 1 wt% peptide solution was prepared in ddH$_2$O and jellified with 0.1 M NaOH.

Then, peptide gel was diluted with 1 mM NaOH solution and 5×10^{-4} M peptide solution was measured from 300 nm to 190 nm with 0.1 data pitch, 100 nm/min scanning speed, 1 nm band width and 4 s D.I.T. Average of three measurements were used and sensitivity was selected as standard.

3.2.5 Rheology

Anton Paar MCR-301 rheometer was used for mechanical characterization of peptide amphiphile gels. I prepared 1% (w/v) peptide solution in distilled water, and added 0.1 M NaOH solution. After sweep measurements, amplitude kept constant as 0.1% and amplitude frequency as 10 rad/s during 60 min. In frequency sweep measurements, angular frequency varied between 0.1 and 100 rad/s while amplitude was 0.1 %. In strain sweep experiments, amplitude varied between 0.001 and 1000% while angular frequency was constant at 10 rad/s. In all rheometer graphs, x and y axises were in logarithmic scale.

3.2.6 Transmission Electron Microscopy

1% (w/v) peptide solution was prepared and alkalified with 0.1 M NaOH solution. Peptide gel was diluted with 1 mM NaOH solution, a small amount of solution was dropped to carbon covered copper grid. To image organic peptide fibers, 2% (w/v) uranyl acetate solution was used. Finally, carbon grid was dried at atmosphere. FEI Tecnai G2 F30 transmission electron microscope (TEM) was used to display peptide amphiphile nanofibers. In the characterization of palladium nanoparticles, samples were dropped to carbon covered copper grids, allowed to dry at atmosphere conditions and imaged with TEM.

3.2.7 Scanning Electron Microscopy/Critical Point Dryer

FEI Quanta 200 FEG environmental scanning electron microscope (SEM) was used to image peptide amphiphile gel after removing solvent with Tousimis Autosamdri-815B, Series C critical point dryer (CPD). 1.5 wt% solution of peptide in distilled water were prepared and 0.1 M NaOH solution was added to peptide solution on metal mesh to adjust the pH around 7. Since critical point dryer can be used with samples in isopropanol, we washed peptide gels with 20%, 40%, 60%, 80% and 100% (v/v) isopropanol solutions. Then, gels were dried with a critical point dryer. Finally, peptide amphiphile network was imaged with SEM.

3.2.8 Synthesis of Palladium Nanostructures

First, 1 wt% peptide was dissolved in hydrogel was prepared at pH 7. 0.5 eq. of Na_2PdCl_4 in 1 mM NaOH solution was added for overnight. Then, 0.5 eq. of Na_2PdCl_4 in 1 mM NaOH solution was added to the sol-gel. After 1 h of incubation for seeding, 0.5 equimolar of ascorbic acid in 1 mM NaOH was added. When all of the palladium ions were reduced to Pd^0 (Figure S7), sol-gel was divided into two and while one was kept for further characterization, other one was diluted with same amount of palladium by keeping the final palladium concentration constant but decreasing the peptide concentration to half. After incubation for another hour, ascorbic acid solution was added to reduce palladium ions. This cycle was repeated three times. After each addition and reduction of palladium ions, samples were imaged with TEM. In all characterizations, sample after third addition of palladium ions was used.

3.2.9 Characterization of Pd Nanostructures

To monitor stability of structures, various treatments were applied to nanostructures. Pd nanostructure sample was washed with $3xH_2O$ then 3xEtOH. After evaporation of EtOH, sample

was dissolved in EtOH; some amount was poured into Si wafer and heated at 100 ^{0}C for 1 h. Finally, SEM images were taken.

3.2.10 X-Ray Diffraction Analysis

In crystallographic analysis of palladium nanostructures, PAN analytical X'Pert X-ray Diffractometer was performed by using Cu K radiation. Mylar foil of 6 μm thickness was used as the surface to drop peptide/palladium samples. Rotation time was 16 seconds, scan range was from 30° to 90°, and step size was 0.0525°.

3.2.11 Thermogravimetric Analysis

Thermal gravimetric analysis was performed with TA Q500 instrument. Samples were dried under atmosphere conditions and then analysis was performed under high purity nitrogen purge (40.0 ml/min) with heating the samples from 30 °C to 550 °C with 20 °C/min heating rate.

3.2.12 Suzuki Coupling Reactions

All reactions and manipulations were run under air atmosphere. Under air atmosphere, a reaction tube was charged with aryl iodide (0.5 mmol), aryl boronic acid (0.75 mmol), Pd@Peptide (1.5 mmol%), K_3PO_4 (1 mmol) and deionized water (3 mL). The mixture was stirred at room temperature, it was monitored by GC until aryl iodide was totally reacted. The crude product was characterized by GC-MS analysis (Agilent GCMS-7890A-5975C equipped with a 0.25 mm ×30 m HP-5MS capillary column).

For bromobenzene coupling reactions, typically, under air atmosphere, a reaction tube was charged with aryl bromide (0.5 mmol), aryl boronic acid (0.75 mmol), Pd@Peptide (1.5 mmol %), K_3PO_4 (1 mmol) and deionized water: ethanol into 1:1 ratio (4 mL). The mixture was stirred

66

at 80 ^{o}C, it was monitored by GC until aryl bromide was totally reacted. The crude product was characterized by GC-MS analysis (Agilent GCMS-7890A-5975C equipped with a 0.25 mm $\times$30 m HP-5MS capillary column).

For bromobenzene coupling reactions in neat water at room temperature, typically, under air atmosphere, a reaction tube was charged with aryl bromide (0.5 mmol), aryl boronic acid (0.75 mmol), Pd@Peptide (1.5 mmol %), NaOH (1 mmol) and deionized water (5 mL). The mixture was stirred at room temperature; it was monitored by GC until aryl bromide was totally reacted. The crude product was characterized by GC-MS analysis (Agilent GCMS-7890A-5975C equipped with a 0.25 mm $\times$30 m HP-5MS capillary column).

For chlorobenzene coupling reaction in neat water at room temperature, typically, under air atmosphere, a reaction tube was charged with chlorobenzene (0.5 mmol), aryl boronic acid (0.75 mmol), Pd@Peptide (1.5 mmol %), NaOH (1 mmol) and deionized water (5 mL). The mixture was stirred at room temperature; it was monitored by GC until aryl bromide was totally reacted. The crude product was characterized by GC-MS analysis (Agilent GCMS-7890A-5975C equipped with a 0.25 mm $\times$30 m HP-5MS capillary column).

For the recyclability test, Suzuki coupling reaction was performed with bromobenzene (0.5 mmol), 4-methoxyphenylboronic acid (0.75 mmol), Pd@Peptide (1.5 mol% with respect to bromobenzene concentration), K_3PO_4 (2.0 equiv), water/EtOH (1:1) at 80 ^{o}C. Each time, the catalyst was isolated from the reaction solution at the end of catalytic reaction, washed with water and ethanol. The dried catalyst was then reused in a next run.

3.3 Results and Discussion

In this study, we designed and synthesized a de novo peptide amphiphile molecule (Lauryl-VVAGHH-Am that can coordinate to Pd^{II} ions through lone pair electrons in imidazole moieties
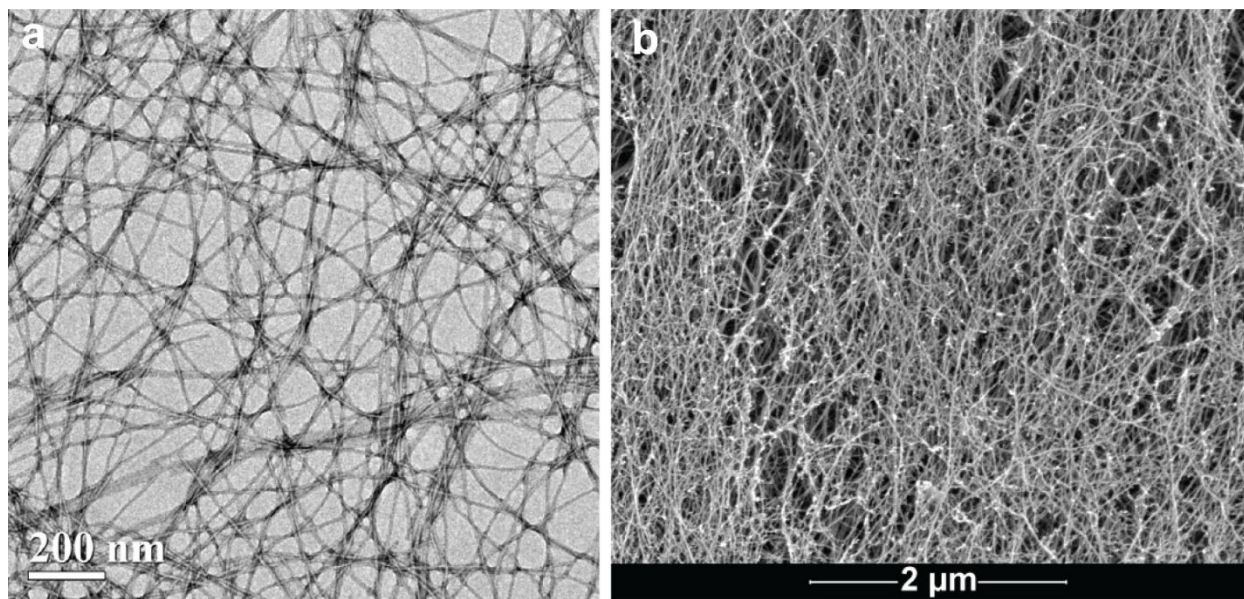
Figure 3.1 (a) TEM and (b. SEM images of PA at pH 7.0

of histidine residues in the peptide (Scheme 2) [122]. At pH >6, the PA molecules can self-assemble into nanofibers with a diameter of ca.10 nm (Figure 3.1a-b) directed by β-sheet structures (Figure 3.2). Three-dimensional network of the PA nanofibers forms a self-supporting hydrogel at concentration of 1 wt% (Figure 3.3a-b). In this work, we exploited peptide nanofibers as a nanoscale template for formation of Pd^0 nanoparticles. Following a multi-step reduction methodology, closely-packed one-dimensional palladium nanoparticles were grown on peptide nanofibers. Pd^{II} ions accumulated on the peptide nanofibers due to their affinity to imidazole residues.
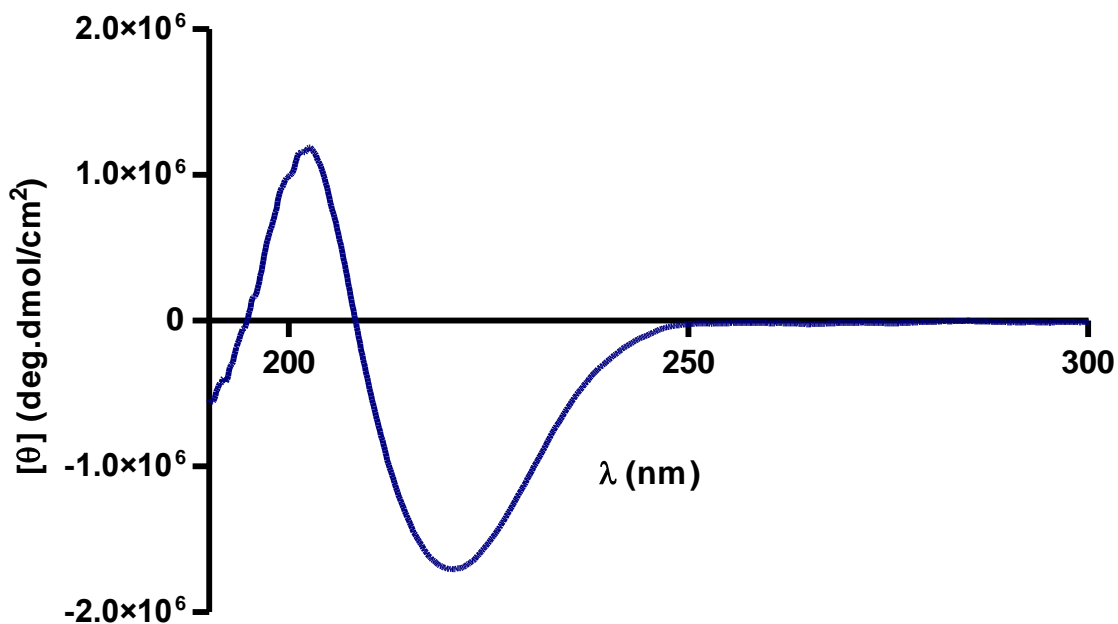
Figure 3.2 CD spectra of peptide amphiphile.
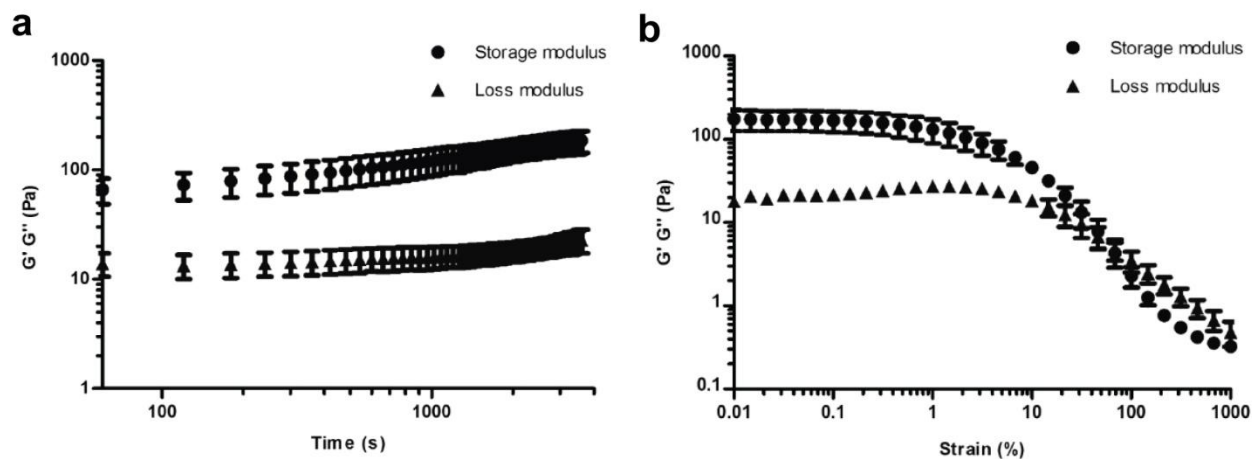
Figure 3.3 (a) Time sweep graph of peptide amphiphile gel. (b) Strain sweep graph of peptide amphiphile gel.

After peptide nanofiber formation at pH 7, palladium solution was added to peptide nanofiber hydrogel and mixture was left at room temperature overnight to enable interaction of the ions

with imidazole moiety of histidine residues in the peptide. Later, reducing agent (L-(+)-ascorbic acid) was added to the mixture. After the first reduction, the Pd^{II} ion amount was increased for second and third reduction cycles by increasing Pd/Peptide molar ratio. Nanoparticle formation on peptide template was observed in the first reduction cycle (Figure 3.4). After the third cycle, coating of peptide nanofibers with closely packed palladium nanoparticles was clearly observed with larger nanoparticle size (Figure 3.5). To remove peptide molecules without Pd, the sample was filtered through cellulose membrane with 0.2 µm cut off. Filtration was found to be the most effective and easy way of eliminating the excess peptide without disturbing the integrity of the catalyst assembly. To best of our knowledge, this type of highly ordered Pd nanostructures was obtained for the first time by use of peptide nanofiber template methodology.
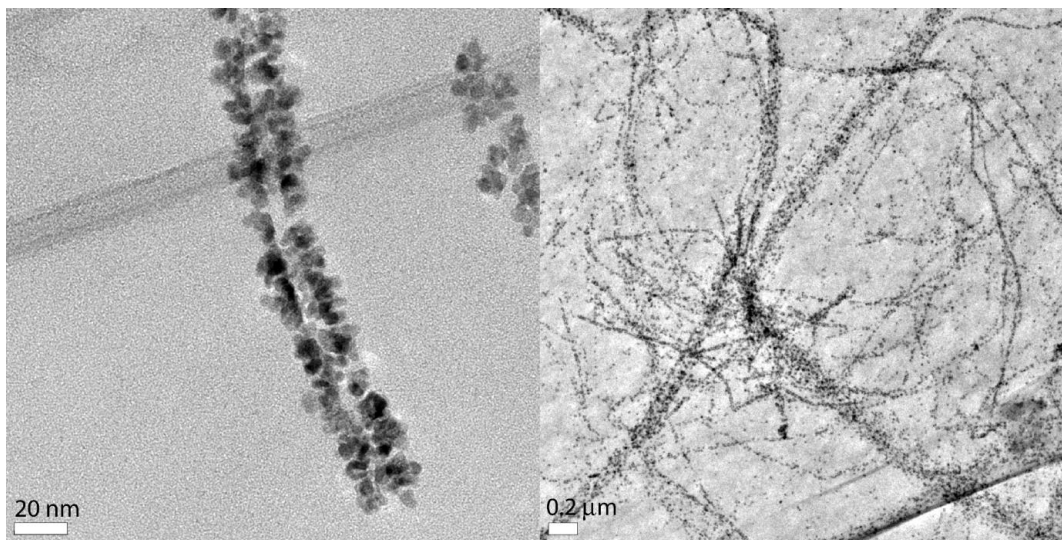
Figure 3.4 TEM of Pd nanostructures after first reduction cycle.

Metal nanoparticle loading capacity of the peptide nanofiber templates was assessed by thermogravimetric analysis (TGA). The Pd@Peptide sample was dried at 100 °C in an oven, and heated to 550 °C. Inorganic content was found to be 42.5%.
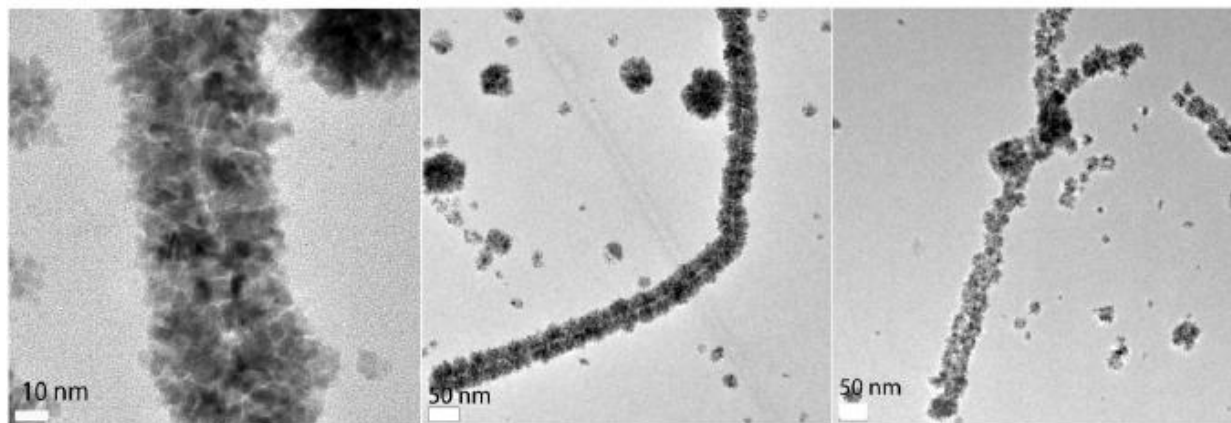
Figure 3.5 TEM images of Pd nanostructures after third reduction cycle.

Crystalline structure of Pd@Peptide sample was analyzed by HRTEM (Figure 3.6a) and X-ray diffractometry (XRD). The dominant surface is (111). Pd (111) is the lowest energy facet and the most stable facet of Pd [123]. The presence of broad Pd (111) peak expresses low periodic and atomic order of Pd nanoparticles, because as grain size decreases, its XRD peak broadens (Figure 3.6b). Suzuki coupling reactions were performed as a model reaction to determine catalytic activity of the Pd nanostructures on the peptide nanofibers.

Water was used for coupling reactions as an attractive green and cheap solvent [124]. We optimized Pd@Peptide loading as 1.5 mol% (Table 1). Then suitable reaction conditions for iodobenzene (Table 1, Entry 1) in water at room temperature were optimized. The reaction was completed in less than 4 h with 99% biphenyl conversion (Table 1, Entry 1). Mixing ethanol,

which is another environmentally friendly solvent, expedited the reaction rate four folds (Table 1, Entry 2).
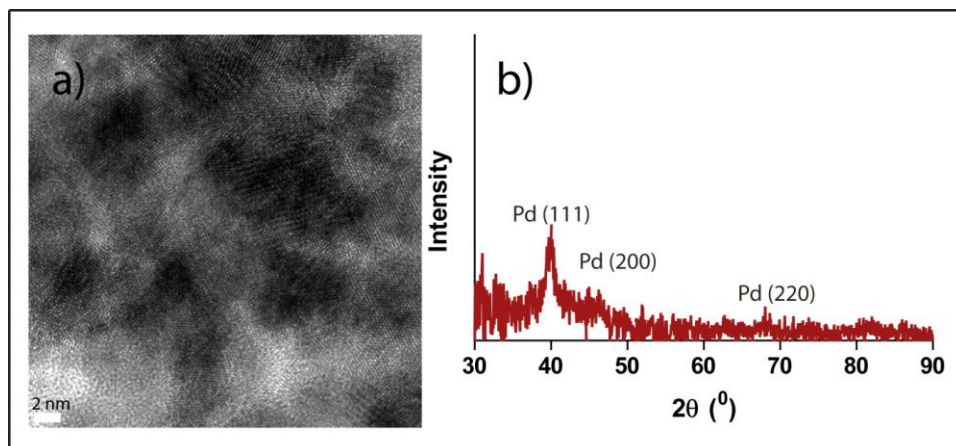
Figure 3.6 (a) HRTEM image of Pd nanostructures. (b) XRD pattern of Pd nanostructures.

Table 1 Suzuki-Miyaura coupling of aryl halides with Pd@Peptide[a]

Entry	X	Base	Solvent	Time (h)	T [°C]	Conversion (%)[b]
1	I	K_3PO_4	H_2O	4	25	99
2	I	K_3PO_4	H_2O:EtOH	1	25	99
3	Br	K_3PO_4	H_2O	10	25	< 3
4	Br	K_3PO_4	H_2O	10	80	< 5
5	Br	K_2CO_3	H_2O	10	25	0
6	Br	K_2CO_3	H_2O	10	80	< 1
7	Br	K_2CO_3	H_2O:EtOH	10	25	< 3
8	Br	K_3PO_4	H_2O:EtOH	10	25	10
9	Br	K_3PO_4	H_2O:EtOH	4	80	99
10	Br	NaOH	H_2O	4	25	99
11	Cl	NaOH	H_2O	16	25	99

[a] Reaction conditions: aryl halide (0.5 mmol), arylboronic acid (0.75 mmol), Pd@Peptide (1.5 mol% with respect to aryl halide concentration), K_3PO_4 (2.0 equiv), solvent (4 mL). [b] Reaction conversions were determined by GC-MS.

The rate enhancement is potentially due to improved solubility of the starting materials in water/ethanol mixture [125]. Various aryl iodides were employed to investigate the diversity of aryl iodides tolerated in Suzuki-Miyaura coupling reactions with aryl boronic acids (Table 2). The Pd@Peptide nanocatalyst revealed excellent catalytic activity towards diverse substrates under the optimized reaction conditions (Table 2, Entry 1). When activated aryl iodide (1-fluoro-4-iodobenzene) was used instead of iodobenzene, the biaryl product (Table 2, Entry 2) was obtained in only 1h with 99% conversion.

Table 2 Suzuki-Miyaura coupling of aryl iodides with Pd@Peptide Nanocatalyst[a]
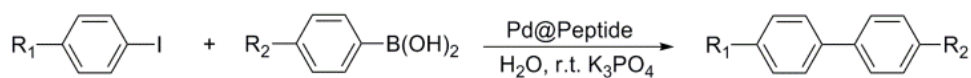
Entry	R_1	R_2	Time (h)	Conversion (%)[b]
1	H	H	4	99
2	F	H	1	99
3	OMe	H	2	99
4	H	OMe	1	99
5	F	OMe	1	85
6	OMe	OMe	1	99

[a] Reaction conditions: aryl iodide (0.5 mmol), arylboronic acid (0.75 mmol), Pd@Peptide (1.5 mol% with respect to aryl iodide concentration), K_3PO_4 (2.0 equiv), water (4 mL). [b] Reaction conversions were determined by GC-MS.

It should also be noted that the corresponding biaryl product was obtained in only 2h with quantitive yield when deactivated 1-iodo-4-methoxybenzene (Table 2, Entry 3) was used.

Table 3 Miyaura coupling of aryl bromide with Pd@Peptide [a]

$$R_1\text{—}\langle\text{—}\rangle\text{—Br} \ + \ R_2\text{—}\langle\text{—}\rangle\text{—B(OH)}_2 \xrightarrow[\substack{H_2O/EtOH,\ 80\ ^\circ C \\ K_3PO_4}]{Pd@Peptide} R_1\text{—}\langle\text{—}\rangle\langle\text{—}\rangle\text{—}R_2$$
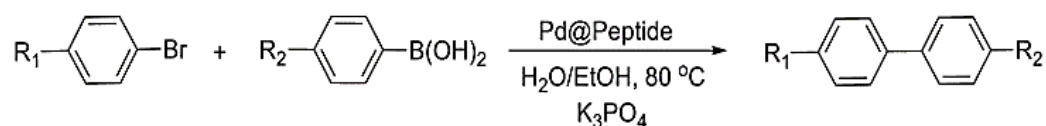
Entry	R_1	R_2	Time [h]	Conversion (%)[b]
1	H	H	4	99
2	H	OMe	1.5	99
3	H	COH	2	99
4	H	CH$_2$OH	2	89
5	NO$_2$	H	2	85
6	NO$_2$	OMe	2	83
7	H	HC=CH	4	58

[a] Reaction conditions: aryl bromide (0.5 mmol), arylboronic acid (0.75 mmol), Pd@Peptide (1.5 mol% with respect to aryl bromide concentration), K$_3$PO$_4$ (2.0 equiv), water/EtOH (1:1) at 80 °C. [b] Reaction conversions were determined by GC-MS.

The Pd@Peptide nanocatalyst can activate 4-iodoanisol efficiently. Replacing phenyl boronic acid with 4'-methoxybiphenyl-4-ylboronic acid demonstrated interesting results. 4'-methoxybiphenyl-4-ylboronic acid reacted with Iodobenzen, 1-fluoro-4-iodobenzene (activated), and 1-iodo-4-methoxybenzene (deactivated) and yielded the desired products (Table 1, Entry 5, 6, and 7) with high yields in only 1h. The electron-withdrawing and electron-donating groups in

aryl iodides did not have considerable effect on the reaction rates. We tried several conditions for aryl bromides as summarized in Table 1. It was previously reported that activation of Br-C bond is more challenging than I-C bond [126]. Only trace amount of biphenyl product was observed for bromobenzene in water at room temperature (Table 1, entry 3) and at 80 °C (Table 1, Entry 4). The nature of the base is reported to be crucial in different Suzuki coupling reactions [127]. Therefore, the base was changed from K_3PO_4 to K_2CO_3.

Table 4 Suzuki-Miyaura coupling of aryl bromides with Pd@Peptide Nanocatalyst[a]
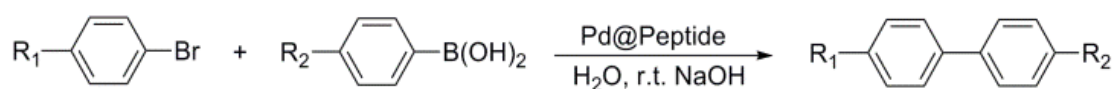
Entry	R_1	R_2	Time [h]	Conversion (%)[c]
1	H	H	4	99
2	NO_2	H	24	99
3[b]	NO_2	H	12	99
4	OMe	H	24	99
5	H	OMe	4	83

[a] Reaction conditions: aryl bromide (0.5 mmol), arylboronic acid (0.75 mmol), Pd@Peptide (1.5 mol% with respect to aryl bromoide concentration),NaOH (2.0 equiv), water (5 mL) at room temperature. [b] 10% ethanol was used. [c] Reaction conversions were determined by GC-MS.

However, it did not improve the reactions for bromobenzene derivatives (Table 1, Entry 5, 6). Inspired from four fold rate enhancement in Entry 2 (Table 1), we mixed ethanol as a green, organic and water miscible solvent with water. When ethanol was mixed with water in 1:1 ratio, some rate enhancement was observed at room temperature (Table 1, Entry 8). Increasing temperature to 80 °C yielded desired product in almost quantitative yield in less than 4 h. High activation of Br-C bond and low solubility of bromobenzene in water caused low catalytic activity due to limited interaction between the reactants. The Pd@Peptide nanocatalyst revealed high catalytic activity in water/ethanol mixture for Br-C bond activation. Interestingly, most of the Suzuki coupling reactions was completed in almost 2 h with very high conversions regardless of the presence of electron donating and withdrawing groups in the reactant molecules (Table 3). Moderate conversion (57%) in Entry 7 is due to formation of by-products due to Heck reaction. The substituted styrene can produce both Suzuki and Heck coupling products in the presence of a base.

In addition, we optimized conditions for aryl bromides in water at room temperature. The NaOH was used as a base (Table 1, Entry 10). The Pd@Peptide nanocatalyst showed excellent catalytic activity with aryl bromides in water at room temperature (Table 4). Most of the reactions were completed with 99% yield. We also investigated the effect of different groups attached to the aryl bromide. The electron withdrawing (Table 4, Entry 2) and electron donating groups (Table 4, Entry 4) present in bromobenzene demonstrated similar results. Interestingly, when 10% ethanol (Table 4, Entry 3) was added as a co-solvent, two folds rate enhancement was observed due to increased solubility of the reactants in ethanol. The 4'-methoxybiphenyl-4-ylboronic acid also showed high yield (83%) when reacted with bromobenzene (Table 4, Entry 5). The Pd@Peptide nanocatalyst also showed excellent catalytic activity even with least reactive chlorobenzene

derivative [127] at room temperature in water (Table 1, entry 11).

Isolation of the catalysts from the reaction mixture and using them in successive reactions make chemical process cost effective on industrial scale and prevent accumulation of mass palladium waste. Therefore, we further evaluated recyclability of our catalyst at harsh conditions (in ethanol/water mixture at 80 °C). The catalyst was reused in consequent reactions and showed efficient catalytic activity even after fifth use (95 % product conversion, Table 5). The cause of deactivation of Pd@Peptide nanocatalyst could be agglomeration of Pd nanoparticles during catalytic reactions and therefore decreasing in total surface area of nanoparticles. Moreover, Pd nanoparticles could leach out from the peptide support and as a result lesser amount of catalyst is available in next catalytic run.

Table 5 Recyclability test of bromobenzene with 4-methoxyphenylboronic at 80 ^{0}C.
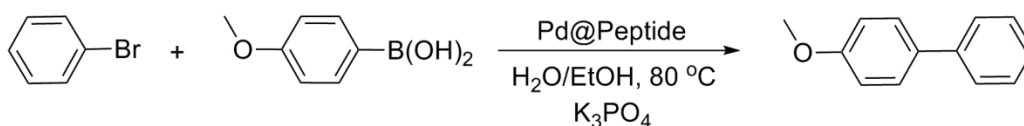
Entry	Time [min]	Conversion (%)
1st	90	99
2nd	90	97
3rd	100	97
4th	100	97
5th	100	95

The GC-MS spectra of the products are given in Figure 3.7- 3.12.
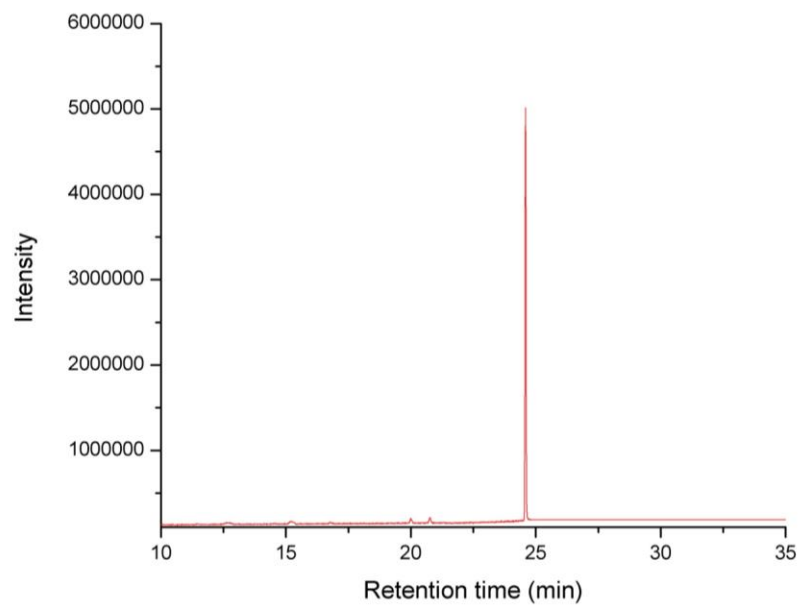
Figure 3.7 Gas Chromatogram of 4-methoxybiphenyl (first run).
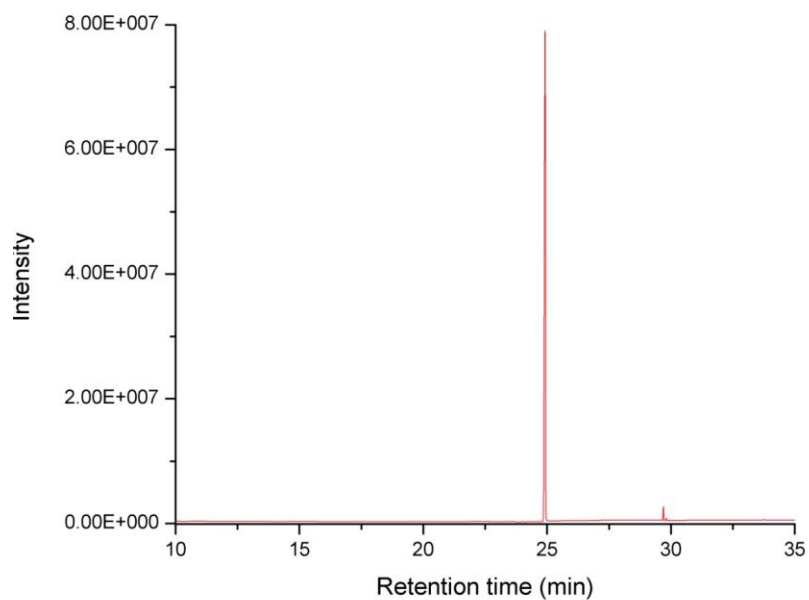
Figure 3. 8 Gas Chromatogram of 4-methoxybiphenyl (second run).
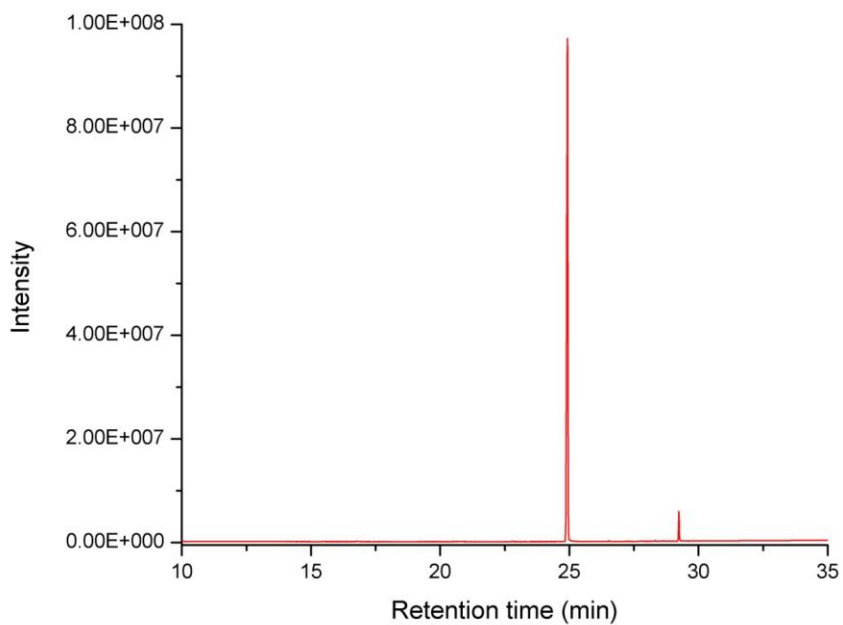
Figure 3.9 Gas Chromatogram of 4-methoxybiphenyl (Third run).
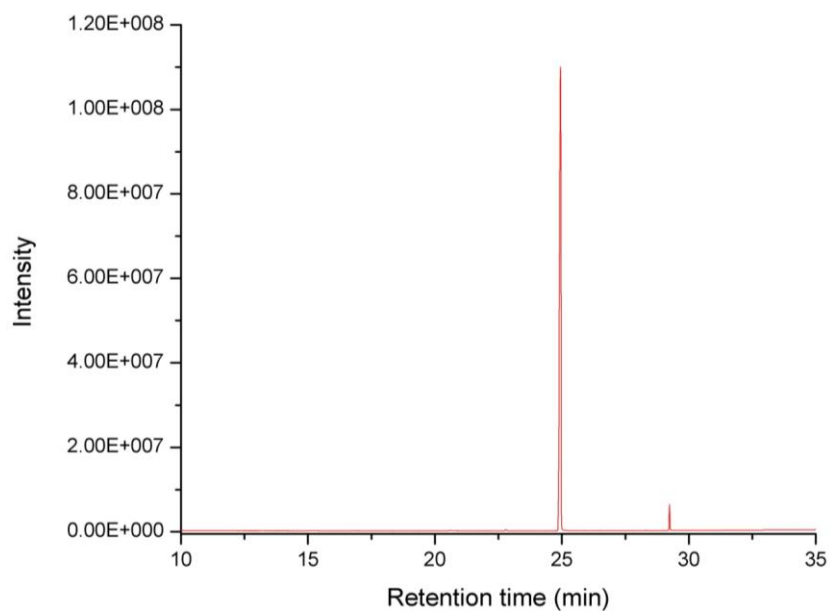
Figure 3.10 Gas Chromatogram of 4-methoxybiphenyl (Fourth run).
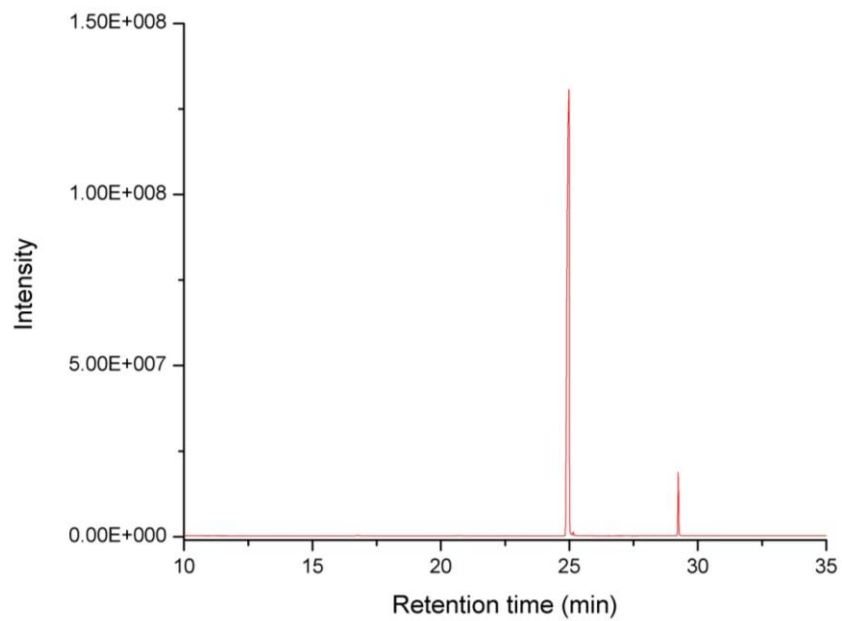
Figure 3.11 Gas Chromatogram of 4-methoxybiphenyl (Fifth run).
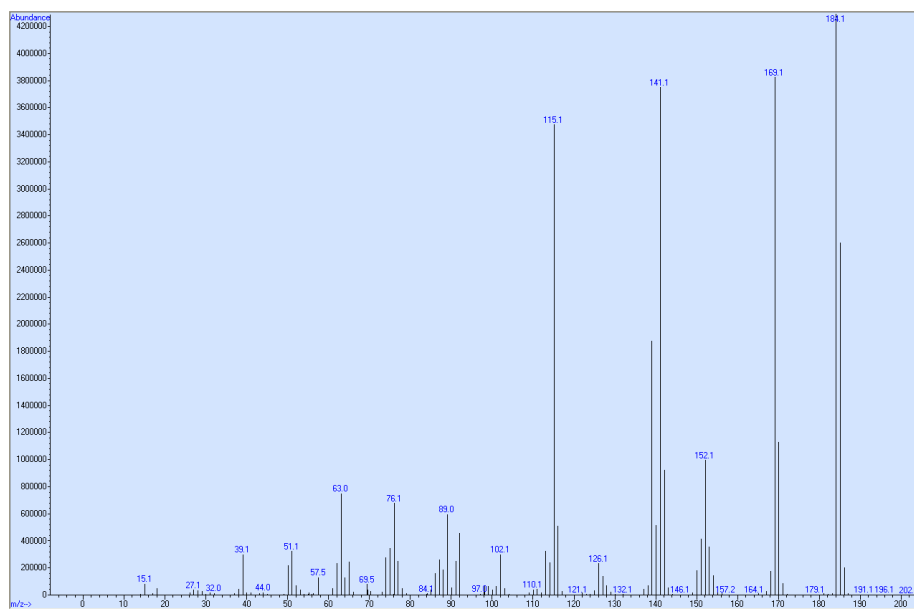
Figure 3.12 Mass spectrum of 4-methoxybiphenyl.

3.4 Conclusion

Developing efficient and green catalysts is important for new technologies to eliminate waste, to avoid using hazardous solvents and reagents, and to possess high recyclability. Here, we demonstrated a bioinspired peptide amphiphile nanofiber template for formation of one-dimensional Pd nanostructures. The Pd@Peptide nanocatalyst system provided high catalytic activity in Suzuki coupling reactions in environmentally friendly conditions. Moreover, the nanocatalyst can be easily isolated and reused at least 5 times in consecutive reactions without significant loss in activity and structural integrity. We believe that this novel approach can find applications in many industrially important catalytic processes in environmentally friendly conditions

Chapter 4

Biocompatible Supramolecular Catalytic One-Dimensional Nanofibers for Efficient Labeling of Live Cells

This work is partially described in the following publication:

4.1 Introduction

Understanding complex cellular functions requires studying and tracking of biomolecules such as proteins, glycans, and lipids in their natural environment. Variety of bioorthogonal reactions such as ketone/hydroxylamine condensation, Staudinger ligation, strain promoted alkyne-azide cycloaddition (SPAAC), strain promoted alkyne-nitrone catalyzed cross coupling, Diels-Alder cycloaddition, and copper-catalyzed azide–alkyne cycloaddition (CuAACa) have been developed to label biomolecules in their native environment [128]. Owing to low cytotoxicity and inertness of alkyne-azide functional groups under physiological conditions including excellent reaction kinetics, and high specificity, CuAACa has received great attention to label and specifically probe different biomolecules in living cells [129]. However, a major problem of this reaction is the cytotoxicity of Cu^I, which causes the generation of reactive oxygen species (ROS) from O_2

[130]. To overcome this problem, two different approaches have been developed. The first approach is to perform the strain promoted alkyne-azide cycloaddition (SPAAC) without using Cu^I as catalyst [131]. This method suffers from slow reaction kinetics. Even the fastest SPAAC is 10 times slower than the Cu^I-mediated one [132]. Moreover, very hydrophobic and reactive cyclooctynes have pharmacokinetic problems in mice and can cause unwanted side reactions with endogenous nucleophiles such as thiols [133]. Another approach is to design ligands, which coordinate to Cu^I and enhance its biocompatibility.
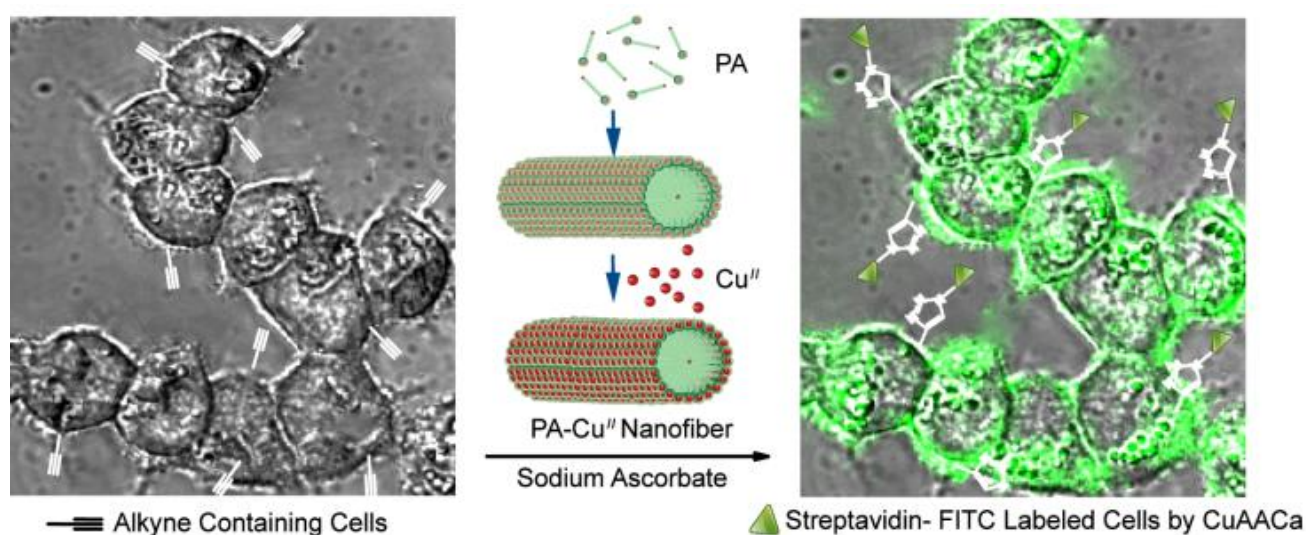
Scheme 3. Schematic representation of labeling live-cells by PA-Cu^{II} nanofibers.

Typical ligands include bathophenanthroline disulfonate disodium salt (BPS)[134], 14,41 tris((1-benzyl-1H-1,2,3-triazol-4-yl)methyl)amine (TBTA)[135], tris- (hydroxypropyltriazolyl)-methylamine (THPTA)[136], bis[(tertbutyltriazoyl) methyl]-[(2-carboxymethyltriazoyl)methyl]-amine (BTTAA)[137] and L-histidine [138]. Despite promising results, it is still challenging to design biocompatible and biodegradable ligands that show excellent catalytic activity in complex living environment with minimal Cu^I cytotoxicity.

In this work, we demonstrated the first supramolecular nanocatalyst, which has lower cytotoxicity and superior catalytic activity than molecular catalysts employed in bioorthogonal click reactions. We exploited advantage of self-assembling peptide amphiphile (PA) molecules to construct biocompatible and biodegradable copper decorated supramolecular one- dimensional nanofibers (PA-Cu^{II}) for efficient labeling of live-cells (Scheme 1).

4.2 Experimental Section

4.2.1 Synthesis of Peptide Amphiphile Molecule

Peptide amphiphile molecules were synthesized using standard solid phase peptide synthesis. MBHA Rink Amide resin was used as solid phase. Amino acid couplings were performed by 2 equivalents of fluorenylmethyloxycarbonyl (Fmoc) protected amino acids, 1.95 equivalents O-Benzotriazole-N,N,N',N'-tetramethyl-uronium-hexafluoro-phosphate (HBTU) and 3 equivalents of N,N-diisopropylethylamine (DIEA) for 3 h. Fmoc protecting groups were removed by 20% piperidine /dimethylformamide solution for 20 min. Cleavage of the product from the Rink Amide was carried out by a mixture of trifluoroacetic acid: triisopropylsilane: H$_2$O in the ratio of 95:2.5:2.5 for 2 h. The resin was washed thoroughly with DCM. Collected peptide solution was concentrated by rotary evaporation. The remaining viscous peptide solution was triturated with cold ether and the resulting precipitate was lyophilized to get a white powder. The peptide was purified by Prep HPLC. Anal. Calcd for C$_{43}$H$_{67}$F$_6$N$_{11}$O$_{11}$: C, 50.24; H, 6.57; F, 11.09; N, 14.99; O, 17.12. Found: C, 50.07; H, 6.88; F, 11.33; N, 14.23; O, 17.45

4.2.2 Preparation of PA-Cu^{II} Complex

4.8 mg of peptide was dissolved in 480 μl of ddH$_2$O, and then CuSO$_4$.5H$_2$O (1.5 mg in 60 μl) solution was used to jellify. The bluish hydrogel was aged overnight, and washed thoroughly by ddH$_2$O (5 x 500 μl) to get rid of unbound peptides or CuSO$_4$.5H$_2$O molecules. The peptide hydrogel was further lyophilized to get a pale blue powder (S4). This powder was used for elemental analysis, ICP-MS, and XPS. Anal. Calcd for C$_{43}$H$_{67}$CuF$_6$N$_{11}$O$_{15}$S: C, 43.49; H, 5.69; Cu, 5.35; F, 9.60; N, 12.97; O, 20.21; S, 2.70. Found: C, 44.70; H, 6.58; Cu, 4.18; F, 11.6; N, 12.17; O, 19.91; S, 2.86

4.2.3 Liquid Chromatography-Mass Spectrometry

Agilent Technologies 6530 Accurate-Mass Q-TOF LC-MS and Zorbax SB-C18 column were used to perform liquid chromatography-mass spectrometry. The concentration of the sample was adjusted as 1 mg/ml. 0.1% formic acid in water and 0.1% formic acid in acetonitrile were used as mobile phase.

4.2.4 Determination of Critical Aggregation Concentration (CAC)

A stock solution of Nile red (78.12 μM) was prepared in ethanol. Then 3 ml of PA solutions were prepared with concentrations ranging 1-250 μM. 6.4 μl of Nile red was added to each PA solution and aged for 24 hours. Fluorescence emission spectra were recorded from 580 nm to 750 nm for each sample (λ_{ex} = 550 nm). Background fluorescence (fluorescence of Nile red in water without PA) was subtracted and then fluorescence emission intensity at 635 nm versus concentration of PA was constructed. The CAC was calculated from the plot of fluorescence intensity versus Log (concentration). The CAC is the point where two linear lines intersect.

4.2.5 Circular Dichroism (CD) Spectroscopy

Secondary structure of PA and PA-Cu^{II} was analyzed with Jasco **J**-815 circular dichroism spectrometer. 2 mg of peptide was dissolved in 200 μl of ddH$_2$O and for PA-Cu^{II}, 2 mg of peptide was dissolved in 150 μl of ddH$_2$O and was jellified by 50 μl of 0.05 M CuSO$_4$ solution. The samples were aged overnight and then were diluted ten times by ddH$_2$O addition. The samples were measured from 500 nm to 190 nm with 0.1 data pitch, 100 nm/min scanning speed, 1 nm band width and 4 s D.I.T. Average of three measurements were adjusted and sensitivity was selected as standard.

4.2.6 Rheological Analysis

Mechanical characterizations of hydrogels were performed using Anton Paar MCR-301 Rheometer. 300 μL of samples were prepared for the analysis. PP25-SN17979 measuring device with 25 mm diameter was used. Measuring distance was fixed at 0.5 mm. Time sweep of sample was performed for 1h. Angular frequency and strain magnitudes were adjusted as ω=10 rad/s and γ=0.1%, respectively.

4.2.7 Isothermal Titration Calorimetry (ITC)

0.3 mM of Ac-HH-Am was titrated by 3 mM of CuSO$_4$ solution using iTC200 system (MicroCal, GE Healthcare). The titration was performed at 25 °C with 800 rpm stirring speed. Twenty injections were done, where the injection period was 4 s and the space between injections was 180 s. ITC binding isotherms were best fitted by a two-sets of site mode.

4.2.8 Elemental Analysis

Thermo Scientific FLASH 2000 series CHNS-O analyzer was used for the analysis. 1-2 mg of powdered PA and lyophilized PA-Cu^{II} were used for the analysis. BBOT (2, 5-(bis (5-tert-butyl-2-benzo-oxazol-2-yl)) thiophene was used as standard for calibrations.

In addition, 8-10 mg of vanadium (V) oxide was used in each analysis as catalyst for complete thermal decomposition of the samples.

4.2.9 Inductively Coupled Plasma-Mass Spectrometry (ICP-MS)

Thermo X series II inductively coupled plasma-mass spectrometer (ICP-MS) was used to measure the concentration of copper in PA-Cu^{II} powder. 500 ppb, 250 ppb, 100 ppb, and 50 ppb of copper standards were prepared in 2% nitric acid solution and 2% nitric acid solution was used as blank. 0.554 mg of PA-Cu^{II} was dissolved in 1 ml of concentrated nitric acid and then 100 μL of the stock solution was diluted to 10 ml of 2% nitric acid solution. The ICP-MS operating parameters were: dwell time – 10 000 ms, channel per mass – 1, acquisition duration – 7380, channel spacing – 0.02, carrier gas-argon

4.2.10 X-Ray Photoelectron Spectroscopy (XPS) Analysis

X-ray photoelectron spectra of samples were recorded by using Thermo K-alpha monochromatic high performance X-ray photoelectron spectrometer. The bluish PA-Cu^{II} powder was used for the analysis. The survey analyses were performed at 5 scans. For enhancing Cu signal intensities the measurements were recorded at 50 scans.

4.2.11 Transmission Electron Microscopy (TEM)

FEI Tecnai G2 F30 transmission electron microscope (TEM) was used to image the peptide and PA-Cu^{II} nanofibers without staining.2 mg of peptide was dissolved in 150 μL of ddH$_2$O and was jellified by 50 μL of 0.05 M CuSO$_4$ solution. The sample was aged overnight and then was diluted ten times by ddH$_2$O addition. A minute of the solution was further diluted thirty times. Small amount of solution was dropped on carbon covered copper grid and was dried at room temperature.

4.2.12 Scanning Electron Microscopy/Critical Point Dryer

FEIQuanta 200 FEG environmental scanning electron microscope (SEM) was used to image PA-Cu^{II} hydrogel after removing solvent with Tousimis Autosamdri-815B, Series C critical point dryer (CPD). 20 μl of PA solution (1 wt %) in dd water was prepared. Then 0.05 M CuSO$_4$ solution was mixed to peptide solution on a silicon wafer. After aging for 5 minutes, we washed PA-Cu^{II} hydrogel with 20%, 40%, 60%, 80% and 100% (v/v) ethanol solutions. Then, gels were dried with a critical point dryer. The samples were coated 5 nm Pd/Au before imaging by SEM.

4.2.13 Synthesis of benzyl azide

2 ml of benzyl bromide (1.0 eq) was dissolved in 50 ml of water/acetone mixture (1:4). Then 1.64g of NaN$_3$ (1.5 eq) was added to the benzyl bromide solution. The resulting solution was stirred at room temperature for 24 hours. The aqueous mixture was extracted with 3 x 10 ml of DCM and the combined organic layers were dried over MgSO4. Solvent was removed under reduced pressure to get benzyl azide in high purity as yellowish oil. 99 % yield. ^{1}H NMR (400 MHz, CDCl3): 7.35-7.53 (m, 5H), 4.4 (s, 2H); ^{13}C NMR (100.59 MHz, CDCl3): δ 135.57, 128.95, 128.40, 128.34, and 54.84
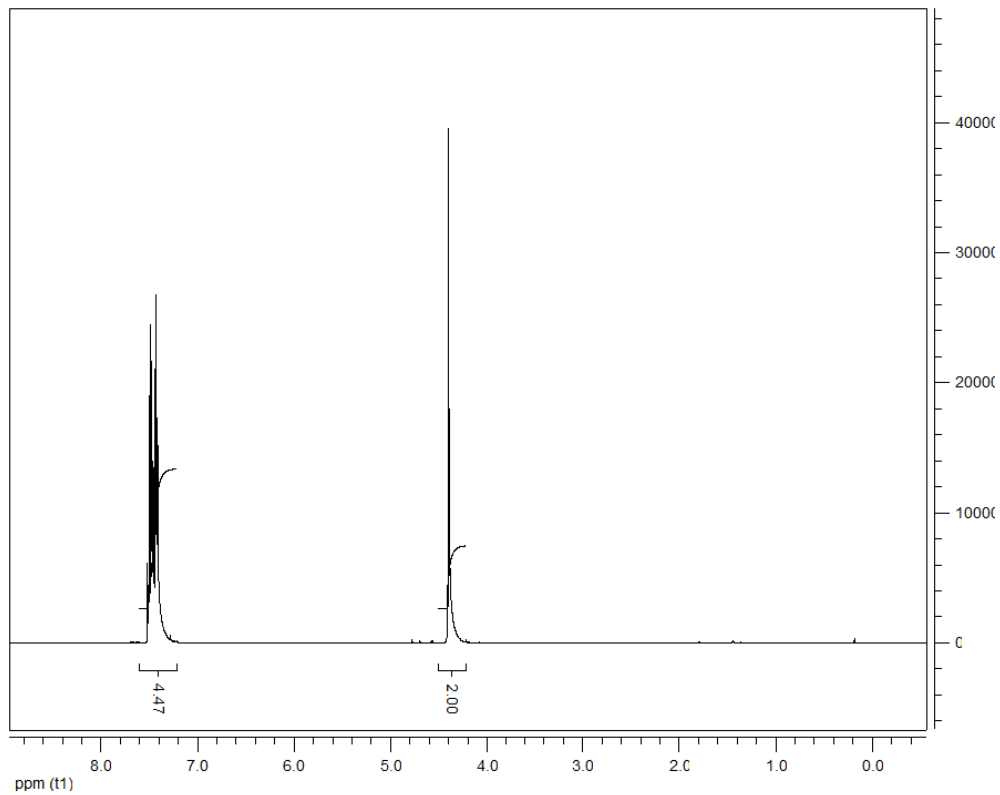
Figure 4.1 ^{1}H NMR of benyl azide
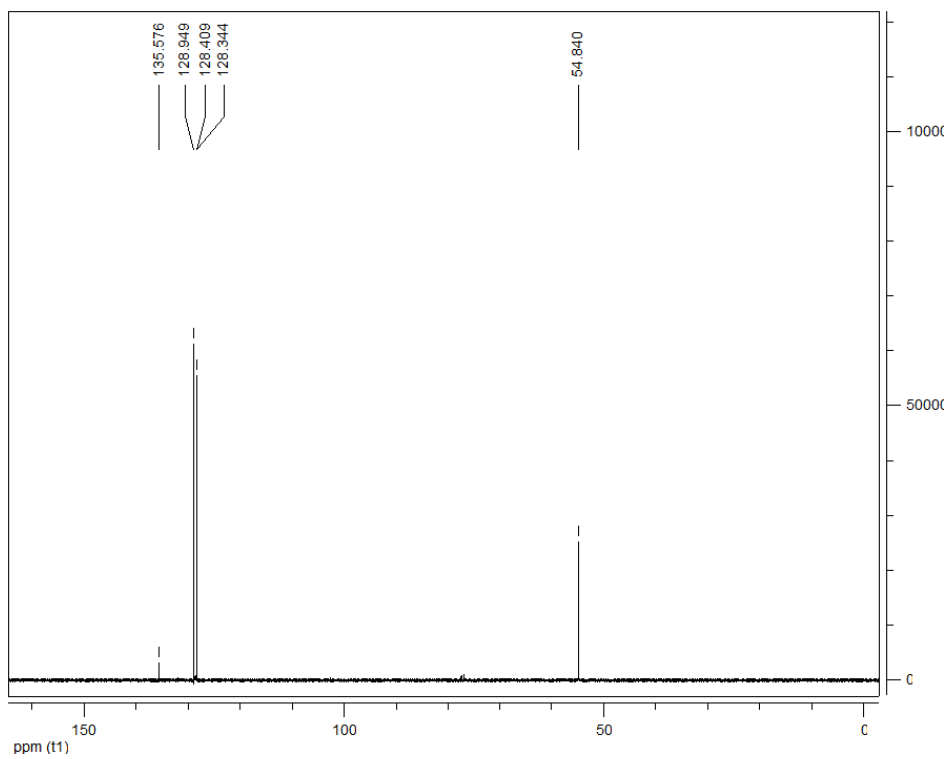
Figure 4.2 ^{13}C NMR of benyl azide

4.2.14 Synthesis of 3-aminopropyl-1azide

3-Bromopropylamine hydrobromide (320 mg, 0.0146 mmol, 1.0 eq.) was dissolved in water (2 ml). Then 3 ml solution of sodium azide (320 mg, 0.0492 mmol, 3.4 eq.) was added slowly. The resulting solution was allowed to reflux overnight. After cooling, most of the water was evaporated and the residue was dissolved in diethyl ether (5 ml). The biphasic mixture was cooled to 0 °C and KOH (4.0 g) was added slowly. The aqueous phase was extracted with diethyl ether (2 X 30 ml), and dried over $MgSO_4$. The solvent was evaporated after filtration. Pale yellow liquid product was stored under argon at -20 °C and used without further purification (110 mg, 75%). ^{1}H NMR (400 MHz, $CDCl_3$) δ ppm 3.39 (t, J = 6.67 Hz, 2H), 2.83 (t, J = 6.72 Hz, 2H), 1.75 (q, J = 6.75 Hz, 1H), 1.33 (s, 2H). ^{13}C NMR (100 MHz, $CDCl_3$): δ 49.18, 39.35, 32.49. ESI-TOF-HRMS m/z: calculated for C3H8N4 (M + H)[+] 101.07, found 101.08

Figure 4.3 ^{13}C NMR of benyl azide
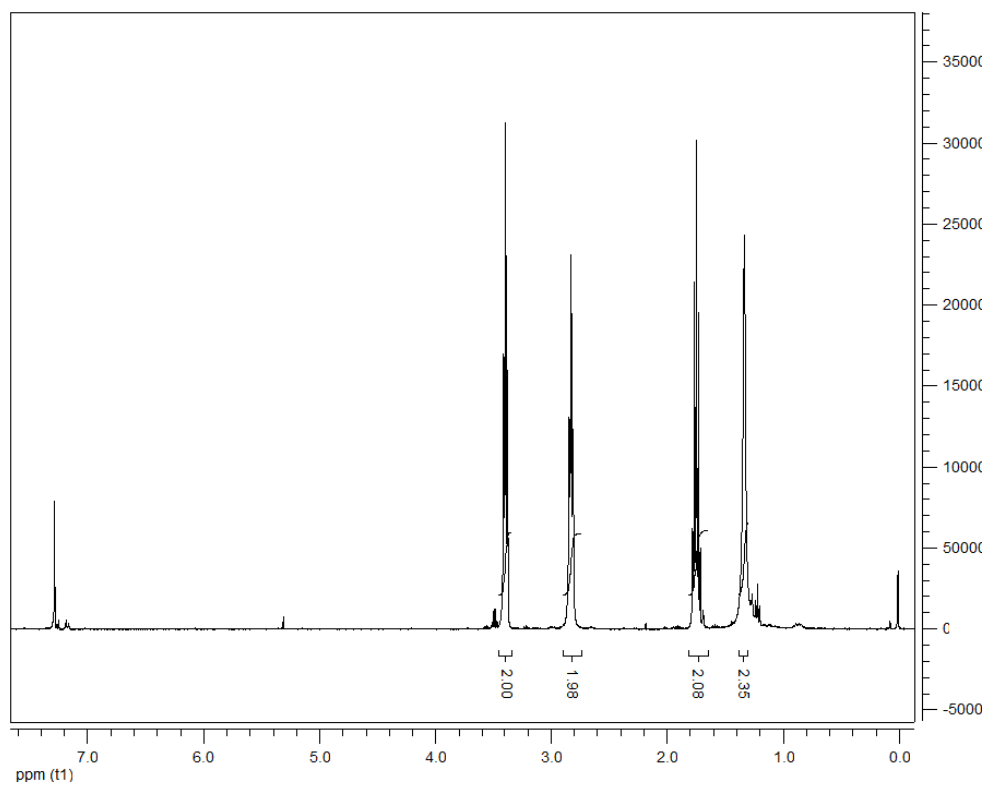
Figure 4.4 ^{1}H NMR of 3-aminopropyl-1azide
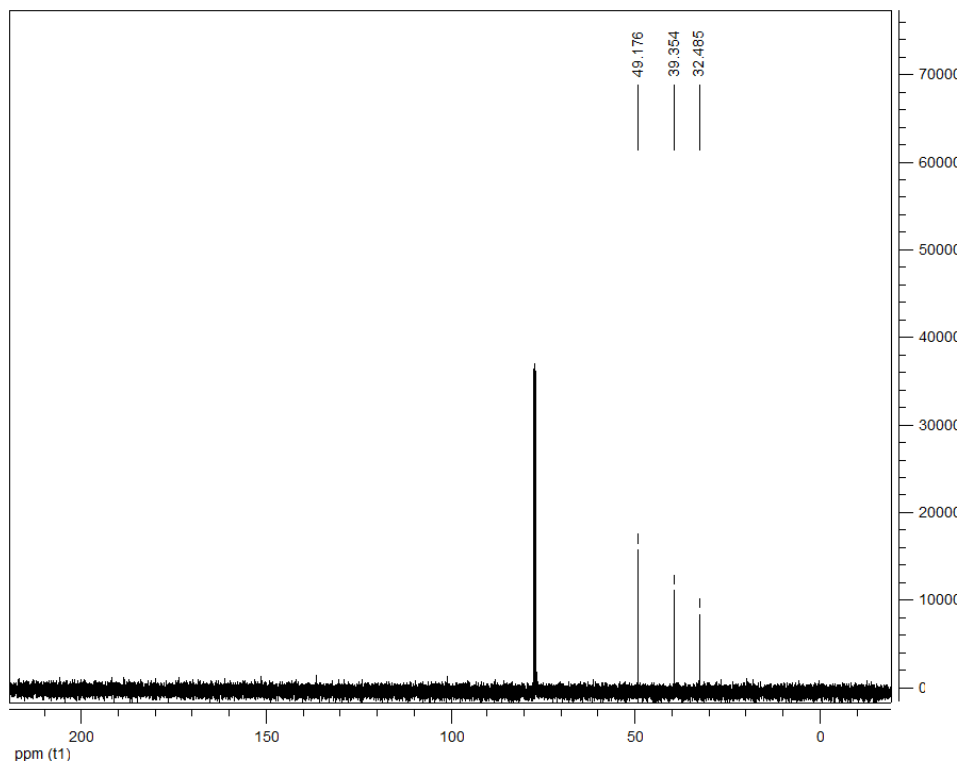
Figure 4. 5 ^{13}C NMR of 3-aminopropyl-1azide

4.2.15 Synthesis of Biotin-Azide

240 mg of d-biotin (1.0 mmol) was dissolved in 5 ml of DMF then *N*-hydroxysuccinimide (1.2 equiv) along with EDC (1.2 equiv) were added. The reaction was allowed to proceed at room temperature overnight. DMF was evaporated and resulting residue was washed with water and methanol to afford the Biotin-NHS as a white solid (163.8 mg, 48% yield)).

ESI-TOF-HRMS m/z: calculated for $C_{14}H_{19}N_3O_5SNa$ 364.1 $[M+Na]^+$, found 364.1. Biotin-NHS was used without further purification. In a Shaleng tube, solutions of Biotin-NHS (100 mg, 0.28 mmol, 1.0 eq.) and dry triethylamine (78 μl, 0.56 mmol, 2.0 eq.) in dry DMF (6ml) was added 3-aminopropyl-1azide (40 μl, 0.42 mmol, 1.5 eq.) and the reaction was left to stir at room temperature under argon overnight. The reaction was concentrated at 11 mbar at 60 ^{o}C to dryness. The mixture was purified using flash column chromatography (10% MeOH/EtOAc) to give the product as a white solid (80 mg). ^{1}H NMR (400 MHz, CDCl$_3$) δ ppm 6.34-6.2 (bs, 2H), 5.42 (s, 1H), 4.55 (dd, J = 7.75, 4.71 Hz, 1H), 4.35 (dd, J = 7.34, 4.78 Hz, 1H), 3.39 (t, *J* = 6.61 Hz, 2H), 3.37 – 3.30 (m, 2H), 3.18 (m, 1H), 2.45-2.30 (m, 2H), 2.24 (t, J = 7.44 Hz, 2H), 1.95 – 1.60 (m, 6H), 1.52-1.44 (m, 2H); ^{13}C NMR (100 MHz, CDCl$_3$) δ 173.37, 163.90, 61.86, 60.20, 55.54, 49.39, 40.56, 37.06, 35.93, 29.69, 28.78, 28.13, 25.56. ESI-TOF-HRMS m/z: calculated for $C_{13}H_{22}N_6O_2S$ (M + H)$^+$ 327.1525, found 327.16681

Biotin-NHS   Biotin-Azide
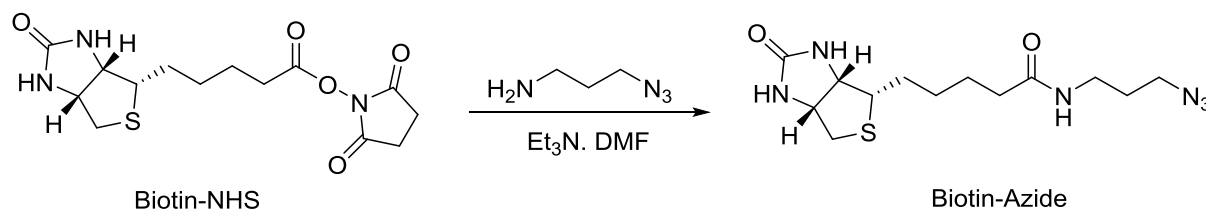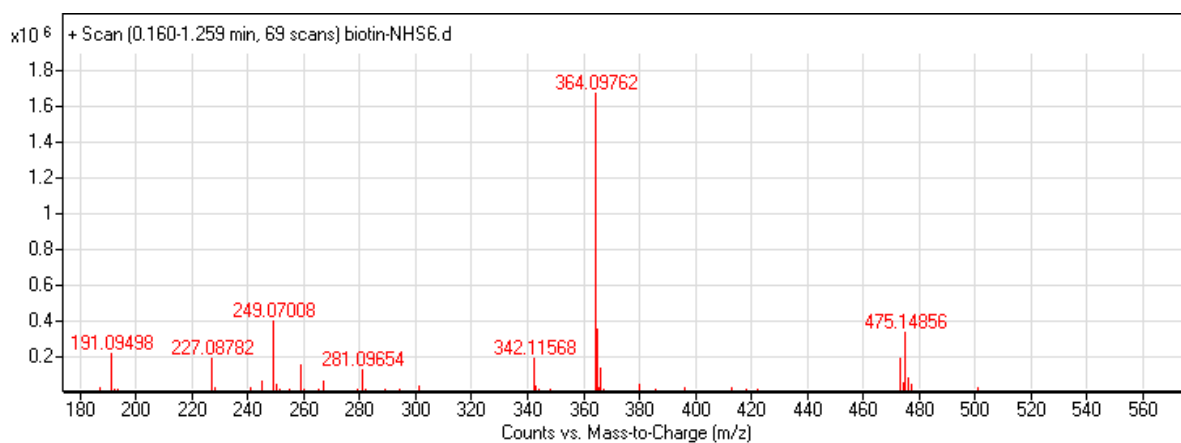
Figure 4.6 HRMS spectrum of Biotin-NHS
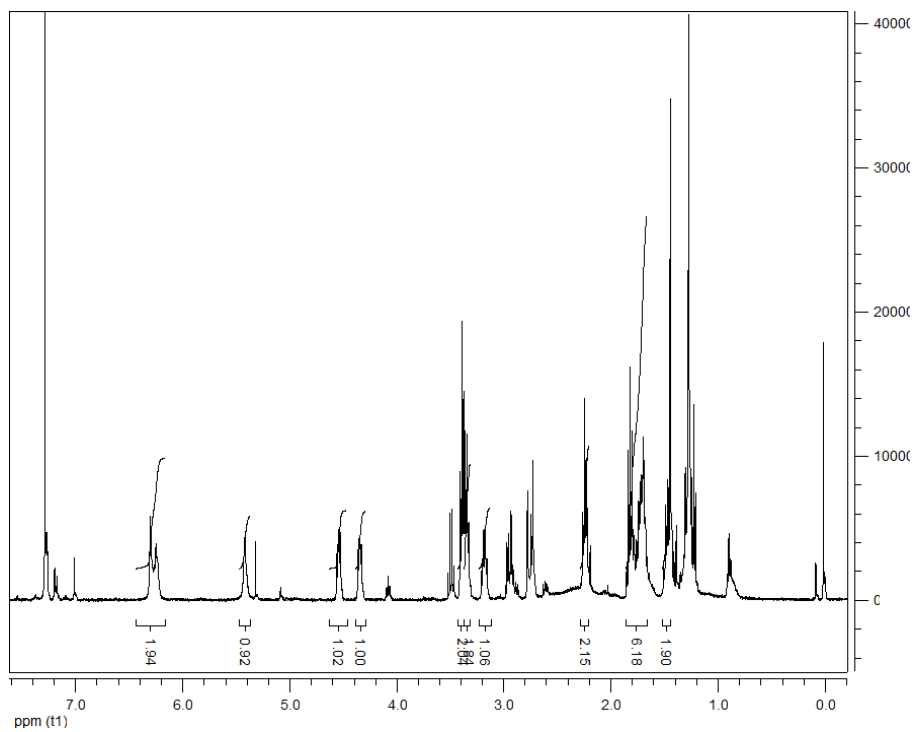
Figure 4.7 ^{1}H NMR of Biotin-azide
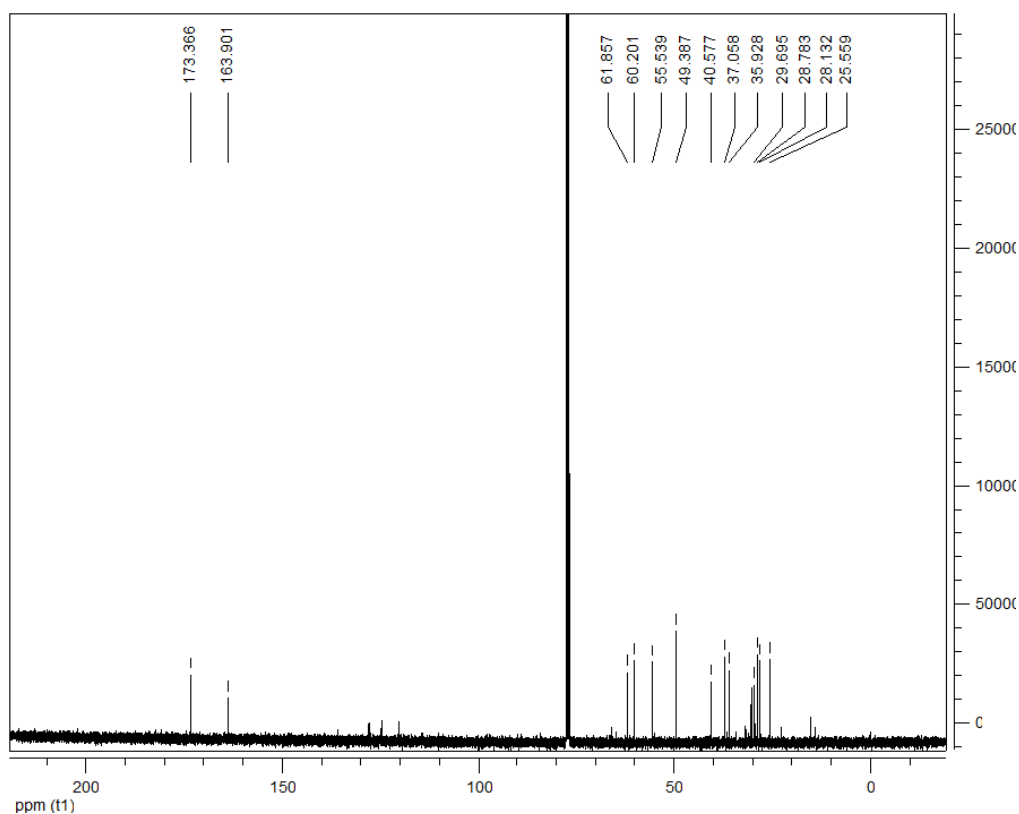
Figure 4.8 ^{13}C NMR of Biotin-azide

4.2.16 Synthesis of *N*-succinimidyl-4-pentynoate

To a solution of 4-pentynoic acid (200mg, 2.04 mmol) in DCM (10ml) were added NHS (268mg, 2.34 mmol) and EDC (782mg, 4.08 mmol). After 3h, the reaction was extracted by 2.5% NaHSO$_4$ (3* 20ml) and brine. The organic layer was dried over magnesium sulfate and evaporated. ^{1}H NMR (400 MHz, CDCl$_3$) δ ppm 2.89 (t, J = 7.08 Hz, 2H), 2.85 (s, 4H), 2.64 (dt, J = 2.63, 7.13 Hz, 2H), 2.07 (t, J = 2.63 Hz, 1H). ^{13}C NMR (100 MHz, CDCl$_3$): δ 14.09, 25.57, 30.31, 70.04, 80.87, 167.02, 168.92
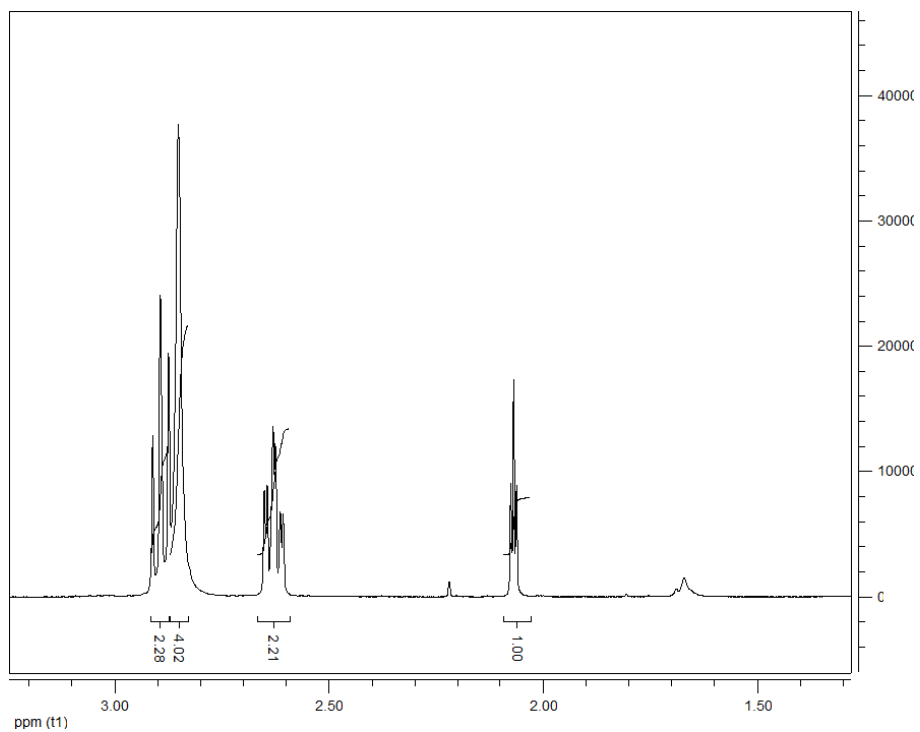
Figure 4.9 ^{1}H NMR of N-succinimidyl-4-pentynoate
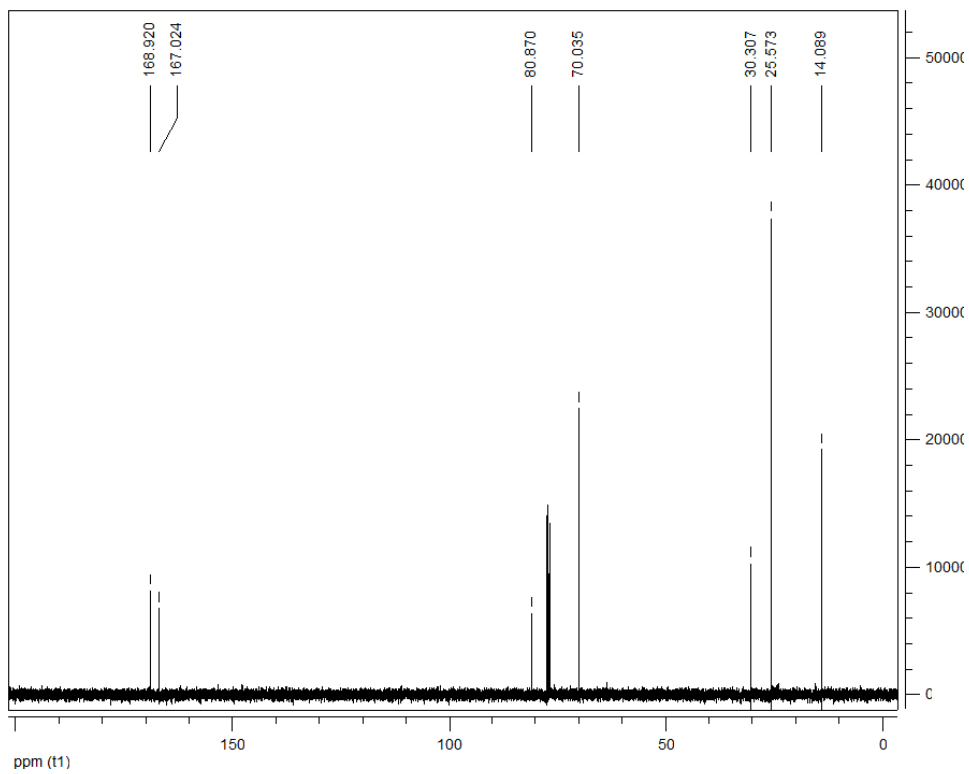
Figure 4.10 ^{13}C NMR of N-succinimidyl-4-pentynoate

95

4.2.17 Synthesis of N-4-Pentynoylmannosamine (ManNAl)

A mixture of d-mannosamine hydrochloride (137 mg, 0.64 mmol, 1 eq.), *N*-succinimidyl-4-pentynoate (125 mg, 0.64 mmol, 1.0 eq.) and triethylamine (267 µl, 1.92 mmol, 3.0 eq.) in DMF (8 ml) was stirred at room temperature overnight. The DMF was completely evaporated and the residue was purified using flash column chromatography (8:1 CHCl3/MeOH) to give the product as a white crystals (**Mixture of Anomers,** 181 mg, 80%). ESI-TOF-HRMS *m/z* calculated for (M+Cl)⁻ C11H17ClNO6 294.0744; found 294.09262.
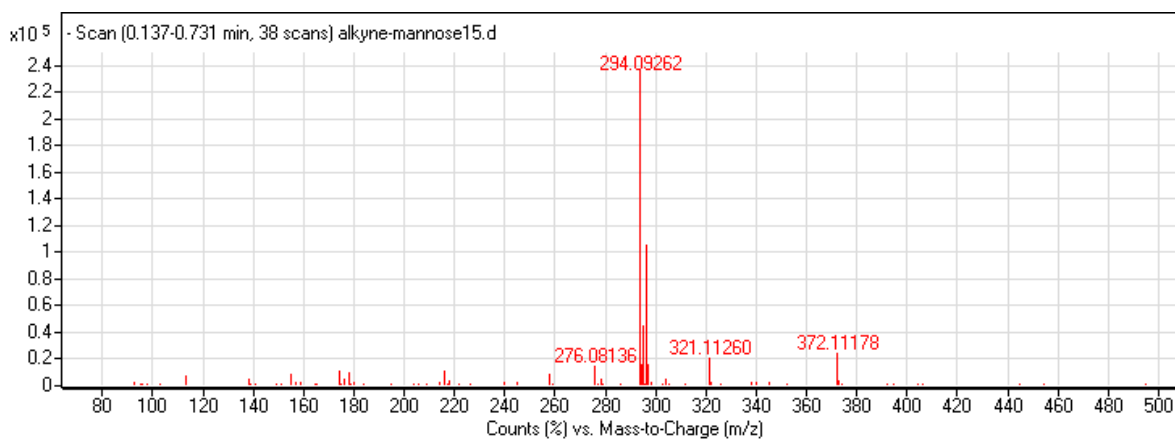
Figure 4.11 HRMS of N-4-Pentynoylmannosamine

4.2.18 Synthesis of 1.3.4.6-Tetra-O-Acetyl-N-4-Pentynoylmannosamine (Ac$_4$ManNAl)

N-4-Pentynoylmannosamine (181 mg) was dissolved in dry pyridine (5ml). Then 350 µl of acetic anhydride was added and stirred at room temperature overnight. The mixture was concentrated *in vacuo* and the residue was dissolved in DCM and extracted with water. The organic layer was evaporated and then purified using flash column chromatography (4:1 Hex/EtAcO) to give the product (**Mixture of Anomers**). 1H NMR (400 MHz, CDCl$_3$) δ ppm 1.98 (s, 9H), 2.04 (s, 9H),

2.08 (s, 12H), 2.15 (s, 6H), 2.44-2.57 (m, 12H), 3.77-3.83 (m, 1H), 3.90-4.14 (m, 6H), 4.20-4.27 (m, 3H), 4.66 (dd, J = 9.13, 4.30 Hz, 2H), 4.79 (dd, *J* = 9.15, 3.75 Hz, 1H), 5.05 (dd, J = 9.87, 3.97 Hz, 1H), 5.14 (t, J = 9.80 Hz, 1H), 5.20 (t, J = 9.97 Hz, 2H), 5.30 (dd, J = 10.15, 4.35 Hz, 2H), 5.87 (s, 1H), 6.02 (s, 2H), 6.18 (d, J = 9.19 Hz, 1H), 6.29 (d, J = 9.24 Hz, 2H); ^{13}C-NMR (100 MHz, CDCl$_3$) 14.93, 15.03, 20.59, 20.61, 20. 65, 20.70, 20.75, 20.81, 35.23, 35.43, 49.21, 49.44, 62.04, 62.19, 65.41, 65.60, 68.85, 70.04, 70.15, 70.34, 71.27, 73.38, 82.60, 82.65, 90.60, 91.68, 168.14, 168.35, 169.63, 170.03, 170.09, 170.52, 171.28, 171.67. ESI-TOF-HRMS *m/z* calculated for (M+Cl)$^-$ C19H25ClNO10 462.1167; found 462.1064
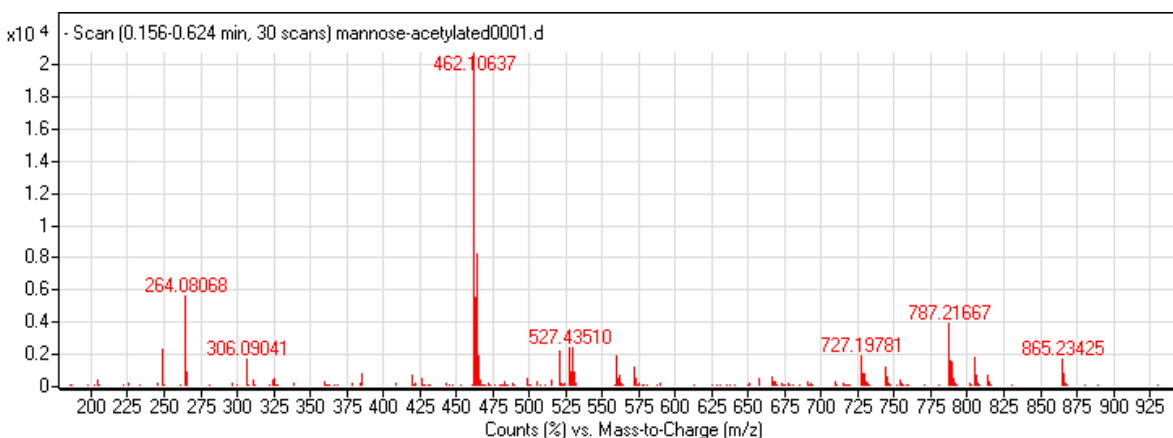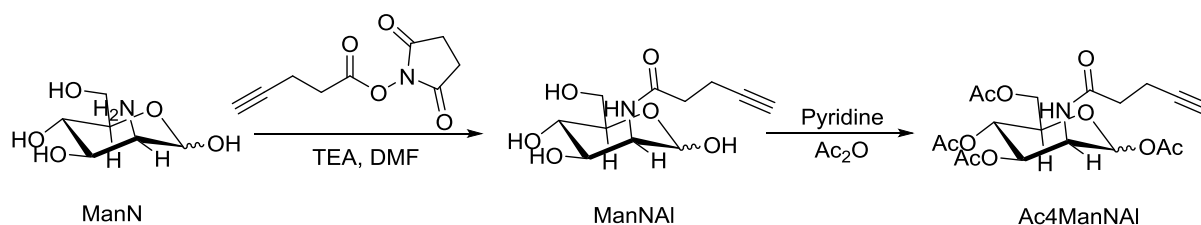
Figure 4.12 HRMS of Ac$_4$ManNAl

97
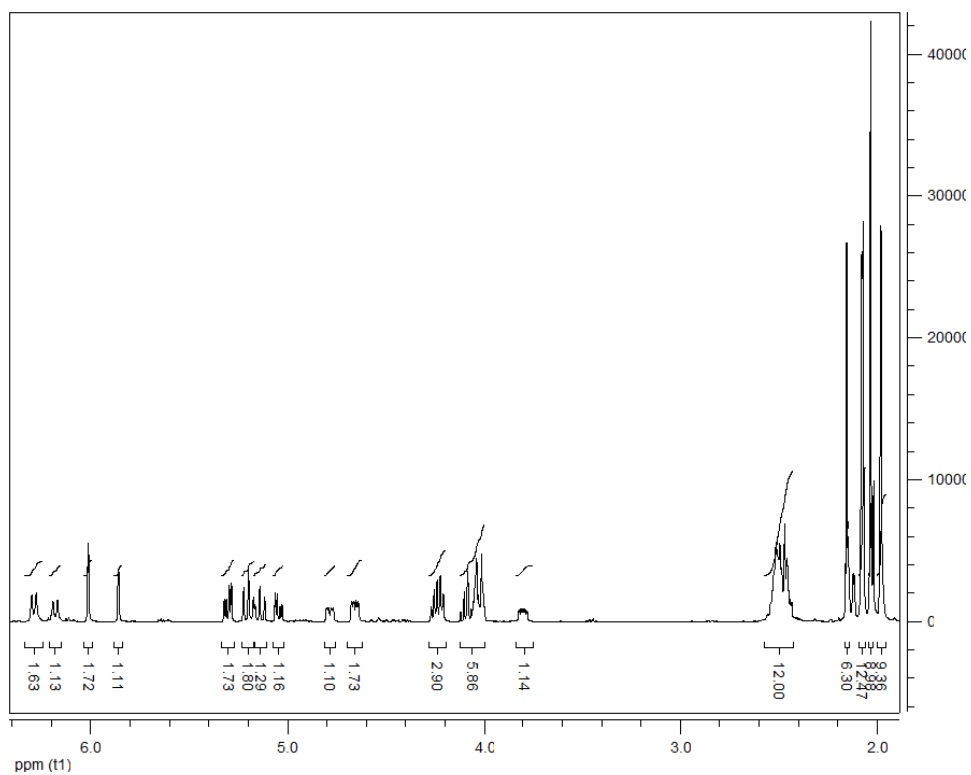
Figure 4.13 ^{1}H spectrum of Ac$_4$ManNAl
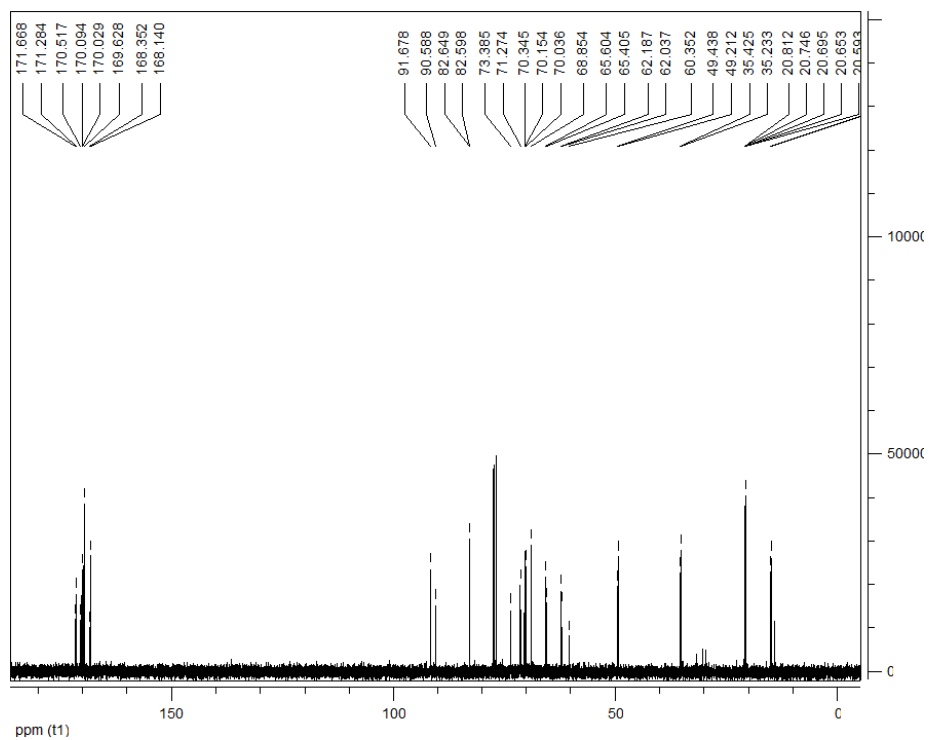
Figure 4.14 ^{13}C spectrum of Ac$_4$ManNAl

4.2.19 Catalytic Reactions

All reactions and manipulations were run under air atmosphere. To a stirred solution of ligand (0.00285 mmol) and $CuSO_4.5H_2O$ (0.71 mg, 0.00285 mmol) in 3 ml of H_2O was added sodium ascorbate (5.6 mg, 0.0285 mmol). Then benzyl azide (36.75 μl, 0.285 mmol) and phenylacetylene (31.25 μl, 0.285 mmol) were supplemented. The mixture was shaken at 150 rpm in an incubator-shaker at defined temperature and time. The crude product (triazole) was extracted by 10 ml of chloroform and dried over $MgSO_4$ then was characterized by NMR and GC-MS analysis (Agilent GCMS-7890A-5975C equipped with a 0.25 mm ×30 m HP-5MS capillary column). ^1H NMR (400 MHz, $CDCl_3$) δ ppm 7.82 (d, 2H), 7.69 (s, 1H), 7.30-7.45 (m, 8H), 5.59 (s, 2H). ^{13}C NMR (100 MHz, CDCl3): δ 54.24, 119.49, 125.72, 128.08, 128.16, 128.80, 129.16, 130.58, 134.72, 148.25.

4.2.20 Cell Culture and Maintenance

MCF-7 human breast adenocarcinoma cell line was used for *in vitro* cell culture experiments. All cells were cultured and propagated in 75 cm^2 cell culture flasks using RPMI medium 1640 supplemented with 10% Fetal Bovine Serum (FBS), 1% penicillin/streptomycin. MCF-7 cells were grown at 37 °C in a humidified chamber supplied with 5% CO_2.

4.2.21 Cell Viability Assay

The cytotoxicity of PA-Cu^I was evaluated by using Alamar Blue^{TM} assay (Invitrogen). MCF-7 cells were cultured in a 96-well plate with a density of 1 x 10^4 cells/well for 24 h. PA-Cu^I and only Cu (I) control group were administered with copper concentrations of 3 mM, 2 mM, 1 mM, 0.5 mM, 0.25 mM and 0.125 mM for 6 h and 24 h (with n=4 per sample). After 6 h and 24 h of treatment, cells were rinsed with phosphate-buffered saline and culture medium was changed

with serum free RPMI containing 1% penicillin/streptomycin and 10% Alamar Blue solutions. These samples were further incubated for 4 hours. Cell viability was assessed by recording the fluorescence at 560/590 nm excitation/emission with a microplate reader (Molecular Devices Spectramax M5).

4.2.22 Microscopic Analysis of Fluorescent Labeling in Fixed Cells

Breast adenocarcinoma cells (MCF-7) were seeded onto 24-well plates (4×10^4/500 μL per well) containing glass coverslips, and were cultivated in 10% FBS/RPMI medium 1640. Growth medium was supplemented with 100 μM Ac$_4$ManNAl. Following incubation for 3 days, cells on coverslips were fixed and permeabilized with cold acetone for 10 min, then subjected to the probe labeling reaction: CuSO$_4$.5H$_2$O (0.125 mM), (+)-sodium-L-ascorbate (1.25 mM), PA (0.125 mM), and biotin-azide (0.125 mM) at room temperature for 6 h. Subsequently, the fixed and labeled cells were washed with PBS and stained with fluorescein-conjugated streptavidin (5 μg/mL in PBS) at room temperature for 30 min. All samples were counterstained with 1 μM TO-PRO-3 (Invitrogen) in PBS for 15 min at room temperature and mounted with Prolong Gold Antifade Reagent (Invitrogen). Fluorescent images were captured by Zeiss AxioCam^{TM} fluorescence microscope

4.2.23 Microscopic Analysis of Fluorescent Labeling of Cells

MCF-7 cells were seeded onto 6-well glass bottom plates (2×10^5 cells/well), and were cultivated in 10% FBS/RPMI medium 1640. After 24 h, appropriate groups were administered with 100 μM Ac$_4$ManNAl and incubated for 3 days. Following 3 day Ac$_4$ManNAl treatment, the cells were washed with PBS and following reagents were applied for 6 h at 37 °C. PA containing labeling group was composed of CuSO$_4$ .5H$_2$O (0.125 mM), (+)-sodium-L-ascorbate (1.25 mM),

PA (0.125 mM), and biotin-azide (0.125 mM). For only copper samples, the same reagents were used except PA. After labeling, cells were washed three times with PBS, blocked with 1% BSA (in PBS) for 20 min at room temperature, and streptavidin-FITC conjugate (5 µg/mL in PBS /0.1 % FBS) was used for staining for 30 min at room temperature. Cells were washed two times with PBS and phenol-red free DMEM. Fluorescent images of cells were captured in 1 mL of phenol-red free DMEM by using confocal (Zeiss LSM510) microscopy system.

4.2.25 Flow Cytometry Analysis of Fluorescent Labeling

MCF-7 cells were cultivated in six-well plates (2×10^5 cells/well) in RPMI medium 1640 supplemented with 10% FBS and 100 µM $Ac_4ManNAl$ for 3 days at 37 °C. Cells were then harvested, washed with 0.1% FBS/PBS, and suspended (2×10^6 cells) in 200 µL of click reaction solution ($CuSO_4.5H_2O$ (0.125 mM), (+)-sodium-L-ascorbate (1.25 mM), PA (0.125 mM), and biotin-azide (0.125 mM)). The reaction was incubated at 37 °C for 6 h. Following incubation, cells were washed twice with 0.1% FBS/PBS. Cells treated with reaction solution and control groups stained with fluorescein-conjugated streptavidin (5 µg/mL in PBS/0.1 % FBS) for 30 min at 4 °C, and washed three times with 1% FBS/PBS. Data were acquired by using BD Accuri™ C6 flow cytometer, and were analyzed by BD Acuri C6 software.

4.3 Results and Discussion

Self-assembled peptide amphiphile nanofibers are a class of supramolecular polymers, which are produced by natural amino acids conjugated to a fatty acid [9]. Due to their intrinsic biocompatibility, biodegradability, biofunctionality, rational design and versatile functional groups, peptide amphiphiles have been widely used in tissue engineering and regenerative medicine applications [4]. Inspired by multipurpose characteristics of self-assembling peptide amphiphiles; we have designed and synthesized a peptide amphiphile molecule, which has binding affinity for copper ions. The PA molecule with a sequence of Lauryl-VVAGHH-Am (Figure 4.15) was successfully synthesized by using standard solid phase peptide synthesis (SPPS) (Figure 4.15-4.17). We also synthesized a soluble Ac-HH-Am peptide as a non-assembling but copper binding dipeptide segment of Lauryl-VVAGHH-Am.

Peptide amphiphile molecules consist of three regions (Figure 4.15). The lauryl moiety is required for hydrophobic collapse of the PA molecules in aqueous medium. Meanwhile, the peptide sequence containing valine and alanine residues promote formation of β-sheet structures. The two histidine residues serve as hydrophilic segment for dissolving the PA molecules in aqueous medium in addition to their high binding affinity for copper ions [139].

Hydrophobic tail　　**ß-sheet forming segment**　　**Copper binding segment**
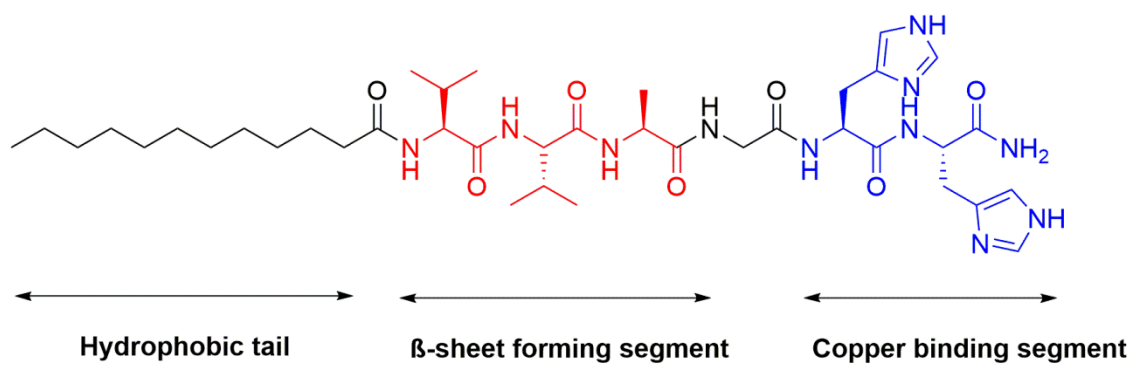
Figure 4.15 Chemical structure of Lauryl-VVAGHH-Am peptide amphiphile molecule.
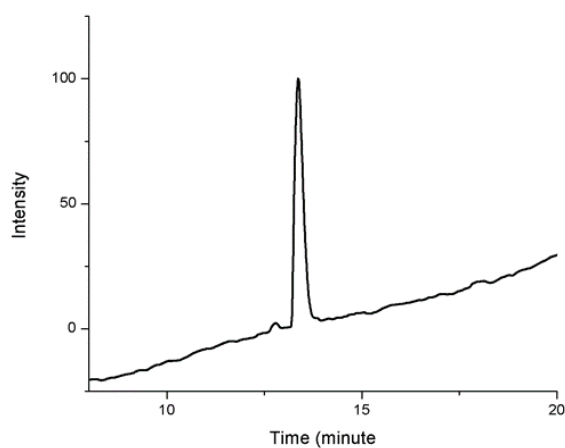
Figure 4.16 Liquid chromatogram of peptide amphiphile.
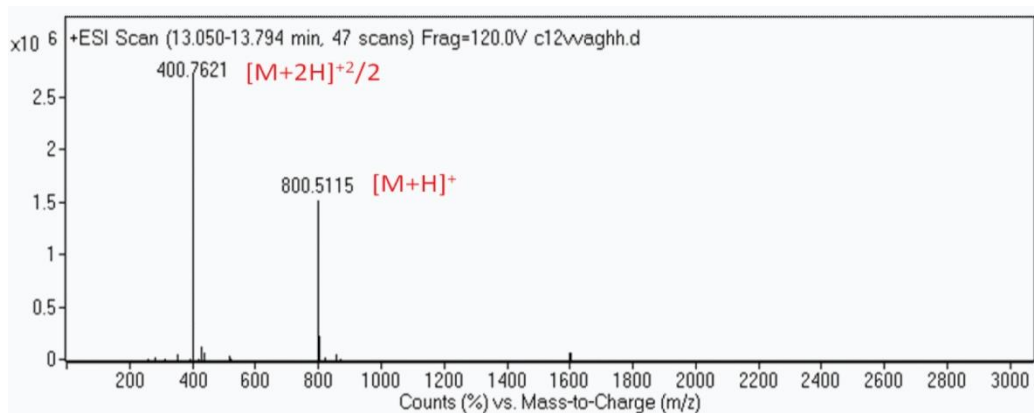
Figure 4.17 Mass spectrum of peptide amphiphile.
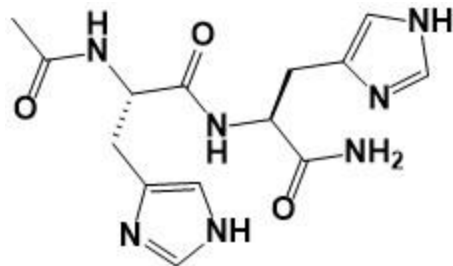
Figure 4.18 Chemical structure of Ac-HH-Am molecule.
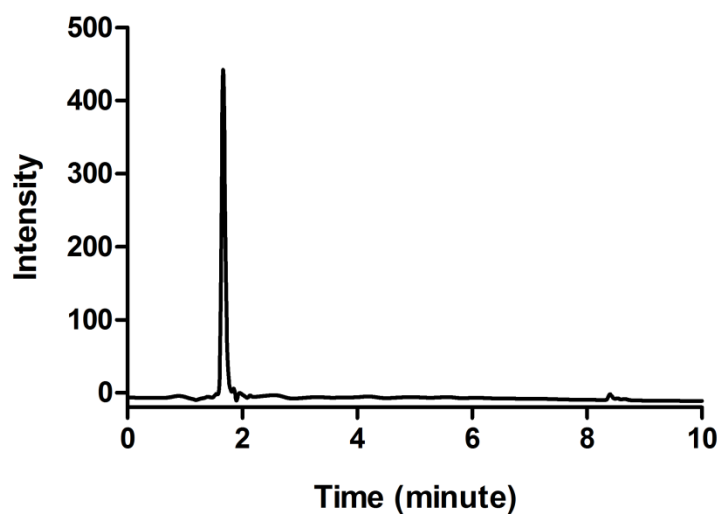
Figure 4.19 Liquid chromatogram of Ac-HH-Am molecule.
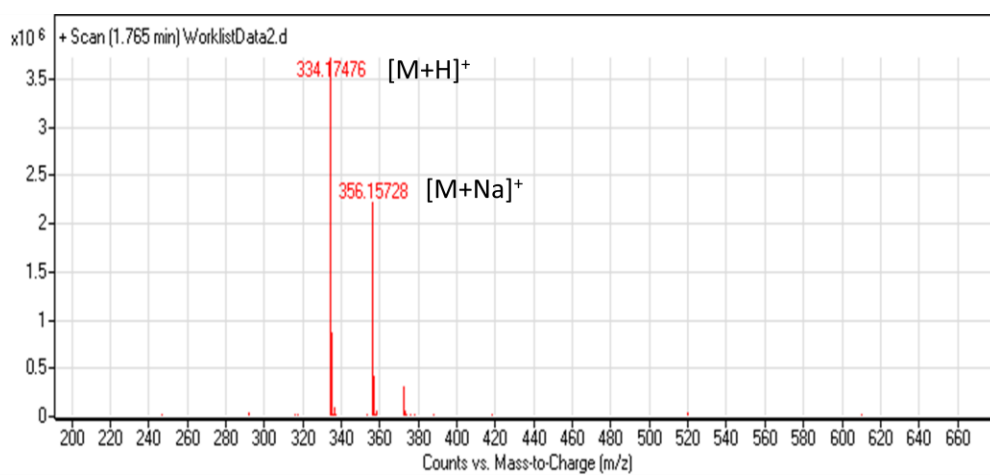
Figure 4.20 Mass spectrum of Ac-HH-Am molecule.

When dissolved in water, the PA molecules aggregate due to noncovalent interactions. Critical aggregation concentration for Lauryl-VVAGHH-Am was calculated as 16 μM (Figure 4.21).The circular dichroism (CD) spectrum of the PAs ((Figure 4.22a) shows a positive peak at 200 nm and a negative peak at 223 nm, which shows the presence of β-sheets [140]. The PA molecules form supramolecular 1-D nanofibers as revealed by transmission electron microscopy (Figure 4.22b) .The supramolecular PA nanofibers have diameters of about 10 nm and lengths in microns.
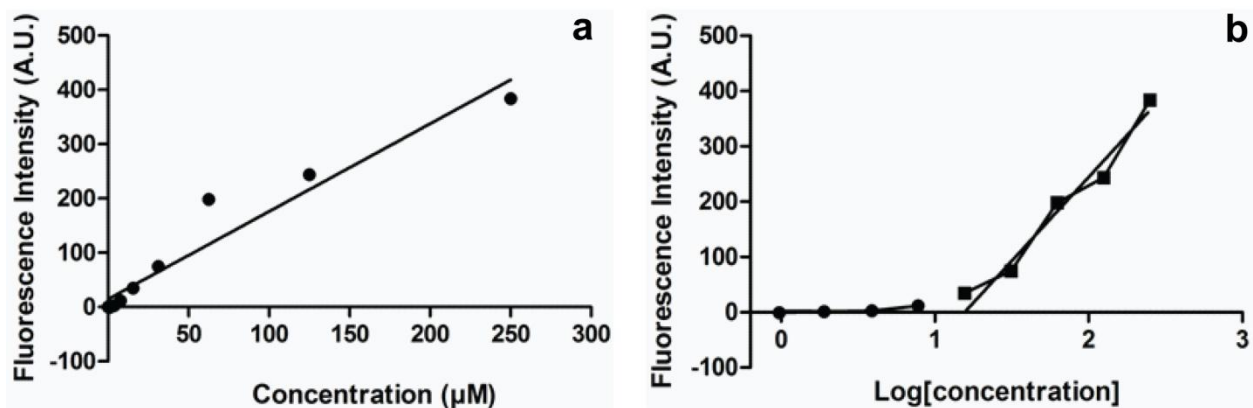
Figure 4.21 CAC plots for C_{12}VVAGHH-Am peptide amphiphile.
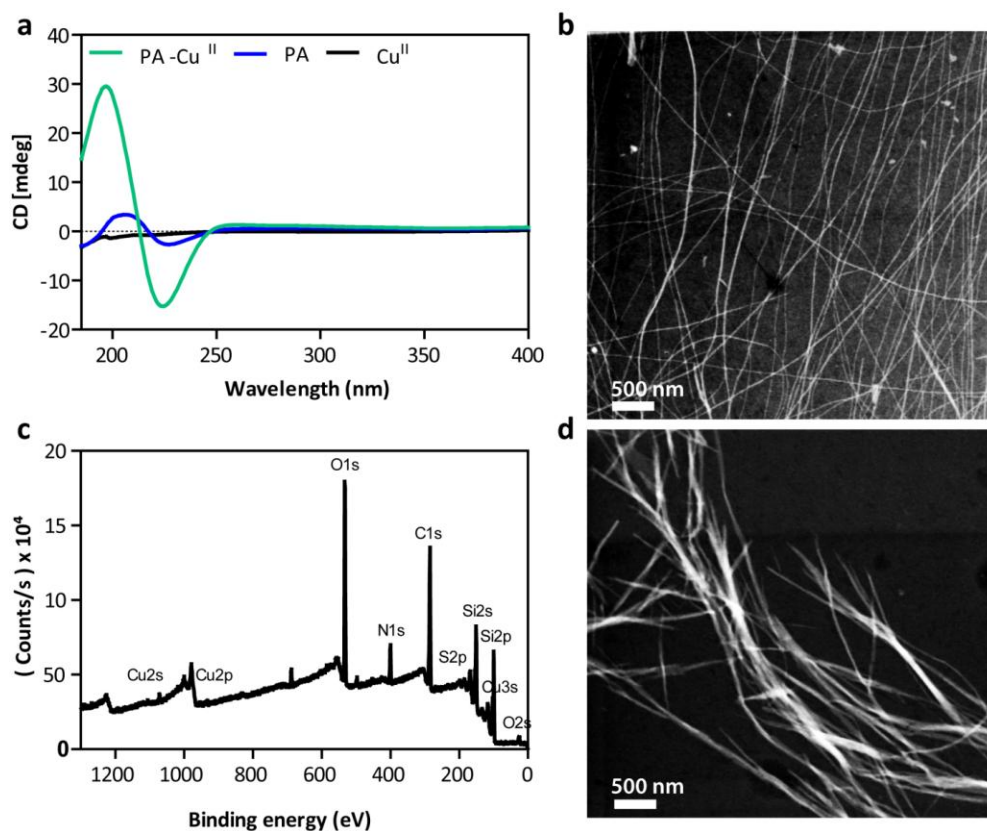
Figure 4.22 (a) CD analysis of PA and PA-Cu^{II},(b) STEM image of the PA nanofibers, (c) XPS and (d) STEM image of PA-Cu^{II} nanofibers.

The surface of the supramolecular PA nanofibers was decorated with Cu^{II} ions by simply mixing the PA and copper sulfate solutions (Figure 4.23). Upon mixing the solutions, a self-supporting PA-Cu^{II} gel was formed (Figure 4.23). The gel formation was further confirmed by oscillatory rheology analysis (Figure 4.23a-b) where the storage modulus (G´) was higher than loss modulus (G´´). Rapid gel formation shows the presence of interactions between PA molecules and the Cu^{II} ions. This interaction was also proved by amplification in β-sheet intensity of PA-Cu^{II} nanofibers (Figure 4.22a).
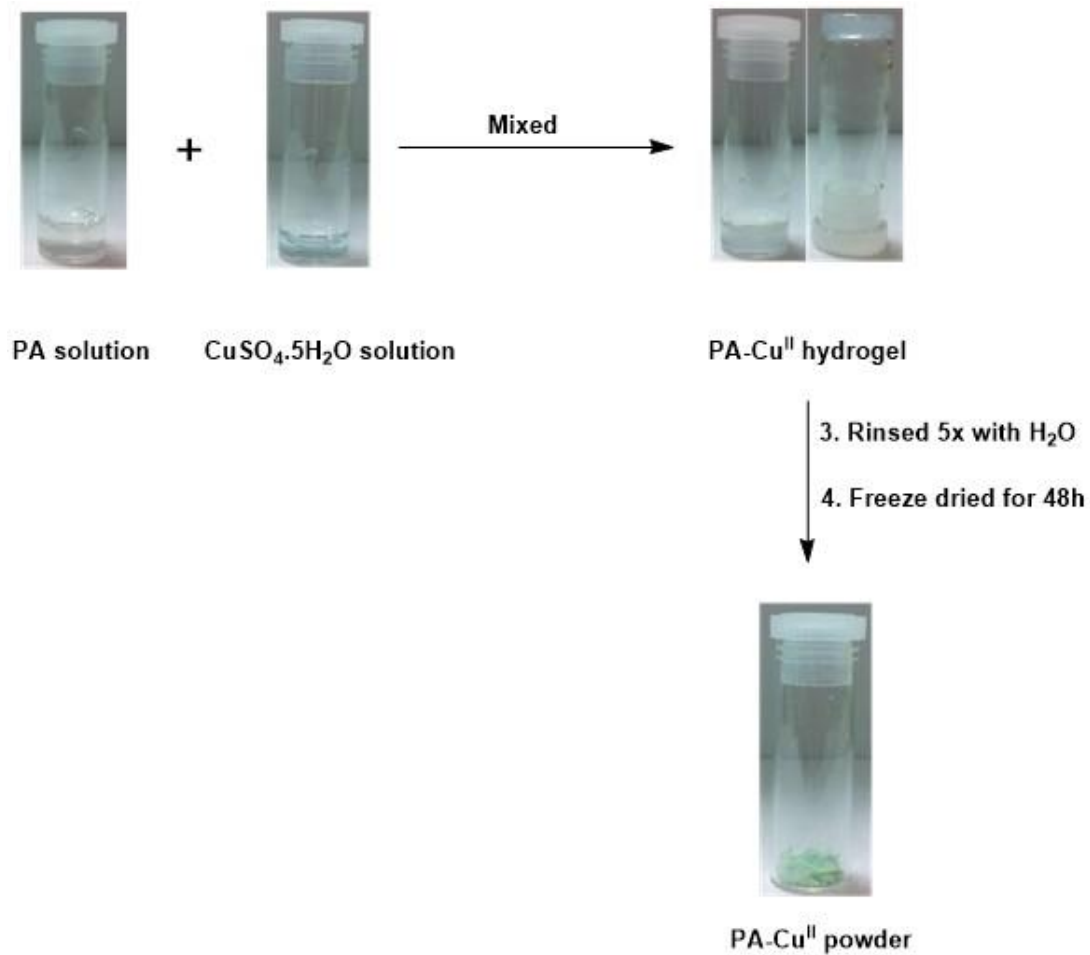
Figure 4.23 Preparation of of PA-Cu^{II}.
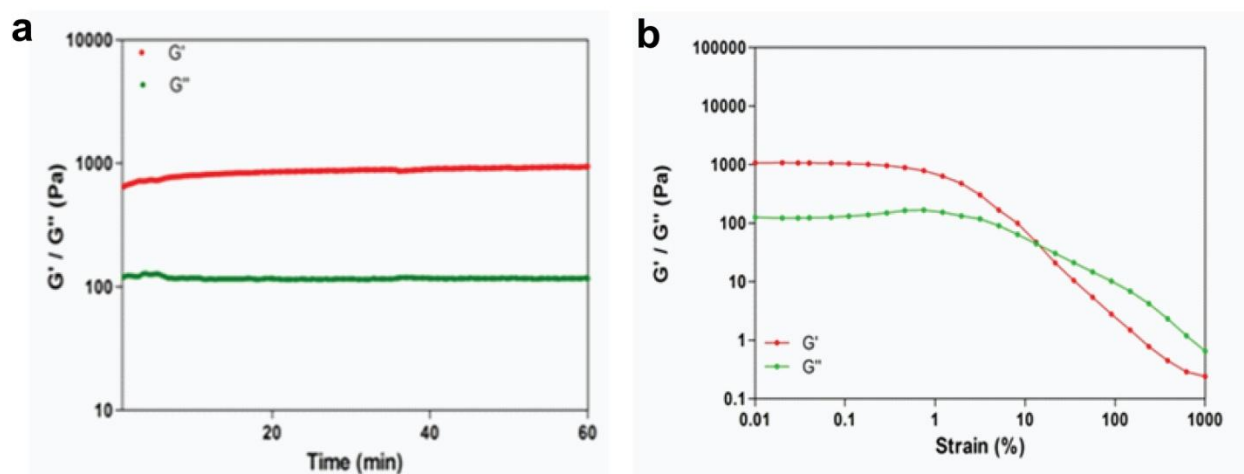
Figure 4.24 Rheological characterization of the PA-Cu^{II} hydrogel. (a) Time sweep, (b) Strain sweep.

The supramolecular PA-Cu^{II} nanofibers were imaged by TEM and bundling of the nanofibers was observed (Figure 4.22d, Figure 4.25a-b) which could be due to the crosslinking of PA nanofibers by Cu^{II} ions. Likewise, the SEM image (Figure 4.25c) of PA-Cu^{II} nanofibers showed that the nanofibrous morphology was conserved. The energy-dispersive X-ray spectroscopy (EDS/SEM) of PA-Cu^{II} verified the existence of the copper and sulfur species on the nanofibers (Figure 4.25d).
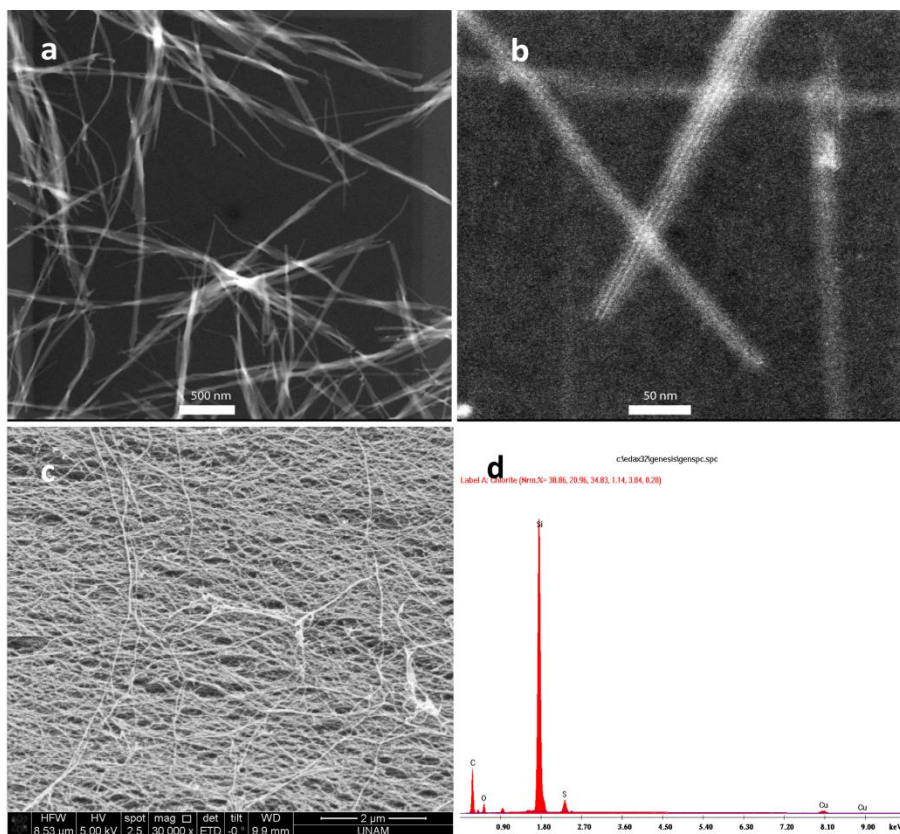
Figure 4.25 STEM (a, b), and SEM images of PA-Cu^{II} nanofibers (c) and EDS of PA-Cu^{II} nanofibers (d).

To further investigate the interactions between the PA molecules and copper ions, the PA-Cu^{II} gel was rinsed thoroughly with water to discard any unbound PA molecules and copper ions. Then the sample was freeze-dried to acquire a bluish powder of PA-Cu^{II}. The X-ray photoelectron spectroscopy (XPS) analysis of PA-Cu^{II} powder revealed peaks at 934.5 and 167.1 eV (Figure Figure 4.26) which corresponds to Cu $2p_{3/2}$ and S $2p$ respectively; these are assigned to Cu^{II} and S ^{IV} (CuSO$_4$) [141]. We also performed inductively coupled plasma mass spectrometry (ICP-MS) to determine the amount of copper in PA-Cu^{II} powder. By analyzing the ICP-MS and elemental analysis results, we calculated that the PA molecule binds to copper ion at 1:1 ratio. These results proved the coordination of CuSO$_4$ to PA nanofibers.
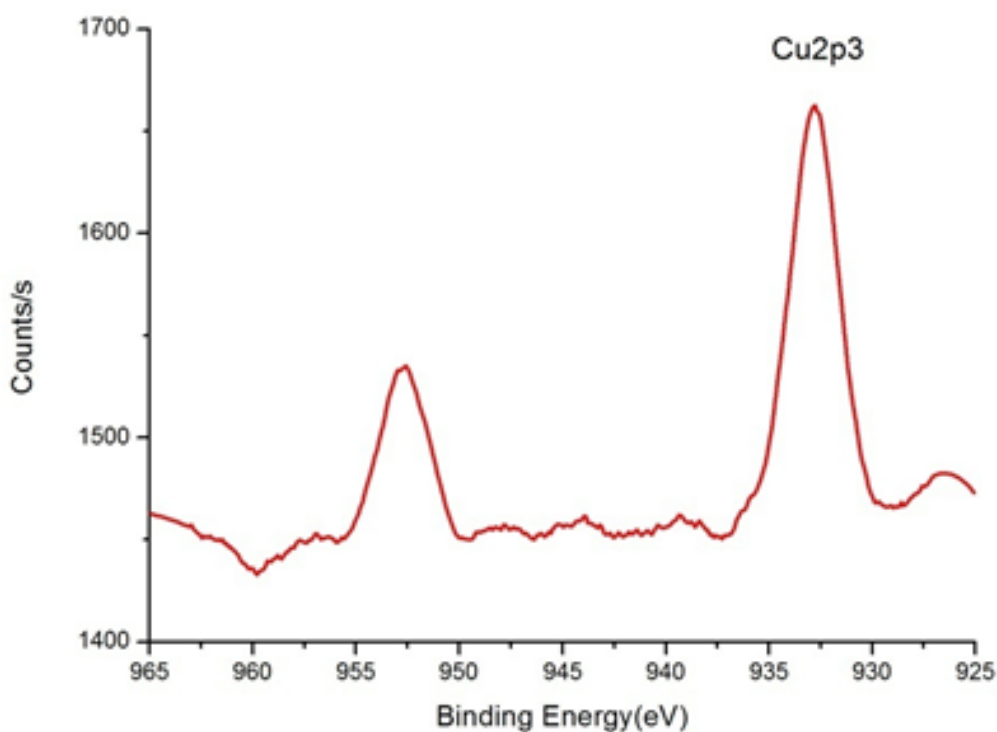
Figure 4.26 High resolution XPS analysis of copper (PA-Cu^{II}).

Data: Data1_NDH
Model: TwoSites
Chi^2 = 56.23
N1   0.127   ±0.0441 Sites
K1   5.11E4 ±3.36E4 M⁻¹
ΔH1   -1389   ±898 cal/mol
ΔS1   16.9 cal/mol/deg
N2   1.03   ±1.07 Sites
K2   2.51E3 ±2.11E3 M⁻¹
ΔH2   -946.8 ±1.29E3 cal/mol
ΔS2   12.4 cal/mol/deg
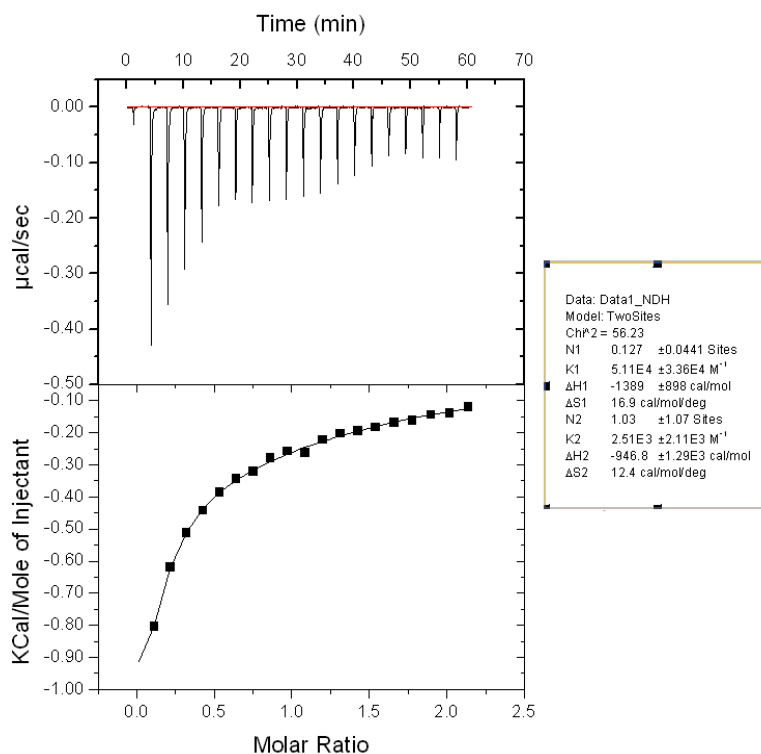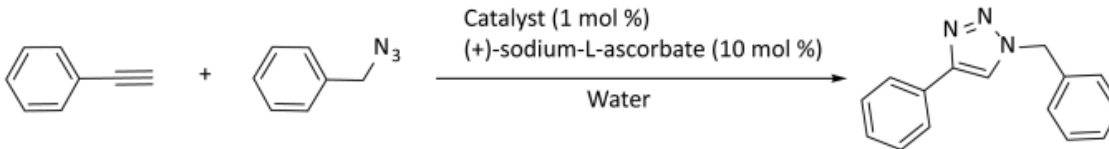
Figure 4.27 Isothermal titration calorimetry of Ac-HH-Am by $CuSO_4$ solution.

We measured the thermodynamic response of Cu^{II} ion binding to peptide molecules by using isothermal titration calorimetry (ITC). To minimize the artifacts due to self-assembly of the PA molecules, we analyzed binding of dipeptide (Ac-HH-Am) molecule to Cu^{II} ion. Binding properties of the single histidine to copper have straightforward interpretation, whereas inclusion of a second histidine introduces the possibility of cooperation in copper binding. In our case, two copper binding sites were observed similar to previous studies [142]. For the active site-metal interaction, ITC binding isotherms were best fitted by a two-sets of site mode with K values; K1 $5.11 \times 10^4 \pm 3.36 \times 10^4 \, M^{-1}$ and K2 $2.51 \times 10^3 \pm 2.11 \times 10^3 \, M^{-1}$ (Figure 4.27). Binding affinity (c values) of each site was calculated as c1=19.44 and c2=7.75, which could be considered as moderate metal ion binding.

Bioorthogonal reactions must be performed in the physiological conditions. Previously, catalyst activities were usually tested in mixture of organic solvents and water then was utilized for labelling of biomolecules [137, 138, 143]. Unlike those studies, we tested activity of the supramolecular PA-Cu[II] nanofibers under physiological conditions to obtain more realistic results. A typical Huisgen 1, 3-dipolar cycloaddition reaction was designed where phenylacetylene and benzylazide were chosen as reactants, sodium ascorbate as reducing agent and water as biological solvent (Table 6). Since L-histidine-copper complex (His-Cu[II]) showed highest catalytic activity in bioorthogonal click reaction among other ligands in the literature [138], we compared our supramolecular nanocatalyst (PA-Cu[II] nanofibers) with this complex.

Table 6 Comparison of catalyst efficiency in CuAACa[a]

Reaction No.	Catalyst	Temperature	Time	Conversion % [b]
1	$CuSO_4$	37 °C	12h	54
2	His-Cu[II]	37 °C	12h	61
3	HH-Cu[II]	37 °C	12h	65
4	PA-Cu[II]	37 °C	12h	95
5	PA-Cu[II]	25 °C	24h	81

[a] Reaction conditions: benzylazide (0.285 mmol), phenylacetylene (0.285 mmol), catalyst (1 mol %), sodium ascorbate (0.0285 mmol, 10 mol %), water (3 mL). [b] The reaction conversions were determined by GC-MS (Figure 4.28–4.37).

His-Cu^{II} complex demonstrated a moderate conversion efficiency of 61% (Table 6). In addition, soluble dipeptide *(*Ac-HH-Am) was complexed with Cu^{II} ion (HH-Cu^{II}) also showed a moderate conversion efficiency of 65% while PA-Cu^{II} nanofibers demonstrated a tremendous conversion efficiency of 95% under the same conditions (Table 6). There are two possible explanations for this striking difference in the reaction efficiencies where all catalysts have histidine as copper binding sites. Assembly of catalytic sites within a nanostructured environment on PA nanofibers could show p*ositive cooperativity* thus increased the reaction rates [144, 145]. Moreover, two histidine motifs are in close proximity to hydrophobic amino acids such as glycine, alanine and valine. When assembled into nanofibers, these amino acids could create a favorable hydrophobic environment for the reactants. Hence, chance of gathering of catalytic sites with reactants was increased on PA nanofibers; as a consequence the rate of the reaction was improved. It is worth to mention that PA-Cu^{II} nanofibers can catalyze azide–alkyne cycloaddition significantly in green conditions (at room temperature in neat water, Table 6, reaction no: 5). During the reaction, pale blue PA-Cu^{II} color changes to yellowish green, which demonstrates the reduction of Cu^{II} to Cu^{I} [141].
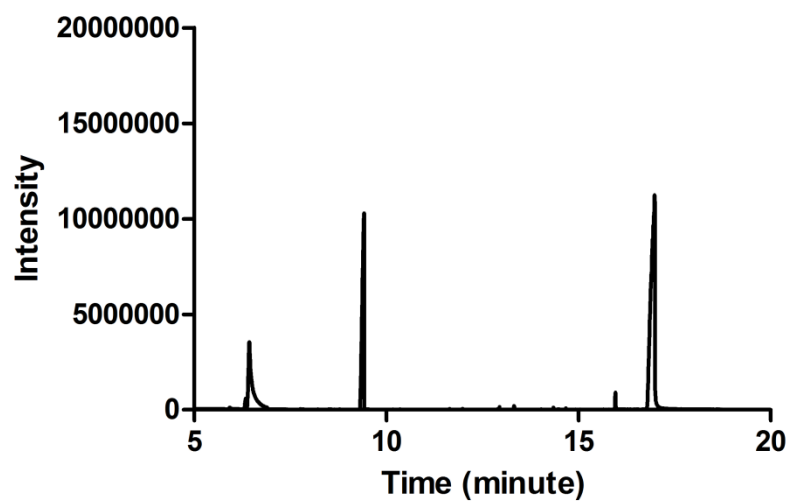
Figure 4.28 Gas chromatogram of crude triazole (CuSO$_4$ as catalyst, 37 $^{\circ}$C).
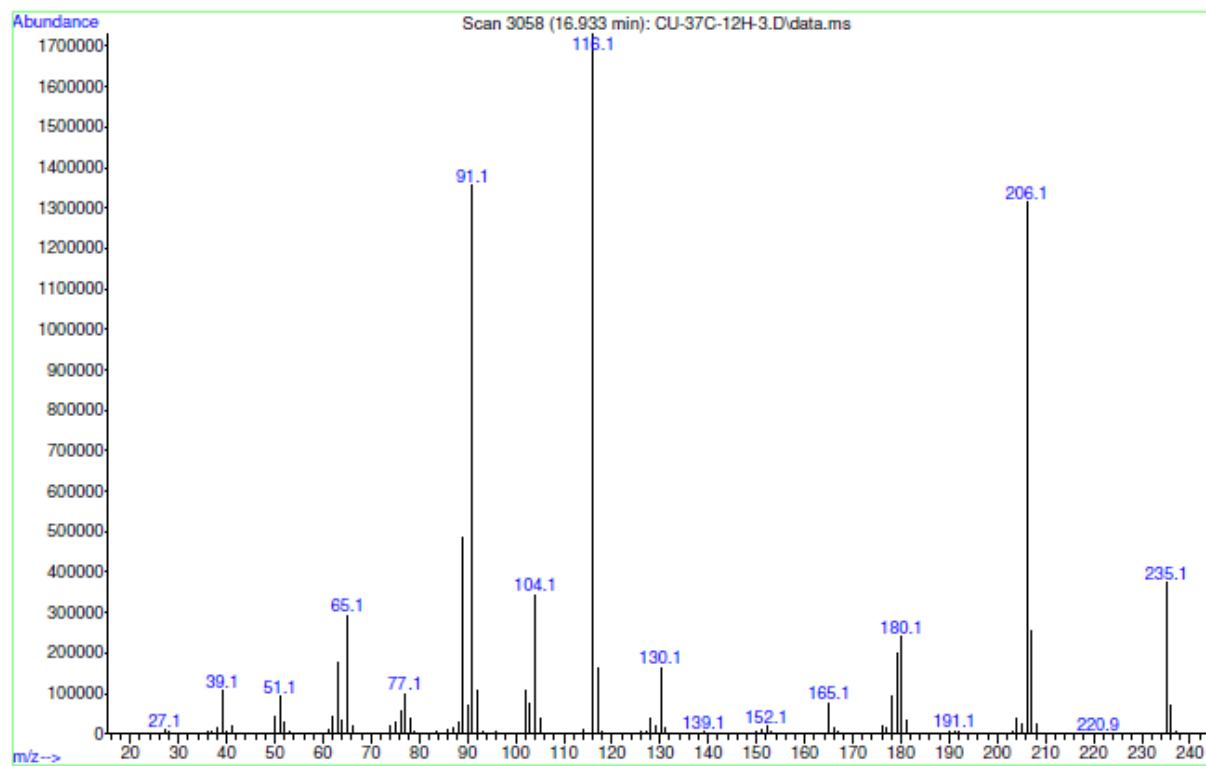
Figure 4.29 Mass spectrum of crude triazole (CuSO$_4$ as catalyst, 37 $^{\circ}$C).

113
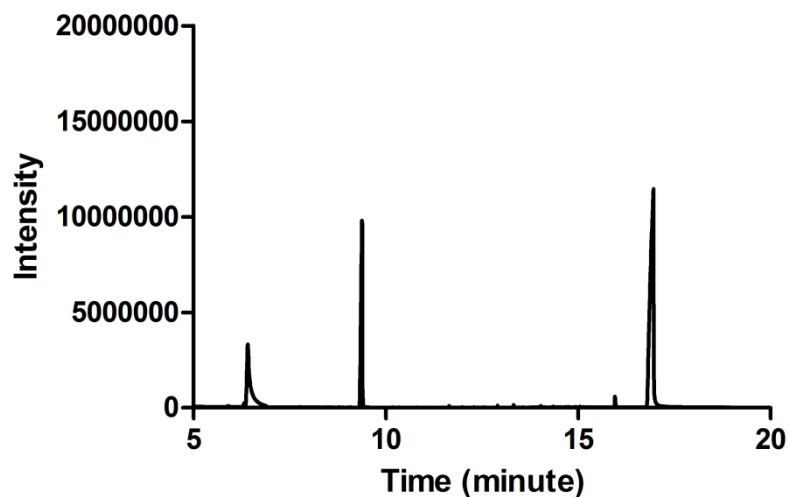
Figure 4.30 Gas chromatogram of crude triazole (His-Cu^{II} as catalyst, 37 ^{o}C).
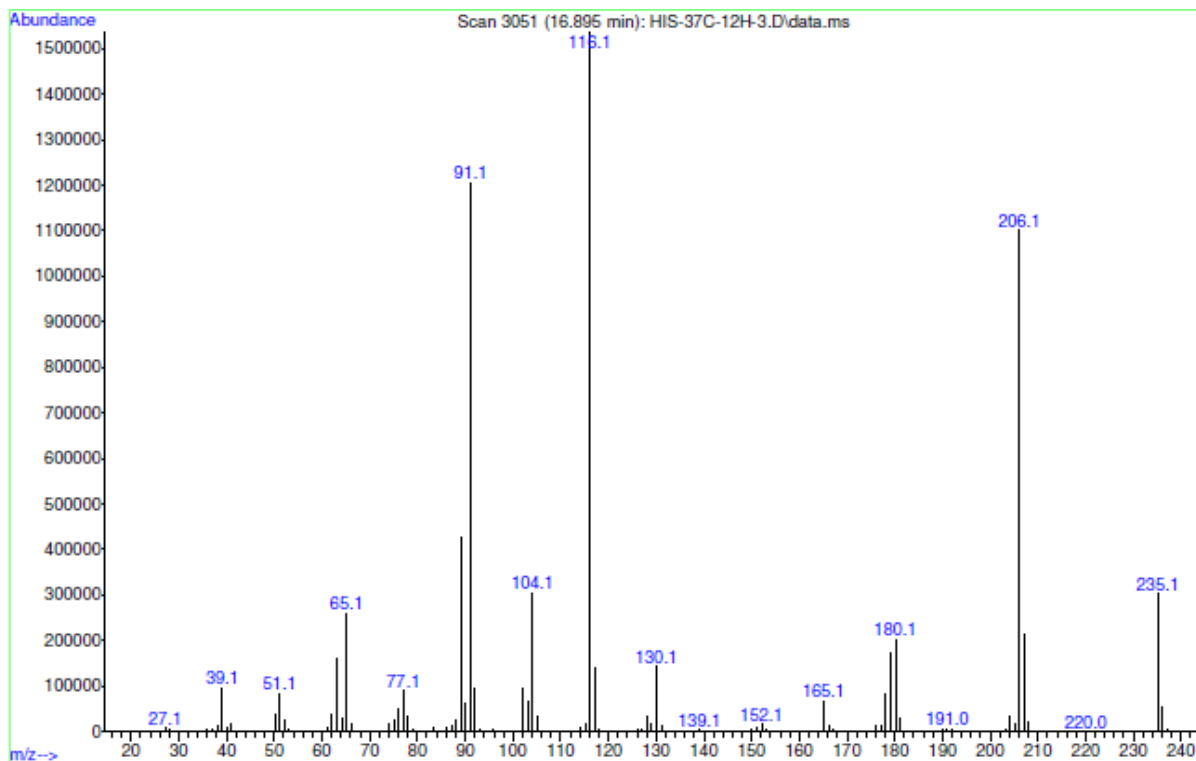
Figure 4.31 Mass spectrum of crude triazole (His-Cu^{II} as catalyst, 37 ^{o}C).
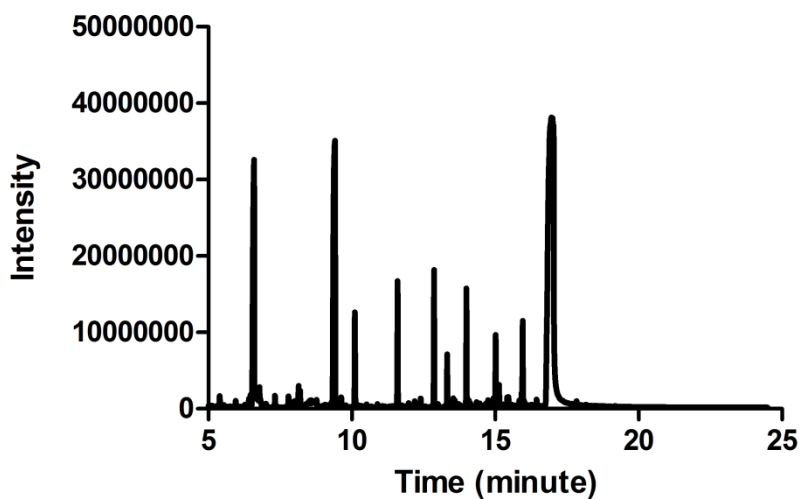
Figure 4.32 Gas chromatogram of crude triazole (HH-Cu^{II} as catalyst, 37 ^{o}C).
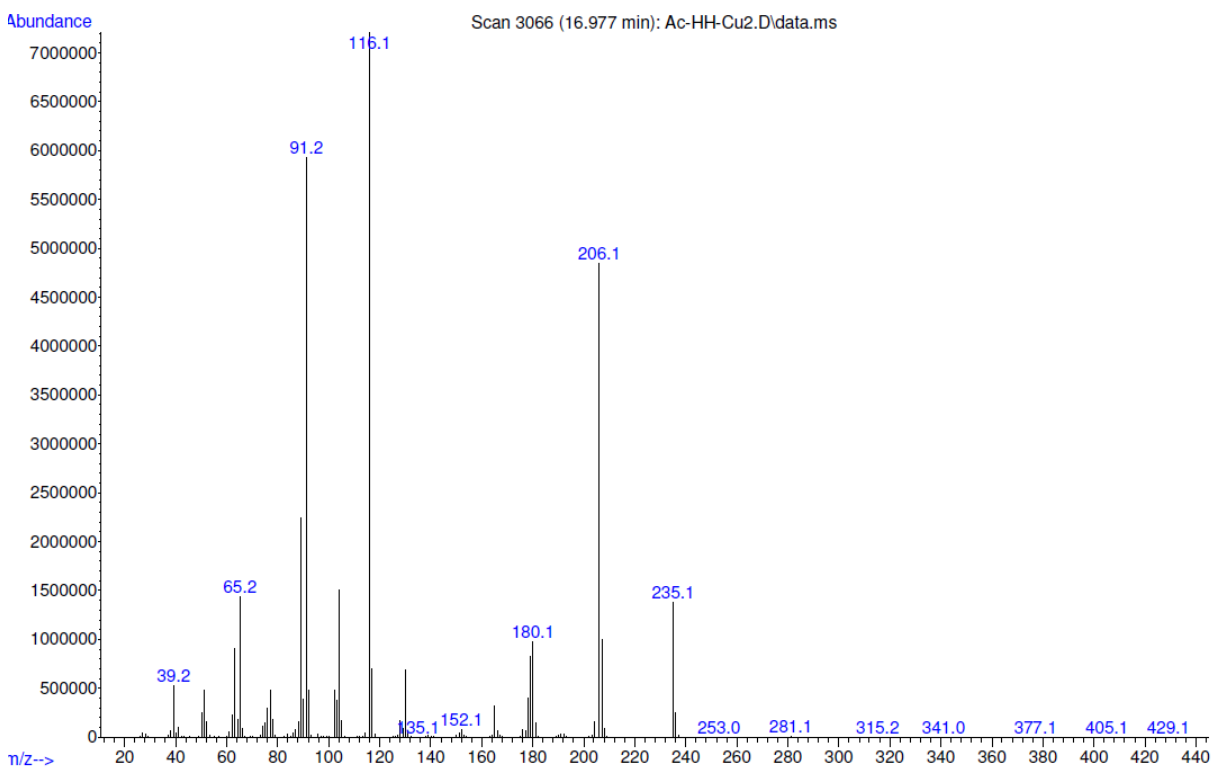
Figure 4.33 Mass spectrum of crude triazole (HH-Cu^{II} as catalyst, 37 ^{o}C).

115
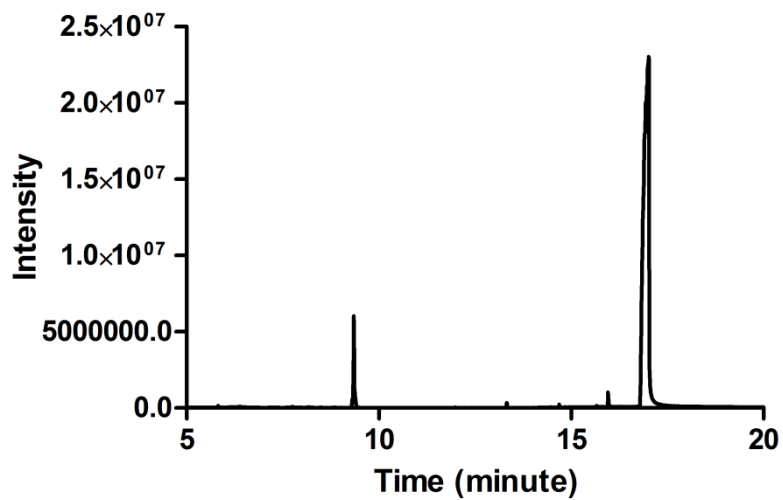
Figure 4. 34 Gas chromatogram of crude triazole (PA-Cu^{II} as catalyst, 37 ^{o}C).
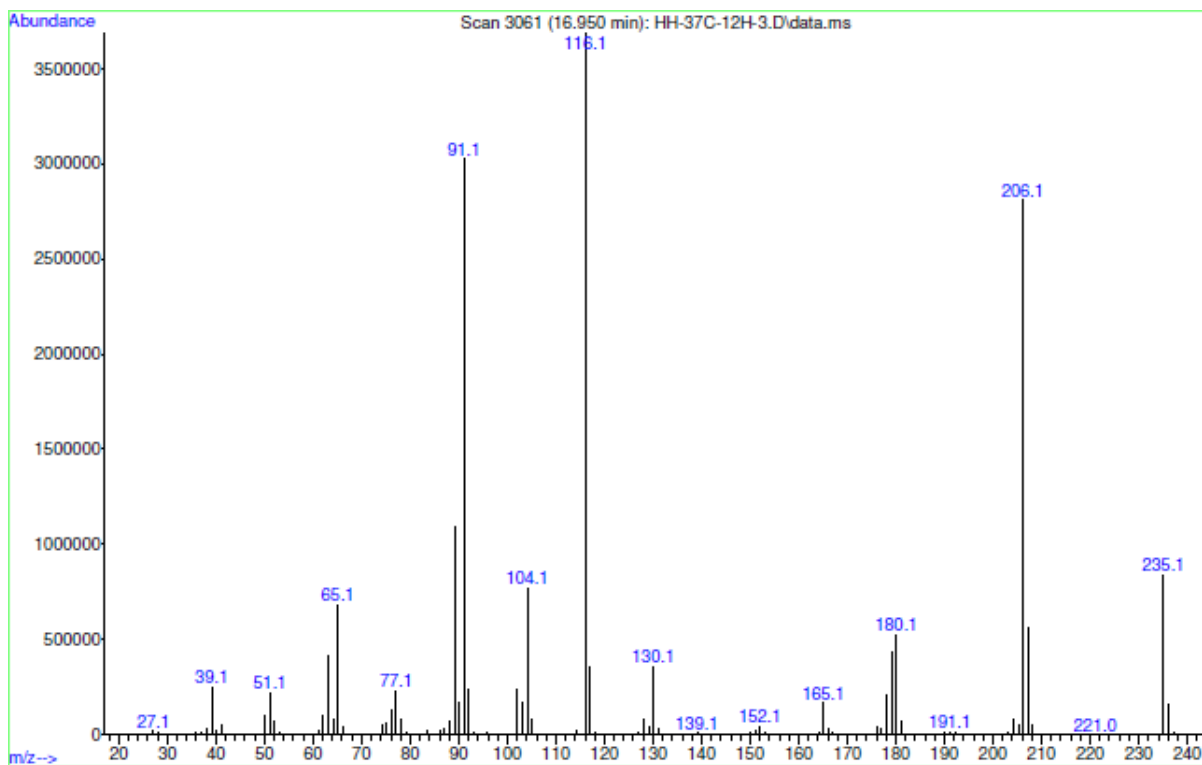
Figure 4.35 Mass spectrum of crude triazole (PA-Cu^{II} as catalyst, 37 ^{o}C).
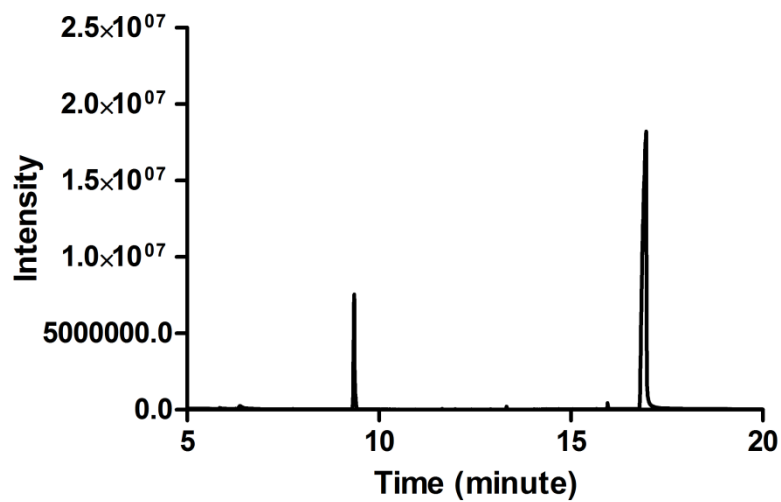
Figure 4.36 Gas chromatogram of crude triazole (PA-Cu^{II} as catalyst, 25 ^{o}C).
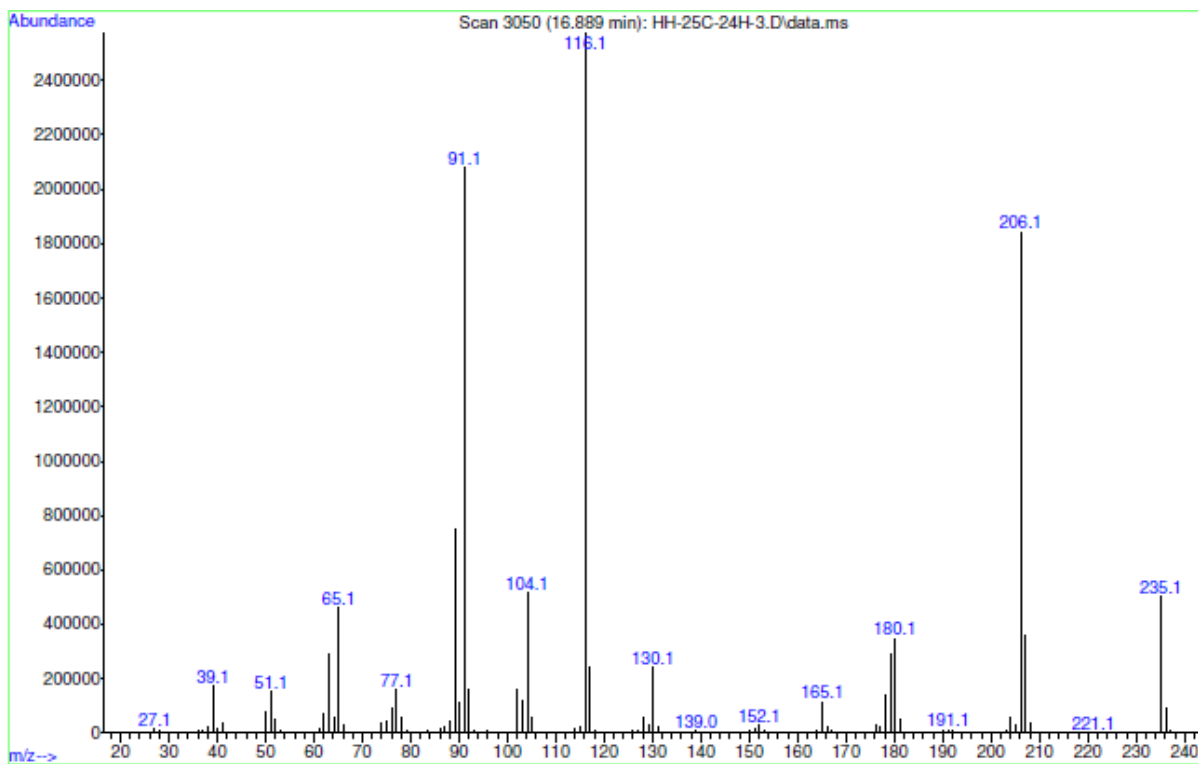
Figure 4.37 Mass spectrum of crude triazole (PA-Cu^{II} as catalyst, 25 ^{o}C).

We have conducted a series of organic synthesis of essential molecules for labelling. A multi synthetic pathway was followed to introduce azide functional group to d-biotin (Biotin-azide, and alkyne functional group to d-mannose amine (Ac$_4$ManNAl,. Intermediate molecules and end products were characterized by NMR and High Resolution Mass Spectrometry (Figure 4.3-4.14). All molecules were synthesized according to methods in the literature with slight modifications.

Copper-catalyzed click chemistry method offers a bioorthogonal strategy that can label live-cells in a complex environment, allowing the function and dynamics of a target biomolecules to be monitored in living organisms. Here, an unnatural sialic acid precursor bearing a bioorthogonal functional group (alkyne functionalized sugar (Ac$_4$ManNAl)) was introduced to living cells by using biosynthetic pathways and a chemical tag (Biotin-azide) was subsequently attached to the alkyne-bearing sialic acid group by CuAACa. The labeling process was then completed with the addition of a streptavidin-fluorescein (FITC) conjugate [146] . Copper-coordinating ligands used for dynamic imaging studies must meet certain criteria; such as high binding affinity for copper ions, biocompatibility, biodegradability and the ability to perform their reactions rapidly under physiological conditions. In view of these requirements, we used PA molecules derived from natural amino acids as a ligand to coordinate and stabilize Cu^I oxidation state and to obtain improved reaction kinetics and minimized cytotoxicity. Cytotoxicity resulting from oxidative damage is one major drawback of copper catalysts for bioorthogonal labeling reactions. Owing to the stabilization of Cu^I, the peptide ligand can prevent the formation of undesired byproducts and minimize the oxidative damage against target biomolecules and cells. In addition to reduced toxicity, biocompatibility and biodegradability, another important feature of the supramolecular nanofiber-based catalysis is the availability of a large number of active sites on a small area, which enhances reactivity by better facilitating surface-substrate interactions.
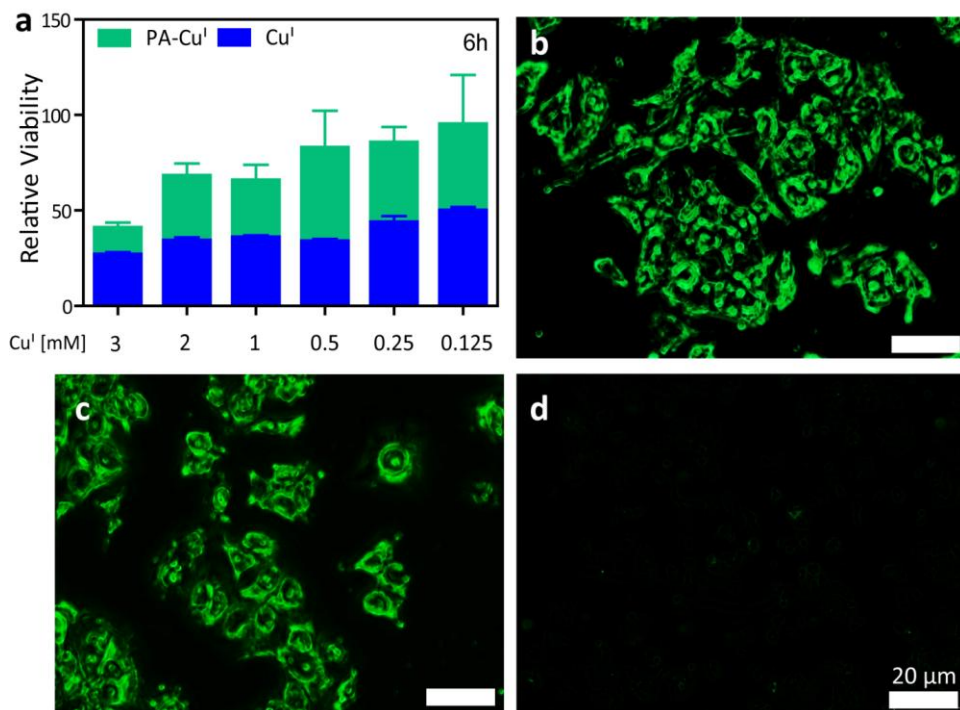
Figure 4.38 Viability of MCF-7 cells in the presence of PA-Cu^{I} and Cu^{I} (a), microscopic analysis of fixed cells labeled with PA-Cu^{I} nanofibers after 6 h (b), and after 24 h reaction (c) and non-treatment group after 24 h reaction (d). (Scale bars = 20 μm)

To evaluate potential of PA-Cu^{I} nanofibers (PA-Cu^{II} + sodium ascorbate) in cell labeling applications, variable concentrations of PA-Cu^{I} nanocatalyst (3 mM - 0.125 mM) were administered to MCF-7 (breast adenocarcinoma) cells. MCF-7 cells were treated with Cu^{I} ions (CuSO$_4$ + sodium ascorbate) in the absence of ligand as positive control, and the effect of ligand incorporation on viability was tested. After 6 h of catalyst exposure, PA-Cu^{I} nanofibers were found to display significantly lower cytotoxicity compared to copper alone samples for all copper concentrations (Figure 4.38a). Toxicities of PA-Cu^{I} nanofibers were also found to be lower than Cu^{I}-only controls over extended exposure times (24 h). In previous bioorthogonal labeling studies with small molecule ligands
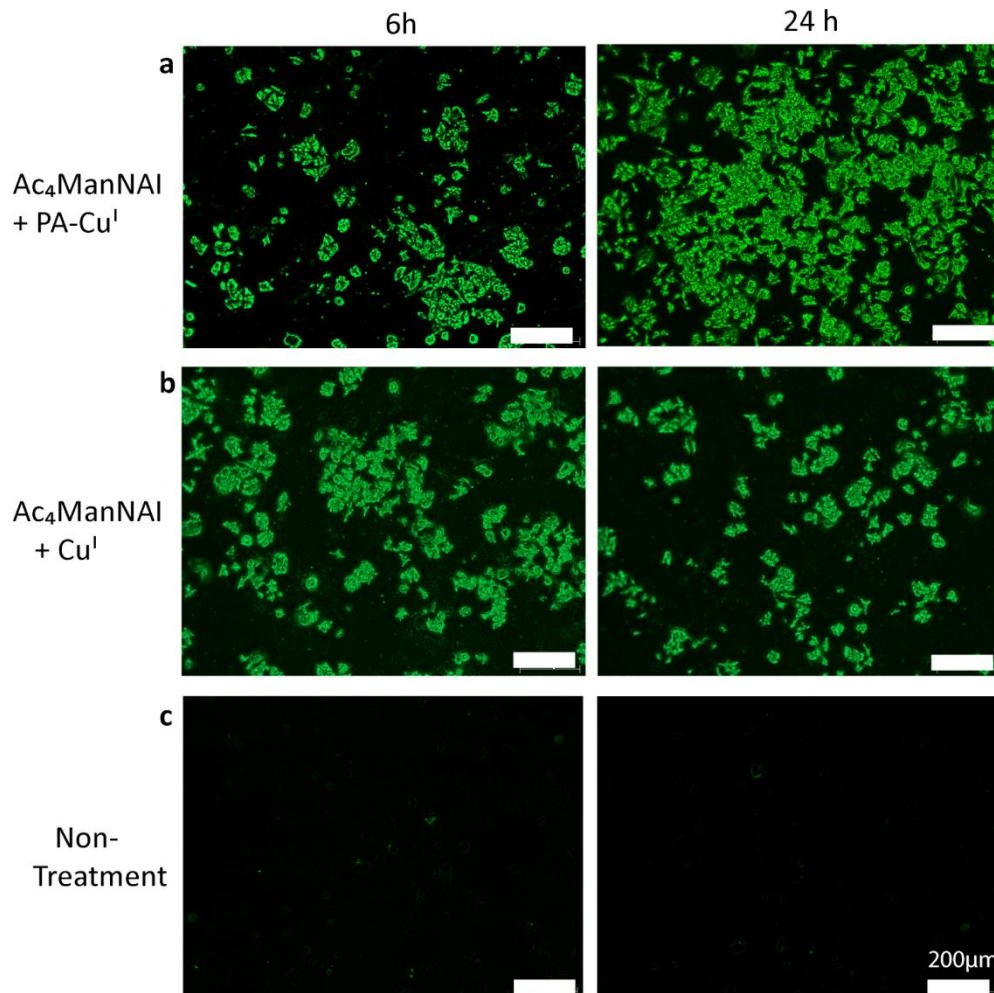
Figure 4.39 Fluorescent imaging of fixed cells labeled with (a) PA-Cu^{I}, (b) Cu^{I} and (c) non-treatment sample after 6 h and 24 h reaction.

toxicity was tested in the presence of Cu^{II}-ligand complexes or lower copper concentrations [137, 138]. However, Cu^{II} is found in the serum as an essential metal and is less toxic than Cu^{I}, which is the main ingredient of the click reaction mixture administered to cells. Our PA-Cu^{I} nanocatalyst approach allows the use of higher Cu^{I} concentrations for click chemistry, which makes PA nanofiber-based click catalysts promising for effective catalysis in the biological environments. Modification of cell membranes by Ac$_4$ManNAl was verified and labeling

reaction duration was optimized by using fixed MCF-7 cells. Cells were incubated with Ac$_4$ManNAl for 3 days to introduce alkyne residues to cell surface sialyl glycoconjugates, and fixed with cold acetone. The acetylated form of the alkynyl sugar was administered to MCF-7 cells since acetylation enhances cellular uptake compared to free sugars [147, 148]. Following Ac$_4$ManNAl incorporation, MCF-7 cells bearing alkyne sialic acid residues were reacted with biotin–azide for 6 h in the presence of PA-Cu^I nanofibers, using a reaction mixture composed of biotin azide, PA-Cu^{II} and sodium ascorbate.
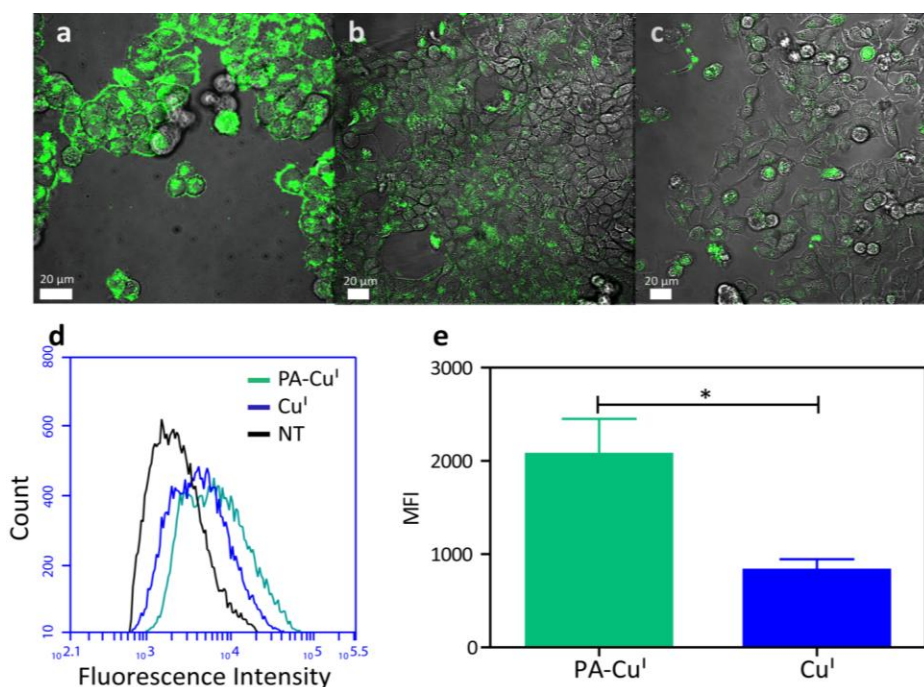
Figure 4.40 Confocal microscopy images of labeled cells with PA-Cu^I nanofibers (a), Cu^I (b) and non-treated (c) groups after 6 h reaction. Flow cytometry analysis of MCF-7 cells (green histogram, cells treated with PA-Cu^I; blue histogram, cells treated with Cu^I; black histogram, non-treated cells) (d). Comparison of cell labeling efficiency by flow cytometry (e). To quantify labeling signals, the mean FITC intensities were calculated for >10000 cells for each condition, averaged and compared. (Mean ± SEM)

Reaction mixture treated MCF-7 cells showed strong labeling signal following the attachment of the biotin residue and staining with a fluorescent streptavidin-FITC probe. Cells treated with Cu^I only were also labeled, while non-treated control groups were not labeled in the presence of the fluorescent probe (Figure 4.38b-d and Figure 4.39). This result suggests that alkynyl-tagged mannose moieties were incorporated into cell glycans and could function as chemical tags for PA-Cu^I complex-mediated specific labeling after 6 h of reaction. After establishing optimum reaction times and PA-Cu^I nanofiber concentrations on fixed cells, we extended our study to the labeling of glycans in living cells. A bioorthogonal cell tracking experiment was carried out using the same procedure used for fixed cell labeling experiments, except that the cells were not fixed prior to the experiment. Labeling efficacy was monitored with confocal microscopy imaging following CuAACa reaction and fluorescent probe conjugation.

Fluorescence microscopy observations demonstrated that alkyne-tagged glycoconjugates are able to successfully modify MCF-7 cells and that PA-Cu^I nanofiber administered group exhibited fluorescence levels above Cu^I-only group and non-treated cells, suggesting that the labeling of Ac$_4$ManNAl is specific and PA-Cu^I nanofibers could mediate adequate live-cell labeling reaction (Figure 4.40a-c). The labeling efficiency of PA-Cu^I nanofibers was also evaluated through flow cytometry analysis of live-cells treated with the PA-Cu^I complex or Cu^I in the presence and absence of ligands. The background signal was excluded by the extraction of the emission signal of non-treated groups in order to facilitate comparison among catalysts. Consistent with the results obtained from confocal microscopy analysis, PA-Cu^I nanofibers yielded higher labeling efficiency when compared to the Cu^I-only group (Figure 4.40d-e).

4.4 Conclusion

In summary, we demonstrated the first supramolecular nanocatalyst, which was used in bioorthogonal click reaction for labelling of live-cells. The nanocatalyst was fabricated by biocompatible and biodegradable supramolecular peptide amphiphile nanofibers. This novel supramolecular nanocatalyst did not only reduce the cytotoxicity of Cu^I ions but also enhanced the reaction yields under physiological conditions. This novel labeling approach offers a promising method for studying biomolecular dynamics and functions in cells and living organisms and will open new directions in bioorthogonal chemistry field.

Chapter 5

Facile Synthesis of Three-Dimensional Pt-TiO$_2$ Nanonetworks: Highly Active Catalyst for Hydrolytic Dehydrogenation of Ammonia Borane

This work is partially described in the following publication:

Mohammad Aref Khalily**,** Hamit Eren, Serdar Albayrak, Hepi Hari Susapato, Saim Ozkar, Necmi Biyikli, and Mustafa O. Guler **"**Facile Synthesis of Three-Dimensional Pt-TiO$_2$ Nanonetworks: Highly Active Catalyst for Hydrolytic Dehydrogenation of Ammonia Borane**"** *Angew. Chem. Int. Ed. 2016, 55, 12257–12261*

5.1 Introduction

Three-dimensional (3D) porous metal and metal oxide aerogels have recently attracted enormous interest since assembly of bulk inorganic materials into 3D nanomaterials generates exciting features such as low density, high porosity, and high surface area [149-151]. Porous 3D aerogels allow rapid flow of electrons, ions, and molecules, which makes them extremely attractive for applications such as catalysis [152], sensing [153], fuel cells [154, 155], and supercapacitors [156]. Numerous techniques have been developed to prepare porous metal and metal oxide nanomaterials, including templating, combustion, cathodic corrosion, and aerogel formation [155]. However, a significant challenge exists to synthesize metal and metal oxide 3D nanomaterials in controlled and reproducible manner. Therefore, uniform and highly controlled deposition of metals and metal oxides at ambient temperatures on soft organic templates, which

can assemble into desired structures (1D, 2D and 3D), shape and morphology, could be a promising strategy to prepare variety of porous inorganic 3D nanomaterials. Self-assembling peptides are a class of supramolecular polymers, which exploit noncovalent interactions such as hydrogen bonding, hydrophobic, electrostatic, π-π, and van der Waals interactions to generate well-defined supramolecular nanostructures including nanospheres, nanosheets, nanotubes, and nanofibers [4]. These versatile supramolecular polymers can encapsulate large amounts of water to form gels, which have been extensively utilized as 2D and 3D scaffolds [157]. Critical and air-dried self-assembled peptide nanofiber gels can form self-standing porous 3D aerogels and xerogels, which are made up of highly dense 1D nanofibers. These 3D aerogels can be used as soft templates to deposit and support various inorganic nanomaterials from 1D to 3D [158, 159].
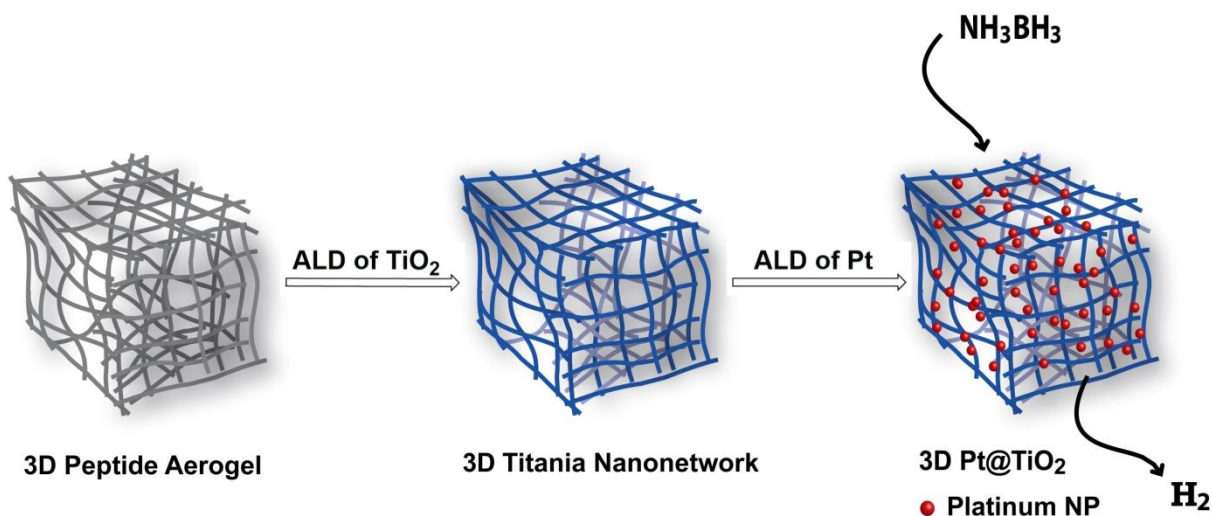
Scheme 4. Fabrication of 3D Pt@TiO$_2$ nanonetworks via ALD.

In this work, we combined advantages of two bottom-up nanofabrication techniques to engineer a novel metal/metal oxide 3D nanonetwork in highly controlled manner. Self-assembling peptides were used to produce a 3D nanonetwork of high-aspect-ratio nanofibers as soft organic template. The 3D peptide nanofiber aerogel was conformally coated with TiO$_2$ via ALD. The 3D

peptide-TiO$_2$ nanonetwork was further decorated with highly monodisperse Pt nanoparticles by using ALD (Pt@TiO$_2$, Scheme 4). These high-surface-area 3D Pt@TiO$_2$ nanonetworks were utilized for hydrolysis of ammonia borane (AB) for H$_2$ generation. Due to its high hydrogen content (19.6 wt %), high stability in the solid state and solution under ambient conditions, nontoxicity, and high solubility [160, 161], AB has been considered as one of the most promising hydrogen storage materials for on-board applications [162]. We systematically studied the effect of platinum nanoparticle size on catalytic activity and found that platinum nanoparticles with size of ca. 2.4 nm provide the highest turnover frequency of 311 min^{-1} for hydrogen generation in the hydrolysis of AB at ambient temperature.

5.2 Experimental Section

5.2.1 Peptide Synthesis

Peptide molecule was synthesized and characterized according established procedure. MBHA Rink Amide resin was used as solid phase. Amino acid couplings were performed by 2 equivalents of fluorenylmethyloxycarbonyl (Fmoc) protected amino acids, 1.95 equivalents O-Benzotriazole-N,N,N',N'-tetramethyl-uronium-hexafluoro-phosphate (HBTU) and 3 equivalents of N,N-diisopropylethylamine (DIEA) for 3 h. Fmoc protecting groups were removed by 20% piperidine /dimethylformamide solution for 20 min. Cleavage of the product from the Rink Amide was carried out by a mixture of trifluoroacetic acid: triisopropylsilane: water in the ratio of 95:2.5:2.5 for 2 h. The resin was washed thoroughly by DCM. Collected peptide solution was concentrated by rotary evaporation. The remaining viscous peptide solution was triturated with cold ether and the resulting precipitate was lyophilized to get a white powder.

5.2.2 Circular Dichroism (CD) Spectroscopy

1% by weight peptide gel was prepared by dissolving the peptide in dd water then adjusting the pH to 10 by adding 1M NaOH. Another sample was prepared by dissolving the peptide in dd water then adjusting the pH to 2 by adding 1M HCl. The two samples were diluted to 1×10^{-4} M. Jasco J-815 circular dichroism spectrometer was used to measure from 300 nm to 190 nm with 0.1 data pitch, 100 nm/min scanning speed, 1 nm band width and 4 s D.I.T.

5.2.3 Rheological Analysis

290 μL of 1 wt % peptide solution was prepared in dd water. Peptide solution was jellified by 10 μl of 1M NaOH. The mechanical characterizations were performed using Anton Paar MCR-301

Rheometer. PP25-SN17979 measuring device with 25 mm diameter was used. Measuring distance was fixed as 0.5 mm. Time sweep of sample was performed for 1h. Angular frequency and strain magnitudes were adjusted as ω=10 rad/s and γ=0.1%, respectively.

5.2.4 Scanning Electron Microscopy/Critical Point Dryer

1 wt % peptide gel was prepared on silicon wafer in the presence of concentrated NH_4OH vapor. Peptide hydrogel was washed by 15%, 30%, 45%, 75%, 90% and 100% (v/v) ethanol solutions to exchange water with ethanol. Tousimis Autosamdri-815B, Series C critical point dryer was utilized to dry the gel without collapsing 3D nanonetwork. FEI Quanta 200 FEG environmental scanning electron microscope (SEM) was used to image the peptide nanonetwork system. The samples were coated 6 nm Pt before imaging by SEM.

5.2.5 Transmission Electron Microscopy (ALD)

Minute amount of Pt@TiO_2 samples were dispersed in ethanol then were dropped on a carbon grid. FEI Tecnai G2 F30 transmission electron microscope (TEM) was used to image the samples.

5.2.6 Atomic Layer Deposition (ALD)

Atomic layer deposition technique was employed on aerogel to coat TiO_2 by using Savannah S100 ALD reactor (Ultratech Inc.). The substrate temperature was kept at 150 °C during the ALD process using $Ti(NMe_2)_4$ and H_2O as titanium and oxygen precursors, respectively. Prior to deposition, $Ti(NMe_2)_4$ precursor was preheated to 75 °C and as the carrier gas, N_2 was used with a flow rate of 20 sccm. The deposition was carried out using 150 deposition cycles of TiO_2 with the estimated growth rate ~0.44 Å/cycle onto the peptide nanofibers. Subsequently, Pt

nanoparticles were decorated onto TiO$_2$-coated nanofibers by using trimethyl(methylcyclopentadienyl)*platinum*(IV) (MeCpPtMe$_3$) as Pt precursor and O$_3$ as counter reactant. The temperature of Pt precursor was held at 65 °C to obtain a proper vapor pressure. O$_3$ was produced from a pure O$_2$ flow with a Cambridge NanoTech Savannah Ozone Generator. ALD Pt deposition was carried out at 150 °C as well.

5.2.7 Inductively Coupled Plasma-Mass Spectrometry (ICP-MS)

Pt@TiO$_2$ samples were dissolved in HF: HCl: HNO$_3$ solution. The samples were diluted to 10 ml of 2% HCl solution. Platinum standards of 250 ppb, 125 ppb, 62.5 ppb and 31.25 ppb were prepared in 2% HCl solution and 2% HCl solution was used as blank. Thermo X series II inductively coupled plasma-mass spectrometer was used to accomplish the measurements. The ICP-MS operating parameters were: dwell time – 10 000 ms, channel per mass – 1, acquisition duration – 7380, channel spacing – 0.02, carrier gas-argon.

5.2.8 X-Ray Photoelectron Analysis (XPS)

Pt@TiO$_2$ samples were placed on copper tape then were analyzed by Thermo K-alpha monochromatic high performance X-ray photoelectron spectrometer. Survey analyses were performed at 5 scans while high resolution XPS for Pt were recorded at 30 scans.

5.2.9 X-Ray Diffraction Analysis (XRD)

Pt@TiO$_2$ samples were analyzed by PANalytical X'Pert Powder Diffractometer. All data were recorded by using CuK$_\alpha$ radiation in the range of 2θ= 20°–80° and with the spinning rate of 8 rpm in order to achieve homogenous data acquisition from samples.

5.2.10 Catalytic hydrolysis of AB using Pt@TiO₂ nanocatalysts

An isolated reaction flask (20 mL) containing AB and magnetic stir bar was placed on a magnetic stirrer and thermostated to 25.0 ± 0.1 °C by passing water through its jacket from a constant temperature bath. A graduated glass cylinder (60 cm in height and 3.0 cm in diameter) filled with water was connected to the reaction container to determine the volume of the hydrogen gas to be given out from the reaction. Then, a known quantity of Pt@TiO₂ was dispersed in 10 mL distilled water in the reaction medium. Then, 31.8 mg AB (1.0 mmol $H_3N \cdot BH_3$) was added into the container and the reaction mixture was stirred at 1200 rpm. The volume of hydrogen gas given out was quantified by tracking the displacement of water level every one minute at fixed atmospheric pressure of 693 Torr.

5.2.11 Determination of the most active Pt ALD cycle for Pt@TiO₂ nanocatalysts used in hydrolysis of AB

The catalytic activity of Pt@TiO₂ samples with various platinum loading in the range of 2.0–30 wt % was tested in hydrogen generation from the hydrolysis of AB starting with a certain amount of catalyst and 100 mM AB in 10 mL solution at 25.0 ± 0.1 °C. The highest catalytic activity was achieved by using 13.5% wt platinum loaded titania nanowire, which corresponds to 25 Pt ALD cycle.

5.2.11 Catalyst durability study of hydrolysis of AB catalyzed by Pt@TiO₂ nanocatalysts

Recyclability test was started with 10 mL of 100 mM AB (31.8 mg H_3NBH_3), and a certain amount of Pt@TiO₂ at 25.0 ± 0.1 °C. When the AB present in the solution was completely hydrolyzed, 1 mmol AB was added for another run of hydrolysis.

5.3 Results and Discussion
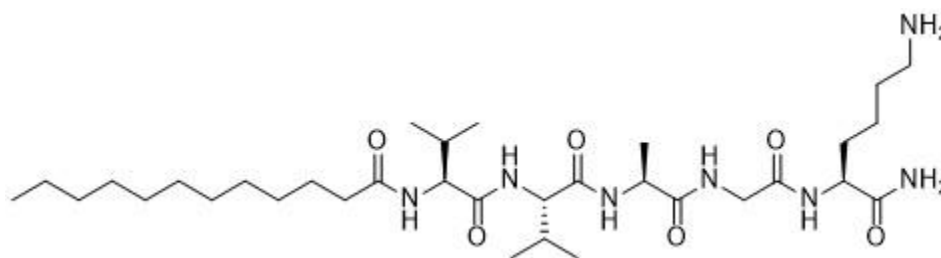
Figure 5.1 Chemical Structure of Peptide Molecule (K-PA).
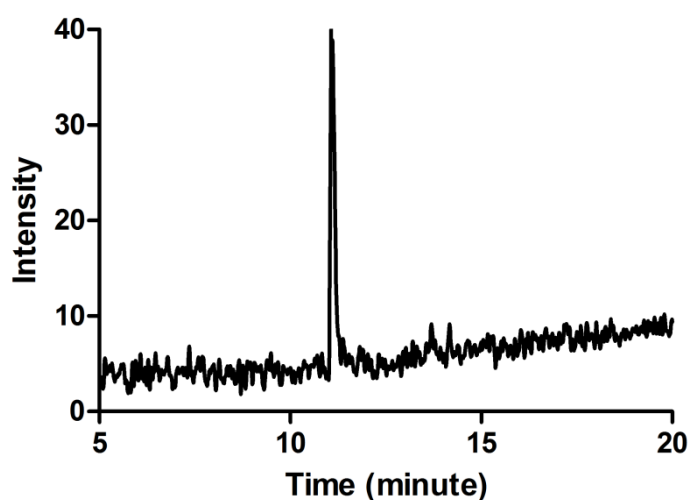
Figure 5.2 Liquid Chromatogram of Peptide Molecule (K-PA).
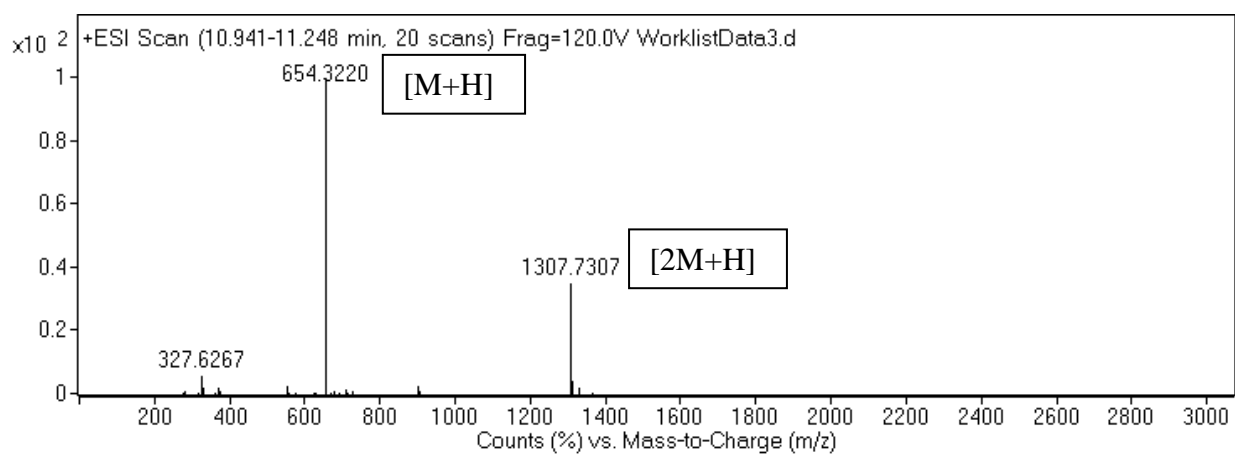
Figure 5.3 Mass spectrum of peptide molecule (K-PA).

A self-assembling peptide amphiphile molecule with a sequence of Lauryl-VVAGK-Am (K-PA, Figure 5.1) was synthesized by using solid-phase peptide synthesis [34] and characterized by liquid chromatography-mass spectrometry (Figure 5.2-5.3). Self-assembly of K- PA molecule was studied by circular dichroism (CD) spectroscopy. The K- PA molecules were dissolved in acidic medium (pH 2) and self-assembled due to hydrophobic collapse and hydrogen bonding. The CD spectrum (Figure 5.4a) exhibited a broad negative band at around 200 nm due to random coil structure of the K-PA molecules at acidic conditions caused by electrostatic repulsions among protonated amine groups. This band in the CD spectrum of K-PA (Figure 5.4a) is converted to a positive peak at 195 nm and a negative band at 220 nm upon raising the pH to 10. The observed change in the CD spectrum upon charge neutralization indicated the transformation of random structure to highly ordered β-sheets [34].
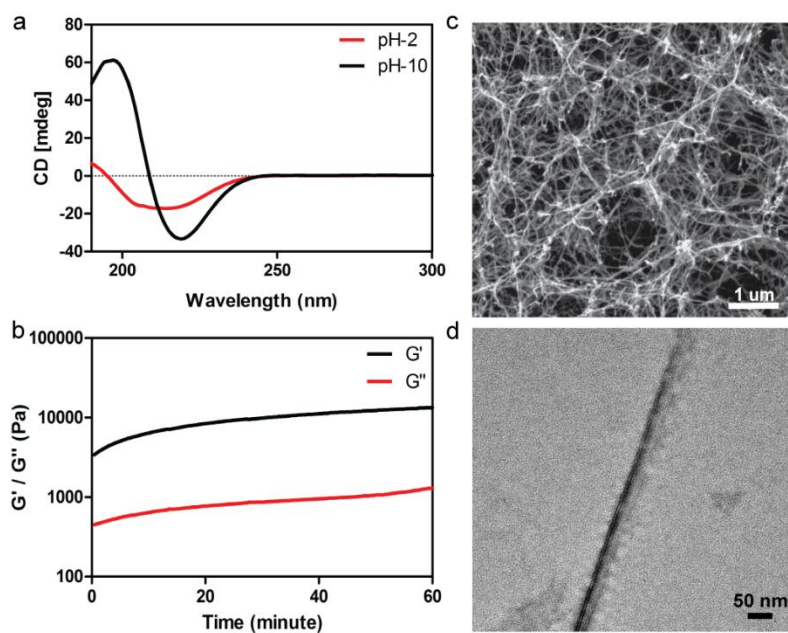
Figure 5.4 CD spectra of K-PA in acidic (pH 2) and basic medium (pH 10) (a), rheological analysis of K- PA gel (b), SEM image of peptide 3D aerogel (c) and TEM image of peptide nanofibers.

As intrinsic characteristic of self-assembling peptide amphiphile molecules, they can encapsulate large amount of water forming hydrogel. A solution of 1 wt % K-PA was converted to a self-supporting hydrogel with a storage modulus (G′) of 13 kPa and loss modulus (G″) of 1.3 kPa as measured by an oscillatory rheometer (Figure 5.4b). The K-PA gel with a damping factor (G″/G′) of 0.01 showed dominantly elastic over viscous character [92]. Scanning electron microscope (SEM) image of critically dried K-PA aerogel revealed a 3D network of high-aspect-ratio 1D peptide nanofibers (Figure 5.4c) with length in microns and diameter of *ca*.10 nm (Figure 5.4d) as shown by transmission electron microscope (TEM). Utilization of 3D peptide aerogels as sacrificial template to synthesize 3D metal and metal oxide aerogels offer many advantages such as tuning of porosity and surface area by simply playing with concentration of peptide gel. The 3D peptide aerogel was used as sacrificial organic template to deposit titania by atomic layer deposition (ALD). Titania is a cheap, nontoxic, and chemically stable metal oxide, which is widely used as a support for various types of catalytic nanoparticles [163]. Deposition of 150 cycles of titania at 150 ^{o}C was optimized to grow uniform ultrathin film having 6 ± 1 nm thickness (Figure 5.5a-b and Figure 5.6). Deposition of TiO_2 at ambient temperature is extremely crucial for preserving the skeletal structure of 3D peptide aerogel (Figure 5.6a). As-prepared 3D TiO_2 nanonetwork is amorphous as demonstrated by powder XRD pattern (Figure 5.5c) and has a surface area of 45 m^2/g as estimated from the Brunauer–Emmett–Teller (BET) analysis (Figure 5.5d). Interestingly, the ALD not only provides highly conformal, uniform, and controlled deposition of metals and metal oxides, but also allows low-temperature growth of these nanomaterials, which makes it attractive for thermally sensitive substrates such as soft organic templates.
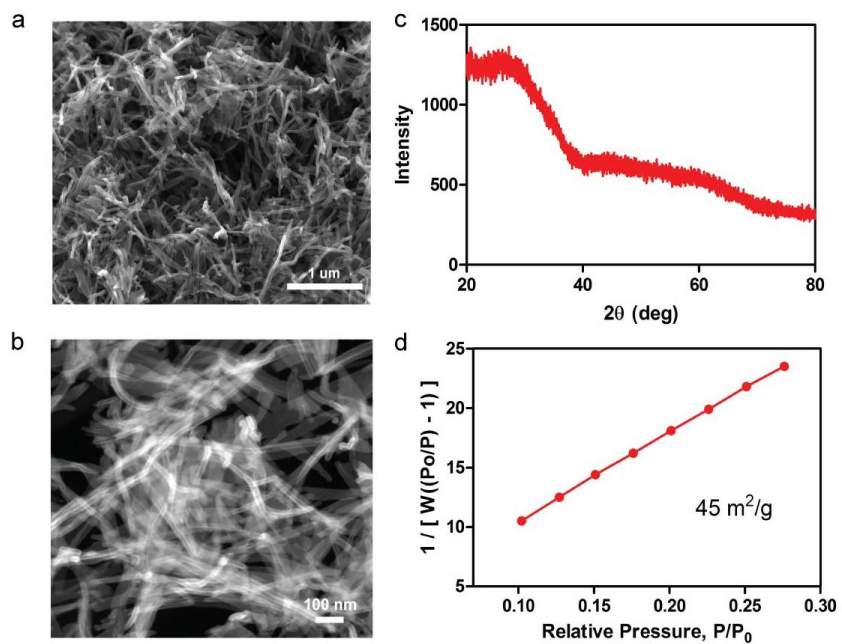
Figure 5.5 SEM (a) and STEM (b) images of 3D TiO$_2$ nanonetwork. Powder XRD pattern (c), and BET analysis (d) of 3D TiO$_2$ nanonetwork.
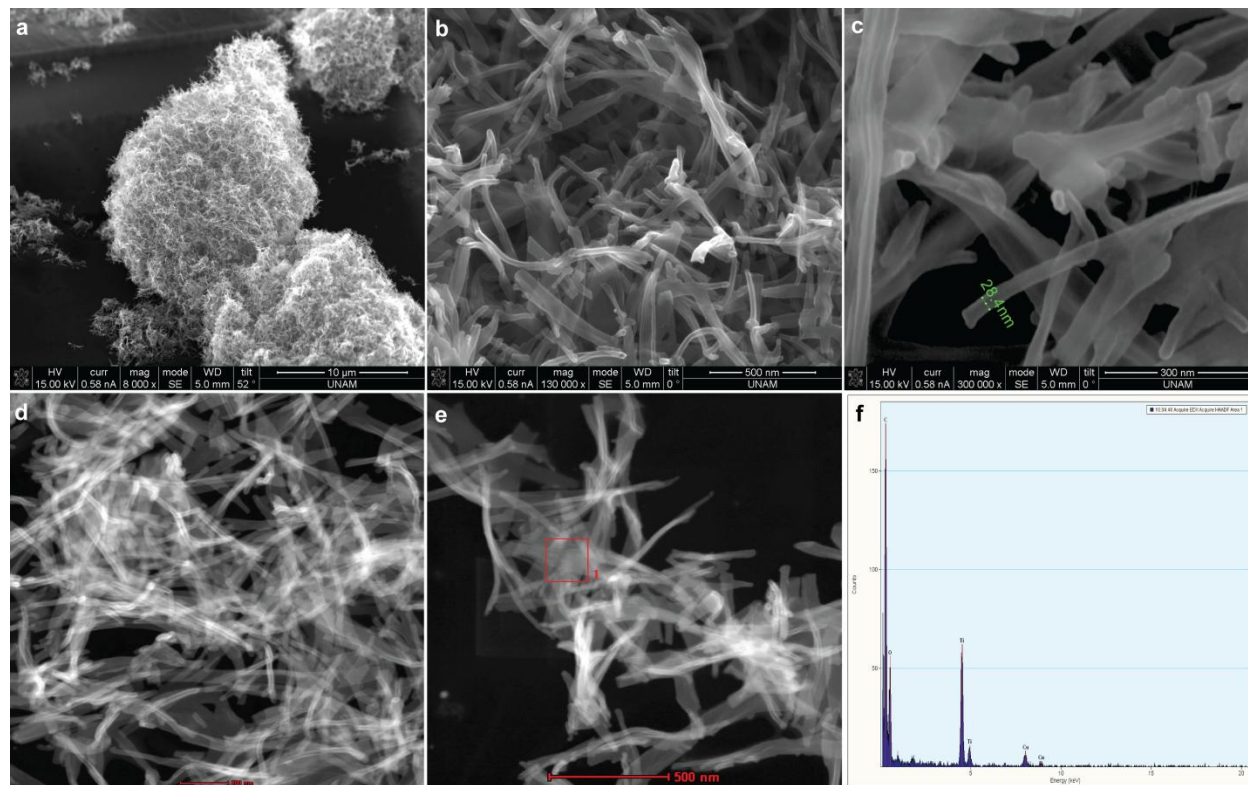
Figure 5.6 SEM images (a-c), STEM images (d-e) and EDS (f) of 3D TiO$_2$ nanonetwork.

We utilized MeCpPtMe$_3$ as Pt precursor and O$_3$ as reactant gas to grow Pt nanoparticles with precise sizes on as-synthesized 3D TiO$_2$ nanonetwork (Figure 5.7). We deposited Pt with different cycles to produce 3D nanonetworks containing Pt nanoparticles (Pt5@ TiO$_2$-Pt30@ TiO$_2$) in a controlled size ranging from 0.8 to 2.8 nm (Table 5.1 and Figure 5.7a- l). Histograms in Figure 5.7 show very narrow range of nanoparticle size distribution. A linear increase of nanoparticle size was observed with increasing number of Pt cycles (Figure 5.7m). Likewise, Pt loading linearly increased from 2.2% to 16% as number of Pt cycles was increased from 5 to 30 (Figure 5.7n). The highly uniform deposition and presence of Pt nanoparticles on 3D TiO$_2$ nanonetwork were confirmed by STEM images and energy dispersive spectrometry (EDS), respectively (Figure 5.8).
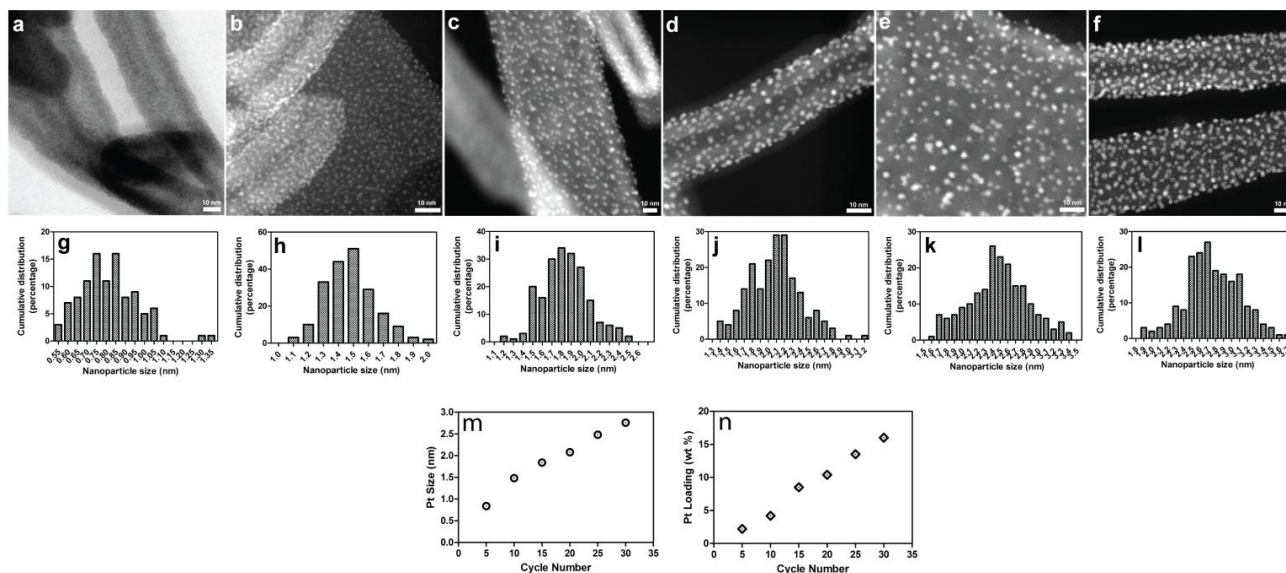
Figure 5.7 STEM images and size distribution of Pt5@TiO$_2$ (a, g), Pt10@TiO$_2$ (b, h) Pt15@TiO$_2$ (c, i), Pt20@TiO$_2$ (d, j), Pt25@TiO$_2$ (e, k) and Pt30@TiO$_2$ (f, l). Effect of Pt cycle on Pt nanoparticle size (m) and Pt loading (n). Histograms of particle size distribution were constructed by counting 100 nanoparticles for 5 cycle and 200 nanoparticles for the rest of cycles.
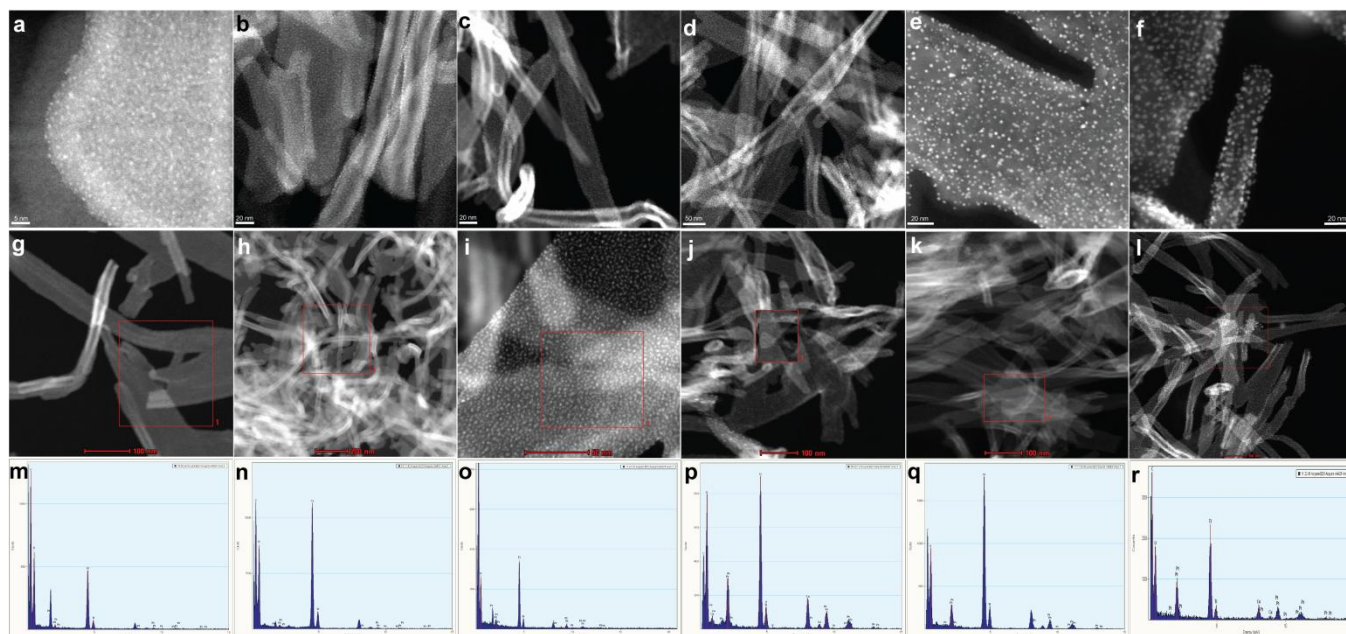
Figure 5.8 STEM images and EDS of Pt5@TiO$_2$ (a, g and m), Pt10@TiO$_2$ (b, j and n), Pt15@TiO$_2$ (c, i and o), Pt20@TiO$_2$ (d, j and p), Pt25@TiO$_2$ (e, k and q) and Pt30@TiO$_2$ (f, l and r).
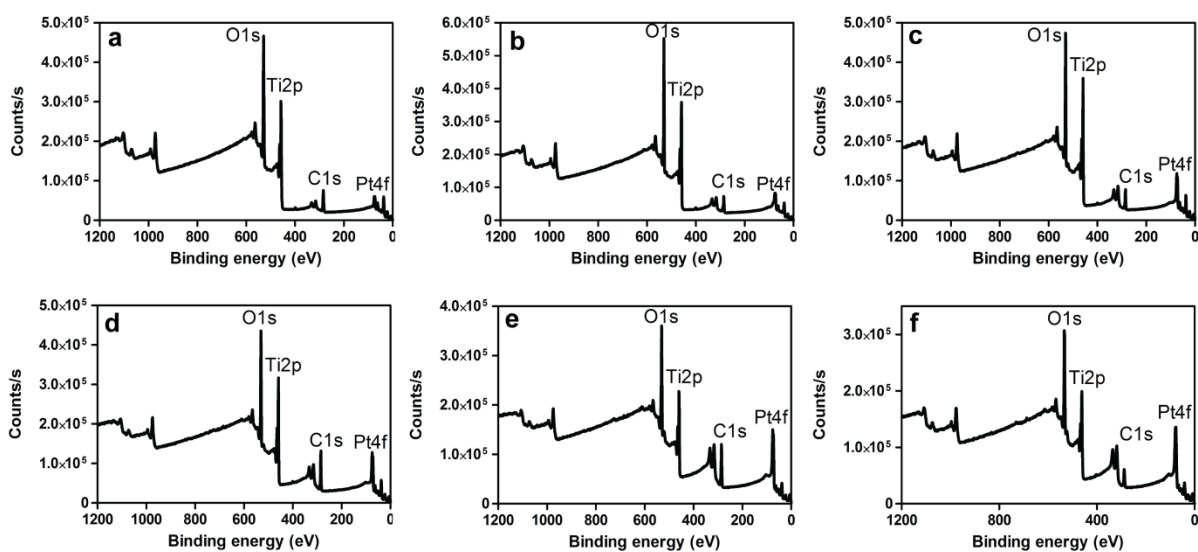
Figure 5.9 XPS analysis of (a) Pt5@TiO$_2$, (b) Pt10@TiO$_2$, (c) Pt15@TiO$_2$, (d) Pt20@TiO$_2$, (e) Pt25@TiO$_2$ and Pt30@TiO$_2$.

We performed X-ray photoelectron spectroscopy *(XPS)* to analyze elemental composition of our nanocatalysts (Figure 5.9). The peaks at 530, 400 and 285 eV, arising from peptide template, confirmed the presence of oxygen, nitrogen and carbon, respectively. The signal at 458 eV is caused by TiO_2 [158] while peak at 73 eV showed presence of Pt species. We further conducted high-resolution XPS to analyze the electronic states of Pt species (Figure 5.10). Deconvolution of Pt 4f bands reveals the existence of Pt(0), Pt(II) and Pt(IV) species (Figure 5.10) [164, 165].
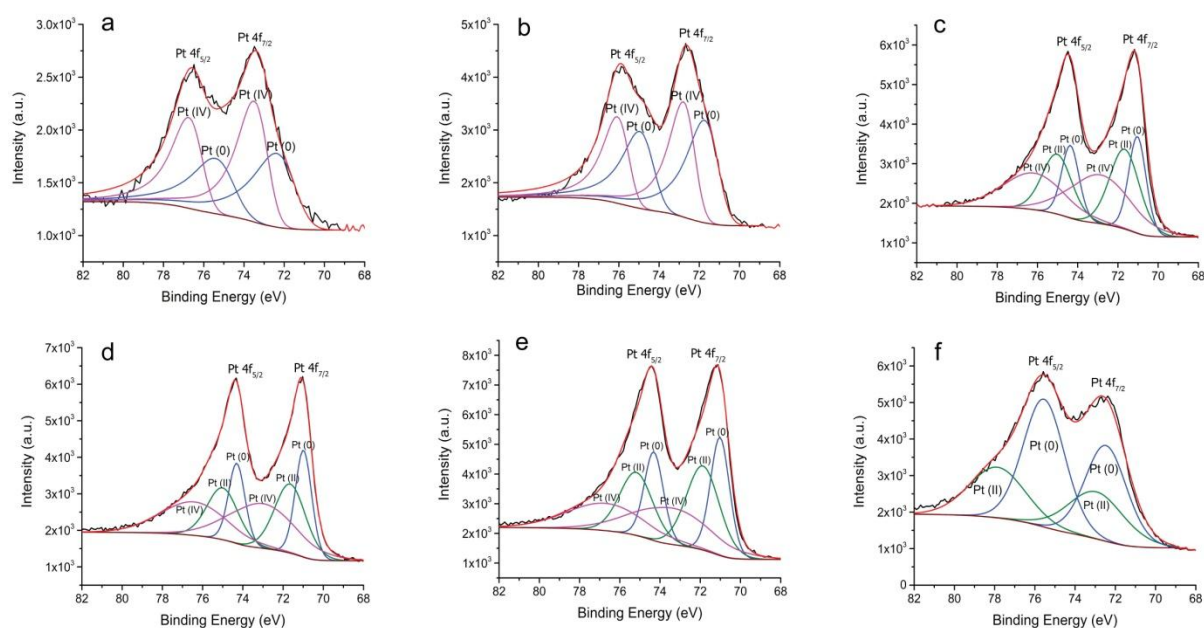
Catalyst	Envelope Curve (%)	Pt (IV)			Pt (II)			Pt (0)			Pt 4f$_{5/2}$			Pt 4f$_{7/2}$		
		Higher eV	Lower eV	Total	Higher eV	Lower eV	Total	Higher eV	Lower eV	Total	Pt(IV)	Pt(II)	Pt(0)	Pt(IV)	Pt(II)	Pt(0)
Pt5@TiO$_2$	100.00%	23.46%	31.30%	54.76%				19.38%	25.86%	45.24%	76.78 eV		75.48 eV	73.48 eV		72.38 eV
Pt10@TiO$_2$	100.00%	20.74%	27.67%	48.41%				22.10%	29.49%	51.59%	76.14 eV		75.04 eV	72.84 eV		71.84 eV
Pt15@TiO$_2$	99.99%	18.15%	24.22%	42.37%	14.47%	19.31%	33.78%	10.21%	13.63%	23.84%	76.28 eV	75.08 eV	74.38 eV	72.98 eV	71.68 eV	71.08 eV
Pt20@TiO$_2$	100.00%	18.46%	24.63%	43.09%	13.41%	17.89%	31.30%	10.97%	14.64%	25.61%	76.53 eV	75.03 eV	74.33 eV	73.13 eV	71.73 eV	71.03 eV
Pt25@TiO$_2$	100.00%	15.40%	20.55%	35.95%	15.19%	20.27%	35.46%	12.25%	16.34%	28.59%	76.82 eV	75.22 eV	74.32 eV	73.32 eV	71.92 eV	71.02 eV
Pt30@TiO$_2$	100.00%	17.88%	19.23%	37.11%				26.95%	35.94%	62.89%	77.88 eV		75.58 eV	73.08 eV		72.48 eV

*envelope curve = red colored curve

Figure 5.10 High resolution XPS and deconvolution analysis of (a) Pt5@TiO$_2$, (b) Pt10@TiO$_2$, (c) Pt15@TiO$_2$, (d) Pt20@TiO$_2$, (e) Pt25@TiO$_2$ and (f) Pt30@TiO$_2$. Table shows summary of deconvolution analysis of Pt.

The powder XRD pattern of Pt5@TiO$_2$ and Pt10@TiO$_2$ showed amorphous structures and no detectable Pt diffraction peaks (Figure 5.11). Uniform spreading, low loading, and small size of Pt nanoparticles could be the reason for undetectable Pt signals in XRD. Interestingly, amorphous titania was converted to anatase (A) and rutile (R) crystal structures as the number of Pt cycle was switched from 10 to 15 and above (Figure 5.11). Pt (0) nanoparticles are formed from combustion reaction of Pt precursor ligands in the presence of O$_3$. During combustion reaction, heat given out could have caused local crystallization of TiO$_2$. The 3D nanonetworks (Pt15@ TiO$_2$- Pt30@ TiO$_2$) demonstrated a broad diffraction pattern between 38°-40°. Pt (111) resonates at 39.76^o and could have been overlapped with crystal plane of TiO$_2$ (004) and (112) [166].
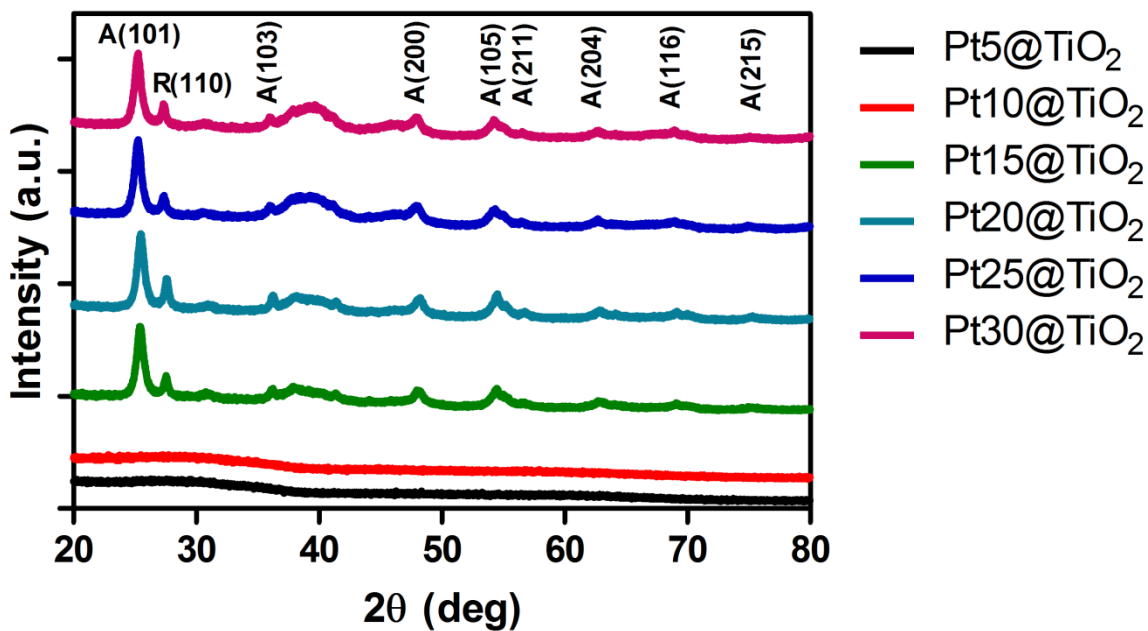
Figure 5.11 XRD of 3D Pt@TiO$_2$ nanonetworks.

Catalytic activity is highly dependent on crystal plane of the nanoparticles, therefore, we further conducted high-resolution transmission electron microscopy (HRTEM) to acquire crystal plane of Pt (Figure 1d and Figure S12). The distance between two adjacent lattice fringes is about 0.23 nm, which is attributed to (111) crystal plane of fcc Pt [167]. Pt (111) is the dominant catalytic active surface for hydrolysis of ammonia borane [168]. Highly ordered crystal patterns were also observed for TiO_2 (Figure 5.12) which is consistent with XRD data.
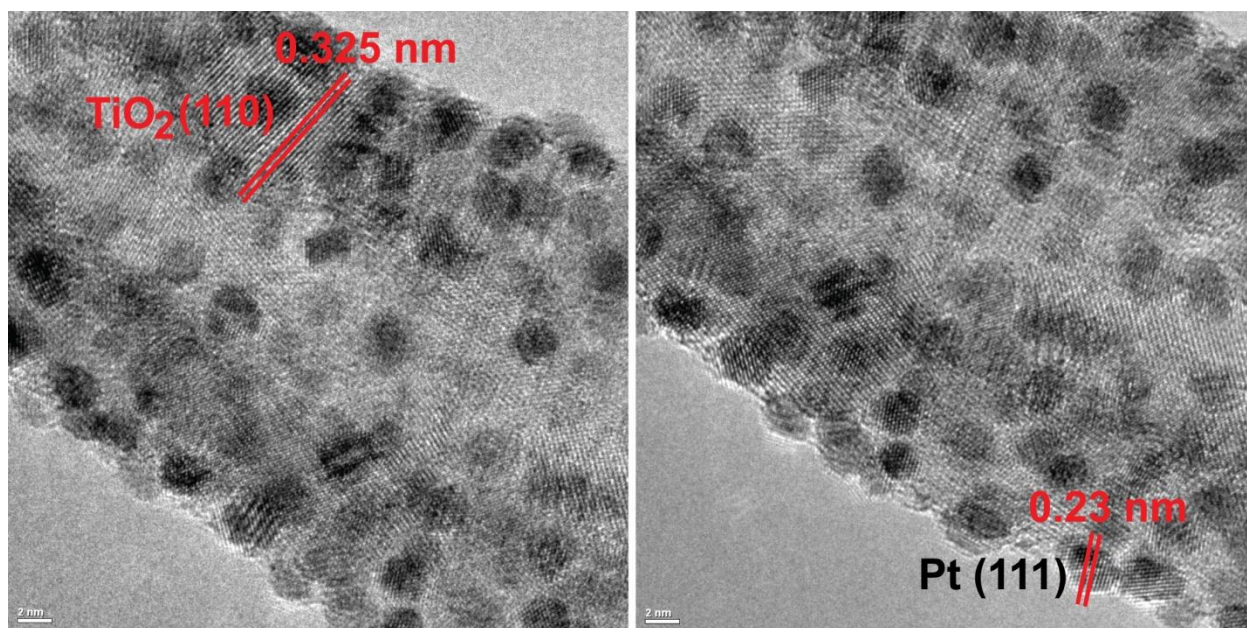
Figure 5. 12 HRTEM of 3D Pt@TiO_2 nanonetwork.

To study the catalytic activity of 3D Pt@TiO_2 nanonetworks, we used hydrolytic dehydrogenation of ammonia borane. Hydrolysis (Eq. 1) is the most efficient way of releasing hydrogen from AB mainly due to favorable kinetics under mild conditions.[169, 170]

$$H_3NBH_3(aq) + 2H_2O(l) \rightarrow NH_4^+(aq) + BO_2^-(aq) + 3H_2(g) \quad (1)$$
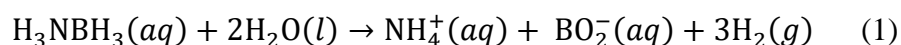
Since the reaction is required to be catalyzed at an appreciable rate at ambient temperature, developing efficient and stable catalysts for hydrogen generation from AB is a challenge for fuel cell applications. Although various supported transition metal nanoparticles have been tested for H_2 generation from the hydrolysis of ammonia borane[171], Pt has been shown to be the superior catalyst.[168, 172] However, high price and low abundance of Pt in the Earth Crust limit its catalytic application. Therefore, synthesis of Pt nanoparticles with controlled size and desired crystal lattice plane is of importance for reducing the cost by efficient use of Pt catalyst. Moreover, uniform deposition of Pt nanoparticles on high-surface-area 3D nanonetwork support can further boost reaction kinetics by allowing rapid diffusion of reactants through 3D support, which possibly will improve substrate-catalyst interactions. Therefore, 3D Pt@TiO$_2$ nanonetwork can be an efficient catalyst to generate H_2 from AB.
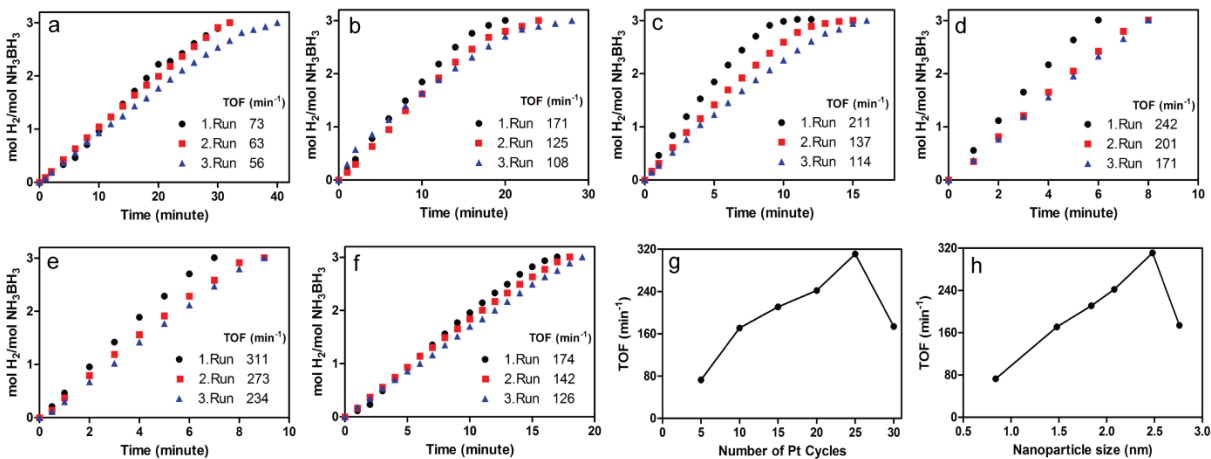
Figure 5.13 Turnover frequencies of (a) Pt5@TiO$_2$, (b) Pt10@TiO$_2$, (c) Pt15@TiO$_2$, (d) Pt20@TiO$_2$, (e) Pt25@TiO$_2$ and (f) Pt30@TiO$_2$. Effect of Pt cycle (g) and Pt nanoparticle size (h) on TOF.

The 3D TiO$_2$ nanonetwork is shown to be inactive in H$_2$ generation from the hydrolysis of AB at room temperature. However, the 3D Pt@TiO$_2$ nanonetworks are found to be highly active in the hydrolysis of AB generating 3.0 equivalents of H$_2$ per mole of AB under the same conditions. The 3D Pt@TiO$_2$ nanonetworks with different particle size and Pt loading were fabricated by varying the number of ALD cycles and tested in H$_2$ generation from the hydrolysis of AB. Figure 5.13 shows the plots of time dependent H$_2$ production per mole of catalyzed by 3D Pt@TiO$_2$ nanonetwork with varying metal loading at 25.0 ± 0.1 °C. In all cases, H$_2$ evolution starts immediately without induction period, a consequence of using preformed catalyst, and continues almost linearly until the consumption of all of the AB present in the solution. The turnover frequency (TOF), calculated from the hydrogen generation rate in the linear portion of each plot, shows variation with the number of ALD cycles (Figure 5.13g and Table 7) and with the size of Pt nanoparticles (Figure 5.13h and Table 7).

Table 7 Characteristics of 3D Pt@TiO$_2$ nanonetworks and their turnover frequency (TOF, min^{-1}) in hydrolysis of AB at 25.0 ± 0.1 °C.

Catalyst	ALD Pt cycle[a]	Pt loading[b]	Particle size[c]	Binding Energy of Pt(0) Pt4f$_{7/2}$	[Pt][d]	TOF$_{app}$ (min^{-1})		
		(%wt)	(nm)	(eV)	mM	1. cycle	2. cycle	3.cycle
Pt5@TiO$_2$	5	2.20	0.8± 0.15	72.38	0.178	73	63	56
Pt10@TiO$_2$	10	4.20	1.5± 0.17	71.84	0.164	171	125	108
Pt15@TiO$_2$	15	8.50	1.8± 0.25	71.08	0.218	211	137	114
Pt20@TiO$_2$	20	10.4	2.1± 0.32	71.03	0.231	242	201	171
Pt25@TiO$_2$	25	13.5	2.4± 0.40	71.02	0.159	311	273	234
Pt30@TiO$_2$	30	16.0	2.8± 0.34	72.48	0.147	174	142	126

[a] Number of Pt cycle in ALD. [b] Pt loading determined by ICP-MS. [c] Determined by TEM, which was taken from the catalyst before catalytic activity test. [d] Pt concentrations during catalysis.

The volcano curve of activity versus the Pt particle size suggests that the (111) facets of Pt@TiO$_2$ nanocatalyst are dominating active sites with some contribution from (100) facets

[168]. The increase in the catalytic activity of 3D Pt@TiO$_2$ nanocatalyst with the number of ALD cycles up to 25 correlates well with the decrease in the Pt4f$_{7/2}$ binding energy (Table 7 and Figure 5.10). As the number of ALD cycles increases the Pt(0) 4f$_{7/2}$ bands shift to the lower energy values, which indicates higher electron transfer from the surface oxygen to Pt [173]. It is conceivable that the electron transfer increases with increasing surface interaction of Pt nanoparticles and oxide surface of titania as nanoparticles become larger. Note that the crystallinity of titania surface also increases with the increasing number of ALD cycles, which might be induced by the same surface interaction. The Pt25@TiO$_2$ nanocatalyst with 25 Pt ALD cycle (2.4 nm Pt nanoparticle size and 13.5% Pt loading) provides the highest catalytic activity, with a TOF value of 311 min^{-1} in H$_2$ generation from the hydrolysis of AB at 25.0 ± 0.1 ℃ (Table 7, Fig. 5.13e). TOF values of the reported Pt catalysts used in the hydrolysis of AB are listed in Table 8 for comparison. More clearly seen from the TOF values, Pt25@TiO2 (311 min-1) has approximately 3 times greater catalytic activity than that of commercial Pt/C catalyst (111 min^{-1}). In addition, Pt25@TiO$_2$ shows higher catalytic activity than most of the Pt-based catalysts such as Pt/ɤ-Al$_2$O$_3$, Pt/CeO$_2$, Ni$_{0.33}$@Pt$_{0.67}$/C,Co$_{0.32}$Pt$_{0.68}$/C, Pt cube/CeO$_2$/RGO, Pt/SiO$_2$ and PtRu/C (Table 8). However, the catalytic activity of Pt25@TiO$_2$ is slightly lower than that of Pt/CNTs-O-HT and Pt@MIL-101. The lower catalytic activity of Pt25@TiO$_2$ compared to Pt/CNTs-O-HT and Pt@MIL-101 may be attributed to the lower surface area of 3D titania nanonetwork (45 m^2/g) as compared to that of carbon nanotube (221 m^2/g) and metal organic frame work (5900 m^2/g). Durability of 3D Pt@TiO$_2$ nanocatalysts was tested by recycling experiment (Table 7); when AB is completely hydrolyzed, another batch of AB is added for the next run of hydrolysis. Pt25@TiO$_2$ nanocatalyst retains at least 87% of its initial activity in the second cycle and 75% in the third cycle (Table 7). The decrease in the catalytic activity can be

attributed to the agglomeration of Pt nanoparticles as shown by STEM images taken after recycling experiments (Figure 5.14) and to the deactivation effect of the hydrolysis product metaborate, which accumulates during the hydrolysis. We further analyzed and compared the electronic properties of the fresh catalyst with the recycled one (Figure 5.15).

Table 8 Turnover frequency value (TOF) of the platinum catalysts reported for the hydrolysis of AB at $25.0 \pm 0.1\,°C$.

Catalyst	mol_{metal}/mol_{AB}	TOF (mol H_2/(mol Pt×min)	
Pt/CNTs-O-HT	0.0047	468	
Pt@MIL-101	0.0029	414	
Pt25@TiO$_2$	**0.0016**	**311**	**This study**
Pt/ɤ-Al$_2$O$_3$	0.018	222	
Pt/CeO$_2$	0.018	182	
Pt/C	0.018	111	
Ni$_{0.33}$@Pt$_{0.67}$/C	0.018	81	
Co$_{0.32}$Pt$_{0.68}$/C	0.038	67	
Pt cube/CeO$_2$/RGO	0.0025	48	
Pt/SiO2 (2 wt%)	0.018	33	
PtO$_2$	0.018	21	
Pt black	0.018	14	
K$_2$PtCl$_4$	0.018	9	
PtRu/C	0.03	8	

The fresh Pt25@TiO$_2$ catalyst contains 23.59% Pt(0) specie while the deactivated catalyst contains 12.68% Pt(0). The drastic decrease in Pt(0) content is another reason for the decrease in catalytic activity of catalyst after recycling. Previous studies have shown that agglomeration /sintering of nanoparticles can be efficiently prevented by atomic layer deposition technique. Deposition of thin layers of Al$_2$O$_3$ on supported Pd nanoparticles [174] and thin layers of TiO$_2$ on supported Co nanoparticles [175] prevented sintering, therefore, improved life-time of nanocatalysts to great extent. This is another striking advantage of the ALD. We further measured the leaching of Pt nanoparticles from 3D Pt@TiO$_2$ nanonetwork after third use. The ICP-MS results demonstrated that Pt leached less than 0.1%, which confirmed strong anchoring of Pt nanoparticles on 3D TiO$_2$ nanonetworks.
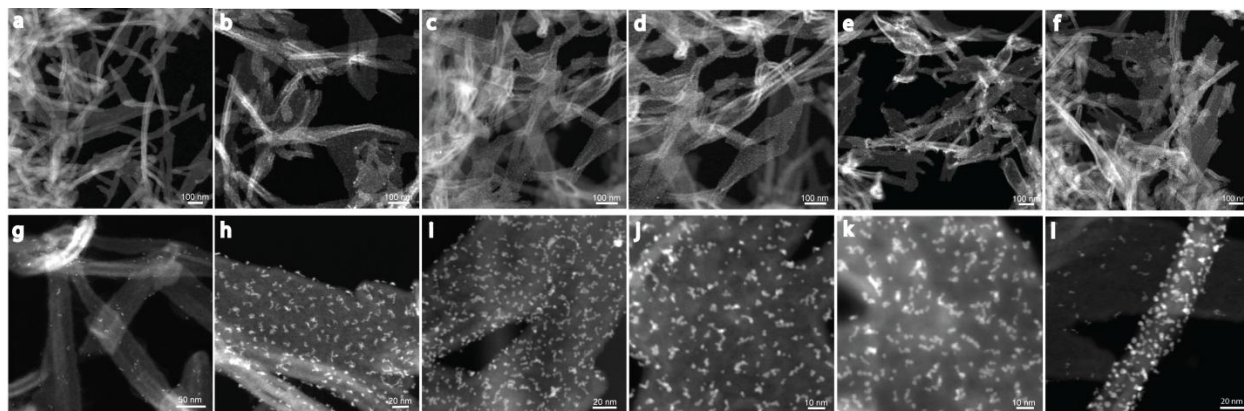
Figure 5.14 STEM images of (a, g) Pt5@TiO$_2$, (b, h) Pt10@TiO$_2$ (c, i), Pt15@TiO$_2$ (d, j), Pt20@TiO$_2$ (e, k) Pt25@TiO$_2$ and (f, l) Pt30@TiO$_2$ after recycling.

Catalyst	Pt(IV)	Pt(II)	Pt(0)
Fresh Pt25@TiO$_2$	36.355%	40.07%	23.59%
Deactivated Pt25@TiO$_2$	34.35%	52.96%	12.68%
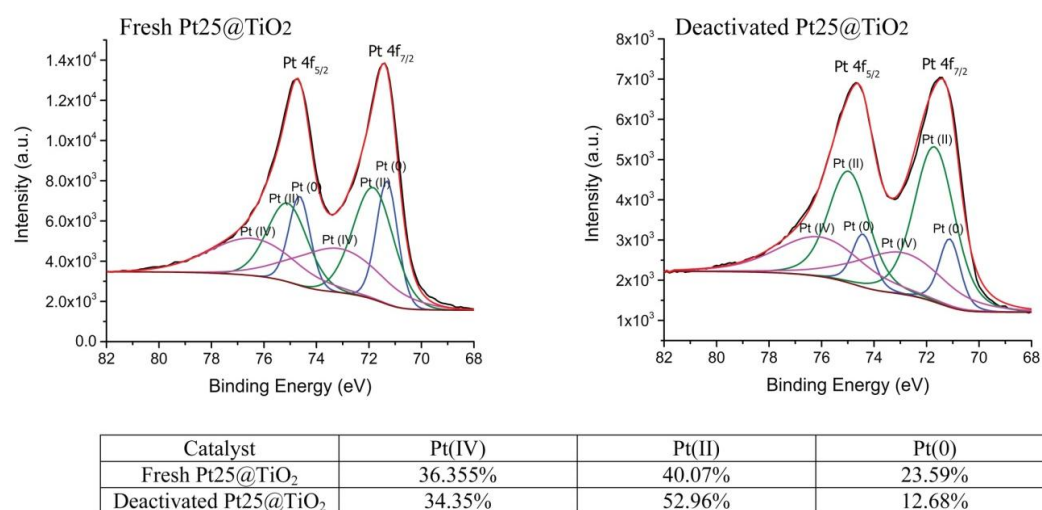
Figure 5.15 High resolution XPS and deconvolution analysis of fresh and deactivated Pt25@TiO$_2$.

5.4 Conclusion

In summary, we exploited self-assembled peptide nanofiber 3D aerogel as a template to fabricate highly uniform, conformal, and porous 3D TiO$_2$ nanonetworks. The 3D TiO$_2$ nanonetworks were further decorated by Pt nanoparticles with controlled and precise size using ozone-assisted ALD technique. Pt particle size and loadings were tuned by altering the number of Pt ALD cycles. The Pt25@TiO$_2$ with ~2.4 nm particle size showed superior catalytic activity in H$_2$ generation from AB with a TOF value of 311 min^{-1} at room temperature. Moreover, Pt leaching was fairly low from 3D Pt@TiO$_2$ nanonetworks. Combination of supramolecular peptide nanofiber 3D templates with ALD technique allows facile, straightforward and highly reproducible preparation of metal, metal oxide, and semiconductor 3D nanomaterials as next generation nanocatalysts with light weight, high-surface-area and porosity.

Chapter 6

Conclusion and Future Prospects

Supramolecular chemistry is a powerful tool to fabricate innovative materials which could satisfy the need of next generation devices and industries. In last decade, short sequenced peptides have extensively been utilized to produce functional nanomaterials. In this thesis, I reviewed self-assembling peptide designs and recent novel applications of short self-assembled peptide nanostructures. Although self-assembled peptide nanostructures have promising applications in tissue engineering and biomedical applications, it's beyond scope of this dissertation.

In the first part of my dissertation, I designed and synthesized β-sheet forming p-type peptide-chromophore (pPC) and n-type peptide-chromophore (nPC) sequences. Positively charged pPC and negatively charged nPC molecules individually assemble into highly uniform p-type and n-type nanofibers, respectively, having diameters of 11±1 nm and microns in length as imaged by transmission electron microscopy. These complementary p-type and n-type nanofibers coassembled via hydrogen-bonding and electrostatic interactions to generate well-ordered supramolecular n/p-coassembled 1D nanowires. This facile strategy allows fabrication of well-defined supramolecular electroactive nanomaterials, which can find a variety of applications in optoelectronics, photovoltaics, bioelectronics and tissue engineering.

In second and third part, a metal biding short self-assembling peptide was designed and synthesized to fabricate Pd nanoparticles in highly environmental friendly conditions. These peptide-Pd hybrid nanostructures showed superior catalytic activity in Suzuki coupling reactions in aqueous media at ambient temperatures. Moreover, same supramolecular peptide nanofiber

was complexed with copper ions to produce a biocompatible and highly active 1D nanocatalyst. This supramolecular 1D nanocatalyst did not only show low cytotoxicity but also demonstrated enhanced catalytic activity in azide-alkyne cycloaddition reaction under physiological conditions.

In last part of my dissertation, we exploited supramolecular self-assembled peptide nanostructures as a 3D nanonetwork as organic template for a catalytic 3D Pt-TiO$_2$ nanonetwork fabrication. A 3D peptide nanofiber aerogel was conformally coated with TiO$_2$ by atomic layer deposition (ALD) with angstrom-level thickness precision. The 3D peptide-TiO$_2$ nanonetwork was further decorated with highly monodisperse Pt nanoparticles by using ozone-assisted ALD. The 3D TiO$_2$ nanonetwork decorated with Pt nanoparticles showed superior catalytic activity in hydrolysis of ammonia borane generating three equivalents of H$_2$. These low density, high porosity, and high surface area metal and metal oxide aerogels will receive considerable research interest.

Our research results and others clearly illustrate that bottom-up fabrication of novel and functional nanomaterials using self-assembled peptide nanostructures is quite straightforward but promising. Due to rich number of functional groups present in amino acids, there still is a large room to discover both bioinspired and synthetic short sequence peptide nanostructures. Innovative researches in short self-assembling peptides area will not only contribute to nanotechnology field but also will assist scientists to get insight into understanding complex structure and function of biomolecules, therefore, origin of life.

Bibliography

[1]   C. C. Koch, "Top-down Synthesis of Nanostructured Materials: Mechanical and Thermal Processing Methods," *Reviews on Advanced Materials Science,* vol. 5, pp. 91-99, Oct 2003.

[2]   R. Thiruvengadathan, V. Korampally, A. Ghosh, N. Chanda, K. Gangopadhyay, and S. Gangopadhyay, "Nanomaterial processing using self-assembly-bottom-up chemical and biological approaches," *Reports on Progress in Physics,* vol. 76, Jun 2013.

[3]   S. G. Zhang, "Fabrication of novel biomaterials through molecular self-assembly," *Nature Biotechnology,* vol. 21, pp. 1171-1178, Oct 2003.

[4]   X. B. Zhao, F. Pan, H. Xu, M. Yaseen, H. H. Shan, C. A. E. Hauser*, et al.*, "Molecular self-assembly and applications of designer peptide amphiphiles," *Chemical Society Reviews,* vol. 39, pp. 3480-3498, 2010.

[5]   M. A. Koussa, M. Sotomayor, and W. P. Wong, "Protocol for sortase-mediated construction of DNA-protein hybrids and functional nanostructures," *Methods,* vol. 67, pp. 134-141, May 15 2014.

[6]   N. Ashkenasy and J. Schneider, "Functional Peptide and Protein Nanostructures," *Israel Journal of Chemistry,* vol. 55, pp. 621-621, Jun 2015.

[7]   T. G. W. Edwardson, K. L. Lau, D. Bousmail, C. J. Serpell, and H. F. Sleiman, "Transfer of molecular recognition information from DNA nanostructures to gold nanoparticles," *Nature Chemistry,* vol. 8, pp. 162-170, Feb 2016.

[8]   M. Zelzer and R. V. Ulijn, "Next-generation peptide nanomaterials: molecular networks, interfaces and supramolecular functionality," *Chemical Society Reviews,* vol. 39, pp. 3351-3357, 2010.

[9]   R. V. Ulijn and A. M. Smith, "Designing peptide based nanomaterials," *Chemical Society Reviews,* vol. 37, pp. 664-675, 2008.

[10]   S. Scanlon and A. Aggeli, "Self-assembling peptide nanotubes," *Nano Today,* vol. 3, pp. 22-30, Jun-Aug 2008.

[11]   G. Cinar, H. Ceylan, M. Urel, T. S. Erkal, E. D. Tekin, A. B. Tekinay*, et al.*, "Amyloid inspired self-assembled peptide nanofibers," *Abstracts of Papers of the American Chemical Society,* vol. 246, Sep 8 2013.

[12]   M. Amit, G. Cheng, I. W. Hamley, and N. Ashkenasy, "Conductance of amyloid beta based peptide filaments: structure-function relations," *Soft Matter,* vol. 8, pp. 8690-8696, 2012.

[13]   Q. Li, Y. Jia, L. R. Dai, Y. Yang, and J. B. Li, "Controlled Rod Nanostructured Assembly of Diphenylalanine and Their Optical Waveguide Properties," *Acs Nano,* vol. 9, pp. 2689-2695, Mar 2015.

[14]   S. Marchesan, A. V. Vargiu, and K. E. Styan, "The Phe-Phe Motif for Peptide Self-Assembly in Nanomedicine," *Molecules,* vol. 20, pp. 19775-19788, Nov 2015.

[15]   H. Shao, J. Seifert, N. C. Romano, M. Gao, J. J. Helmus, C. P. Jaroniec*, et al.*, "Amphiphilic Self-Assembly of an n-Type Nanotube," *Angewandte Chemie-International Edition,* vol. 49, pp. 7688-7691, 2010.

[16]   D. T. Bong, T. D. Clark, J. R. Granja, and M. R. Ghadiri, "Self-assembling organic nanotubes," *Angewandte Chemie-International Edition,* vol. 40, pp. 988-1011, 2001.

[17]   N. Ashkenasy, W. S. Horne, and M. R. Ghadiri, "Design of self-assembling peptide nanotubes with delocalized electronic states," *Small,* vol. 2, pp. 99-102, Jan 2006.

[18]   M. S. Ekiz, G. Cinar, M. A. Khalily, and M. O. Guler, "Self-assembled peptide nanostructures for functional materials," *Nanotechnology,* vol. 27, p. 402002, Oct 7 2016.

[19]   X. Zhao, F. Pan, H. Xu, M. Yaseen, H. Shan, C. A. Hauser*, et al.*, "Molecular self-assembly and applications of designer peptide amphiphiles," *Chem Soc Rev,* vol. 39, pp. 3480-98, Sep 2010.

[20]   J. Kopecek and J. Yang, "Smart self-assembled hybrid hydrogel biomaterials," *Angew Chem Int Ed Engl,* vol. 51, pp. 7396-417, Jul 23 2012.

[21]   R. B. Merrifield, "Solid-Phase Peptide Synthesis. 3. An Improved Synthesis of Bradykinin," *Biochemistry,* vol. 3, pp. 1385-90, Sep 1964.

[22]   M. J. Wiester, P. A. Ulmann, and C. A. Mirkin, "Enzyme Mimics Based Upon Supramolecular Coordination Chemistry," *Angewandte Chemie-International Edition,* vol. 50, pp. 114-137, 2011.

[23]   M. O. Guler and S. I. Stupp, "A self-assembled nanofiber catalyst for ester hydrolysis," *Journal of the American Chemical Society,* vol. 129, pp. 12082-+, Oct 10 2007.

[24]   N. Singh, M. Tena-Solsona, J. F. Miravet, and B. Escuder, "Towards Supramolecular Catalysis with Small Self-assembled Peptides," *Israel Journal of Chemistry,* vol. 55, pp. 711-723, Jun 2015.

[25]   D. Enders, M. R. M. Huttl, C. Grondal, and G. Raabe, "Control of four stereocentres in a triple cascade organocatalytic reaction," *Nature,* vol. 441, pp. 861-863, Jun 15 2006.

[26]   F. Rodriguez-Llansola, B. Escuder, and J. F. Miravet, "Remarkable increase in basicity associated with supramolecular gelation," *Organic & Biomolecular Chemistry,* vol. 7, pp. 3091-3094, 2009.

[27]   F. Rodriguez-Llansola, B. Escuder, and J. F. Miravet, "Switchable Perfomance of an L-Proline-Derived Basic Catalyst Controlled by Supramolecular Gelation," *Journal of the American Chemical Society,* vol. 131, pp. 11478-11484, Aug 19 2009.

[28]   F. Rodriguez-Llansola, J. F. Miravet, and B. Escuder, "A supramolecular hydrogel as a reusable heterogeneous catalyst for the direct aldol reaction," *Chemical Communications,* pp. 7303-7305, 2009.

[29]   Z. P. Huang, S. W. Guan, Y. G. Wang, G. N. Shi, L. N. Cao, Y. Z. Gao*, et al.*, "Self-assembly of amphiphilic peptides into bio-functionalized nanotubes: a novel hydrolase model," *Journal of Materials Chemistry B,* vol. 1, pp. 2297-2304, 2013.

[30]   C. Q. Zhang, X. D. Xue, Q. Luo, Y. W. Li, K. N. Yang, X. X. Zhuang*, et al.*, "Self-Assembled Peptide Nanofibers Designed as Biological Enzymes for Catalyzing Ester Hydrolysis," *Acs Nano,* vol. 8, pp. 11715-11723, Nov 2014.

[31]   F. T. Yu, V. M. Cangelosi, M. L. Zastrow, M. Tegoni, J. S. Plegaria, A. G. Tebo*, et al.*, "Protein Design: Toward Functional Metalloenzymes," *Chemical Reviews,* vol. 114, pp. 3495-3578, Apr 9 2014.

[32]   Q. X. Jin, L. Zhang, H. Cao, T. Y. Wang, X. F. Zhu, J. Jiang*, et al.*, "Self-Assembly of Copper(II) Ion-Mediated Nanotube and Its Supramolecular Chiral Catalytic Behavior," *Langmuir,* vol. 27, pp. 13847-13853, Nov 15 2011.

[33]   C. M. Rufo, Y. S. Moroz, O. V. Moroz, J. Stohr, T. A. Smith, X. Z. Hu*, et al.*, "Short peptides self-assemble to produce catalytic amyloids," *Nature Chemistry,* vol. 6, pp. 303-309, Apr 2014.

[34] M. A. Khalily, G. Gulseren, A. B. Tekinay, and M. O. Guler, "Biocompatible Supramolecular Catalytic One-Dimensional Nanofibers for Efficient Labeling of Live Cells," *Bioconjugate Chemistry,* vol. 26, pp. 2371-2375, Dec 2015.

[35] A. P. H. J. Schenning and E. W. Meijer, "Supramolecular electronics; nanowires from self-assembled pi-conjugated systems," *Chemical Communications,* pp. 3245-3258, 2005.

[36] J. D. Tovar, "Supramolecular Construction of Optoelectronic Biomaterials," *Accounts of Chemical Research,* vol. 46, pp. 1527-1537, Jul 16 2013.

[37] S. Kim, J. H. Kim, J. S. Lee, and C. B. Park, "Beta-Sheet-Forming, Self-Assembled Peptide Nanomaterials towards Optical, Energy, and Healthcare Applications," *Small,* vol. 11, pp. 3623-3640, Aug 12 2015.

[38] C. A. E. Hauser, S. Maurer-Stroh, and I. C. Martins, "Amyloid-based nanosensors and nanodevices," *Chemical Society Reviews,* vol. 43, pp. 5326-5345, Aug 7 2014.

[39] H. Shao, T. Nguyen, N. C. Romano, D. A. Modarelli, and J. R. Parquette, "Self-Assembly of 1-D n-Type Nanostructures Based on Naphthalene Diimide-Appended Dipeptides," *Journal of the American Chemical Society,* vol. 131, pp. 16374-+, Nov 18 2009.

[40] H. A. M. Ardona, K. Besar, M. Togninalli, H. E. Katz, and J. D. Tovar, "Sequence-dependent mechanical, photophysical and electrical properties of pi-conjugated peptide hydrogelators," *Journal of Materials Chemistry C,* vol. 3, pp. 6505-6514, 2015.

[41] S. R. Diegelmann, J. M. Gorham, and J. D. Tovar, "One-dimensional optoelectronic nanostructures derived from the aqueous self-assembly of pi-conjugated oligopeptides," *Journal of the American Chemical Society,* vol. 130, pp. 13840-13841, Oct 22 2008.

[42]   S. R. Diegelmann, N. Hartman, N. Markovic, and J. D. Tovar, "Synthesis and Alignment of Discrete Polydiacetylene-Peptide Nanostructures," *Journal of the American Chemical Society,* vol. 134, pp. 2028-2031, Feb 1 2012.

[43]   A. M. Sanders, T. J. Dawidczyk, H. E. Katz, and J. D. Tovar, "Peptide-Based Supramolecular Semiconductor Nanomaterials via Pd-Catalyzed Solid-Phase "Dimerizations"," *Acs Macro Letters,* vol. 1, pp. 1326-1329, Nov 2012.

[44]   B. D. Wall, S. R. Diegelmann, S. M. Zhang, T. J. Dawidczyk, W. L. Wilson, H. E. Katz*, et al.*, "Aligned Macroscopic Domains of Optoelectronic Nanostructures Prepared via Shear-Flow Assembly of Peptide Hydrogels," *Advanced Materials,* vol. 23, pp. 5009-5014, Nov 16 2011.

[45]   G. S. Vadehra, B. D. Wall, S. R. Diegelmann, and J. D. Tovar, "On-resin dimerization incorporates a diverse array of pi-conjugated functionality within aqueous self-assembling peptide backbones," *Chemical Communications,* vol. 46, pp. 3947-3949, 2010.

[46]   Y. H. Sun, L. Jiang, K. C. Schuermann, W. Adriaens, L. Zhang, F. Y. C. Boey*, et al.*, "Semiconductive, One-Dimensional, Self-Assembled Nanostructures Based on Oligopeptides with pi-Conjugated Segments," *Chemistry-a European Journal,* vol. 17, pp. 4746-4749, Apr 2011.

[47]   E. K. Schillinger, E. Mena-Osteritz, J. Hentschel, H. G. Borner, and P. Bauerle, "Oligothiophene Versus beta-Sheet Peptide: Synthesis and Self-Assembly of an Organic Semiconductor-Peptide Hybrid," *Advanced Materials,* vol. 21, pp. 1562-+, Apr 27 2009.

[48]   D. A. Stone, L. Hsu, and S. I. Stupp, "Self-assembling quinquethiophene-oligopeptide hydrogelators," *Soft Matter,* vol. 5, pp. 1990-1993, 2009.

[49]   M. Amit, S. Appel, R. Cohen, G. Cheng, I. W. Hamley, and N. Ashkenasy, "Hybrid Proton and Electron Transport in Peptide Fibrils," *Advanced Functional Materials,* vol. 24, pp. 5873-5880, Oct 8 2014.

[50]   G. L. Eakins, R. Pandey, J. P. Wojciechowski, H. Y. Zheng, J. E. A. Webb, C. Valery*, et al.*, "Functional Organic Semiconductors Assembled via Natural Aggregating Peptides," *Advanced Functional Materials,* vol. 25, pp. 5640-5649, Sep 16 2015.

[51]   C. Berdugo, S. K. M. Nalluri, N. Javid, B. Escuder, J. F. Miravet, and R. V. Ulijn, "Dynamic Peptide Library for the Discovery of Charge Transfer Hydrogels," *Acs Applied Materials & Interfaces,* vol. 7, pp. 25946-25954, Nov 25 2015.

[52]   S. K. M. Nalluri, C. Berdugo, N. Javid, P. W. J. M. Frederix, and R. V. Ulijn, "Biocatalytic Self-Assembly of Supramolecular Charge-Transfer Nanostructures Based on n-Type Semiconductor-Appended Peptides," *Angewandte Chemie-International Edition,* vol. 53, pp. 5882-5887, Jun 2014.

[53]   S. K. M. Nalluri and R. V. Ulijn, "Discovery of energy transfer nanostructures using gelation-driven dynamic combinatorial libraries," *Chemical Science,* vol. 4, pp. 3699-3705, 2013.

[54]   S. K. M. Nalluri, N. Shivarova, A. L. Kanibolotsky, M. Zelzer, S. Gupta, P. W. J. M. Frederix*, et al.*, "Conducting Nanofibers and Organogels Derived from the Self-Assembly of Tetrathiafulvalene-Appended Dipeptides," *Langmuir,* vol. 30, pp. 12429-12437, Oct 21 2014.

[55]   H. A. M. Ardona and J. D. Tovar, "Energy transfer within responsive pi-conjugated coassembled peptide-based nanostructures in aqueous environments," *Chemical Science,* vol. 6, pp. 1474-1484, 2015.

[56] L. Chen, S. Revel, K. Morris, and D. J. Adams, "Energy transfer in self-assembled dipeptide hydrogels," *Chemical Communications,* vol. 46, pp. 4267-4269, 2010.

[57] J. Lopez-Andarias, M. J. Rodriguez, C. Atienza, J. L. Lopez, T. Mikie, S. Casado*, et al.*, "Highly Ordered n/p-Co-assembled Materials with Remarkable Charge Mobilities," *Journal of the American Chemical Society,* vol. 137, pp. 893-897, Jan 21 2015.

[58] J. L. Huang, L. Q. Lin, D. H. Sun, H. M. Chen, D. P. Yang, and Q. B. Li, "Bio-inspired synthesis of metal nanomaterials and applications," *Chemical Society Reviews,* vol. 44, pp. 6330-6374, 2015.

[59] K. Cung, B. J. Han, T. D. Nguyen, S. Mao, Y. W. Yeh, S. Y. Xu*, et al.*, "Biotemplated Synthesis of PZT Nanowires," *Nano Letters,* vol. 13, pp. 6197-6202, Dec 2013.

[60] S. Y. Lee, J. S. Lim, and M. T. Harris, "Synthesis and application of virus-based hybrid nanomaterials," *Biotechnology and Bioengineering,* vol. 109, pp. 16-30, Jan 2012.

[61] N. Nuraje, X. N. Dang, J. F. Qi, M. A. Allen, Y. Lei, and A. M. Belcher, "Biotemplated Synthesis of Perovskite Nanomaterials for Solar Energy Conversion," *Advanced Materials,* vol. 24, pp. 2885-2889, Jun 5 2012.

[62] S. N. Beznosov, P. S. Veluri, M. G. Pyatibratov, A. Chatterjee, D. R. MacFarlane, O. V. Fedorov*, et al.*, "Flagellar filament bio-templated inorganic oxide materials - towards an efficient lithium battery anode," *Scientific Reports,* vol. 5, Jan 13 2015.

[63] T. J. Zhang, W. Wang, D. Y. Zhang, X. X. Zhang, Y. R. Ma, Y. L. Zhou*, et al.*, "Biotemplated Synthesis of Gold Nanoparticle-Bacteria Cellulose Nanofiber Nanocomposites and Their Application in Biosensing," *Advanced Functional Materials,* vol. 20, pp. 1152-1160, Apr 9 2010.

[64] J. F. Liu, B. Uprety, S. Gyawali, A. T. Woolley, N. V. Myung, and J. N. Harb, "Fabrication of DNA-Templated Te and Bi2Te3 Nanowires by Galvanic Displacement," *Langmuir,* vol. 29, pp. 11176-11184, Sep 2013.

[65] E. Jackson, M. Ferrari, C. Cuestas-Ayllon, R. Fernandez-Pacheco, J. Perez-Carvajal, J. M. de la Fuente*, et al.*, "Protein-Templated Biomimetic Silica Nanoparticles," *Langmuir,* vol. 31, pp. 3687-3695, Mar 31 2015.

[66] R. A. McMillan, J. Howard, N. J. Zaluzec, H. K. Kagawa, R. Mogul, Y. F. Li*, et al.*, "A self-assembling protein template for constrained synthesis and patterning of nanoparticle arrays," *Journal of the American Chemical Society,* vol. 127, pp. 2800-2801, Mar 9 2005.

[67] H. Matsui, S. Pan, B. Gologan, and S. H. Jonas, "Bolaamphiphile nanotube-templated metallized wires," *Journal of Physical Chemistry B,* vol. 104, pp. 9576-9579, Oct 19 2000.

[68] R. Djalali, Y. Chen, and H. Matsui, "Au nanowire fabrication from sequenced histidine-rich peptide," *Journal of the American Chemical Society,* vol. 124, pp. 13660-13661, Nov 20 2002.

[69] B. M. Rabatic, R. C. Claussen, and S. I. Stupp, "Templated mineralization of peptide-based unsymmetric bolaamphiphiles," *Chemistry of Materials,* vol. 17, pp. 5877-5879, Nov 29 2005.

[70] E. D. Sone and S. I. Stupp, "Bioinspired Magnetite Mineralization of Peptide-Amphiphile Nanofibers," *Chemistry of Materials,* vol. 23, pp. 2005-2007, Apr 26 2011.

[71] A. Yildirim, H. Acar, T. S. Erkal, M. Bayindir, and M. O. Guler, "Template-Directed Synthesis of Silica Nanotubes for Explosive Detection," *Acs Applied Materials & Interfaces,* vol. 3, pp. 4159-4164, Oct 2011.

[72]   H. Acar, R. Garifullin, L. E. Aygun, A. K. Okyay, and M. O. Guler, "Amyloid-like peptide nanofiber templated titania nanostructures as dye sensitized solar cell anodic materials," *Journal of Materials Chemistry A,* vol. 1, pp. 10979-10984, 2013.

[73]   H. Acar, R. Genc, M. Urel, T. S. Erkal, A. Dana, and M. O. Guler, "Self-Assembled Peptide Nanofiber Templated One-Dimensional Gold Nanostructures Exhibiting Resistive Switching," *Langmuir,* vol. 28, pp. 16347-16354, Nov 27 2012.

[74]   M. A. Khalily, O. Ustahuseyin, R. Garifullin, R. Genc, and M. O. Guler, "A supramolecular peptide nanofiber templated Pd nanocatalyst for efficient Suzuki coupling reactions under aqueous conditions," *Chemical Communications,* vol. 48, pp. 11358-11360, 2012.

[75]   H. Ceylan, C. Ozgit-Akgun, T. S. Erkal, I. Donmez, R. Garifullin, A. B. Tekinay*, et al.*, "Size-controlled conformal nanofabrication of biotemplated three-dimensional TiO2 and ZnO nanonetworks," *Scientific Reports,* vol. 3, Jul 29 2013.

[76]   K. Tao, J. Q. Wang, Y. P. Li, D. H. Xia, H. H. Shan, H. Xu*, et al.*, "Short peptide-directed synthesis of one-dimensional platinum nanostructures with controllable morphologies," *Scientific Reports,* vol. 3, Sep 2 2013.

[77]   B. B. Zhou, Z. F. Sun, D. Li, T. Zhang, L. Deng, and Y. N. Liu, "Platinum nanostructures via self-assembly of an amyloid-like peptide: a novel electrocatalyst for the oxygen reduction," *Nanoscale,* vol. 5, pp. 2669-2673, 2013.

[78]   C. L. Chen, P. J. Zhang, and N. L. Rosi, "A new peptide-based method for the design and synthesis of nanoparticle superstructures: Construction of highly ordered gold nanoparticle double helices," *Journal of the American Chemical Society,* vol. 130, pp. 13555-+, Oct 15 2008.

[79]   J. A. Jiang, T. Y. Wang, and M. H. Liu, "Creating chirality in the inner walls of silica nanotubes through a hydrogel template: chiral transcription and chiroptical switch," *Chemical Communications,* vol. 46, pp. 7178-7180, 2010.

[80]   F. J. M. Hoeben, P. Jonkheijm, E. W. Meijer, and A. P. H. J. Schenning, "About supramolecular assemblies of pi-conjugated systems," *Chemical Reviews,* vol. 105, pp. 1491-1546, Apr 2005.

[81]   J. D. Tovar, "Supramolecular construction of optoelectronic biomaterials," *Acc Chem Res,* vol. 46, pp. 1527-37, Jul 16 2013.

[82]   M. Hasegawa and M. Iyoda, "Conducting supramolecular nanofibers and nanorods," *Chem Soc Rev,* vol. 39, pp. 2420-7, Jul 2010.

[83]   E. Moulin, J. J. Cid, and N. Giuseppone, "Advances in Supramolecular Electronics - From Randomly Self-assembled Nanostructures to Addressable Self-Organized Interconnects," *Advanced Materials,* vol. 25, pp. 477-487, Jan 18 2013.

[84]   H. A. Ardona and J. D. Tovar, "Peptide pi-Electron Conjugates: Organic Electronics for Biology?," *Bioconjug Chem,* vol. 26, pp. 2290-302, Dec 16 2015.

[85]   H. Shao, T. Nguyen, N. C. Romano, D. A. Modarelli, and J. R. Parquette, "Self-assembly of 1-D n-type nanostructures based on naphthalene diimide-appended dipeptides," *J Am Chem Soc,* vol. 131, pp. 16374-6, Nov 18 2009.

[86]   Y. K. Che, A. Datar, K. Balakrishnan, and L. Zang, "Ultralong nanobelts self-assembled from an asymmetric perylene tetracarboxylic diimide," *Journal of the American Chemical Society,* vol. 129, pp. 7234-+, Jun 13 2007.

[87] S. K. Nalluri, N. Shivarova, A. L. Kanibolotsky, M. Zelzer, S. Gupta, P. W. Frederix, *et al.*, "Conducting nanofibers and organogels derived from the self-assembly of tetrathiafulvalene-appended dipeptides," *Langmuir,* vol. 30, pp. 12429-37, Oct 21 2014.

[88] K. J. Channon, G. L. Devlin, and C. E. MacPhee, "Efficient Energy Transfer within Self-Assembling Peptide Fibers: A Route to Light-Harvesting Nanomaterials," *Journal of the American Chemical Society,* vol. 131, pp. 12520-+, Sep 9 2009.

[89] J. Lopez-Andarias, M. J. Rodriguez, C. Atienza, J. L. Lopez, T. Mikie, S. Casado*, et al.*, "Highly ordered n/p-co-assembled materials with remarkable charge mobilities," *J Am Chem Soc,* vol. 137, pp. 893-7, Jan 21 2015.

[90] Y. Yamamoto, T. Fukushima, Y. Suna, N. Ishii, A. Saeki, S. Seki*, et al.*, "Photoconductive coaxial nanotubes of molecularly connected electron donor and acceptor layers," *Science,* vol. 314, pp. 1761-1764, Dec 15 2006.

[91] C. Wang, Y. S. Guo, Y. P. Wang, H. P. Xu, R. J. Wang, and X. Zhang, "Supramolecular Amphiphiles Based on a Water-Soluble Charge-Transfer Complex: Fabrication of Ultralong Nanofibers with Tunable Straightness," *Angewandte Chemie-International Edition,* vol. 48, pp. 8962-8965, 2009.

[92] M. A. Khalily, M. Goktas, and M. O. Guler, "Tuning viscoelastic properties of supramolecular peptide gels via dynamic covalent crosslinking," *Organic & Biomolecular Chemistry,* vol. 13, pp. 1983-1987, 2015.

[93] I. Choi, I. S. Park, J. H. Ryu, and M. Lee, "Control of peptide assembly through directional interactions," *Chemical Communications,* vol. 48, pp. 8481-8483, 2012.

[94] R. Garifullin and M. O. Guler, "Supramolecular chirality in self-assembled peptide amphiphile nanostructures," *Chemical Communications,* vol. 51, pp. 12470-12473, 2015.

[95] G. B. Demirel, B. Daglar, and M. Bayindir, "Extremely fast and highly selective detection of nitroaromatic explosive vapours using fluorescent polymer thin films," *Chemical Communications,* vol. 49, pp. 6140-6142, 2013.

[96] S. Bhosale, A. L. Sisson, P. Talukdar, A. Furstenberg, N. Banerji, E. Vauthey*, et al.*, "Photoproduction of proton gradients with pi-stacked fluorophore scaffolds in lipid bilayers," *Science,* vol. 313, pp. 84-86, Jul 7 2006.

[97] H. E. Katz, A. J. Lovinger, J. Johnson, C. Kloc, T. Siegrist, W. Li*, et al.*, "A soluble and air-stable organic semiconductor with high electron mobility," *Nature,* vol. 404, pp. 478-481, Mar 30 2000.

[98] N. S. S. Kumar, M. D. Gujrati, and J. N. Wilson, "Evidence of preferential pi-stacking: a study of intermolecular and intramolecular charge transfer complexes," *Chemical Communications,* vol. 46, pp. 5464-5466, 2010.

[99] R. Garifullin, T. S. Erkal, S. Tekin, B. Ortac, A. G. Gurek, V. Ahsen*, et al.*, "Encapsulation of a zinc phthalocyanine derivative in self-assembled peptide nanofibers," *Journal of Materials Chemistry,* vol. 22, pp. 2553-2559, 2012.

[100] J. S. Stevens, A. C. de Luca, M. Pelendritis, G. Terenghi, S. Downes, and S. L. M. Schroeder, "Quantitative analysis of complex amino acids and RGD peptides by X-ray photoelectron spectroscopy (XPS)," *Surface and Interface Analysis,* vol. 45, pp. 1238-1246, Aug 2013.

[101] S. Roux, E. Zekri, B. Rousseau, M. Paternostre, J. C. Cintrat, and N. Fay, "Elimination and exchange of trifluoroacetate counter-ion from cationic peptides: a critical evaluation of different approaches," *Journal of Peptide Science,* vol. 14, pp. 354-359, Mar 2008.

[102] H. A. Behanna, J. J. J. M. Donners, A. C. Gordon, and S. I. Stupp, "Coassembly of amphiphiles with opposite peptide polarities into nanofibers," *Journal of the American Chemical Society,* vol. 127, pp. 1193-1200, Feb 2 2005.

[103] A. Das and S. Ghosh, "Supramolecular Assemblies by Charge-Transfer Interactions between Donor and Acceptor Chromophores," *Angewandte Chemie-International Edition,* vol. 53, pp. 2038-2054, Feb 17 2014.

[104] M. Kumar, K. V. Rao, and S. J. George, "Supramolecular charge transfer nanostructures," *Physical Chemistry Chemical Physics,* vol. 16, pp. 1300-1313, 2014.

[105] J. S. Renny, L. L. Tomasevich, E. H. Tallmadge, and D. B. Collum, "Method of Continuous Variations: Applications of Job Plots to the Study of Molecular Associations in Organometallic Chemistry," *Angewandte Chemie-International Edition,* vol. 52, pp. 11998-12013, Nov 11 2013.

[106] B. F. G. Johnson, "Nanoparticles in catalysis," *Topics in Catalysis,* vol. 24, pp. 147-159, Oct 2003.

[107] T. Tagata and M. Nishida, "Palladium charcoal-catalyzed Suzuki-Miyaura coupling to obtain arylpyridines and arylquinolines," *Journal of Organic Chemistry,* vol. 68, pp. 9412-9415, Nov 28 2003.

[108] D. Astruc, "Palladium catalysis using dendrimers: molecular catalysts versus nanoparticles," *Tetrahedron-Asymmetry,* vol. 21, pp. 1041-1054, May 17 2010.

[109] C. Ornelas, A. K. Diallo, J. Ruiz, and D. Astruc, ""Click" Polymer-Supported Palladium Nanoparticles as Highly Efficient Catalysts for Olefin Hydrogenation and Suzuki Coupling Reactions under Ambient Conditions," *Advanced Synthesis & Catalysis,* vol. 351, pp. 2147-2154, Sep 2009.

[110] B. Yuan, Y. Pan, Y. Li, B. Yin, and H. Jiang, "A Highly Active Heterogeneous Palladium Catalyst for the Suzuki–Miyaura and Ullmann Coupling Reactions of Aryl Chlorides in Aqueous Media," *Angewandte Chemie,* vol. 122, pp. 4148-4152, 2010.

[111] C. M. Crudden, M. Sateesh, and R. Lewis, "Mercaptopropyl-modified mesoporous silica: A remarkable support for the preparation of a reusable, heterogeneous palladium catalyst for coupling reactions," *Journal of the American Chemical Society,* vol. 127, pp. 10045-10050, Jul 20 2005.

[112] S. Patra, B. Viswanath, K. Barai, N. Ravishankar, and N. Munichandraiah, "High-Surface Step Density on Dendritic Pd Leads to Exceptional Catalytic Activity for Formic Acid Oxidation," *Acs Applied Materials & Interfaces,* vol. 2, pp. 2965-2969, Nov 2010.

[113] H. F. Lang, R. A. May, B. L. Iversen, and B. D. Chandler, "Dendrimer-encapsulated nanoparticle precursors to supported platinum catalysts," *Journal of the American Chemical Society,* vol. 125, pp. 14832-14836, Dec 3 2003.

[114] I. T. Horvath, "Solvents from nature," *Green Chemistry,* vol. 10, pp. 1024-1028, 2008.

[115] S. Minakata and M. Komatsu, "Organic Reactions on Silica in Water," *Chemical Reviews,* vol. 109, pp. 711-724, Feb 2009.

[116] B. Yuan, Y. Pan, Y. Li, B. Yin, and H. Jiang, "A Highly Active Heterogeneous Palladium Catalyst for the Suzuki–Miyaura and Ullmann Coupling Reactions of Aryl Chlorides in Aqueous Media," *Angewandte Chemie International Edition,* vol. 49, pp. 4054-4058, 2010.

[117] C.-W. Yang, K. Chanda, P.-H. Lin, Y.-N. Wang, C.-W. Liao, and M. H. Huang, "Fabrication of Au–Pd Core–Shell Heterostructures with Systematic Shape Evolution

Using Octahedral Nanocrystal Cores and Their Catalytic Activity," *Journal of the American Chemical Society,* vol. 133, pp. 19993-20000, 2011/12/14 2011.

[118] E. Dujardin, C. Peet, G. Stubbs, J. N. Culver, and S. Mann, "Organization of metallic nanoparticles using tobacco mosaic virus templates," *Nano Letters,* vol. 3, pp. 413-417, Mar 2003.

[119] H. I. Ryoo, J. S. Lee, C. B. Park, and D. P. Kim, "A microfluidic system incorporated with peptide/Pd nanowires for heterogeneous catalytic reactions," *Lab on a Chip,* vol. 11, pp. 378-380, 2011.

[120] H. Acar, R. Garifullin, and M. O. Guler, "Self-Assembled Template-Directed Synthesis of One-Dimensional Silica and Titania Nanostructures," *Langmuir,* vol. 27, pp. 1079-1084, Feb 1 2011.

[121] H. Ceylan, S. Kocabey, A. B. Tekinay, and M. O. Guler, "Surface-adhesive and osteogenic self-assembled peptide nanofibers for bioinspired functionalization of titanium surfaces," *Soft Matter,* vol. 8, pp. 3929-3937, 2012.

[122] P. Tsiveriotis and N. Hadjiliadis, "Studies on the interaction of histidyl containing peptides with palladium(II) and platinum(II) complex ions," *Coordination Chemistry Reviews,* vol. 192, pp. 171-184, Sep 1999.

[123] Y. Xia, Y. Xiong, L. Byungkwon, and S. E. Skrabalak, "Shape-Controlled Synthesis of Metal Nanocrystals:Simple Chemistry Meets Complex Physics?," *angewandte Chemie International Edition,* vol. 48, pp. 60-103, 2009.

[124] B. Cornils and W. A. Herrmann, *Aqueous-Phase Organometallic Catalysis: Concepts and Applications*: Wiley-VCH, 2004.

[125] H. Bernsmann, M. van den Berg, R. Hoen, A. J. Minnaard, G. Mehler, M. T. Reetz*, et al.*, "PipPhos and MorfPhos: Privileged monodentate phosphoramidite ligands for rhodium-catalyzed asymmetric hydrogenation," *Journal of Organic Chemistry,* vol. 70, pp. 943-951, Feb 4 2005.

[126] N. Miyaura and A. Suzuki, "Palladium-Catalyzed Cross-Coupling Reactions of Organoboron Compounds," *Chemical Reviews,* vol. 95, pp. 2457-2483, Nov 1995.

[127] B. Z. Yuan, Y. Y. Pan, Y. W. Li, B. L. Yin, and H. F. Jiang, "A Highly Active Heterogeneous Palladium Catalyst for the Suzuki-Miyaura and Ullmann Coupling Reactions of Aryl Chlorides in Aqueous Media," *Angewandte Chemie-International Edition,* vol. 49, pp. 4054-4058, 2010.

[128] K. Lang and J. W. Chin, "Bioorthogonal reactions for labeling proteins," *ACS Chem Biol,* vol. 9, pp. 16-20, Jan 17 2014.

[129] M. Boyce and C. R. Bertozzi, "Bringing chemistry to life," *Nat Methods,* vol. 8, pp. 638-42, Aug 2011.

[130] V. Hong, N. F. Steinmetz, M. Manchester, and M. G. Finn, "Labeling Live Cells by Copper-Catalyzed Alkyne-Azide Click Chemistry," *Bioconjugate Chemistry,* vol. 21, pp. 1912-1916, Oct 2010.

[131] J. C. Jewett and C. R. Bertozzi, "Cu-free click cycloaddition reactions in chemical biology," *Chem Soc Rev,* vol. 39, pp. 1272-9, Apr 2010.

[132] C. Uttamapinant, A. Tangpeerachaikul, S. Grecian, S. Clarke, U. Singh, P. Slade*, et al.*, "Fast, cell-compatible click chemistry with copper-chelating azides for biomolecular labeling," *Angew Chem Int Ed Engl,* vol. 51, pp. 5852-6, Jun 11 2012.

[133] P. V. Chang, J. A. Prescher, E. M. Sletten, J. M. Baskin, I. A. Miller, N. J. Agard*, et al.*, "Copper-free click chemistry in living animals," *Proceedings of the National Academy of Sciences of the United States of America,* vol. 107, pp. 1821-1826, Feb 2 2010.

[134] S. Sen Gupta, J. Kuzelka, P. Singh, W. G. Lewis, M. Manchester, and M. G. Finn, "Accelerated bioorthogonal conjugation: a practical method for the ligation of diverse functional molecules to a polyvalent virus scaffold," *Bioconjug Chem,* vol. 16, pp. 1572-9, Nov-Dec 2005.

[135] T. R. Chan, R. Hilgraf, K. B. Sharpless, and V. V. Fokin, "Polytriazoles as copper(I)-stabilizing ligands in catalysis," *Organic Letters,* vol. 6, pp. 2853-2855, Aug 19 2004.

[136] V. Hong, S. I. Presolski, C. Ma, and M. G. Finn, "Analysis and optimization of copper-catalyzed azide-alkyne cycloaddition for bioconjugation," *Angew Chem Int Ed Engl,* vol. 48, pp. 9879-83, 2009.

[137] C. Besanceney-Webler, H. Jiang, T. Q. Zheng, L. Feng, D. S. del Amo, W. Wang*, et al.*, "Increasing the Efficacy of Bioorthogonal Click Reactions for Bioconjugation: A Comparative Study," *Angewandte Chemie-International Edition,* vol. 50, pp. 8051-8056, 2011.

[138] D. C. Kennedy, C. S. McKay, M. C. B. Legault, D. C. Danielson, J. A. Blake, A. F. Pegoraro*, et al.*, "Cellular Consequences of Copper Complexes Used To Catalyze Bioorthogonal Click Reactions," *Journal of the American Chemical Society,* vol. 133, pp. 17993-18001, Nov 9 2011.

[139] H. B. Albada, F. Soulimani, B. M. Weckhuysen, and R. M. J. Liskamp, "Scaffolded amino acids as a close structural mimic of type-3 copper binding sites," *Chemical Communications,* pp. 4895-4897, Dec 14 2007.

[140] Z. Y. Ong, S. J. Gao, and Y. Y. Yang, "Short Synthetic beta-Sheet Forming Peptide Amphiphiles as Broad Spectrum Antimicrobials with Antibiofilm and Endotoxin Neutralizing Capabilities," *Advanced Functional Materials,* vol. 23, pp. 3682-3692, Aug 7 2013.

[141] Y. M. A. Yamada, S. M. Sarkar, and Y. Uozumi, "Amphiphilic Self-Assembled Polymeric Copper Catalyst to Parts per Million Levels: Click Chemistry," *Journal of the American Chemical Society,* vol. 134, pp. 9285-9290, Jun 6 2012.

[142] P. Davies, P. C. McHugh, V. J. Hammond, F. Marken, and D. R. Brown, "Contribution of Individual Histidines to Prion Protein Copper Binding," *Biochemistry,* vol. 50, pp. 10781-10791, Dec 20 2011.

[143] V. Bevilacqua, M. King, M. Chaumontet, M. Nothisen, S. Gabillet, D. Buisson, *et al.*, "Copper-chelating azides for efficient click conjugation reactions in complex media," *Angew Chem Int Ed Engl,* vol. 53, pp. 5872-6, Jun 2 2014.

[144] M. O. Guler and S. I. Stupp, "A self-assembled nanofiber catalyst for ester hydrolysis," *J Am Chem Soc,* vol. 129, pp. 12082-3, Oct 10 2007.

[145] N. Singh, M. P. Conte, R. V. Ulijn, J. F. Miravet, and B. Escuder, "Insight into the esterase like activity demonstrated by an imidazole appended self-assembling hydrogelator," *Chemical Communications,* vol. 51, pp. 13213-13216, 2015.

[146] T. L. Hsu, S. R. Hanson, K. Kishikawa, S. K. Wang, M. Sawa, and C. H. Wong, "Alkynyl sugar analogs for the labeling and visualization of glycoconjugates in cells," *Proc Natl Acad Sci U S A,* vol. 104, pp. 2614-9, Feb 20 2007.

[147] C. L. Jacobs, K. J. Yarema, L. K. Mahal, D. A. Nauman, N. W. Charters, and C. R. Bertozzi, "Metabolic labeling of glycoproteins with chemical tags through unnatural

sialic acid biosynthesis," *Applications of Chimeric Genes and Hybrid Proteins Pt B,* vol. 327, pp. 260-275, 2000.

[148] A. K. Sarkar, T. A. Fritz, W. H. Taylor, and J. D. Esko, "Disaccharide uptake and priming in animal cells: inhibition of sialyl Lewis X by acetylated Gal beta 1-->4GlcNAc beta-O-naphthalenemethanol," *Proc Natl Acad Sci U S A,* vol. 92, pp. 3323-7, Apr 11 1995.

[149] W. Liu, A. K. Herrmann, N. C. Bigall, P. Rodriguez, D. Wen, M. Oezaslan*, et al.*, "Noble Metal Aerogels-Synthesis, Characterization, and Application as Electrocatalysts," *Accounts of Chemical Research,* vol. 48, pp. 154-162, Feb 2015.

[150] S. Sanchez-Paradinas, D. Dorfs, S. Friebe, A. Freytag, A. Wolf, and N. C. Bigall, "Aerogels from CdSe/CdS Nanorods with Ultra-long Exciton Lifetimes and High Fluorescence Quantum Yields," *Advanced Materials,* vol. 27, pp. 6152-6156, Oct 28 2015.

[151] C. Z. Zhu, D. Du, A. Eychmuller, and Y. H. Lin, "Engineering Ordered and Nonordered Porous Noble Metal Nanostructures: Synthesis, Assembly, and Their Applications in Electrochemistry," *Chemical Reviews,* vol. 115, pp. 8896-8943, Aug 26 2015.

[152] D. Wen, A. K. Herrmann, L. Borchardt, F. Simon, W. Liu, S. Kaskel*, et al.*, "Controlling the Growth of Palladium Aerogels with High-Performance toward Bioelectrocatalytic Oxidation of Glucose," *Journal of the American Chemical Society,* vol. 136, pp. 2727-2730, Feb 19 2014.

[153] J. T. Korhonen, P. Hiekkataipale, J. Malm, M. Karppinen, O. Ikkala, and R. H. A. Ras, "Inorganic Hollow Nanotube Aerogels by Atomic Layer Deposition onto Native Nanocellulose Templates," *Acs Nano,* vol. 5, pp. 1967-1974, Mar 2011.

[154] W. Liu, A. K. Herrmann, D. Geiger, L. Borchardt, F. Simon, S. Kaskel*, et al.*, "High-Performance Electrocatalysis on Palladium Aerogels," *Angewandte Chemie-International Edition,* vol. 51, pp. 5743-5747, 2012.

[155] W. Liu, P. Rodriguez, L. Borchardt, A. Foelske, J. P. Yuan, A. K. Herrmann*, et al.*, "Bimetallic Aerogels: High-Performance Electrocatalysts for the Oxygen Reduction Reaction," *Angewandte Chemie-International Edition,* vol. 52, pp. 9849-9852, Sep 9 2013.

[156] A. Mahmood, R. Q. Zou, Q. F. Wang, W. Xia, H. Tabassum, B. Qiu*, et al.*, "Nanostructured Electrode Materials Derived from Metal-Organic Framework Xerogels for High-Energy-Density Asymmetric Supercapacitor," *Acs Applied Materials & Interfaces,* vol. 8, pp. 2148-2157, Jan 27 2016.

[157] E. Arslan, I. C. Garip, G. Gulseren, A. B. Tekinay, and M. O. Guler, "Bioactive supramolecular peptide nanofibers for regenerative medicine," *Adv Healthc Mater,* vol. 3, pp. 1357-76, Sep 2014.

[158] H. Ceylan, C. Ozgit-Akgun, T. S. Erkal, I. Donmez, R. Garifullin, A. B. Tekinay*, et al.*, "Size-controlled conformal nanofabrication of biotemplated three-dimensional TiO(2) and ZnO nanonetworks," *Sci Rep,* vol. 3, p. 2306, 2013.

[159] M. A. Khalily, O. Ustahuseyin, R. Garifullin, R. Genc, and M. O. Guler, "A supramolecular peptide nanofiber templated Pd nanocatalyst for efficient Suzuki coupling reactions under aqueous conditions," *Chem Commun (Camb),* vol. 48, pp. 11358-60, Nov 28 2012.

[160] P. Chen, Z. T. Xiong, J. Z. Luo, J. Y. Lin, and K. L. Tan, "Interaction of hydrogen with metal nitrides and imides," *Nature,* vol. 420, pp. 302-304, Nov 21 2002.

[161] F. Durap, M. Zahmakiran, and S. Ozkar, "Water soluble laurate-stabilized rhodium(0) nanoclusters catalyst with unprecedented catalytic lifetime in the hydrolytic dehydrogenation of ammonia-borane," *Applied Catalysis a-General,* vol. 369, pp. 53-59, Nov 15 2009.

[162] A. Staubitz, A. P. M. Robertson, and I. Manners, "Ammonia-Borane and Related Compounds as Dihydrogen Sources," *Chemical Reviews,* vol. 110, pp. 4079-4124, Jul 2010.

[163] S. Chaturvedi, P. N. Dave, and N. K. Shah, "Applications of nano-catalyst in new era," *Journal of Saudi Chemical Society,* vol. 16, pp. 307-325, Jul 2012.

[164] J. Dendooven, R. K. Ramachandran, K. Devloo-Casier, G. Rampelberg, M. Filez, H. Poelman*, et al.*, "Low-Temperature Atomic Layer Deposition of Platinum Using (Methylcyclopentadienyl)trimethylplatinum and Ozone," *Journal of Physical Chemistry C,* vol. 117, pp. 20557-20561, Oct 10 2013.

[165] C. R. Parkinson, M. Walker, and C. F. McConville, "Reaction of atomic oxygen with a Pt(111) surface: chemical and structural determination using XPS, CAICISS and LEED," *Surface Science,* vol. 545, pp. 19-33, Nov 1 2003.

[166] H. Hua, C. G. Hu, Z. H. Zhao, H. Liu, X. Xie, and Y. Xi, "Pt nanoparticles supported on submicrometer-sized TiO2 spheres for effective methanol and ethanol oxidation," *Electrochimica Acta,* vol. 105, pp. 130-136, Aug 30 2013.

[167] Q. M. Shen, L. P. Jiang, H. Zhang, Q. H. Min, W. H. Hou, and J. J. Zhu, "Three-dimensional Dendritic Pt Nanostructures: Sonoelectrochemical Synthesis and Electrochemical Applications," *Journal of Physical Chemistry C,* vol. 112, pp. 16385-16392, Oct 2008.

[168] W. Y. Chen, J. Ji, X. Feng, X. Z. Duan, G. Qian, P. Li, *et al.*, "Mechanistic Insight into Size-Dependent Activity and Durability in Pt/CNT Catalyzed Hydrolytic Dehydrogenation of Ammonia Borane," *Journal of the American Chemical Society,* vol. 136, pp. 16736-16739, Dec 3 2014.

[169] S. Akbayrak and S. Ozkar, "Ruthenium(0) Nanoparticles Supported on Multiwalled Carbon Nanotube As Highly Active Catalyst for Hydrogen Generation from Ammonia-Borane," *Acs Applied Materials & Interfaces,* vol. 4, pp. 6302-6310, Nov 2012.

[170] W. Chen, D. Li, Z. Wang, G. Qian, Z. Sui, X. Duan, *et al.*, "Reaction mechanism and kinetics for hydrolytic dehydrogenation of ammonia borane on a Pt/CNT catalyst," *AIChE Journal,* pp. n/a-n/a, 2016.

[171] M. Zahmakiran and S. Ozkar, "Metal nanoparticles in liquid phase catalysis; from recent advances to future goals," *Nanoscale,* vol. 3, pp. 3462-3481, 2011.

[172] A. Aijaz, A. Karkamkar, Y. J. Choi, N. Tsumori, E. Ronnebro, T. Autrey, *et al.*, "Immobilizing Highly Catalytically Active Pt Nanoparticles inside the Pores of Metal-Organic Framework: A Double Solvents Approach," *Journal of the American Chemical Society,* vol. 134, pp. 13926-13929, Aug 29 2012.

[173] W. Y. Chen, J. Ji, X. Z. Duan, G. Qian, P. Li, X. G. Zhou, *et al.*, "Unique reactivity in Pt/CNT catalyzed hydrolytic dehydrogenation of ammonia borane," *Chemical Communications,* vol. 50, pp. 2142-2144, 2014.

[174] J. L. Lu, B. S. Fu, M. C. Kung, G. M. Xiao, J. W. Elam, H. H. Kung, *et al.*, "Coking- and Sintering-Resistant Palladium Catalysts Achieved Through Atomic Layer Deposition," *Science,* vol. 335, pp. 1205-1208, Mar 9 2012.

[175] J. C. Lee, D. H. K. Jackson, T. Li, R. E. Winans, J. A. Dumesic, T. F. Kuech*, et al.*, "Enhanced stability of cobalt catalysts by atomic layer deposition for aqueous-phase reactions," *Energy & Environmental Science,* vol. 7, pp. 1657-1660, May 2014.